HYPERSONIC STATIONARY CROSSFLOW WAVES: RECEPTIVITY TO ROUGHNESS

A Thesis

Submitted to the Faculty

of

Purdue University

by

Varun Viswanathan

In Partial Fulfillment of the

Requirements for the Degree

of

Master of Science in Aeronautics and Astronautics

December 2019

Purdue University

West Lafayette, Indiana

THE PURDUE UNIVERSITY GRADUATE SCHOOL
STATEMENT OF DISSERTATION APPROVAL

Dr. Steven Schneider, Chair

School of Aeronautics and Astronautics

Dr. Matt Borg

School of Aeronautics and Astronautics

Dr. John Sullivan

School of Aeronautics and Astronautics

Approved by:

Dr. Gregory Blaisdell

Head of the School Graduate Program

I dedicate this to my middle school teachers who made me realize my passion for engineering.

ACKNOWLEDGMENTS

Firstly, I would like to thank Professor Steven Schneider for his advice, guidance, and encouragement as my advisor. I would also like to thank Professor John Sullivan, and Dr. Matt Borg for their help and insight as members of my committee. Funding for this project was provided by the Air Force Office of Scientific Research under grant FA-9550-17-1-0419.

I also want to thank Jerry Hahn, Robin Snodgrass, and Jim Younts of the ASL machine shop for building my model, additional inserts for the model, and other pieces of equipment that were used in this experiment. I would also like to thank John Phillips for his suggestions to help me fix my sensor wiring problems.

I would like thank all the members of Professor Schneider's Lab group: Elizabeth Benitez, Bradon Chynoweth, Josh Edeleman, Katie Gray, Adam Lay, Greg McKiernan, Phillip Portoni, Drew Turbeville, Mark Wason and Chris Yam. All the time spent in the lab would not have been as fun without you all.

Finally, I would like to thank my family for all their love and support.

TABLE OF CONTENTS

Page

LIST OF TABLES

LIST OF FIGURES

Figure Page

Figure Page

Figure Page

Figure Page

SYMBOLS

A	Disturbance amplitude
A_o	Initial disturbance amplitude
c	Chord length
d	Diameter of roughness element
f	Frequency
H	Shape factor
I	Pixel intensity matrix
k	Roughness height
L	Paint layer thickness
M	Mach number
N	Integrated amplification factor
P	Pressure
q	Heat transfer flux
R	Ideal gas constant for air
St	Stanton Number
T	Temperature
Re	Free stream Reynolds number per unit length
u	Velocity in inviscid streamline direction
u'	Disturbance of u
v	Velocity normal to invisicd streamline direction towards edge of boundary layer
v'	Disturbance of v

Greek

γ	Ratio of specific heats

δ	Boundary layer thickness
Δ	Change in a quantity
κ	Thermal conductivity
λ	Wavelength of roughness elements
μ	Kinematic viscosity
ρ	Density
χ	Crossflow Reyolds number

Subscripts

0	Stagnation condition
a	Method 1 of amplitude calculation
aw	adiabatic wall
b	Method 2 of amplitude calculation
$dark$	Camera data without blue LED or flow
e	Boundary layer edge condition
i	Initial condition
$model$	Temperature of surface of model below paint and insulating layer during a run
off	Camera data with blue LED and without flow
on	Camera data with blue LED and flow
ref	Reference condition
th	Theoretical laminar value
w	Pre-run temperature of the model
∞	Freestream condition

ABBREVIATIONS

AFOSR	Air Force Office of Scientific Research
BAM6QT	Boeing/AFOSR Mach-6 Quiet Tunnel
CFD	Computational Fluid Dynamics
CJC	Cold Junction Compensator
DAQ	Data Acquisition System
DNS	Direct Numerical Simulation
EMF	Electromagnetic Field
HIFiRE	Hypersonic International Flight Research Experimentation
HLB	Hypersonic Ludwieg Tube of Braunschweig
IR	Infrared
LPSE	Linear Parabolized Stability Equations
LST	Linear Stability Theory
NPSE	Nonlinear Parabolized Stability Equations
RIM	Rod Insertion Method
rms	root mean square
SB	Schmidt-Boelter Heat Transfer Gauge
SLDT	Supersonic Low Disturbance Wind Tunnel
TSP	Temperature Sensitive Paint

ABSTRACT

Viswanathan, Varun MSAA, Purdue University, December 2019. Hypersonic Stationary Crossflow Waves: Receptivity to Roughness. Major Professor: Steven P. Schneider.

Experiments were performed on a sharp-nosed 7° half-angle cone at a 6° angle of attack in the Boeing/AFOSR Mach-6 Quiet Tunnel (BAM6QT) to study the stationary crossflow instability and its receptivity to small surface roughness. Heat transfer measurements were obtained using temperature sensitive paint (TSP) and Schmidt Boelter (SB) heat transfer gauges. Great care was taken to obtain repeatable, quantitative measurements from TSP.

Consecutive runs were performed at a 0° angle of attack, and the heat transfer measured by the SB was found to drop as the initial model temperature increased, while other initial conditions such as stagnation pressure were held constant. This agreed with calculations done using a similarity solution. It was found that repeatable measurements at a 6° angle of attack could be made if the initial model temperature was controlled and the patch location that was used to calibrate the TSP was picked in a reasonable and consistent manner.

The Rod Insertion Method (RIM) roughness, which was used to excite the stationary crossflow instability, was found to be responsible for the appearance of the streaks that were analyzed. The signal-to-noise ratio in the TSP was too low to properly measure the streaks directly downstream of the roughness insert. The heat transfer along the streak experienced linear growth, peaked, and then slightly decayed. It is possible this peak was saturation. The general trend was that the growth of the streaks moved farther upstream as the roughness element height increased, which agreed with past computations and low speed experiments. The growth of the streak also moved farther upstream as the freestream Reynolds number increased. The amplitude of the

streaks was calculated by non-dimensionalizing the heat transfer using the laminar theoretical mean-flow solution for a 7° half-angle cone at a 6° angle of attack. The relationship between the amplitude and the non-dimensional roughness height was approximately linear in the growth region of the streaks.

1. INTRODUCTION AND MOTIVATION

1.1 Hypersonic Laminar-to-Turbulent Transition

As air flows past a surface, or a vehicle travels through air, a region of viscous fluid develops near the surface. This region is defined as the boundary layer. A laminar boundary layer exhibits smooth, ordered streamlines that are parallel to the surface. However, as disturbances from the surface or surroundings enter the boundary layer through the process of receptivity, this boundary layer becomes gradually less stable and may develop instabilities. These disturbances can grow both linearly and non-linearly until they start to break down. At this point, turbulent spots start to appear. These spots widen downstream until they finally coalesce into a fully transitioned, turbulent boundary layer [1]. Figure 1.1 outlines this path (labeled as path A) as well as other possible paths the flow can take to turbulence [2].

Boundary-layer transition can affect the drag, heating, moments, and skin friction a vehicle may experience. In fact, a turbulent boundary layer may cause 3-8 times more heating than its laminar counter-part. Consequently, predicting the onset of transition is important when designing the thermal protection system of a vehicle. If the boundary layer transitions earlier than expected, the heat shield may be inadequate, causing the vehicle to fail. On the other hand, if the vehicle is designed using the worst case scenario, the costs will be higher and the vehicle's performance will be limited due to the excess weight.

1.2 Importance of Quiet Wind Tunnels

Freestream noise levels in wind tunnels are usually characterized by the magnitude of the pressure fluctuations of the pitot pressure normalized by the mean pitot

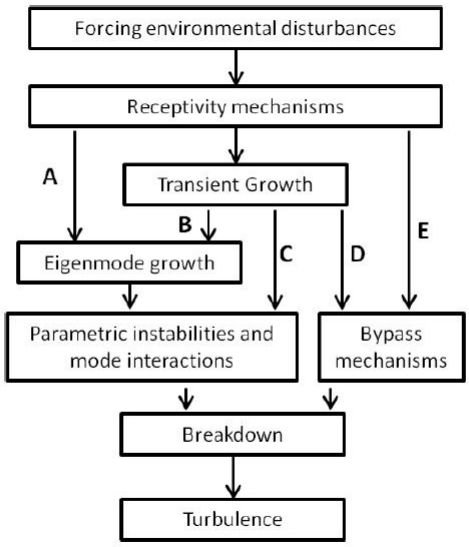

Figure 1.1. Diagram depicting the possible pathways to transition from laminar to turbulent flow. Figure redrawn from Fedorov [2].

pressure. Conventional (noisy) tunnels have a turbulent nozzle-wall boundary layer which radiates acoustic noise, causing freestream fluctuations several orders of magnitude higher than what is measured in flight [3]. These tunnels have noise levels on the order of 1-3 %, while flight noise levels are on the order of 0.05 % [4]. This noise can significantly impact laminar-turbulent transition [3], causing transition to occur farther upstream in conventional wind tunnels than it does in flight due to the higher noise levels [4].

This problem is visualized in Figure 1.2 which shows a shadowgraph image of a straight cone moving at Mach 4.3 down a ballistics range from left to right. The details can be found in Reference [5]. The bottom boundary layer is fully turbulent, and the acoustic noise radiating from this boundary layer can be seen. On the top boundary layer, there are two turbulent spots which also emit noise. In between, however, the boundary layer is laminar and no radiated acoustic noise can be seen. Thus, a laminar nozzle-wall boundary layer, which is a property of quiet tunnels, is

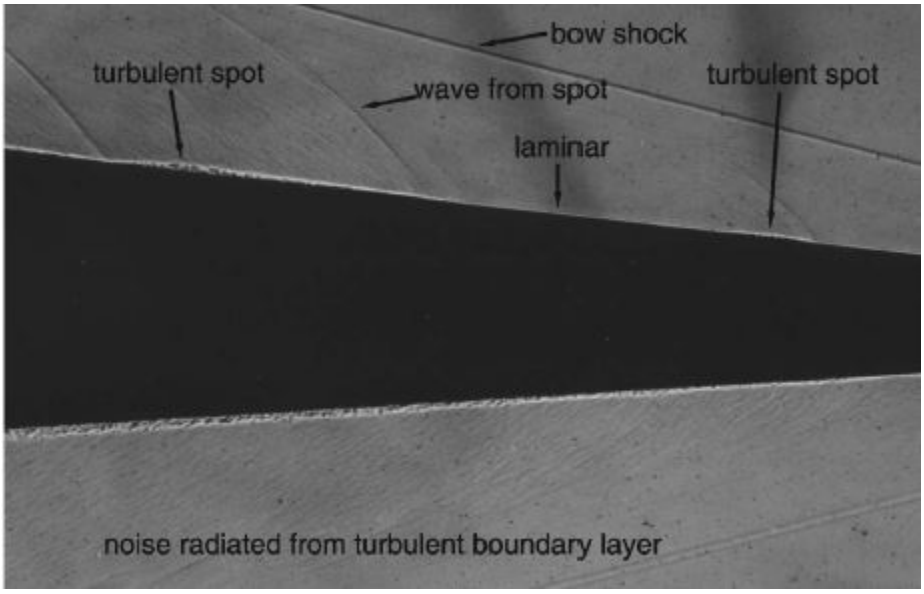

Figure 1.2. Shadowgraph of a sharp cone at Mach 4.3 traveling in a ballistics range depicting the noise radiated from a turbulent boundary layer. Photograph from Reference [3].

clearly vital to study flow phenomenon such as laminar-turbulent transition. Quiet tunnels have noise levels comparable to those measured in flight [4]. However, while quiet tunnels maintain realistic noise levels, they cannot simulate all aspects of flight such as high Reynolds numbers, high enthalpy flow, and chemically reacting flow.

1.3 Crossflow Instability

The crossflow instability occurs in a three-dimensional flow field in which spanwise pressure gradients exist. This includes geometries such as straight cones at an angle of attack, elliptical cones, swept wings, and rotating disks. For a cone at an angle of attack, the shock angle is higher at the wind ray than the lee ray, causing the pressure to be higher on the windward side compared to the leeward side. This circumferential pressure gradient drives flow from the windward side to the leeward side, resulting in a thinning and thickening of the boundary layer on each side.

Figure 1.3 depicts the boundary-layer mass flux profile resulting from crossflow [6]. Because the circumferential pressure gradient has a greater impact on the low momentum fluid near the wall than the fluid at the outer edge, the fluid near the wall is turned more than the outer flow. This induces a crossflow component of the velocity vector which is perpendicular to the inviscid streamlines. It is important to make the distinction that the crossflow component is not perpendicular to the freestream velocity vector but the edge velocity vector, which is inherently curved due to the pressure gradient.

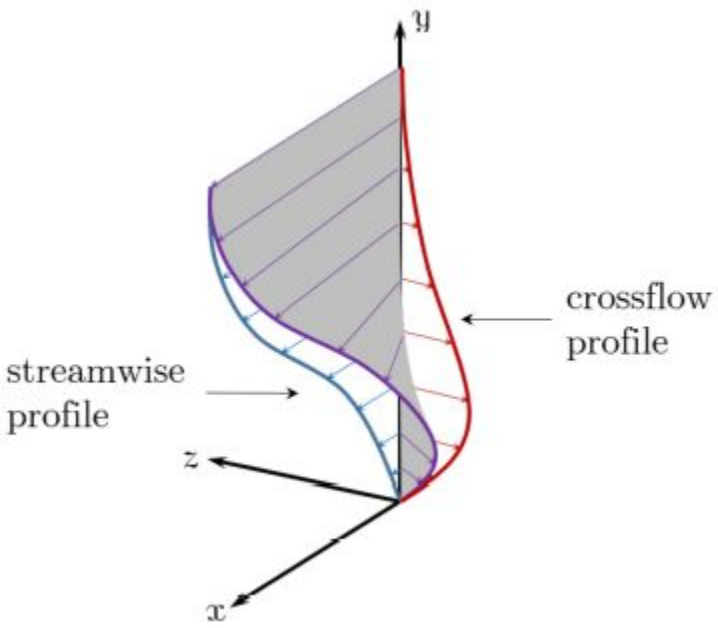

Figure 1.3. Schematic of crossflow in a three-dimensional boundary layer. The crossflow mass flux profile is inflected and is perpendicular to the streamwise profile. Image from Edelman [6]. Printed with permission from Edelman.

The crossflow component must be zero at the surface and the edge of the boundary layer because of the no-slip condition and the inviscid boundary condition, respectively. Also, its derivative must be zero at the edge to maintain continuity. Thus,

the crossflow profile is inflectional, which is a source of an inviscid instability. The crossflow instability manifests itself as co-rotating vortices that can be both travelling and stationary.

Stationary crossflow waves, as their name implies, are fixed with respect to the surface. These waves are nearly aligned with the inviscid streamlines [7]. Experimental studies on swept wings have revealed that stationary crossflow is sensitive to surface roughness parameters including diameter, height, and wavenumber [7] [8]. In addition, linear stability prediction methods are not helpful as the waves saturate long before transitioning [9]. Travelling waves, on the other hand, are vortices that move with respect to the surface.

Although both of these instabilities may be present at any given time, transition is usually caused by one or the other but not both. Even though linear theory for a swept wing predicts travelling waves to have a higher growth rate, many experiments have shown that transition is dominated by stationary crossflow [10]. Thus, figuring out which of the two mechanisms is the dominant disturbance is a question of receptivity. It has been shown at low speeds that stationary waves are the dominant transition mechanism in low noise environments while travelling waves dominate in noisy environments with higher levels of free stream turbulence [11].

It is less certain whether this also holds for high speed flows. Ward found the magnitude of the travelling waves to be stronger under noisy conditions in Mach 6 flow for a 7° half-angle cone at a 6° angle of attack. In addition, TSP streaks caused by stationary crossflow vortices were absent [12]. However, Borg was not able to observe any travelling disturbances under noisy flow at the same speed [13] [14]. Thus, more work may need to be done to fully understand the receptivity problem at high speeds.

As previously mentioned, stationary crossflow waves saturate long before transition. As they grow, they modulate the boundary layer, creating high shear layers in both the spanwise and normal directions. The shear layers caused by this instability give rise to a high frequency secondary instability which causes breakdown into transition [15] [16]. The secondary instability can be further classified into type-I

and type-II depending on the associated shear layer. The type-I secondary instability is driven by a velocity gradient in the spanwise direction and the type-II instability is driven by a velocity gradient in the normal direction. Figure 1.4 illustrates the location of both these instabilities [6].

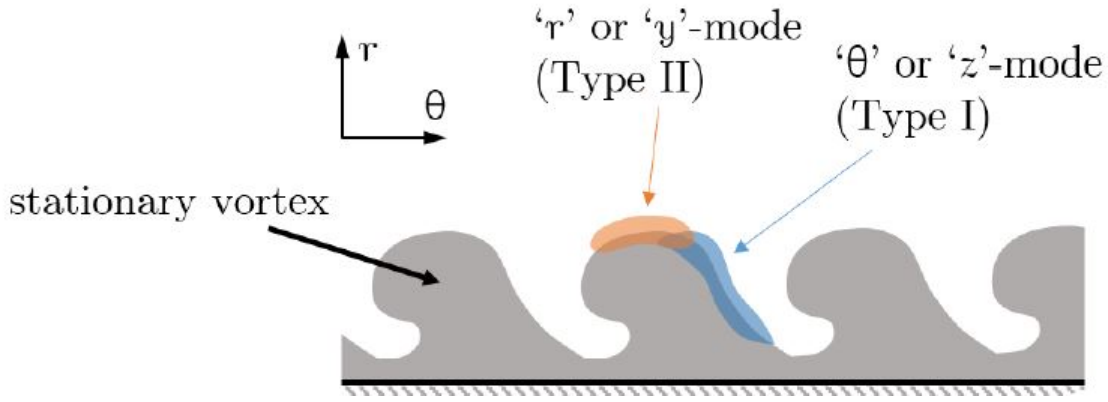

Figure 1.4. Schematic depicting the eigenfunction locations of the two types of secondary instabilities. Plot from Reference [6]. Printed with permission from Edelman.

At low speeds, the type-II instability was found to have a frequency approximately double that of the type-I instability. Both have been found to occur at a frequency an order of magnitude higher than the travelling wave [17]. More recent work by Edelman et al. on a straight cone at an angle of attack has also shown a measured instability with a frequency an order of magnitude higher than the travelling wave, in agreement with the predicted estimate for the type I instability [18]. In addition, the dominant breakdown mechanism when using discrete roughness seemed to be the modulated second mode instead of the secondary instability which was found to be the breakdown mechanism when using distributed roughness [19].

1.4 Objectives

The purpose of the current research is to understand how small roughness excite the stationary crossflow instability at Mach 6 using TSP. Thus, it should be noted that the secondary instabilty is outside the scope of this research. A hypersonic vehicle will have some amount of roughness on the surface which may excite the stationary crossflow instability because of the three-dimensionality of the flow. Compared to travelling waves, stationary crossflow waves have been shown to be the dominant mode of transition in flight conditions at low speeds, and is likely the dominant mode at high speeds as well. Thus, obtaining a better understanding of stationary crossflow is vital to predicting transition in hypersonic vehicles. The objectives of the present experiment are as follows:

- Use discrete roughness elements to induce stationary crossflow vortices over a 7° half-angle cone at a 6° angle of attack. Demonstrate that they are creating the streaks that are being analyzed.

- Quantify how the height of the roughness elements affects the amplitude of the stationary crossflow waves.

- Improve the TSP collection process by obtaining repeatable, consistent, and quantitative TSP heat transfer data of stationary crossflow vortices.

2. REVIEW OF LITERATURE

2.1 Low-Speed Primary Crossflow Instability

Results for low-speed crossflow may not necessarily be the same for high-speed crossflow. Thus, this literature review will be broken into two sections: one for low speed and one for high speed. It should also be noted that most of this review will cover the primary stationary crossflow instability instead of the travelling velocity as the stationary mode is the focus of this research. Most low-speed work on crossflow has been performed on swept wings. Crossflow work dates to the late 1940s. With the introduction of the swept wing, it was noticed that transition occured farther upstream on a swept wing than an unswept wing. In 1952, Gray conducted flow visualization experiments on a swept wing [20]. Using sublimation techniques, Gray noticed a pattern of streamwise streaks that were stationary and closely spaced together. Theoretical work by Owen and Randall confirmed that this pattern of streamwise streaks was the result of a crossflow instability [21]. They also defined a crossflow Reynolds number as

$$\chi = \frac{\rho_e w_{max} \delta}{\mu_e} \tag{2.1}$$

and concluded that this number was the governing parameter for crossflow induced transition. In this equation, ρ_e and μ_e are the density and dynamic viscosity at the edge of the boundary layer respectively, w_{max} is the maximum crossflow velocity, and δ is the boundary-layer thickness.

About 30 years later in 1984, Poll performed transition experiments on a yawed cylinder at speeds around 30 $\frac{m}{s}$ [22]. Both china clay evaporation and oil flow were used to visualize the stationary vortices. Measurements revealed a pattern of tightly spaced streaks followed by a transition front with a distinct sawtooth pattern. This front moved upstream as the freestream velocity and yaw angle increased. Measure-

ments were also taken with a hot wire and pitot probe. An instability on the order of 1 kHz was measured, which is now accepted as the primary travelling wave. A high frequency disturbance was also found on the order of 17.5 kHz, which is now generally accepted as the secondary instability [16]. Poll also stated that the crossflow Reynolds number was not enough to characterize transition, and that two other flow parameters were needed such as the shape factor, H, and the Reynolds number.

Bippes and Nitschke-Kowsky studied stationary crossflow on a swept flat plate [23] [24]. Using hot wire probes and flow visualization, they found the stationary vortices to be approximately aligned with the edge velocity within 3-5°. It was also found that the traveling waves were amplified at the same crossflow Reynolds number, suggesting that traveling waves are a primary instability as well. By using two hot wires and measuring the phase difference between the wave packets, a propagation angle was calculated. Only one propagation direction was found for the traveling waves, which contradicted the results from linear stability theory (LST). In addition, the frequency of the traveling wave was found to decrease with the growth of the boundary layer as the flow moved downstream.

Linear theory predicts travelling waves to have higher growth rates than stationary waves in low disturbance environments which would lead one to think that travelling waves are the dominant mode of transition, although this is not what was seen in experiments. This is likely due to two reasons [25]. First of all, linear theory does not take into account receptivity, which shows that the initial amplitudes of stationary crossflow waves are much higher than the traveling wave in low disturbance environments, with typical surface roughness. Second, the stationary vortices are virtually aligned with the invisicd streamlines, allowing the same v' and u' disturbances to act on a fluid element as it moves downstream. Note that v and u are the normal and axial velocities respectively. This results in a net effect significantly altering the mean flow, even though linear theory may predict low growth of stationary waves. This modification of the mean flow results in high shear layers subject to secondary instabilities which eventually lead to breakdown. Because of the nonlinear saturation

of stationary crossflow vortices long before breakdown, the use of linear methods such as LST and linear parabolized stability equations (LPSE) is of limited usefulness. To help verify this, Radeztksy et al. performed transition experiments on a swept wing with varying surface roughness [26]. Although linear theory did seem to predict the expected wavelengths and mode shapes accurately, the experimental amplitude data showed clear saturation, while several different linear computations over-predicted the growth rate. In fact, the predicted growth rates were not even of the right signs at some axial locations. On the other hand, linear theory can predict growth rates for travelling crossflow waves relatively well [25]. Because there is no mean flow modification, this mode continues to grow up until transition. Thus the e^N method for travelling waves may still be valid in high-disturbance environments.

In an effort to figure out the receptivity problem, Müller and Bippes translated a swept flat plate inside a test section in the spanwise direction [27]. It was found that both the spanwise variation of the wavelength and the amplitude of the stationary crossflow vortices shifted with the model. This showed that surface roughness was more effective at stimulating the stationary mode than the characteristics of the freestream flow. Deyhle and Bippes then performed experiments to determine which conditions determined whether stationary or travelling crossflow dominated transition [28]. It was found that neither instability was receptive to sound, 2-D roughness, or non-uniformities in the test section. The latter was especially interesting since Görtler vortices, which are another type of longitudinal vortices, can be initiated by small non-uniformities produced by screens in wind tunnels [29]. Additionally, it was found that at higher turbulence levels ($> 0.02\%$), the travelling mode dominated transition depending on the surface roughness, while at lower levels of turbulence, stationary crossflow dominated [28]. Many other experiments showcase similar results [30].

Following this work, Radeztsky et al. studied the receptivity of stationary crossflow to both distributed surface roughness and discrete roughness elements on a swept wing [8]. This study was the first experiment to make controlled measurements of how the surface roughness induced stationary crossflow. A combination of naphthalene

flow visualization via sublimation and hot-wire measurements were used to study the stationary crossflow. It was found that the transition location moved farther downstream as the surface roughness or the height of the individual roughness elements decreased. In fact, roughness elements with a roughness Reynolds number, Re_k, as low as 0.12 were able to excite stationary crossflow waves. The roughness Reynolds number is defined as

$$Re_k = \frac{kU_k}{\nu_k} \tag{2.2}$$

where k is the roughness height, U_k is the streamwise velocity of the flow at a height k in absence of the roughness element, and ν_k is the kinematic viscosity of the flow at a height k in the absence of the roughness element. Roughness elements placed far upstream or downstream of the neutral point had no effect on the transition location assuming it was not big enough to directly trip the flow. The neutral point refers to the axial location at which the crossflow waves first begin to amplify. Sound or 2-D roughness had no observed effect on the development of the vortices, similar to results found by Deyhle and Bippes [28]. It was also found that below a critical diameter, isolated roughness elements had almost no effect on the observed waves regardless of height as long as they were not big enough to trip the flow. This seemed to agree with linear computations done by Choudhari [31]. Several other experiments and observations also suggested that the stationary crossflow mode is excited by surface roughness [28].

Many other low-speed experiments have been performed to quantify the relationship between surface roughness and the receptivity and growth of stationary crossflow waves. Reibert et al. performed experiments on a swept wing using discrete roughness elements and measured the velocity profile in the normal and spanwise directions using hot wires [32]. In doing so, they were able to obtain velocity contours at different streamwise positions. From the normal velocity profiles at different spanwise locations at a particular streamwise position, they found the average velocity profile, and then found the deviation from the average for each spanwise location. By plot-

ting the root mean square (rms) value of this deviation at every normal position, the stationary crossflow mode shape was acquired. This process is given as Equation 2.3.

$$\left(\rho\bar{U} - \left\langle \rho\bar{U} \right\rangle_{\theta}\right)_{rms} \tag{2.3}$$

Because the highest rms value was at a wall-normal position of 0.9 mm, this was the location used to gather information pertaining to the decomposition of the instability into multiple spanwise modes. The reader is referred to this reference for a more detailed explanation. When using a roughness spacing of 12 mm, which is the most unstable wavelength as predicted by linear theory, most of the instability was found to be contained in the 12 mm mode in the linear region while there was some modal activity at 4 mm and 2 mm. As the vortices approached saturation, energy seemed to cascade from the 12 mm wavelength into lower wavelength groups signifying nonlinear interaction between the different modes. By exciting crossflow using roughness spaced at 36 mm, the energy was contained in the 36 mm, 18 mm, etc. modes. Again, nonlinear interaction was observed between the different modes as saturation occured. Interestingly, no subharmonics of the roughness spacing ever appeared. These results show that consideration of nonlinear interaction between multiple modes is vital in predicting transition.

Haynes et al. performed a computational study in which nonlinear growth was taken into account as well as curvature and non-parallel effects [33]. Computed N factors, streamwise velocity contour plots, and u_{rms} values (plotted in the normal direction) were compared with experimental results from Reibert et al [32]. Firstly, it was found that the inclusion of curvature had a stabilizing effect on the spatial growth of the stationary vortices, while it had no effect on the streamwise wavenumber. This was attributed to stronger nonlinear interaction in the absence of curvature. It was also found that non-parallel effects were destabilizing. Also, if the initial amplitudes were high enough to cause saturation and nonlinear interaction, it was found that linear theory overestimated the growth rate, while the nonlinear parabolized stability equations (NPSE) agreed remarkably well with experimental data provided by Reibert et al. The streamwise velocity contours also showed excellent agreement. This implied

that DNS may not be necessary for computations such as these. It should be noted, however, that NPSE requires an accurate determination of initial conditions either from experiments or receptivity analysis.

Adding to this work, Saric et al. excited the stationary crossflow mode with roughness elements spaced at subcritical wavelengths, and found transition to be delayed from the smooth case [34]. By using 8 mm spaced roughness elements, early growth of the 12 mm mode was suppressed. Once the 8 mm mode saturated, this led to rapid decay, allowing longer wavelength disturbances caused by surface irregularities to grow and lead to transition. They also found that the saturation amplitude remained constant while the roughness height was varied for a fixed roughness spacing. In contrast, the initial disturbance amplitude has been found to increase as the height of the roughness element is increased [34] [35] [10].

It should be noted that the receptivity process regarding the selection between traveling crossflow and stationary crossflow is not as binary as it seems. In other words, high turbulence levels may not necessarily preclude transition dominated by stationary crossflow [36]. White et al. conducted transition experiments on a swept wing in a wind tunnel with turbulence levels of 0.03% [25], nominally higher than the turbulence criterion of 0.015% found by Deyhle and Bippes [28]. Tests were first conducted on polished aluminum with an rms surface roughness less than 0.5 μm. Using naphthalene, White observed transition to occur between $\frac{x}{c}$=0.40 and 0.50. However, the transition front displayed a saw-tooth pattern characteristic of transition dominated by stationary vortices. Roughness elements with a height of 50 μm were then placed at $\frac{x}{c}$=0.025. Surprisingly, the transition front had moved forward to $\frac{x}{c}$=0.35, and the saw-tooth pattern had disappeared, signifying transition dominated by traveling waves. These results seem to imply that a simple turbulence criterion is not sufficient to discern which mode will be excited, and that one must instead consider the interaction between turbulence levels and surface roughness. It has also been shown that the interaction between freestream turbulence and surface roughness may also play a role in the initial amplitudes of the instability [35]. The

reader is directed to Saric's review [10] for a more comprehensive review of low-speed crossflow experiments and computations.

2.2 High-Speed Primary Crossflow Instability

Although most of the existing crossflow literature is on low-speed flow, the past 10 years has seen a recent influx in supersonic and hypersonic experiments dealing with crossflow. Most of the high-speed work on stationary crossflow is either on a circular cone at an angle of attack or an elliptical cone at a 0° angle of attack. King studied crossflow on 5° half-angle cone at various angle of attacks in Mach 3.5 flow in both noisy and quiet flow conditions [37]. The transition front was observed to be leeside forward in both the noisy and quiet cases, although the pattern occured to much less of a degree in the quiet flow condition case.

In an effort to control and stabilize stationary crossflow in supersonic flow with a Mach number of 2.4, Saric et al. placed roughness elements near the leading edge of a wing with a sweep angle of 73° [36]. This wing was swept past the Mach angle in order to have subsonic flow at the leading edge. By ensuring that the flow was subsonic, there was no leading edge shock and the flow disturbance environment was minimized. The Mach angle was about 25° and can be found using Equation 2.5.

$$\text{Mach angle} = \sin^{-1}\left(\frac{1}{M}\right) \tag{2.4}$$

It was found that transition was delayed when using roughness elements placed at a subcritical wavelength compared to when placed at a critical wavelength predicted by linear theory. Unfortunately, because most of their data was qualitative, they did not provide quantitative comparisons. Similar to their work, Semionov et al. performed experiments on a wing with a sweep of 40° and a Mach number of 2.0 [38]. They studied the development of stationary crossflow by using distributed roughness longitudinal strips as well as dot roughness elements. The roughness dots were found to move transition forward by 30% compared to the smooth case, likely because they

excited an unstable wavelength. However, the longitudinal strips were able to delay transition by 40 %, thus showcasing the importance of the shape and placement of the roughness in the excitation of stationary crossflow.

Stationary crossflow on a 7° half-angle cone at a 6.6° angle of attack was studied by Kroonenberg et al. in the Hypersonic Ludweig Tube Braunschweig (HLB) at Mach 6 [39]. The HLB is a conventional tunnel and therefore has noise levels between 1% and 1.5%. Heat transfer measurements were obtained using IR thermography, and the relative N factors were calculated. The relative N factors are defined as

$$\Delta N_i = ln\left(\frac{A_i}{A_o}\right) \tag{2.5}$$

where A_i is the amplitude at position i on the cone, and A_o is the initial amplitude. It was found that the N factors could be modified by the placement of artificial roughness elements on the cone. Also, roughness elements that were more than 100° from the wind ray had less of an impact on the flow, due to the thickening of the boundary layer.

Choudhari et al. studied Mach 6 flow over a 7° half-angle cone at angles of attack of 3° and 6° [40] using LST, LPSE, and NPSE. The freestream Reynolds number was kept at $10.8 \times 10^6\ m^{-1}$ for all simulations. Also, the stagnation temperature and inital wall temperature were 430 K and 300 K respectively. It was found that the 3-D geometry of the flow caused the boundary layer near the leeward plane of symmetry to thicken, creating a mushroom-like structure. The shear layers in this structure led to second-mode waves being unstable along the lee ray. Using LST and LPSE, they found the maximum N factors for stationary crossflow to be 10 and 20 for the 3° and 6° angle of attack cases respectively. The second-mode N factors for the 6° angle of attack case were found to be 6 and 16 for the wind ray and lee ray respectively. The azimuthal location of maximum crossflow was found to be between 130° to 140° from the wind ray for a 6° angle of attack, while it was found to be 10° lower for the 3° angle of attack case. Finally, the most amplified wavenumber for stationary crossflow was found to be between 42 to 55 per cone circumference.

To complement these results, Balakumar et al. performed a direct numerical simulation (DNS) study of Mach 6 flow on a 7° half-angle cone at a 6° angle of attack and a freestream Reynolds number of 10.4×10^6 m^{-1} [41]. The stagnation temperature and inital wall temperature were 438 K and 300 K respectively. Two types of roughness arrangements were studied. The first setup involved placing roughness elements periodically around the azimuth at a single axial location of 50 mm. The second pattern involved distributing the elements at different axial locations along a ray of a constant azimuthal angle. The most amplified wavenumber of the stationary crossflow instability was found to be between 30-70 per cone circumference which agreed with the linear computations made by Choudhari [40]. With the first arrangement of roughness elements, they were able to track the migration and growth of the vortices originating from the roughness elements from the windward side to the leeward side. No significant disturbances were created by the elements on the leeward side (between 90° to 180°), which was attributed to the boundary layer being 10 times thicker on the leeward plane than the windward plane. However, the perturbations that grew from the second roughness pattern were harder to track as they evolved downstream, due to the vortices combining and separating.

Another DNS study was done by Gronvall et al., of Mach 6 flow on a 7° half-angle cone at a 6° angle of attack with a freestream Reynolds number of 9.5×10^6 m^{-1} [42]. The stagnation temperature and inital wall temperature were 438 K and 300 K respectively. Instead of using discrete roughness elements, they used digitally filtered roughness to mimic the experimental distributed roughness created by the application of TSP in the past [43]. Two roughness heights were used: one with a rms of 10 μm and one with a rms of 20 μm. The roughness with the larger magnitude was observed to induce the development of stationary crossflow farther upstream than the smaller magnitude roughness did. Contours of the heat flux measurements were found to be in good qualitative agreement with experiment results made by Swanson et al. [44]. The disturbance wavenumber of the stationary vortices was between 35 to 50, which agreed with earlier linear computations [40] and DNS computations [41].

Adding to previous work, Schuele performed experiments on a 7° half-angle cone in Mach 3.5 quiet flow [45]. The cone was placed at a 4.2° angle of attack, and the tests were conducted at the Mach 3.5 supersonic low disturbance wind tunnel (SLDT) at the NASA Langley Research Center. To introduce roughness into the flow, dimples were added to Torlon models at wavenumbers of both 45 and 68 per cone circumference. Forty-five was used because it was the most amplified band of stationary crossflow modes (i.e. the critical wavenumber) as calculated by linear theory. Sixty-eight was chosen as a subcritical wavenumber in the hopes of delaying transition, by exciting vortices at a different wavenumber and suppressing the most amplified wavenumber. Transition was measured by looking for a drop in the rms of the pressure variation in the azimuthal direction. For a stagnation pressure of 45 psia, it was found that the transition Reynolds number moved downstream from 2.5×10^6 to 3.5×10^6 when the roughness wavenumber was changed from 45 to 68 per cone circumference. This was the same trend found by Semionov et al. [38].

Craig and Saric performed detailed off-surface measurements in a hypersonic crossflow-dominated flow [46] [47] [48]. They conducted tests in the Mach 6 quiet tunnel at Texas A&M University on a 7° half-angle cone at a 5.6° angle of attack. By using a hot-wire anemometer, they were able to take boundary-layer measurements and obtain contour maps of the mean mass flux outlining the characteristic stationary-vortex rollover structure. The dominant azimuthal wavenumber of the stationary crossflow vortices was found to be between 50 and 60 per cone circumference, which agreed with previous computations and experiments. They found the growth of the stationary vortices to be consistent with the growth at low speeds. As in low speed flow, the stationary instability quickly reached saturation and attenuated, the whole time causing substantial modification to the mean flow. The majority of the modification to the boundary layer was initially concentrated high in the boundary layer, and moved towards the wall as the disturbance grew downstream. This was quantified by the modal shape which is given by Equation 2.3. The modal shape started with one peak high in the boundary layer. As the stationary vortices devel-

oped downstream, a secondary peak beneath the initial peak formed. The formation of the second peak seemed to coincide with the start of nonlinear saturation of the vortices.

To gain more insight on stationary crossflow vortices at high speeds, Ward performed experiments on a 7° half-angle cone at a 6° angle of attack at the Purdue BAM6QT [12]. Thus, the noise levels were less than 0.05 % if the bleed slots were kept open. Data were collected using TSP. Under noisy flow, no evidence for stationary crossflow could be found, so most of his experiments were performed under quiet flow. Ward defined the amplitude of the streak by

$$Amplitude = \frac{q_{max} - q_{th}}{q_{th}} \tag{2.6}$$

where q_{max} is the maximum heat transfer at each axial location and q_{th} is the laminar, theoretical heat transfer on a sharp cone at a zero angle of attack at the respective axial location.

He found that the pattern of growth was qualitatively similar to that in low speed flow in which the amplitude would increase, saturate, and then decay. The growth of the streak would move farther upstream as the freestream Reynolds number was increased. Ward also did work on the receptivity of stationary crossflow to surface roughness. Different roughness inserts were tested which were made from Torlon and consisted of dimples around the azimuth. The effect of roughness was more pronounced as the freestream Reynolds number was increased. It was also found that slight variations in the paint finish due to different paint jobs did not qualitatively affect the flow when roughness was used, while it did under the smooth insert case. Finally, he also concluded that the depth of the dimples had a noticeable effect on the growth of the stationary vortices.

Matlis et al. extended Schuele's work at Mach 3.5 [45] to the Mach 6 regime [49]. They studied the effect of discrete roughness on a 7° half-angle cone at a 6° angle of attack at the Air Force Academy Mach 6 Ludwieg tube. Note that this is a conventional wind tunnel with noise levels on the order of 1-3 %. The flow was excited

using removable nosetips manufactured with dimples around the azimuth. A nosetip with a dimple wavenumber of 45 per cone circumference was kept as the baseline, as this was in the range of the most amplified stationary crossflow wavenumber according to computations. A nosetip with a wavenumber of 68 per cone circumference was used in an attempt to delay transition by following the technique of Scheule et al [45]. Oil flow visualization was used to study the stationary crossflow, and pitot pressure measurements were utilized to detect transition. It was found that using the roughness with a wavenumber of 68 delayed transition by 25 % when compared to a roughness with a wavenumber of 45. The difference between this and the work done by Schuele at al. was attributed to the different Mach number and tunnel noise level.

As previously stated, high speed crossflow work has also been done on elliptical cones. Huntley et al. used Rayleigh scattering to study Mach 8 flow in a conventional tunnel over an elliptical cone at a 0° angle of attack with a 4:1 aspect ratio in which the minor axis had a 4.38° half-angle [50]. Transition was observed to begin closer to the minor axis of the cone than in the regions off the center-line in which the predicted crossflow component was stronger.

Kimmel et al. studied laminar-turbulent transition in a Mach 8 conventional tunnel on an elliptical cone at a 0° angle of attack with a 2:1 aspect ratio in which the minor axis had a 7° half-angle [51]. The freestream Reynolds number was varied from 1.7×10^6 m^{-1} to 6.7×10^6 m^{-1}. The stagnation temperature and initial wall temperature were 728 K and 306 K respectively. Discrete roughness elements were placed around the azimuth and stationary vortices were studied using surface heat transfer gauges and oil-flow visualization. The spacing of peaks in the surface heat transfer around the azimuth obtained from the heat transfer gauges seemed to match up with the spacing of the utilized discrete roughness elements. This alluded to the the potential for receptivity research using controlled disturbances.

The elliptical cone with a 2:1 aspect ratio in which the minor axis has a 7° half-angle is a popular geometry to study crossflow with. Borg has studied this geometry at a 0° angle of attack extensively as part of the Hypersonic International Flight Research

Experimental (HIFire) program in an effort to gather more insight on the transition mechanism for this geometry in both quiet flow and noisy flow [52] [13] [14]. This work was done in the Purdue BAM6QT, and data was collected using a combination of pressure sensors and infrared thermography. The traveling crossflow instability was not found to be the dominant transition mechanism in either quiet or noisy flow. While the traveling crossflow instability was observed in quiet flow, it was absent in noisy flow. In fact, neither traveling nor stationary waves were observed under noisy flow. However, when the angle of attack was changed to 2°, transition moved downstream. This suggests that while the role of the crossflow instability in transition under noisy flow in this geometry may be unclear, it at least has some type of effect. These angle of attack results are similar to those found by Juliano and Borg [53]. They utilized TSP to study the effect of an angle of attack on this geometry in the Purdue BAM6QT under quiet flow. Transition was found to move upstream as the freestream Reynolds number increased. Streaks that were seen when the model was placed at a 0° angle of attack disappeared when the model was placed at an angle of attack of 4°.

A cone of the same geometry at a 0° angle of attack was studied in a Mach 6 conventional wind tunnel using IR thermography by Neel et al [54]. Two models of the same geometry, but a smaller scale, were used. One had patterned roughness near the attachment line due to machining errors and was referred to as the rough model. Streaks caused by the stationary vortices were captured from the IR thermography despite the fact that the tests were done under noisy flow. The rough model displayed higher levels of heat transfer and experienced transition farther upstream than the other model.

To complement the experimental work done on the elliptical cone with this particular geometry at a 0° angle of attack, Dinzl et al. performed a DNS study of Mach 6 flow at a freestream Reynolds number of $8.1 \times 10^6\ m^{-1}$ and $11.8 \times 10^6\ m^{-1}$ [55]. The stagnation temperature was 410 K for the former case and 429 K for the latter case, while the initial wall temperature was 300 K for both cases. Distributed roughness

with maximum heights ranging from 0.5 to 4.0 μm was used to excite the flow. While the most unstable wavenumber remained the same, the overall pattern of the heat transfer along the cone seemed to be extremely sensitive to the initial conditions regarding the distributed roughness. This makes it difficult for a computational solution to match experimental results. However, discrete roughness elements should make this less challenging. The contrast between the heat transfer along streaks and the flow in between was found to be higher than the contrast found on straight cones. This was attributed to the higher curvature found on straight cones causing the vortices to lift from the surface. The streaks spread as the flow traveled downstream, and this was found to be a function of the azimuthal location and the freestream Reynolds number. As the roughness height was increased, the initial amplitude increased, while the growth rate and saturation amplitudes remained the same. Vortices were also found to coalesce and separate as they moved downstream. Figure 2.1 shows density contours in the spanwise direction for multiple axial locations, clearly illustrating the grouping and separating of these vortices. The combination and separation of the vortices is apparent from this image.

The effect of discrete roughness on the same geometry under Mach 6 flow at a 0° angle of attack was studied by Moyes et al [56]. The amplitude was calculated using the NPSE. The initial amplitude, which would mimic discrete roughness, was specified by a velocity which was normalized by the edge velocity. It was found that as the initial amplitude increased, the growth of the stationary vortices moved farther upstream, while the saturation amplitude decreased. This decrease was attributed to the nonlinear effects beginning farther upstream as the initial amplitude increased.

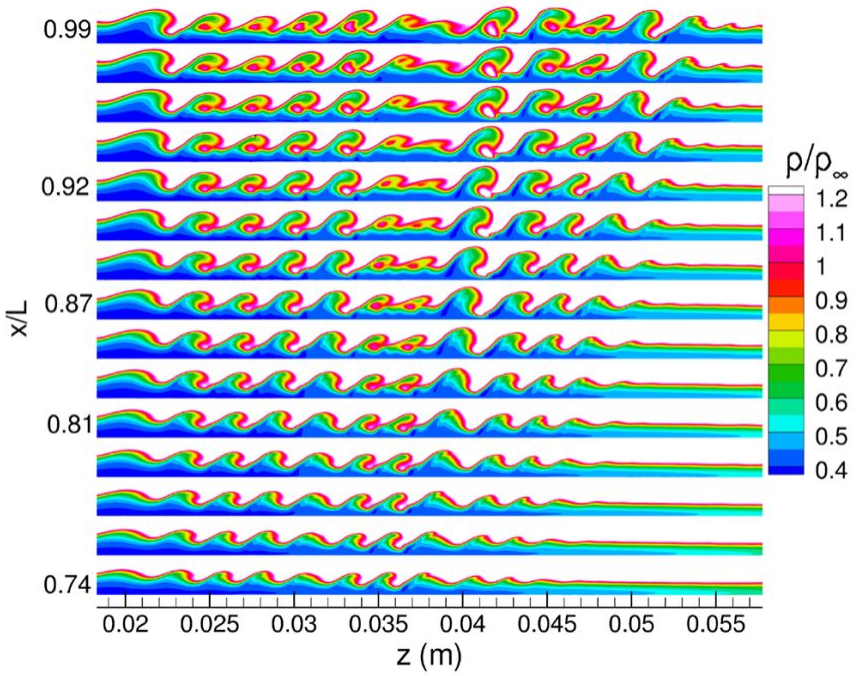

Figure 2.1. DNS solution of the streamwise density contours for Mach 6 flow on an elliptical cone with angles of 7° and 14°. Image from Dinzl et al. [55]. Printed with permission from Dinzl.

3. TEST FACILITY AND MODEL

3.1 Boeing/AFOSR Mach 6 Quiet Tunnel

The experiments were performed in the Boeing/AFOSR Mach 6 Quiet Tunnel (BAM6QT). The BAM6QT is the largest operational hypersonic quiet wind tunnel in the world. This tunnel consists of a driver tube about 122 feet long connected to a converging-diverging nozzle which accelerates the flow to Mach 6. A schematic of the tunnel is shown in Figure 3.1. The Ludwieg tube design minimizes costs while providing relatively high freestream Reynolds numbers and reasonable run times.

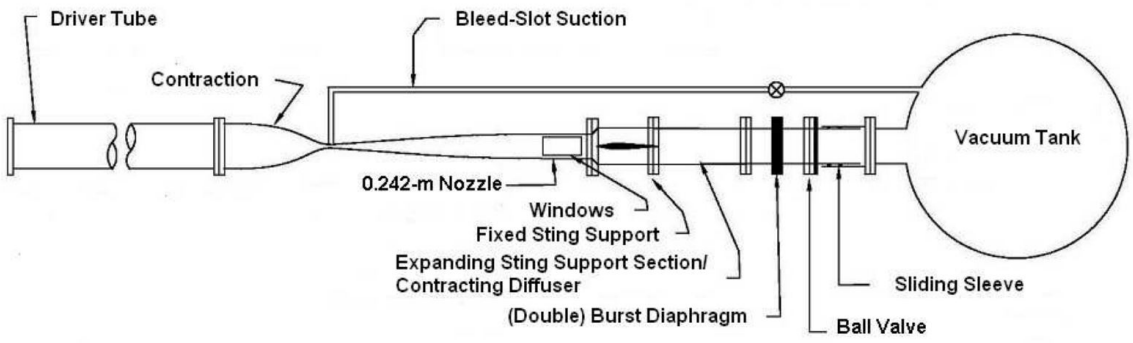

Figure 3.1. Schematic of the Boeing/AFOSR Mach 6 Quiet Tunnel (BAM6QT).

To operate the tunnel, the driver tube is pressurized to the desired pressure while a double burst diaphragm separates the driver tube from the vacuum tank. Everything downstream of the burst diaphragms is maintained at vacuum. The diaphragm system consists of two thin aluminum disks separated by a gap of air. The thickness of the disks depends on the final driver tube pressure. As the driver tube is being pressurized, the pressure in the gap is maintained at the average pressure between the driver tube and the vacuum tank, or roughly half the driver tube pressure. Once the driver

tube is filled to the correct pressure, the gap is evacuated and the diaphragms are burst. The bursting of the diaphragms causes a shock wave to travel downstream and an expansion wave to travel upstream. Once this expansion fan passes through the throat, the air in the nozzle is accelerated and Mach 6 flow begins. The expansion fan reflects between the upstream and downstream ends of the driver tube approximately every 200 ms slightly decreasing the stagnation conditions each time. Thus, the flow can be considered quasi-static during every 200 ms interval. A typical run lasts for about 4-5 seconds, allowing a range of freestream Reynolds numbers to be tested.

Conventional wind tunnels have turbulent boundary layers on the tunnel walls. As previously stated, these boundary layers radiate noise into the freestream, affecting transition data. The BAM6QT uses several features to maintain a laminar boundary layer. This results in freestream fluctuations less than 0.02% of the mean pitot pressure [57]. First, there is a bleed slot at the throat that is connected to the vacuum tank through a fast-acting butterfly valve. This suction removes the turbulent boundary layer in the contraction section, allowing a new laminar one to begin at the bleed lip. The diverging section of the tunnel is elongated to keep the radius of curvature large and minimize the formation of Görtler vortices. The nozzle is also polished to a mirror finish in order to help avoid roughness induced transition on the nozzle wall. To protect this finish, a series of air filters are incorporated to remove any air-borne particulate larger than 0.01 μm. The current maximum stagnation pressure that the nozzle can maintain a laminar boundary layer at is 155 psia. If noise levels comparable to a conventional wind tunnel are desired, the operator can run with the bleed valve closed.

3.1.1 Determining BAM6QT Flow Conditions

Under quiet flow conditions, the Mach number of the BAM6QT is Mach 6.0. However, if the tunnel is run noisy, the Mach number at the test section is actually 5.8 because of the smaller cross-sectional area caused by the thicker turbulent boundary

layer. Before running, the initial stagnation pressure, $P_{0,i}$, and initial stagnation temperature, $T_{0,i}$, are recorded by the operator. The stagnation temperature is recorded from a thermocouple located at the upstream end of the driver tube. There is some uncertainty in this measurement because of temperature variations in the radial and axial directions [57]. The stagnation pressure is measured from a Kulite XTEL-190-500A which is flush-mounted to the wall near the contraction inlet. It is calibrated using a 300 psia Paroscientific Inc. Model 740 Digiquartz Portable Standard pressure gauge which is placed slightly upstream of the diaphragm section. Because the calibration of the contraction Kulite is subject to change over long periods of time, a new calibration curve is obtained during each entry. A typical calibration curve is shown in Figure 3.2.

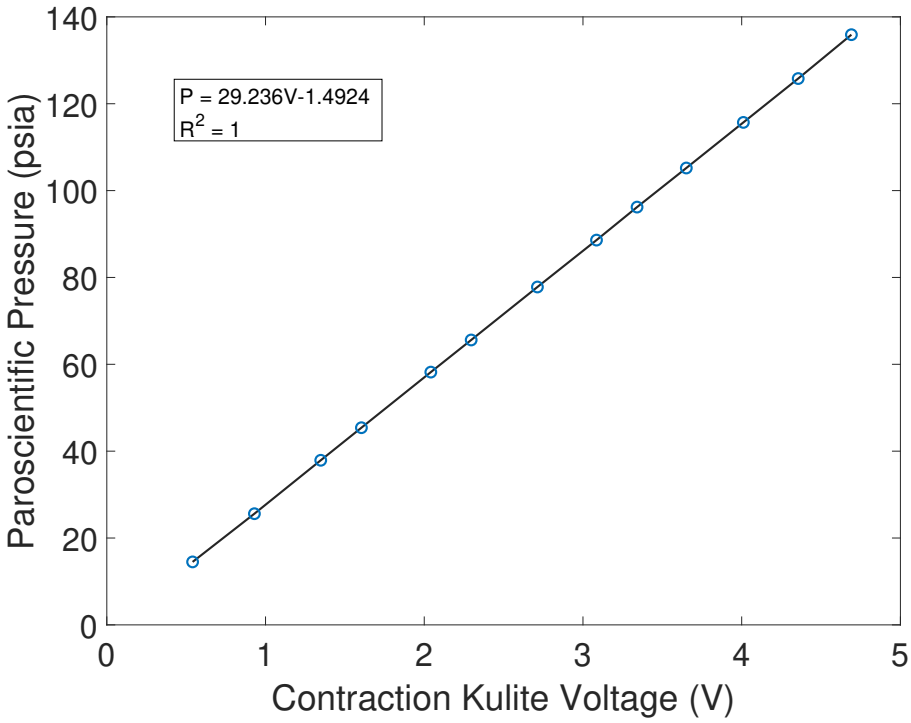

Figure 3.2. Typical calibration of contraction Kulite using a Digiquartz pressure gauge.

To determine the instantaneous stagnation temperature, the following isentropic relation is utilized.

$$T_0 = T_{0,i}\left(\frac{P_0}{P_{0,i}}\right)^{\frac{\gamma-1}{\gamma}} \tag{3.1}$$

Note that γ is the ratio of specific heats and is assumed to be 1.4, the value for air at standard temperature and pressure. To calculate the freestream Reynolds number, the static temperature, T, and pressure, P, are needed. These values are calculated using isentropic relations as shown in Equations 3.2 and 3.3, where M is the Mach number.

$$T = T_0\left(1 + \frac{\gamma-1}{2}M^2\right)^{-1} \tag{3.2}$$

$$P = P_0\left(1 + \frac{\gamma-1}{2}M^2\right)^{\frac{-\gamma}{\gamma-1}} \tag{3.3}$$

The freestream dynamic viscosity, μ_∞, which has the units of Pa $\times$ s is found by the ideal gas assumption and the utilization of Sutherland's law given by Equation 3.4.

$$\mu_\infty = 1.716 \times 10^{-5}\left(\frac{T}{273}\right)^{\frac{3}{2}}\left(\frac{384}{T+111}\right) \tag{3.4}$$

Finally, the freestream Reynolds number (Re_∞) is calculated using Equation 3.5, where R is the specific gas constant for air.

$$Re_\infty = \frac{PM}{\mu_\infty}\sqrt{\frac{\gamma}{RT}} \tag{3.5}$$

Using the freestream conditions, the Stanton number, St, can be found. This is given by Equation 3.6.

$$St = \frac{q}{Re_\infty \mu_\infty C_p(T_o - T_w)} \tag{3.6}$$

In this equation, C_p is the specific heat of air at T_w and q is the heat transfer(flux). The heat transfer is found using the procedure described in Section 4.6. Although the Stanton number is usually defined using the adiabatic wall temperature instead of the

stagnation temperature, the adiabatic wall temperature is harder to obtain. Thus, the stagnation temperature was used as this was readily available. Also note that the Stanton number requires the instantaneous wall temperature. However, because the TSP does not provide a reliable measurement of the wall temperature as explained in Section 5 (it requires an SB calibration), the initial wall temperature was used instead to calculate experimental Stanton numbers.

A hot film is used to measure the uncalibrated shear stress on the nozzle wall. The hot film is used to qualitatively determine if the nozzle boundary wall is laminar (quiet) or turbulent (noisy). In other instances, it can even provide insight onto whether or not the tunnel is started, which is particularly useful when running with larger models. Initially, a Senflex multi-element hot film array was installed on the nozzle wall. This was used for many entries, but it was removed due to possible model interference during testing. It was replaced by a single element hot film made by Dantec [58]. This hot film is flush-mounted to the surface of the nozzle wall at an axial location of 1.913 m, and hence is less intrusive to the flow. A sample trace taken using the new hot film for a quiet run with an initial stagnation pressure of 130 psia is shown in Figure 3.3. The initial spike is due to the tunnel startup process and the noise increase around 4 seconds signifies the end of the run. A quiet run lasts for about 3-4 seconds, while a noisy run lasts for about 5 seconds.

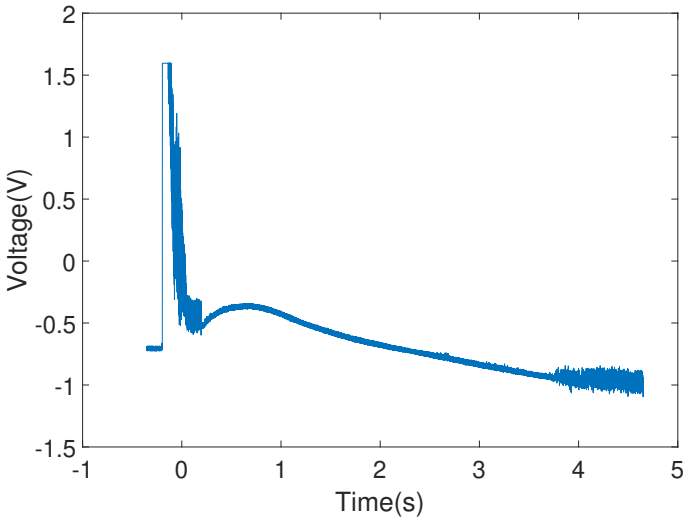

Figure 3.3. Typical hot film data collected during a run. The startup process is seen between 0 s and 0.2 s followed by a region of quiet flow indicated by the lower noise levels. Finally, the tunnel unstart is indicated by the increase in noise at around 3.8 s.

3.2 Mark II Cone

All the experimental data shown in this report was obtained using the Mark II cone designed by Edelman [6]. Shown in Figure 3.4, it is a 7° half-angle cone, with many sensor ports aligned in the direction of the stationary vortices in order to help track the growth of the secondary instabilities. The sensor holes are slanted in the spanwise direction at about 0.11 ° per mm. It contains 3 sections: the nosetip, the roughness insert, and the frustum.

3.2.1 Frustum

The frustum is where all the sensor ports are located. It should be noted that because the objective of this research was only to track the primary instability, which cannot be measured using AC coupled pressure sensors, most of the holes were plugged using dental plaster. The remaining holes were used to install heat-transfer gauges.

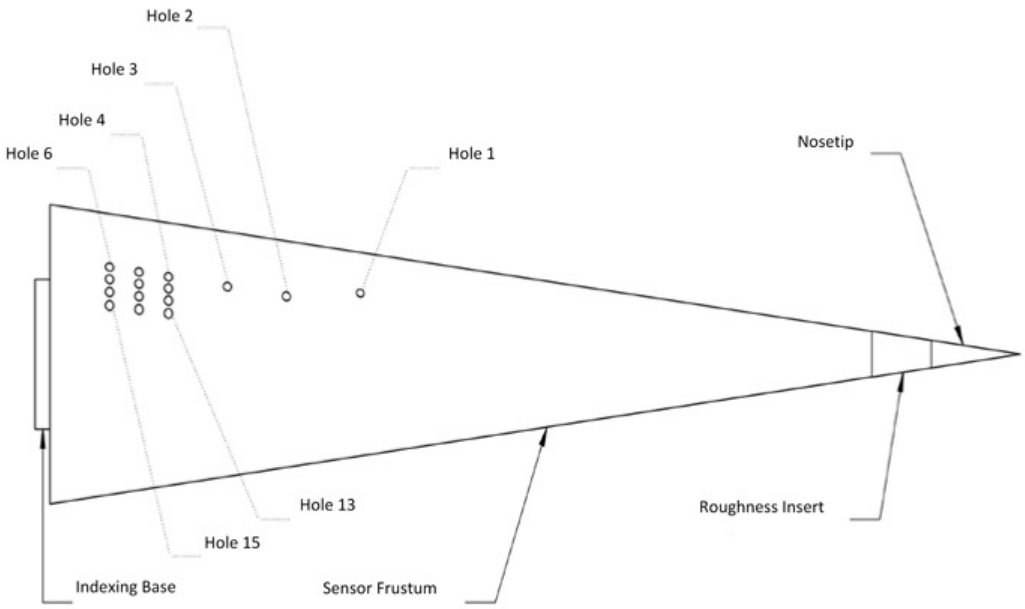

Figure 3.4. Diagram of the 7° half-angle Mark II cone used in the present experiment. Figure redrawn from Reference [6].

Because the cone was rotated in such a way that the imaging portion of the cone that was used to measure the streaks did not include any sensor ports, any possible step caused by the dental plaster or the sensors did not affect the TSP. The cone also includes an indexing ring with a resolution of one degree, which is attached to the base of the model. This allows the azimuthal orientation of the imaging area of the model to be known with respect to the lee ray. However, because the mark on the 6° angle of attack adapter indicating the lee ray is actually about 2.5° wide, the actual azimuthal orientation had an uncertainty of 2.5°. Table 3.1 shows the axial and azimuthal locations of each sensor port on the Mark II cone. The labeled axial location refers to the distance from the nosetip in meters. The azimuthal location labeled 0° is arbitrary and corresponds to the azimuthal location at which the indexing ring at the base of the model starts.

Table 3.1. Location of sensor holes on Mark II cone.

Hole #	**Axial Location [m]**	**Azimuthal Offset [°]**
1	0.2817	1.34
2	0.3132	-7.54
3	0.3383	-4.73
4	0.3635	-2.24
5	0.3762	-1.09
6	0.3886	0
7	0.3635	-8.24
8	0.3762	-7.09
9	0.3886	-6
10	0.3635	-14.24
11	0.3762	-13.09
12	0.3886	-12
13	0.3635	-20.24
14	0.3762	-19.09
15	0.3886	-18

3.2.2 Roughness Inserts

Roughness inserts were made using the Rod Insertion Method (RIM) developed by Chynoweth [59]. This method involves the press-fit of brass rods about 0.056 mm in diameter into an aluminum or Torlon insert. The brass rods were placed at the neutral point of the stationary crossflow instability, about 0.051 meters from the nosetip [40] [12] [19]. In the past, dimpled inserts were used [6] [12]; however, the dimples created by this method were not as consistent as the RIM inserts. It is also unsure if dimples produce the same effect to the flow as a protruding cylindrical roughness. In addition,

the flow disturbed by the cylinders should be easier to compare with computational fluid dynamics (CFD) results, as the cylinders are well defined.

The roughness inserts mate to the top of the cone in between the frustum and nosetip. Each insert contains a dowel pin on the downstream face that can be inserted into one of many holes on the upstream face of the cone. The holes on top of the cone are nominally 12° apart and have a nominal diameter of 0.940 mm. This allows repeatable placement of roughness elements as well as better knowledge of the azimuthal location of the roughness elements with respect to the lee ray. Table 3.2 shows the nominal dimensions of all roughness inserts used in this experiment. Note that there are 2 roughness inserts that have 50.8 μm elements and 2 roughness inserts that have 102 μm elements. This was done because inserts # 2 and # 4 were 2 of the first inserts ever made, and had some possible machine errors. This will be expanded on in Section 5.4.1. The nominal azimuthal angle between each element was 7.2°, making $\frac{\lambda}{D}$ about 1.4, where λ and D are the distance between each element and diameter of the elements, respectively. These elements were packed close together, and it is unsure if there were problems with the flow viewing the roughness elements as a fence. It should be noted that Edelman did not have a problem using elements of the same diameter but 9.0° apart [19]. It was also important that these elements were not too big to trip the flow. However, the tallest roughness element used in this experiment was well below the minimum roughness element used by Edelman that tripped the flow for the same flow geometry.

Zygo measurements of roughness inserts # 2-8 were taken to get a better idea of the dimensions of the roughness elements on each roughness insert. The instrument used was a Zygo Zegage white-light optical profilometer whose vertical resolution is 3 nm. The lens used provided a 5 μm horizontal resolution. To compare the azimuthal location of the roughness elements on one roughness insert to the location of those on another, the dowel pin on the bottom face of the roughness insert was mated to a support structure on the Zygo. From the 3-D contour map obtained from the Zygo, a 2-D image of the roughness height plotted against the azimuthal angle was extracted

Table 3.2. Roughness inserts used in the present experiment.

Insert #	**# of Elements**	**Azimuthal Spacing (°)**	Diameter (mm)	Height (μm)
1 (smooth)	-	-	-	-
2	3	7.2	0.056	50.8
3	3	7.2	0.056	50.8
4	3	7.2	0.056	102
5	3	7.2	0.056	102
6	3	7.2	0.056	152
7	3	7.2	0.056	203
8	3	7.2	0.056	254

from the approximate centerline of the roughness elements. Figure 3.5(a) shows a contour map of the Zygo measurements for roughness insert #8, while Figure 3.5(b) shows a 2-D map of the height of the roughness elements vs the azimuthal angle. While the scales on either axes are accurate, the 0 reference point is arbitrary. The red dotted line in Figure 3.5(b) shows the nominal height of the elements. The reader is referred to section B in the appendix for images of the 6 other roughness inserts which contained roughness elements. It should be noted that the 0 point for both the axial reference and the azimuthal reference is the same for all inserts. The heights of the elements are relatively close to the nominal height. Also, the arrow indicating the direction of the leeward side illustrates the orientation in which every roughness insert was placed for this entry.

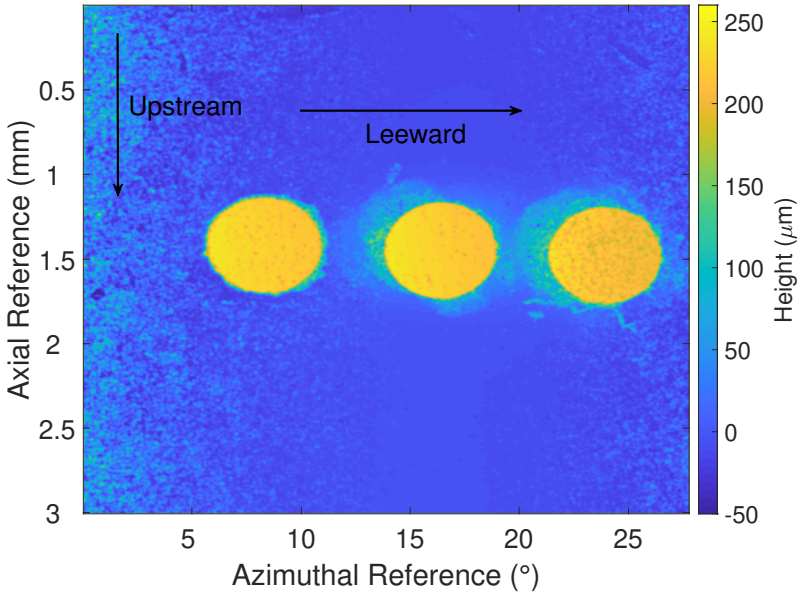

(a) Contour map of roughness insert # 8.

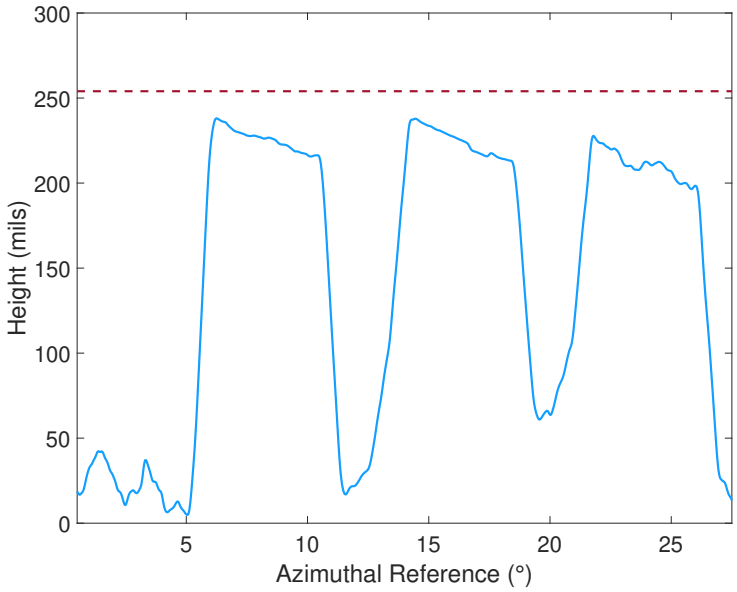

(b) 2-d slice of roughness insert # 8. The red dotted line marks the nominal height.

Figure 3.5. Zygo measurements of Roughness insert # 8 which contains discrete elements with a nominal height of 254 μm.

In order to obtain a non-dimensional roughness height, the boundary layer thickness, δ, at the nominal roughness location was calculated using the method described in Section 4.7. Table 3.3 shows the calculated boundary layer thickness when the most leeward element is placed 52.4° from the wind ray. The stagnation pressure, stagnation temperature, and wall temperature for this computed data are 109.5 psia, 420 K, and 302 K respectively.

Table 3.3. Boundary layer thickness at location of roughness elements. $T_{w,i} = 302$ K, Re $= 8.5 \times 10^6$/m , $p_0 = 109.5$ psia, $T_0 = 420$ K.

Azimuthal Angle from Wind Ray (°)	δ **(mm)**
38.0	0.278
45.2	0.285
52.4	0.298

As expected, the boundary layer thickness increases farther from the wind ray. The values for $\frac{k}{\delta}$ for each run are tabulated in Section A in the appendix. Note that the change in δ from the middle roughness element to the elements closest and farthest from the wind ray is only about 2.5 % and 4.5 % respectively. Thus, to keep it simple, δ was only be found for the middle roughness element for each run. Note that these values are calculated using the initial conditions of each run, so $\frac{k}{\delta}$ will be slightly lower depending on when in the run the data was analyzed.

3.2.3 Nosetip

Finally, the nosetip that was used was sharp and made of stainless steel. Figure 3.6 shows a microscopic image of the tip and the labeled radius which was found to be about 0.046 mm. This was the nosetip that was used for this experiment.

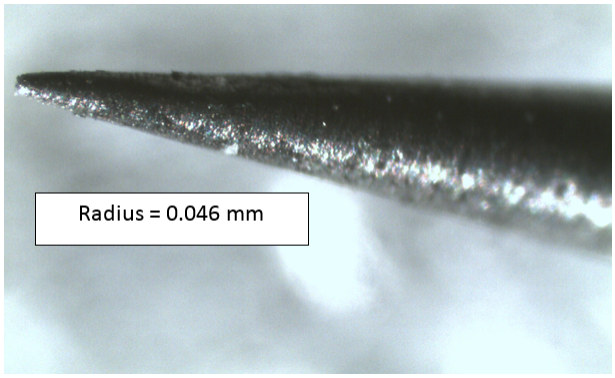

Figure 3.6. Magnified image of nosetip used for the present experiment.

4. EXPERIMENTAL METHODS AND DATA PROCESSING

4.1 Schmidt-Boelter Heat Transfer Gauges

The local heat transfer at discrete locations on the model was measured using SB gauges, the main type of discrete sensor used in the present research. They are manufactured by the Medtherm Corporation. This sensor consists of a thermopile inside a copper housing, coated with a black epoxy, allowing the gauge to more effectively absorb heat. The amount of heat transfer is inferred from the temperature differential between the thermocouples. The sensor head has an outside diameter of 3.175 mm. Because the heat transfer was found to be below 10 kW for the current geometry [43], only one type of SB gauge was used. This gauge has a model number of 8-1-0.25-48-20835TBS and can measure heat transfer rates from 0-10 kW/m^2. These sensors also include two additional outputs: one for the T-type thermocouple closest to the surface and one for the T-type thermocouple farthest from the surface. These thermocouples are placed 0.152 mm and 2.79 mm respectively from the surface [60] and both are used to measure the pre-run temperature of the model. The thermocouples will be explained in greater detail in the next section. Because the heat transfer signal can be on the same order as the noise, the output from the gauges is amplified and filtered utilizing a Stanford Research Systems Low Noise Preamplifier, Model SR560. The gain on the box was set to 100, and the cutoff frequency of the low-pass filters was set to 30 Hz. A typical SB curve during a run with an initial stagnation pressure of about 120 psia for a 7° half-angle cone at a 6° angle of attack can be seen in Figure 4.1. The initial spikes near t=0 are due to the tunnel startup process while the increase in heat transfer at around 4 seconds signifies the end of the run. Obtaining the heat transfer during the initial startup process is vital to the

TSP calibration, which will be explained in further detail in Section 4.6. Also note that the heat transfer before the run is not 0, and subtracting this offset gives better agreement with theory [12].

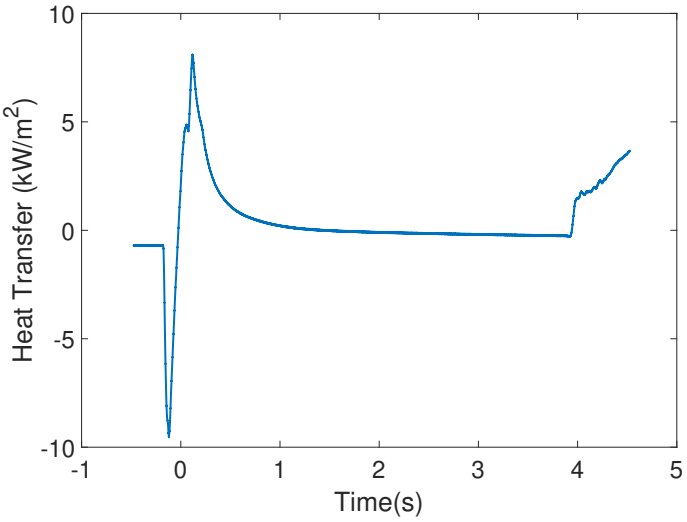

Figure 4.1. Typical output from a Schmidt-Boelter (SB) gauge during a run. The initial spikes in heat transfer are caused by the tunnel startup process, and the increase in heat transfer towards the end is caused by tunnel unstart.

4.2 Thermocouples

As previously mentioned, the Schmidt-Boelter gauge was also equipped with two T-type thermocouples, which were used to obtain the pre-run temperature of the model. A thermocouple is a sensor consisting of two junctions of two dissimilar metals where one junction is exposed to a "hot" side and the other is exposed to a "cold" side which is kept at a reference temperature. A voltage difference can be measured at the hot junction due to the metal's different Seeback coefficients. This voltage can be correlated to the temperature of the hot side of the junction. In this experiment, the "hot" side is the model temperature we are trying to measure. The "cold" side

was kept at a reference temperature by utilizing a type T Omega MCJ miniature cold junction compensator (CJC), which is essentially an electronic ice point. Theoretically, the calibration for every thermocouple-compensator pair is the same and can be obtained from the National Institute of Standards and Technology (NIST) ITS-90 database. However, it was found that the output from the thermocouples was highly dependent on the specific T-type CJC being used, and this variation was outside the quoted uncertainty of the thermocouples. Thus, each compensator had to be calibrated separately using a H-B Instrument B61001-0400 FRIO-Temp Incubator Verification Thermometer which has a quoted accuracy of $\pm$ 0.2 K [61]. This process is described in detail in Section 5.3.2.

4.3 PCB Piezotronics Pressure Sensors

The second type of sensor used in this present experiment was a PCB-132A31 pressure transducer, manufactured by PCB Piezotronics, Inc. These sensors consist of a piezoelectric crystal contained within a metal cylindrical housing. The piezoelectric sensing element is a 0.76 mm square, but the outside housing diameter is 3.18 mm [62]. Because the exact location of the sensing element is unknown, there is some uncertainty involved with the location of the measurements. The sensor is high-pass filtered above 11 kHz, rendering it incapable of mean pressure measurements. It should also be noted that the resonant frequency of these sensors is about 1 MHz, making it suitable for measuring instabilities on the surface of the model which range from 100 to 300 kHz.The manufacturer claims that the sensor has a resolution of 0.001 psi and can measure fluctuations up to 50 psia. These sensors were initially designed to be used to measure the time of arrival of shock waves. Thus, there is uncertainty in the factory calibration. Work has been done to develop a more reliable way of calibrating these sensors to measure instabilities [63] [64].

Because PCBs are high-pass filtered, they are unable to measure stationary vortices. However PCBs were still used in the present experiment in a tunnel entry to

properly ensure the model was at a 0° angle of attack, which required measurements of the second-mode instability. This will be explained further in Section 5.3.3. The data from the PCBs were analyzed by computing a power spectral density (PSD). A PSD describes the power content of a signal by showing the distribution at different frequencies. A script was written in MATLAB which computed the PSD using Welch's method. This involves dividing the signal into windows of equal size and averaging FFTs over each window with an overlap between each window. The frequency resolution is given by equation 4.1, where f_s is the sampling rate.

$$Frequency \quad Resolution = \frac{f_s}{\#\quad of \quad points \quad in \quad window} \tag{4.1}$$

Because the sampling rate was 2 MHz and the window size was 800 points, the frequency resolution was 2.5 kHz. The total time over which the signal was analyzed was 0.1 second, within the max duration of quasi-steady flow in the tunnel. Figure 4.2 shows a typical PSD for a 7° half-angle cone at a nominally 0° angle of attack and a stagnation pressure of about 127 psia. Note that the peaks around 220 kHz indicate the second mode instability. The PCBs used to take these data are at an axial loation of 0.3886 m and are spaced 90° apart in the azimuthal direction. Variation in the frequency of the peaks can be seen because the model is not at a 0° angle of attack. This asymmetry causes variation in the boundary layer thickness which causes different frequencies in the second-mode peaks.

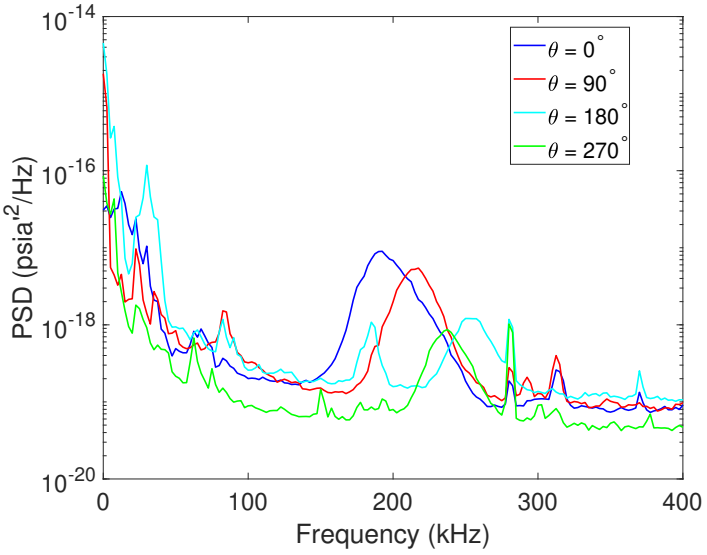

Figure 4.2. Typical power spectral density (PSD) obtained from PCB pressure sensors during a run for a 7° half-angle cone at a $0 \pm 1°$ angle of attack. PCB sensors are at an axial location of 0.3886 m from the nosetip and are spaced 90° apart.

4.4 Oscilloscopes

The measurements of the tunnel conditions, SB heat transfer, and pressure fluctuations were collected using digital oscilloscopes. Both Tektonix DPO7054 and DPO5034B osciloscopes were utilized. The DPO7054 model has a bandwidth of 500 MHz while the DPO5034B has a bandwith of 350 MHz. The PCB fluctuations were AC coupled and generally sampled at 2 MHz thus satisfying the Nyquist criteria for measured frequencies up to 1 MHz. The other measurements were DC coupled and sampled at 1 MHz because a high sampling rate was not necessary. The input impedance was set at 1 MΩ. These oscilloscopes normally had a vertical resolution of 8 bits. However, because they were set to sample in Hi-Res mode, the resolution was increased to 11-12 bits by sampling at the maximum rate and digitally averaging. The Hi-Res mode also acted as an anti-aliasing filter.

4.5 Data Acquisition System

Thermocouple data were collected using a 22-bit 34972A LXI Logger Switch Unit made by Keysight Technologies. This is a data acquisition system (DAQ) that uses mechanical relays to collect input from several different channels sequentially. As previously stated, the temperature data were measured using a T-type thermocouple and converted into a voltage using a CJC. Unfortunately, because the voltage output was on the order of 1 mV, the data could not be directly collected from the oscilloscopes due to the poor vertical resolution. The DAQ was able to solve this problem, but the sampling rate depended on the required resolution as well as the number of inputs being sampled at once. In this present experiment, 3 channels were sampled per run at a 5.5 digit accuracy, making the sampling rate about 6.5 Hz. Although this was not particularly high, it was sufficient to observe the change in temperature during a run.

4.6 Temperature Sensitive Paint (TSP)

While Schmidt-Boelters provide a fairly accurate measurement of the surface heat transfer, they are limited to a local measurement. In order to obtain a global map of the heat transfer on the model, the model was painted with TSP. Global heat transfer measurements are especially important in the study of stationary crossflow, as flow measurement techniques such as PCBs can only measure unsteady instabilities. An extensive review on the theory behind both TSP and pressure sensitive paint (PSP) can be found in Reference [65]. Experiments were carried out by Ward in which a 7° half-angle cone at a 0° angle of attack was tested in the BAM6QT [66]. Proper experimental techniques were discovered with which to apply and process the TSP. The main ingredient in TSP is a luminophore molecule which is dissolved in a solvent and bound together with a paint/activator clearcoat. This molecule provides an indication of the temperature change by a process called thermal quenching. When these molecules are bombarded with photons, usually from a light source of a par-

ticular wavelength, they are excited to a higher energy state. As the molecules relax and move down to a lower energy state, they emit a photon at a longer wavelength through a process known as luminescence [67]. A schematic of this process is shown in Figure 4.3.

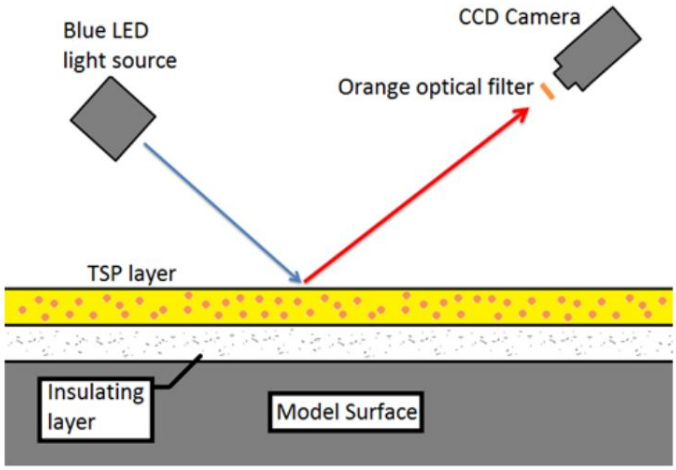

Figure 4.3. Schematic showing the temperature sensitive paint (TSP) layer. Image from Reference [12]. Printed with permission from Ward.

The intensity of the light emitted is proportional to the temperature of the luminophore molecule. The particular luminophore molecule used in the present experiment is 99.95% Trist(2,2'-bipyridyl)ruthenium(II) chloride hexahydrate, or Ru(bpy), and the solvent is ethanol. Ru(bpy) can be excited with light at a wavelength of 320 nm or 452 nm, and has one emission peak at 588 nm [65].

4.6.1 Application of TSP onto Models

In order to ensure skin oils did not contaminate the model surface, latex gloves were worn through this whole process. Before painting, the model was stripped of any residual paint from a previous entry using a paint stripper. The surface was then cleaned extensively using acetone. Finally, the upstream portion of the model which

would not be painted was covered to ensure it remained clean. The nose tip was uninstalled for TSP application.

First, an insulating layer of white primer had to be applied to increase the signal-to-noise ratio when taking images during a run [66]. This primer layer also helped in allowing the TSP to adhere to the surface of the model. Top Flite Lustrekote spray paint was the primer that was utilized. Eight layers of "Jet White" were applied, with 2-3 minutes in between coats as per the instructions on the back of the can. Unfortunately, before the last entry in this experiment, the LustreKote product was discontinued. It was necessary to use Rust-oleum Multi Purpose Enamel instead. This should not affect the measurements with TSP as long as an SB is used for an in-situ calibration [68]. It should be noted that while 8 layers are the recommended amount, it depends on how much primer is added with each layer. As a rule of thumb, the model should be pure white once finished. The paint was feathered at the upstream end of the model to ensure the forward-facing step was minimized. The model was then allowed to dry for 24 hours, and the insulating layer was subsequently sanded with 800-grit, 1200-grit, and 1600-grit wet sand paper. During this process, it was essential to reduce the upstream step as much as possible to ensure the flow would not be tripped.

The TSP was made using the following recipe for one batch. For the present model, 5 batches were necessary to coat the entire model, so the actual recipe would be 5 times the following ingredients. First, 12 mg of Ru(bpy) was dissolved in 10 mL of 190 proof ethanol. The solution was mixed to ensure most of the Ru(bpy) crystals were dissolved. Then, 20 mL of AMTech Am-500-4 Clearcoat was added and stirred. Finally, 5 mL of AMTech Am-570-12 medium hardener was added, and the final mixture was stirred until it was uniform. The paint was then applied using a air pressure paint gun with the pressure set around 25 psia. Normally, 8 coats were applied, but as previously stated, this can vary depending on the thickness of the coats. The coats were applied with approximately a 20 minute waiting period in between to allow each layer to partially dry. Again, care was taken to feather the

paint at the upstream end of the model to minimize the paint edge. Once the paint was allowed to cure for 24 hours, it was sanded with the same grit wet sand paper as used for the insulating layer. Extra precaution was taken when sanding the paint step, as a poorly sanded step could possibly result in paint chipping, ruining the paint job. Finally, the model was seated onto a precision rotary stage and installed in the vise of a milling machine, so that dots could be made with a Sharpie at certain axial and azimuthal locations. 3 rows of dots were made (each row being at the same azimuthal location), and each dot was 2 inches apart in the axial direction. Although the azimuthal location of these dots varied slightly depending on the entry, one row was approximately near the lee ray and the other 2 were 45° apart in either direction. These dots allowed the 2-D images taken during a run to be unwrapped into its true azimuthal and axial coordinates.

The paint thickness was measured using an Elcometer 456 digital thickness gauge, following the process provided by Ward [66]. Because the thickness gauge is meant for use on flat surfaces, error was introduced when attempting to measure on the curved surface of the cone. To account for this, the cone without any TSP was first measured and subtracted from the measured thickness with TSP applied to the cone. This method seems to have provide sufficiently accurate results in the past [69] [66]. The thickness typically averaged around 120 μm. The paint thickness from entry 2 as labeled in section A in the appendix is shown in Figure 4.4. Note that the thickness is relatively constant except for the first point which is low due to the feathering technique that was used to sand the leading edge. However, this is not a problem because no data was ever extracted upstream of the second data point in Figure 4.4.

The paint step was then measured using a Mitutoyo SJ-301 profilometer. The sensor was attached to a vertical gauge, allowing the sensor to be parallel to the model surface. The profilometer was able to measure heights as large as 350 μm, which was almost 2 orders above the measured paint step in any entry. The paint step was measured after each entry to verify that it was well below 25.4 μm (1 mil).

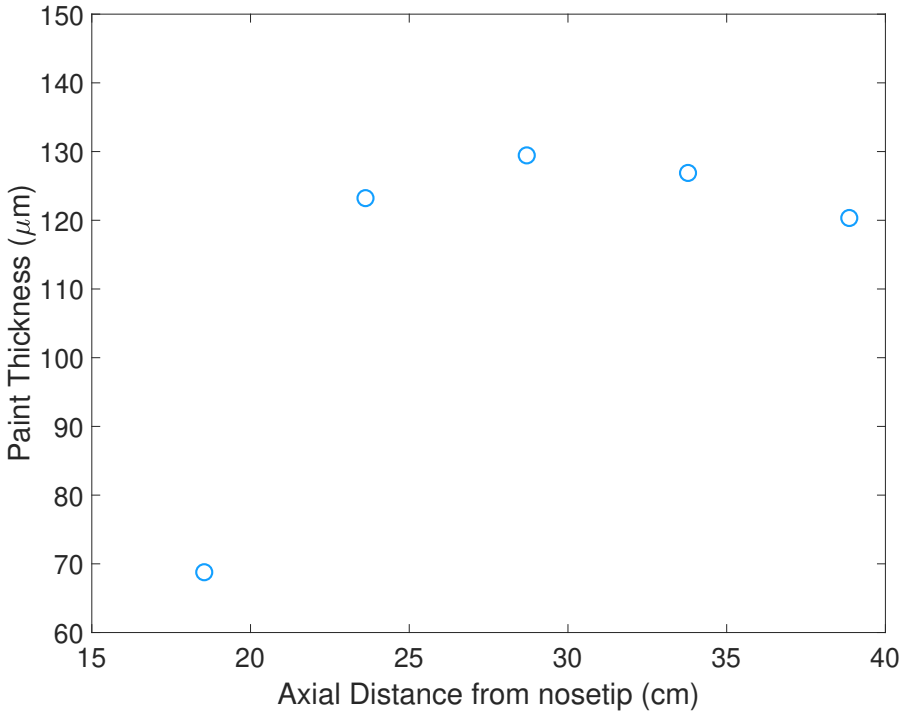

Figure 4.4. Paint thickness for Entry 2. Relatively constant paint thickness excluding the first point, which is low due to the feathering technique and sanding.

4.6.2 TSP Apparatus

As previously stated, Ru(bpy) is excited by light with a wavelength of either 350 nm or 452 nm. Because the Plexiglas window that was used for imaging was made of UAV Plexiglas which has a transmissivity of 0.05 at 320 nm, the incident light had to be around 452 nm. Thus, two blue, light-emitting diode arrays were utilized: an Innovative Scientific Solutions (ISSI) Inc. LMA LM4 LED array and an ISSI LM2xLZ-460 LED array. The former emits blue light with a wavelength of 464 nm while the latter emits light at 460 nm. By using both LEDs, the signal to noise ratio was maximized.

Images were obtained using an ISSI PSP-CCD-M 14-bit camera. An orange 550 nm long-pass filter was placed in front of the camera to allow the emitted light from the TSP but exclude the reflected light from the LEDs. After the 10 minute settling period before the run when filling was over, 15 images were taken with the LEDs off ("dark" images), and 15 images were taken with the LEDs on("off" images). The exposure time was between 7.5 and 15 ms to keep the image intensity levels just below saturation. During the run, 75 images were taken at a frequency of 15 Hz and labeled as "Run". The obtained images were merely a matrix of the intensity of the pixels.

4.6.3 TSP Data Processing

The change in temperature from the pre-run conditions to a certain time during a run can be calculated from Equation 4.2.

$$\Delta T = f\left(\frac{I_{on} - I_{dark}}{I_{off} - I_{dark}}\right) \tag{4.2}$$

Here, f is a function relating the intensity of light emitted and the temperature of the Ru(bpy) particles. This relation can be found in Figure 3.13 from Reference [65]. This curve was digitized and substituted into equation 4.2. With a little algebra, the equation expressing the change in temperature solely as a function of intensities and pre-run temperature can be obtained and is shown in Equation 4.3. Please note that the TSP surface temperature calculated using this method is not reliable as explained in detail in Section 5, due to the uncertainty in the function f, paint job, and other variables.

$$\Delta T = (363 - T_w)\left(1 - \frac{I_{on} - I_{dark}}{I_{off} - I_{dark}}\right) \tag{4.3}$$

T_w is the pre-run temperature of the model which is assumed to be spatially uniform, and is found using the thermocouple output from a SB gauge. Once the temperature of the TSP surface is known, this can be used to calculate the heat transfer to the model, but several assumptions must be made. First, one-dimensional

(normal to the wall) heat transfer must be assumed. Second, the temperature gradient is assumed to be linear. Both these assumptions allow the use of Fourier's law of heat conduction given by Equation 4.4.

$$q = -\kappa \nabla T \tag{4.4}$$

Here, q is the local heat flux and κ is the thermal conductivity of the material in question. Finally, the last assumption is that the temperature of the model remains both temporally and spatially uniform during a run. This assumption was found to be reasonably valid in Reference [43] and more work was performed in the present experiment to evaluate this assumption. Using these assumptions, the relationship between the heat transfer and temperature at the surface of the model can be given by Equation 4.5.

$$q = \frac{\kappa}{L}(T - T_{model}) \tag{4.5}$$

Here, κ and L are the thermal conductivity divided by the thickness of the paint layer and insulating layer. T is the surface temperature of the model which can be calculated from ΔT using Equation 4.6. Finally, substituting Equation 4.6 into 4.5 gives Equation 4.7 which can be utilized in the TSP calibration process to calculate the inferred heat transfer.

$$\Delta T = T - T_w \tag{4.6}$$

$$q = \frac{\kappa}{L}(\Delta T + T_w - T_{model}) \tag{4.7}$$

The global heat transfer can be found by calibrating the TSP with a Schmidt-Boelter gage using equation 4.5. Theoretically, T_{model} should be the same as T_w and $\frac{\kappa}{L}$ is merely the thermal conductivity and thickness of the paint layer respectively, thus precluding the need for a SB gauge. Ward attempted to calculate the heat transfer

in this manner by inputting measured values for the constants, but did not find good agreement between the SB gauge and the inferred heat transfer [66].

The constants are instead found by a least squares fit. This is done by picking a small patch of TSP adjacent to the SB gage, and using a linear fit to find the values of $\frac{\kappa}{L}$, and T_{model} that provides the best coefficient of determination. An example TSP image showing the global temperature change with the calibration patch in red for a 7° half-angle cone at a 6° angle of attack with a stagnation pressure of about 110 psia is shown in Figure 4.5.

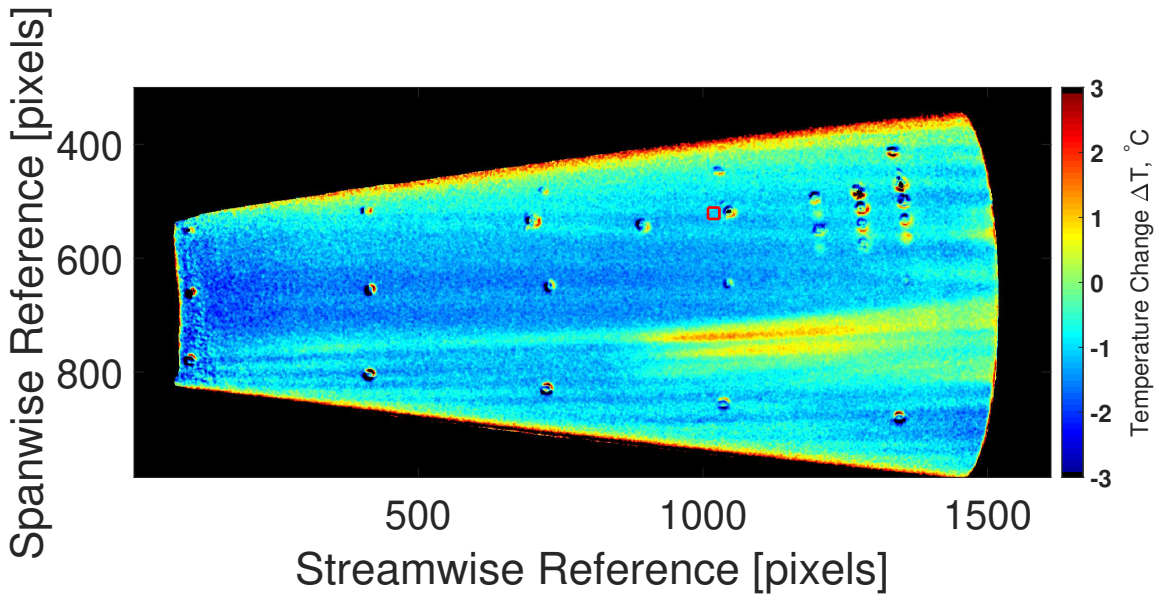

Figure 4.5. Typical temperature sensitive paint (TSP) image showing the global temperature change on the model. The calibration patch that was utilized is marked in red.

Figure 4.6 shows the SB gauge data and the heat transfer points that were calculated from the inferred TSP calibration taken from Figure 4.5. Figure 4.7 shows the linear calibration between the SB gage and the TSP surface temperature data for the run in Figure 4.5 (the middle of the 3 lines) as well as the calibration from 2 other runs done at the same initial conditions. It is evident that the relationship is not perfectly linear, but the fit typically provides a coefficient-of-determination around 0.95. The green horizontal lines mark the lower and upper limits of the heat transfer magnitudes that could be found along the streaks caused by stationary vortices. It can be seen that the linear fit breaks down near the upper limit. The initial kink in the curve near 2 kW/m^2 is found in nearly all run calibrations. Luersen was able to reduce the RMS error by applying a third-order fit as opposed to a linear fit, but a physical justification could be not be found [69]. Thus, all present data uses a linear fit. Clearly, the accuracy of this process leaves room for much improvement.

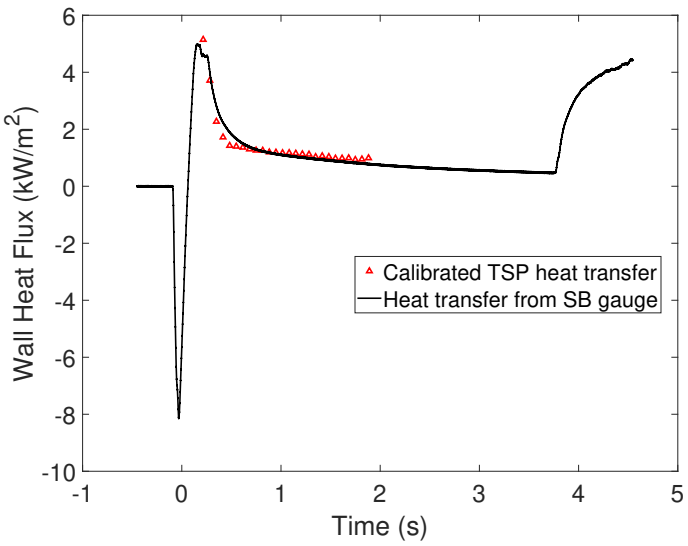

Figure 4.6. Calibrated heat transfer from the temperature sensitive paint (TSP) overlayed onto the data from the Schmidt-Boelter (SB) for the run in Figure 4.5.

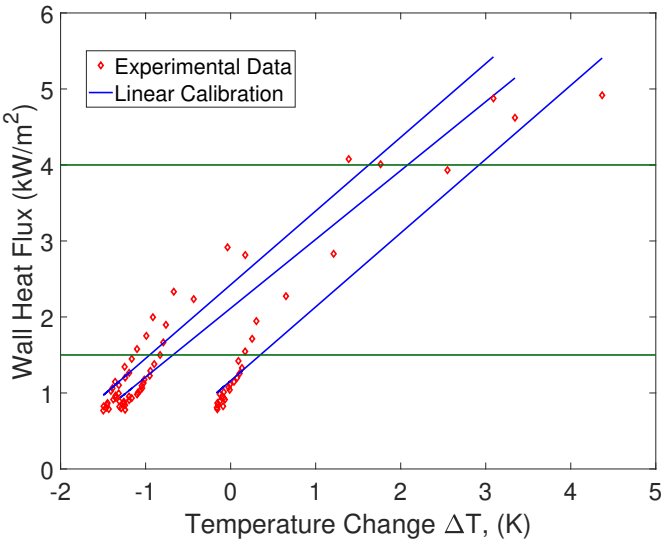

Figure 4.7. Calibration between the temperature change observed from the temperature sensitive paint (TSP) and the data from the Schmidt-Boelter (SB) for the run in Figure 4.5 (middle of the 3 lines) and 2 other runs done at the same initial conditions.

4.7 Mean-flow Computational Fluid Dynamics (CFD) Model

A laminar Navier-Stokes CFD solution for 2 different stagnation conditions was provided by Dr. Neal Bitter at Sandia National Laboratories. This is a mean flow solution calculated using US3D [70]. The stagnation conditions for both computations are shown in Table 4.1. The boundary-layer thickness was defined as the point in the boundary layer at which the total enthalpy reaches 99.5 % of the edge value. Note that this is the default method used in US3D. Equation 4.8 shows the scaling that was used for the boundary layer thickness. Following from this equation, Equation 4.9 was used to adjust the boundary layer thickness to match experimental conditions.

$$\delta \sim \sqrt{Re_{\infty}^{-1}} \tag{4.8}$$

$$\frac{\delta_{computation}}{\delta_{experimental}} = \frac{\sqrt{Re_{\infty,experiemental}^{-1}}}{\sqrt{Re_{\infty,computational}^{-1}}} \tag{4.9}$$

Similarly, Equation 4.10 was used in order to adjust the computed heat transfer to the experimental data.

$$St \sim \sqrt{Re_{\infty}^{-1}} \tag{4.10}$$

Note that the stagnation pressure for most of the runs in this experiment was around 100-110 psia, which is significantly different from either 75 or 155 psia. Figure 4.8(a) and 4.8(b) show the boundary layer thickness and a spanwise cut of the heat transfer using the data scaled from both computations. The stagnation pressure, stagnation temperature, and wall temperature for this computed data are 109.5 psia, 420 K, and 302 K respectively. The axial location of the boundary layer thickness is at 0.051 m (the neutral point), and the axial location of the spanwise heat transfer cut is at 0.30 m.

Table 4.1. Stagnation conditions of mean-flow computation

Solution Number	**Mach #**	**Angle of Attack (°)**	**T_0 (K)**	p_0 (psia)	T_w (K)	Test Gas
1	6	6	415	75	300	air
2	6	6	428	155	300	air

The agreement in the theoretical values found by scaling the different CFD solutions is quite remarkable. It confirms the validity of equations 4.8 and 4.9. Note that the disagreement in the boundary layer thickness, δ, only seems to be near the lee ray, while the disagreement in q is mainly in proximity of the wind ray. This should not be a problem as δ was only analyzed around 40-50° from the wind ray, and the heat transfer was only analyzed between 140-180° from the wind ray, where the values show great agreement. To keep it simple, δ and q will be found by scaling both CFD solutions and averaging to decrease uncertainty.

Figure 4.9, taken from [19], shows a front view of the density gradient in the flowfield at an axial location of 0.3 m using CFD model # 2. Note the mushroom

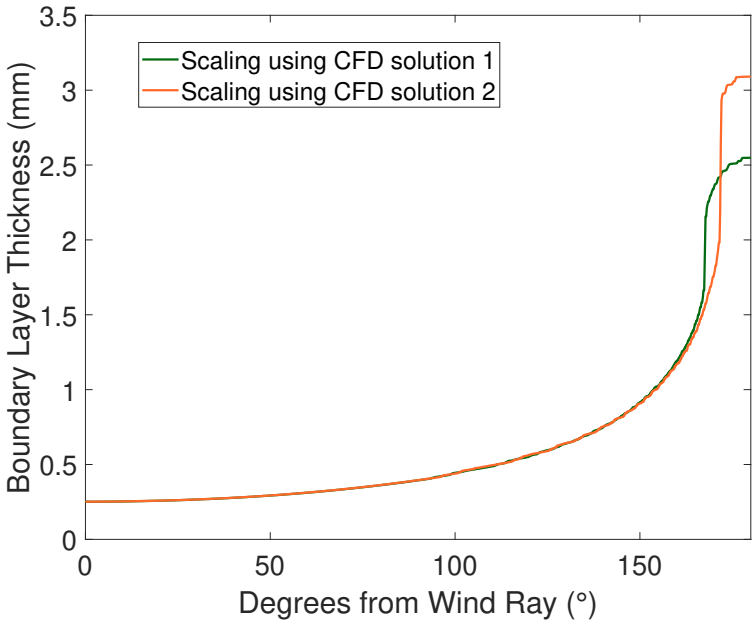

(a) Boundary thickness at an axial location of 0.051 m.

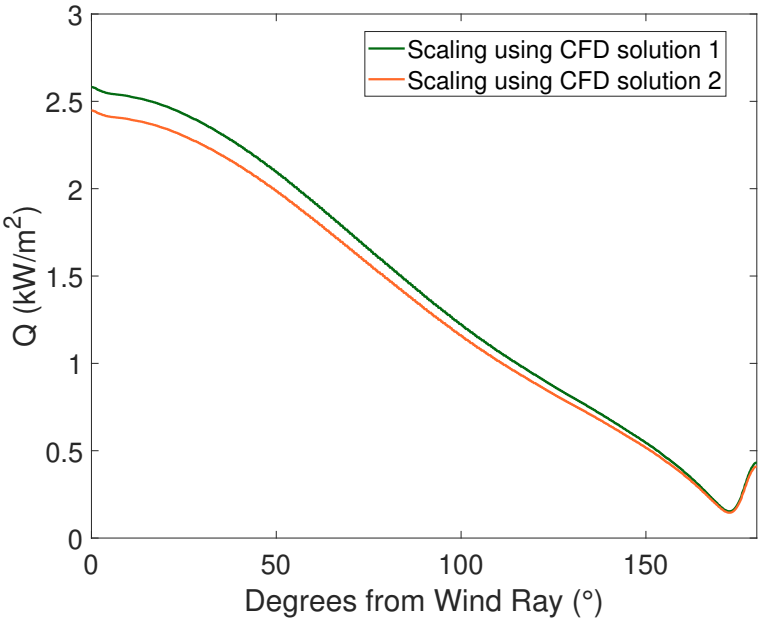

(b) Spanwise cut of the heat transfer at an axial location of 0.30 m.

Figure 4.8. Comparing the scaled theoretical results obtained using computations with 2 different stagnation conditions. $T_{w,i} = 302$ K, Re $= 8.5 \times 10^6$/m , $p_0 = 109.5$ psia, $T_0 = 420$ K.

structure formed near the lee ray. As previously explained, this structure causes the flow in this region to be different than everywhere else on the cone.

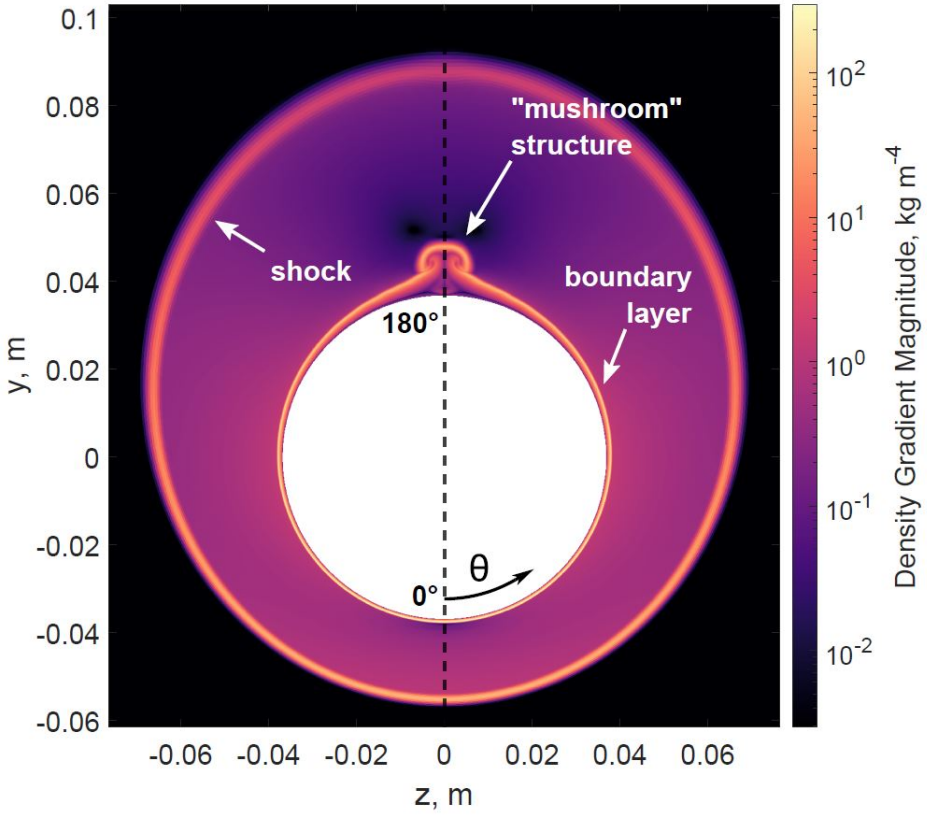

Figure 4.9. Front view of the density gradient of the flowfield at an axial location of 0.3 m. Image from Reference [19]. Printed with permission from Edelman.

4.8 Model Temperature During a Run

One of the reasons for the CJC calibration in Section 5.3.2, besides a more accurate initial wall temperature, was to check one of the assumptions made in the TSP heat transfer reduction code. Recall that the code assumes the heat conduction into the model is 1-D and explained by Fourier's Law. The temperature differential is between the surface of the TSP and the model underneath the TSP and insulating layer, where

the model temperature is assumed to be spatially and temporally constant. The validity of this last assumption was checked using 6 different thermocouples from 3 different SBs. Three of these thermocouples were close to the surface of the model, and the other 3 are were deeper below the surface. They are labeled as surface and base thermocouples respectively. As previously stated, these thermocouples are placed 0.152 mm and 2.79 mm respectively from the surface. Base and surface thermocouples 1, 2, and 3 were 0.2817 m, 0.3383 m, and 0.3762 m from the nosetip, respectively. Also, their azimuthal locations were 32.34°, 27.27°, and 30.91° from the lee ray. Note that these thermocouples are labeled as base and surface thermocouples, but they are not at the actual base or surface of the model. Three channels were captured per run using the Keysight Data Logger with a 5.5 digit accuracy and a sampling rate of approximately 6.5 Hz. Figure 4.10 shows the data collected from the three different base thermocouples during two different runs.

The Mach 6 run time is from about 0 to 4 seconds, after which the tunnel unstart process causes excessive heating, evident by the increase in temperature at around 4 seconds. It seems that most of the temperature change experienced by the model is a result of the tunnel unstart process, in agreement with Ward [43]. Note that all 3 thermocouples show the temperature to be approximately temporally constant during the Mach 6 run. Base thermocouples # 2 and # 3 seem to decrease slightly in temperature, but the decrease seems negligible. Next, notice the difference in pre-run temperature between the different thermocouples. Two are almost the same, while the third differs. The variation is more than 1.5 K which seems to imply that the model temperature is not spatially constant. However, this variation was suspected to be due to the error in the performed thermocouple-CJC calibration, rather than due to an actual spatial variation in the temperature. Thus, the initial temperature was recorded from each thermocouple for a single compensator before several runs. The calibrated temperature is shown in Table 4.2.

From Table 4.2, it is evident that the deviation between differently spaced thermocouples for the same compensator is on average about $\pm$ 0.05 K. This deviation

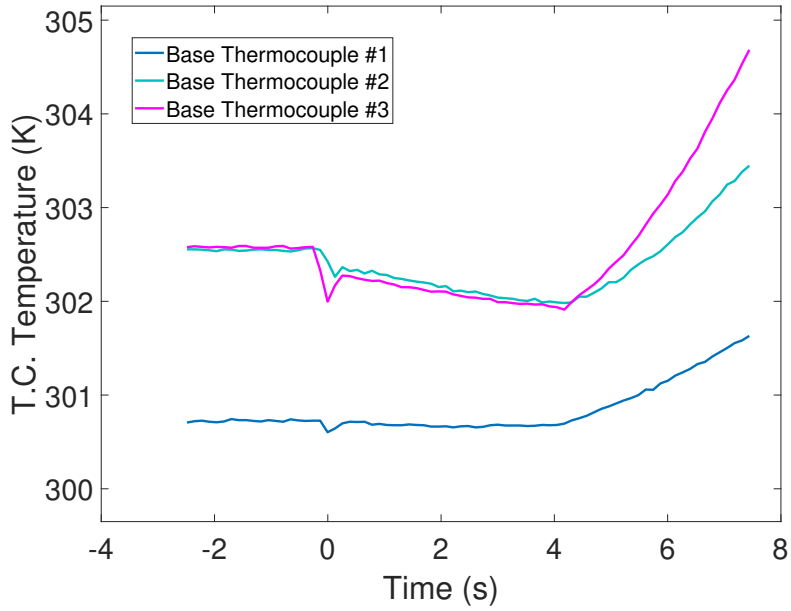

(a) 102 μm insert (# 4). $T_{w,i} = 303$ K, Re $= 8.6 \times 10^6$/m , $p_0 = 110.0$ psia, $T_0 = 419$ K. Run 213.

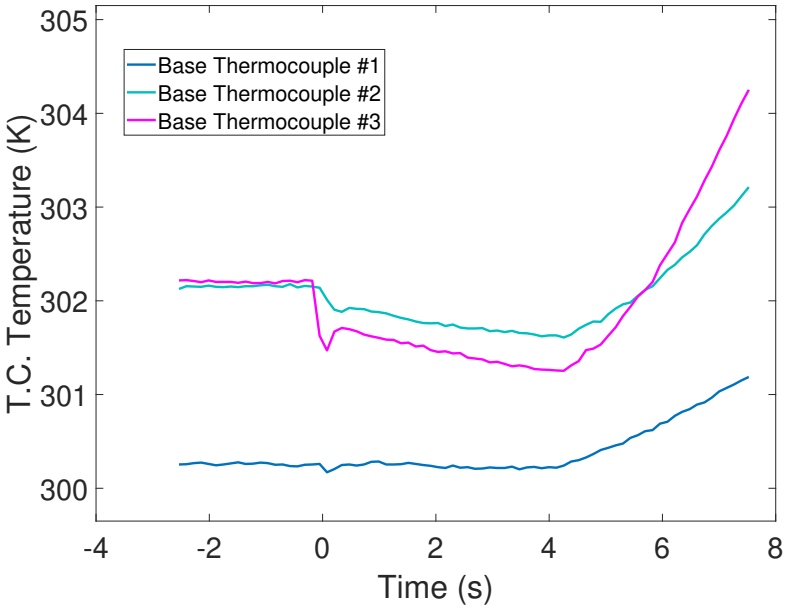

(b) 203 μm insert (# 7). $T_{w,i} = 302$ K, Re $= 8.5 \times 10^6$/m , $p_0 = 109$ psia, $T_0 = 420$ K. Run 215.

Figure 4.10. Temperature of model read from base thermocouples of SB during a run.

Table 4.2. Pre-run thermocouple temperature from a single CJC.

Run #	**Surface T.C. 1 [K]**	**Base T.C. 1 [K]**	**Surface T.C. 2 [K]**	**Base T.C. 2 [K]**	**Surface T.C. 3 [K]**	**Base T.C. 3 [K]**
15	305.78	305.78	305.68	305.73	305.70	305.73
16	306.13	306.13	306.18	306.18	306.10	306.13
17	306.10	306.05	306.10	306.08	306.10	306.05
22	308.92	308.80	308.95	308.87	308.92	308.85

is much lower than the difference seen in Figure 4.10. Thus, the apparent pre-run temperature difference in Figure 4.10 is likely due to calibration error.

To ensure that the trend in the temperature change was not CJC dependent, 2 runs were performed at the same conditions, while the CJC for thermocouple #3 was switched between each run. This can be seen in Figure 4.11. Even though there is a slight offset between both lines due to both calibration uncertainty, and the slightly different initial temperatures, the shape of the line seems to be almost identical. This also reinforces that the discrepancy between the CJCs is linear, and a simple offset can be used as a correction between them.

Finally, it should be noted that the temperature change in the base thermocouple during a run is possibly equivalent to the temperature change of the model under the insulating layer during a run. Even though the base thermocouple is 2.799 mm from the surface of the model, and the paint layer above the model is only about 0.12 mm, the paint layer is more thermally insulating than the aluminum model or the metal casing of the sensor. Thus, the heat is able to penetrate the model more efficiently than the paint layer.

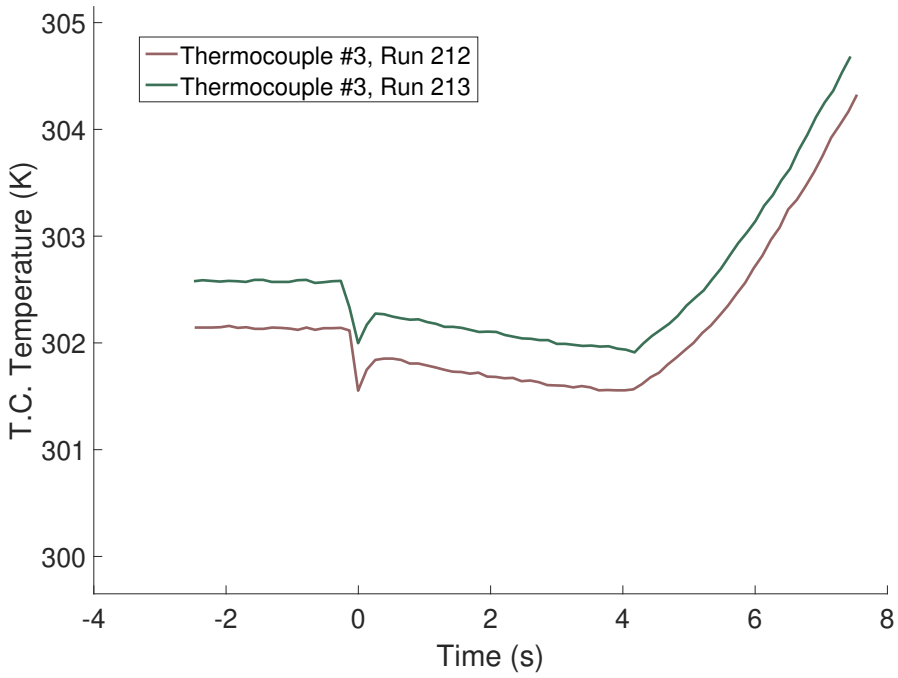

Figure 4.11. Temperature of model read from base thermocouples of SB during a run for the same thermocouple from different CJCs over two separate runs. 102 μm insert (# 3). Approximate run conditions are $T_{w,i} = 303$ K, Re $= 8.6 \times 10^6$/m, $p_0 = 109.8$ psia, $T_0 = 419$ K.

5. RESULTS

5.1 Detailed Processing of Streaks using TSP

TSP has been proven to be a useful technique to attain qualitative measurements of the heat transfer on the surface of the model. It has been used to show flow patterns such as transition, separation, and streaks. Obtaining quantitative measurements has been more challenging, although still possible [59] [12] [66]. The reliability of the heat transfer values depends on many factors such as the accuracy of the SB gage, the quality of the TSP in the patch used for calibration, paint job quality, and the validity of assumptions used.

In addition, discerning the relationship between the change in temperature of the paint layer and the intensity of the emitted light is an issue as well. While ΔT maps are attained using a relationship describing the change in intensity emitted by the luminophore molecules and the change in temperature, the utilized relationship depends on the paint composition, the insulating layer below the paint layer, and the paint thickness. Thus, this relationship may be unique for each paint job. The functional relationship currently in use is actually the calibration for Ru(bpy) in DuPont ChromaClear [65], while the current paint being used is Amtech Clearcoat (AM-500-4). The type of primer used as the insulating layer beneath the coat of paint would also affect the calibration [68]. Essentially, this means that the accuracy of the ΔT maps is uncertain, even though they can be used for qualitative measurements. However, when the temperature change is converted into heat transfer using an accurate SB and an adjacent TSP patch devoid of major streaks, quantitative results can be obtained [66].

5.1.1 Obtaining Unwrapped Heat Transfer Image

The process begins with a TSP image showing the global temperature change of the model. For example, Figure 5.1 shows the temperature change on the model 1 second into the run. Note that the run number is given in the caption, and that all TSP images in this report are taken 1 second into the run unless otherwise specified. This corresponds to a specific run number in Section A in the Appendix.

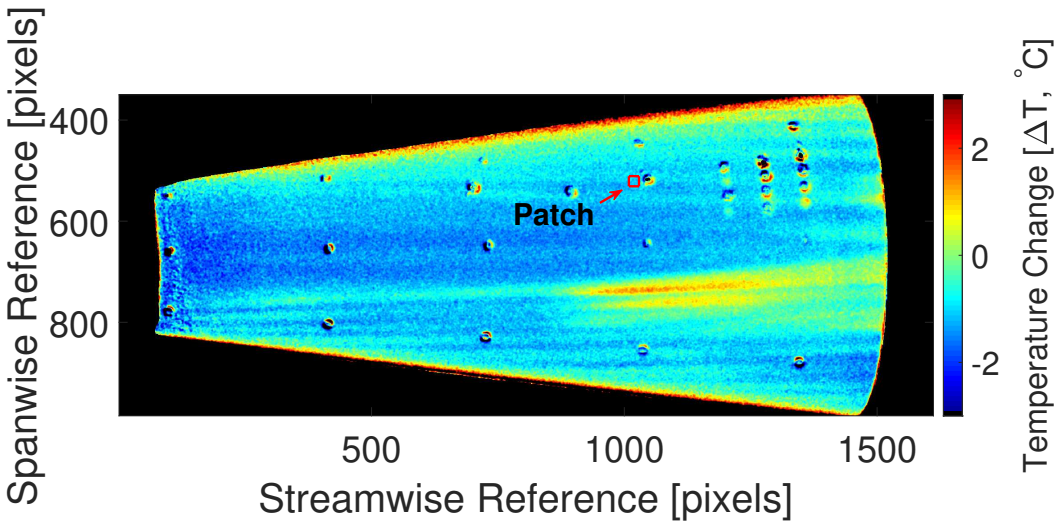

Figure 5.1. Global TSP temperature change map. 152 μm insert (# 6). $T_{w,i} = 303$ K, Re $= 8.5 \times 10^6$/m , $p_0 = 110$ psia, $T_0 = 420$ K. Run 209.

Note that the temperature change on most of the model is negative, illustrating the need for SB calibration. As previously stated, to calibrate the temperature change into a surface heat transfer, a patch of TSP was chosen adjacent to the Schmidt Boelter for comparison. The patch size was taken to be approximately the same area as the surface area of the SB sensor head which is given to be 3.175 mm^2. The TSP algorithm analyzes a TSP patch that is square in shape whose sides are equal to the diameter of the patch. It requires the top right pixel coordinate of the patch as an input. It should be noted that the calibration of the TSP ΔT map into the heat transfer map is sensitive to the pixel coordinate given as an input for the TSP patch.

Thus, to remain consistent, instead of using the pixel coordinate of the top right corner of the patch, the SB's pixel coordinates were inputted. The top right corner of the patch was then taken to be offset in the vertical and horizontal direction from the SB location by a certain amount of pixels. This offset was kept constant between runs to ensure proper comparison in heat transfer could be made. However, by no means did this eliminate the uncertainty in the SB calibration process. For a detailed explanation of the effect of the location of the calibration patch as well as the specific SB sensor used for calibration on the TSP calibration, the reader is referred to Sections 5.1.3 and 5.1.4 respectively. An example of a calibrated TSP heat transfer image is shown in Figure 5.2.

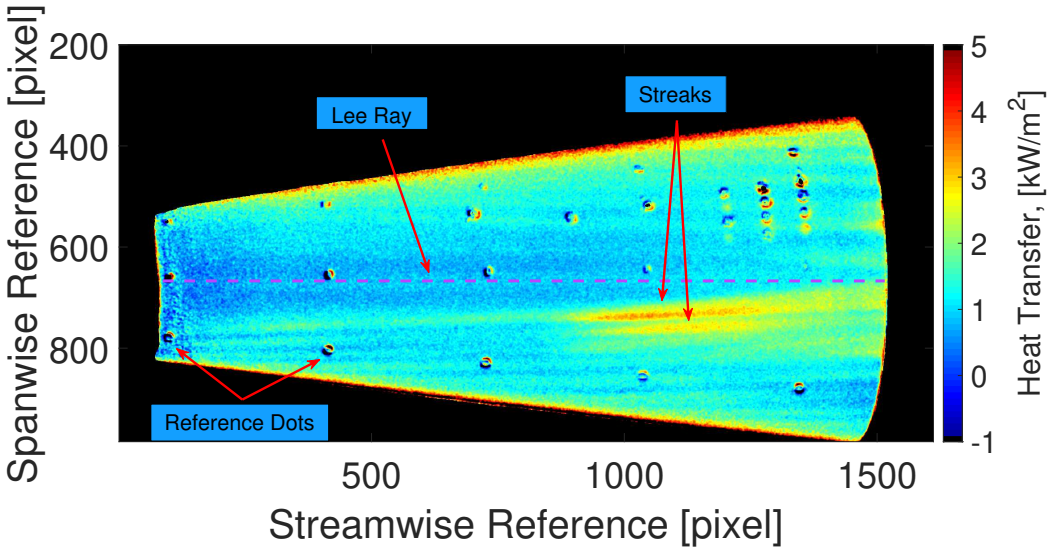

Figure 5.2. TSP Heat transfer image calibrated from Figure 5.1 using an in-situ SB calibration.

In this image and all subsequent images, the flow is from left to right. Also, unless otherwise specified, the imaged side will be the leeward side. The lee ray and the streaks that are analyzed in this experiment are indicated by the arrows. The reference dots are Sharpie marks drawn on the cone, and there are 15 of them

altogether. As previously stated, the dots are 2 inches apart in the axial direction. The middle row of dots are 2° above the lee ray, and the other 2 rows are 45° above and below the middle row respectively. These dots were essential for the next step which was to unwrap the image into physical coordinates, x and θ. X is the axial distance from the nosetip in meters, and θ is the azimuthal reference coordinate in degrees where a value of 0° corresponds to the lee ray. Note that any coordinate labeled by the "azimuthal reference" uses this definition. If the physical locations of the reference dots are known, then the image can be unwrapped by comparing the physical coordinates to the pixel coordinates. The images were unwrapped using a 2nd degree polynomial in the azimuthal direction at each axial location, requiring 3 reference dots at each axial point. The unwrapped TSP image of Figure 5.2 is shown in Figure 5.3. Note that by unwrapping the image, we are restrained to the TSP data bounded by the reference dots.

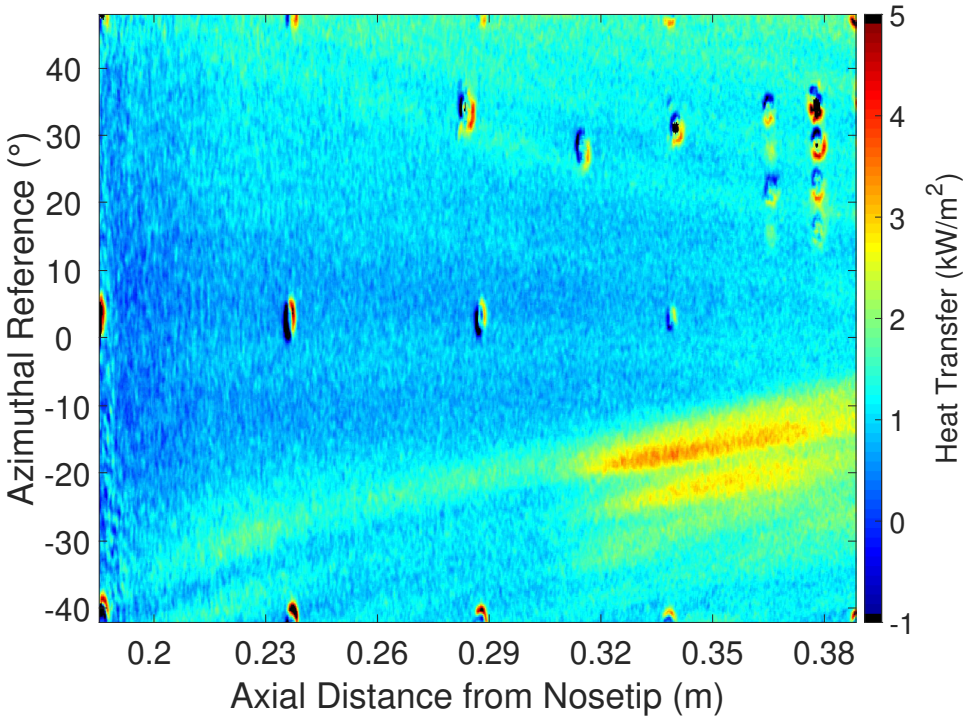

Figure 5.3. Unwrapping Figure 5.2 into physical coordinates.

5.1.2 Extracting Streaks from Unwrapped Image

As the characteristics of the streaks being analyzed is vital to this experiment, it is important to describe the procedure by which the heat transfer along the streak was extracted. Once the true coordinates of the image were known, the next step was to find the location of the vortex-induced streak. Note that there are 2 clearly visible streaks in Figure 5.3 below the lee ray and one faint streak below these 2. Most of the images in this present experiment will consist of the same pattern. The upper and lower streaks will be referred to as the leeward streak and windward streak based on their distance to the lee ray and wind ray respectively. To calculate the location of the streaks, each streak was broken into 3 line segments with the first point of the first line starting at the most upstream location that would be analyzed and the last point of the third line starting at the most downstream location that would be analyzed. The most upstream position was manually picked to be slightly upstream of the pixel where the growth of the streak was detectable from the TSP. The ending position was manually picked to be downstream of the peak of the streak in which the heat transfer reached a peak and had finished growing. The reason for these choices are because this experiment is only concerned with the linear portion of growth of these stationary crossflow vortices. The points on this curve (that was broken into 3 lines) were used as an initial guess for each axial location. At each axial location, a spanwise cut was taken, encompassing 20 pixels on either side of the initial guess for a total of 41 pixels. The maximum value and corresponding azimuthal coordinate in this spanwise cut was taken to be the heat transfer value of the streak and azimuthal location respectively. Once this process was finished for each axial location, the azimuthal location was filtered in the axial direction using a 30 point moving average.

Note that this algorithm must be run separately for each streak. In order to determine the sensitivity of the streak location to the size of the spanwise cut, cuts of different lengths were taken for the leeward streak in Figure 5.3 and the location of the streaks were extracted. This is shown in Figure 5.4.

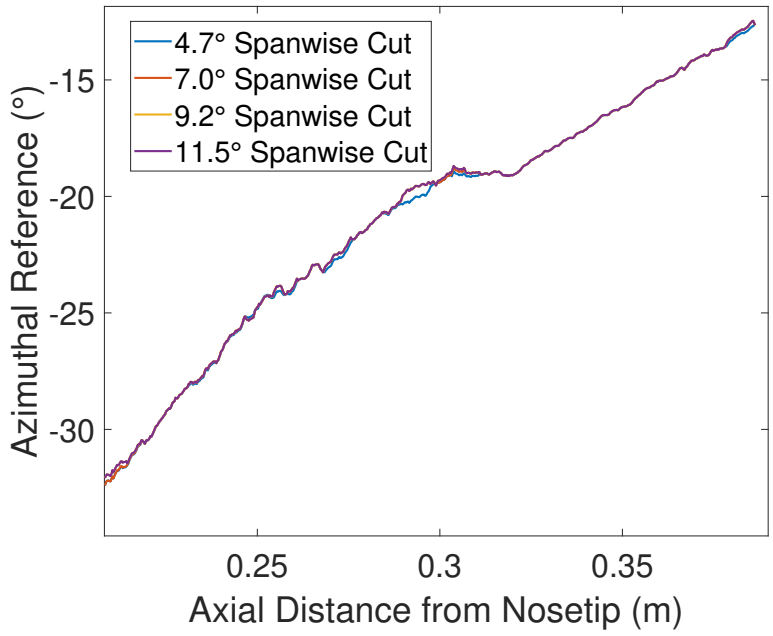

Figure 5.4. Dependency of streak extracting algorithm on length of spanwise cut. Leeward streak in Figure 5.3

.

It is clear from the figure that there is very little variation in the streak location when the length of the spanwise cut is varied. Thus, a spanwise cut of 9.23° (or 20 pixels above and below) was deemed enough. Figure 5.4 implies that with a reasonable initial guess, the algorithm should be able to accurately track the streak. If the spanwise cut was too long and reached into adjacent streaks, the cut was reduced from 20 pixels to 15 pixels on either side. From Figure 5.5, it can be visually seen that the algorithm is able to pick out the streaks relatively well. Figure 5.5 shows Figure 5.3 with the extracted location of the streaks illustrated in red.

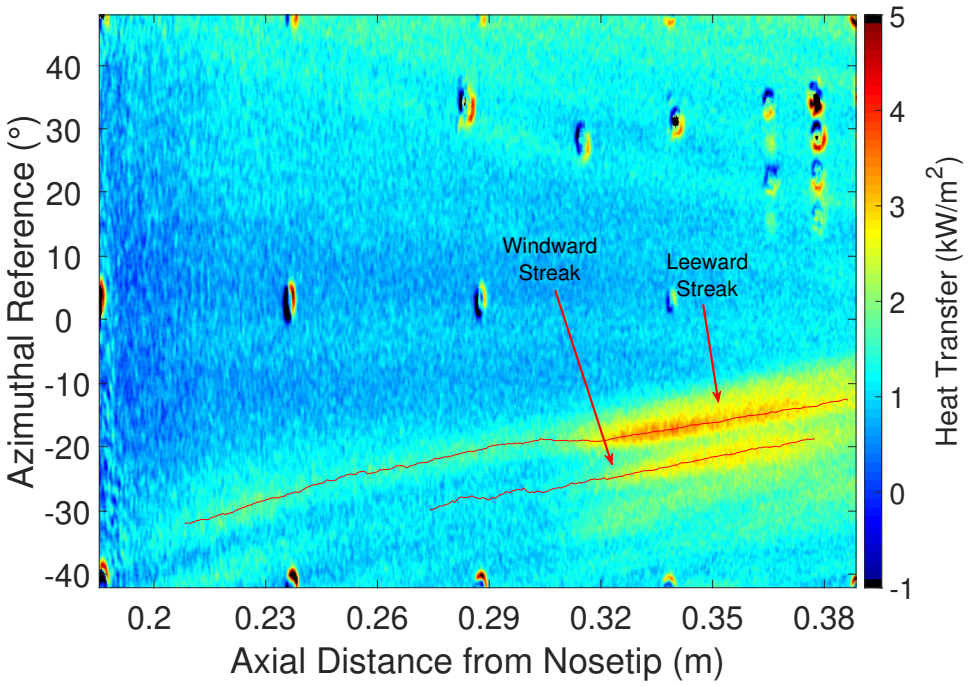

Figure 5.5. Figure 5.3 with lines indicating streaks that were analyzed.

5.1.3 Effect of Patch Location on Calibration and Heat Transfer along Streaks

As previously stated, the location of the patch used in the TSP calibration process was important for the TSP data reduction algorithm. It is important to quantify how sensitive the quantitative results are to this location. It is likely that the results are more sensitive when there is a streak in close proximity to the SB that is used to calibrate the TSP. Unfortunately most of the SBs that were used in this experiment were next to streaks due to the 3-D geometry of crossflow on a yawed straight cone. There were not many places on the cone devoid of streaks. The most ideal place would likely be slightly off the lee ray and upstream. However, due to the painting and sanding techniques, this area also contained less TSP which lead to a lower signal to noise ratio. In order to ascertain how sensitive the data were to the patch

location, TSP heat transfer on a cone at a 6° angle of attack with roughness insert # 6 was analyzed along with the TSP heat transfer on a cone at a 0° angle of attack with the smooth insert using four different patch locations to calibrate the TSP. The different patch locations for each geometry are shown in Figures 5.6(a) and 5.6(b) which show the global temperature change for the 0° angle of attack and 6° angle of attack cases. Patches 1 and 4 are labeled, and the other 2 patches are numbered in a counterclockwise fashion.

The TSP linear calibration fit for each patch for each run is shown in Figure 5.7. Both the linear fits and the experimental patch heat transfer values do not seem to have much variation especially at lower heat transfer magnitudes. This is a good sign that the TSP calibration process is not overly sensitive to the choice of patch location. The heat transfer map was then obtained, the images were unwrapped, and a spanwise cut of the heat transfer was taken at an axial location of 0.3 m, and a moving average of 5 pixels was applied. This is shown in Figures 5.8(a) and Figures 5.8(b) for the 0° and 6° angle of attack cases respectively.

It is interesting that the 0° angle of attack spanwise cut has more variation with respect to the TSP patch location. Although the 6° spanwise cut shows variation in the heat transfer, the maximum difference is about 3%, which is not significant. It should be noted, however, that the variance in heat transfer seems to be higher at peaks and valleys in the heat transfer, which means the patch location should have a more significant impact on the streak heating. Thus, Figure 5.9 shows the heat transfer along the leeward streak in Figure 5.6(b). The variation in heat transfer is almost insignificant except for the the heat transfer at the peak of the streak near x = 0.34 m. The maximum difference is about 8 %.

To further examine the variation in heat transfer based on the patch location, Figure 5.10 shows a run performed with a different roughness element. Figure 5.10(a) shows the global temperature change during the run with the patches that were used, while Figure 5.10(b) shows the heat transfer along the leeward streak.

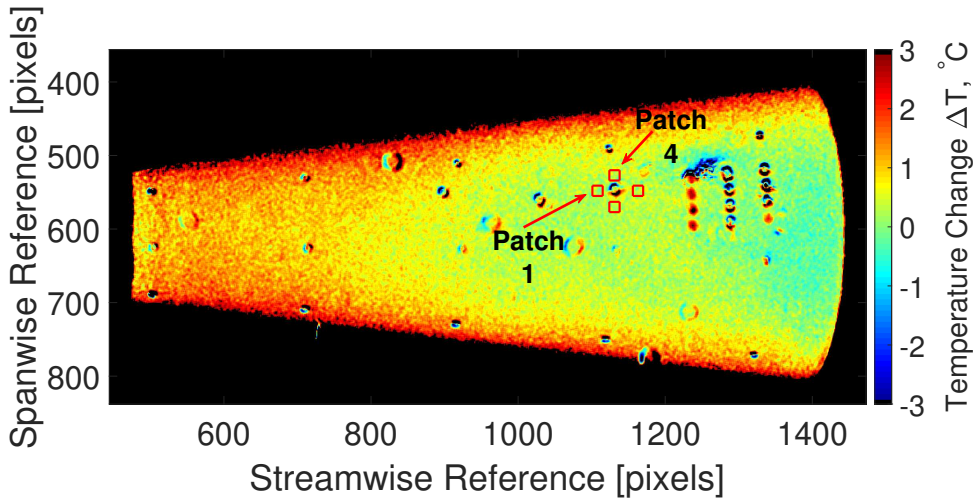

(a) 0° angle of attack. Smooth insert (# 1). $T_{w,i} = 299$ K, Re $= 9.3 \times 10^6$/m, $p_0 = 122.3$ psia, $T_0 = 424$ K. Run 309.

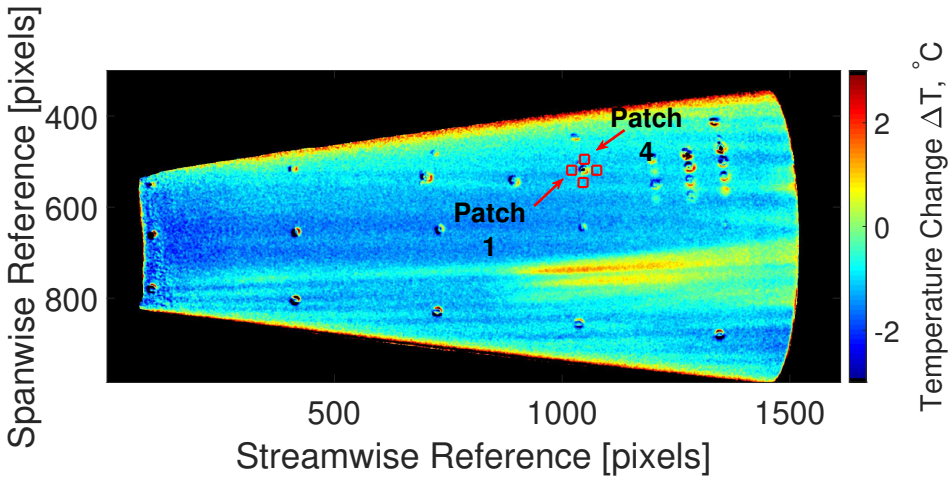

(b) 6° angle of attack. 152 μm (# 6). $T_{w,i} = 302$,K Re $= 8.5 \times 10^6$/m, $p_0 = 109.5$ psia, $T_0 = 420$ K. Run 209.

Figure 5.6. Temperature change during 2 different runs with 4 different calibration patches labeled.

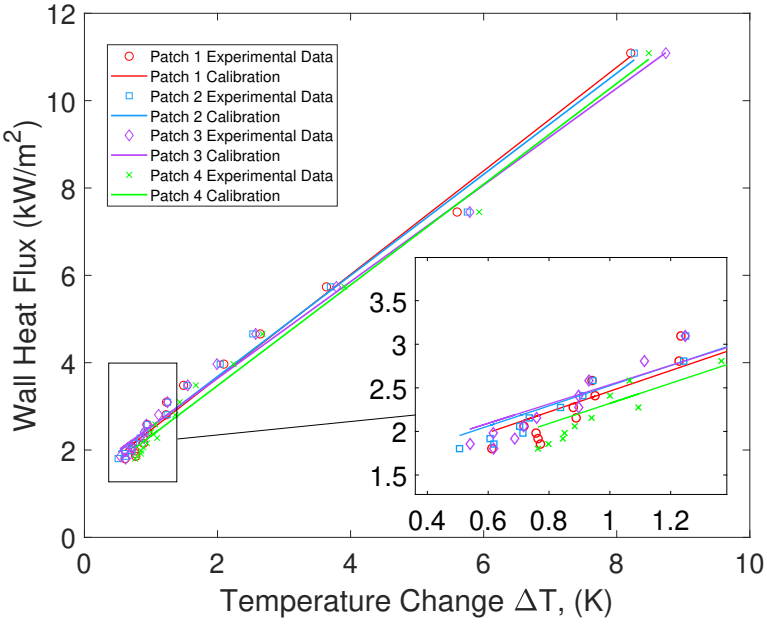

(a) 0° angle of attack. Smooth insert (# 1). $T_{w,i}$ = 299 K, Re = 9.3 × 10^6/m, p_0 = 122.3 psia, T_0 = 424 K. Run 309.

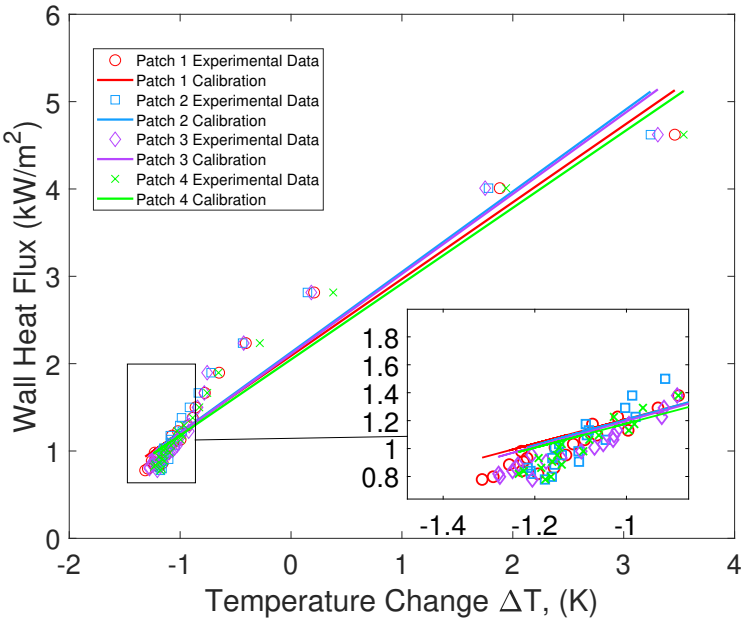

(b) 6° angle of attack. 152 μm (# 6). $T_{w,i}$ = 302 ,K Re = 8.5 × 10^6/m, p_0 = 109.5 psia, T_0 = 420 K. Run 209.

Figure 5.7. TSP linear calibrations for 2 different runs with 4 different calibration patches.

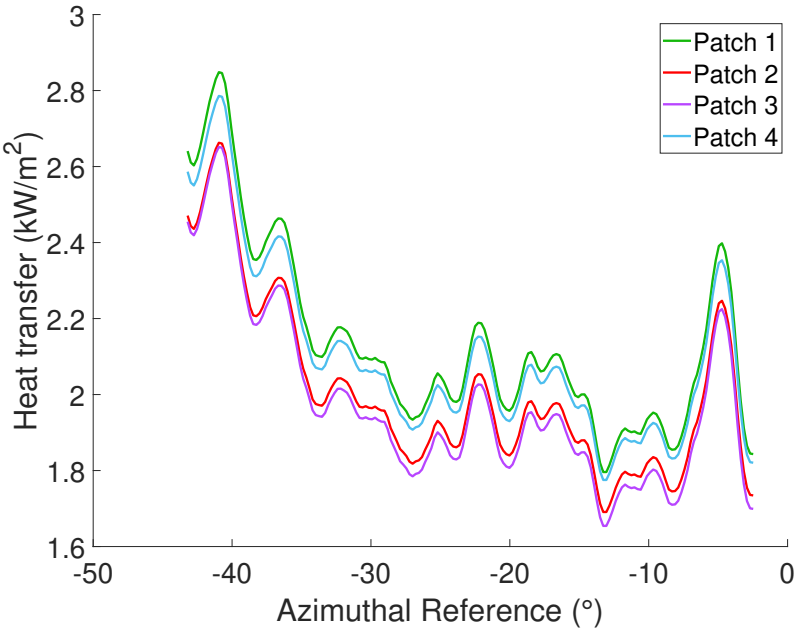

(a) Spanwise cut of image in Figure 5.6(a). Model at 0° angle of attack.

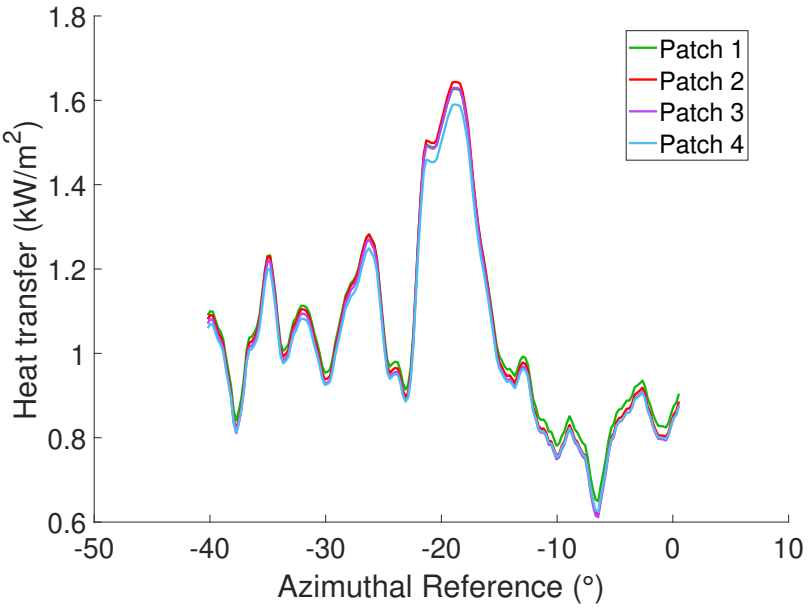

(b) Spanwise cut of image in Figure 5.6(b). Model at 6° angle of attack.

Figure 5.8. Heat transfer of spanwise cut at an axial location of 0.3 m for the different calibration patches in Figure 5.6.

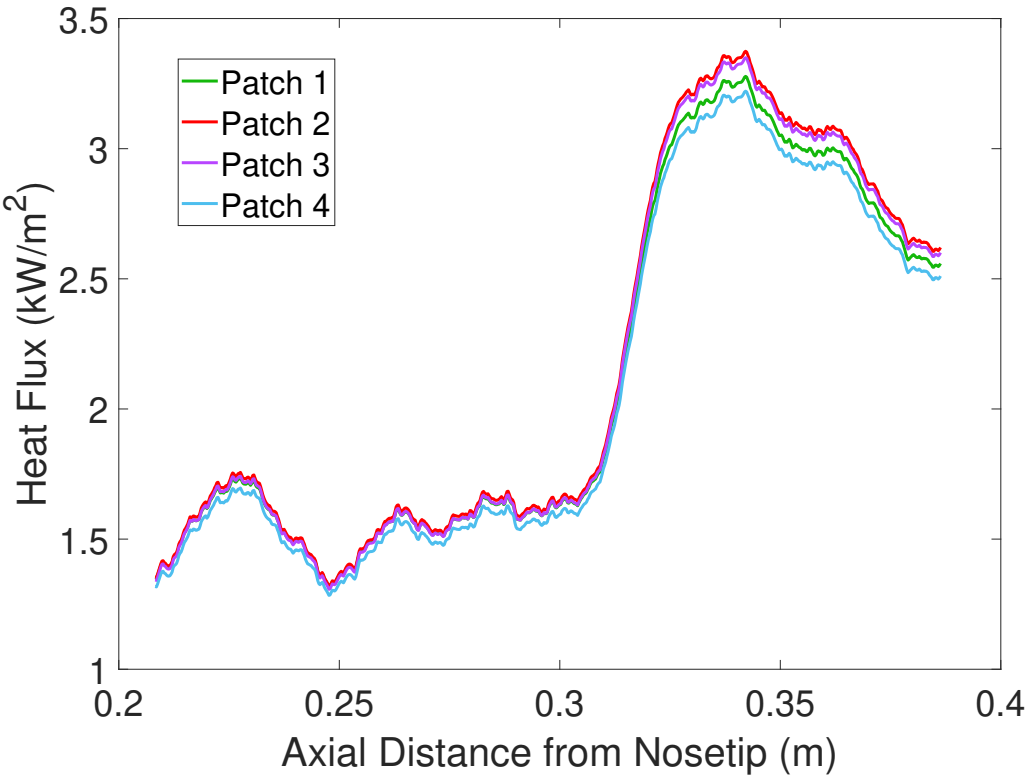

Figure 5.9. Heat transfer along windward streak using different calibration patches for image in Figure 5.6(b).

This run is more sensitive to the patch location than the run in Figure 5.6(b). The maximum difference is about 25 %. To better quantify the variation, the heat transfer was averaged at every axial location over the heat transfer obtained from all 4 calibration patches. Then, a normalized rms variation was found by dividing the deviation from the average heat transfer by the average heat transfer at each axial location for every patch. The normalized rms variations were then found to be 7.67 % , 5.55 % , 8.65 % , 4.81 % for patches 1 to 4 respectively. For comparison, the normalized rms variations for the streaks caused by the 152 μm insert, as shown in Figure 5.9, are 2.20 %, 0.84 % , 1.58 % , 0.54 % for the 4 patches respectively. Although the variations in the heat transfer for the streaks caused by the 203 μm insert are certainly not negligible, they do not seem to be a cause for concern.

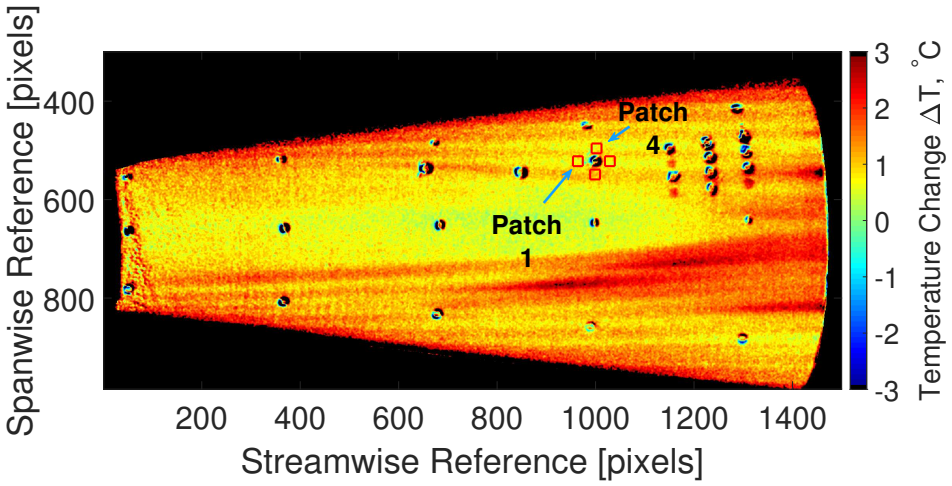

(a) Temperature change map with 4 patches labeled.

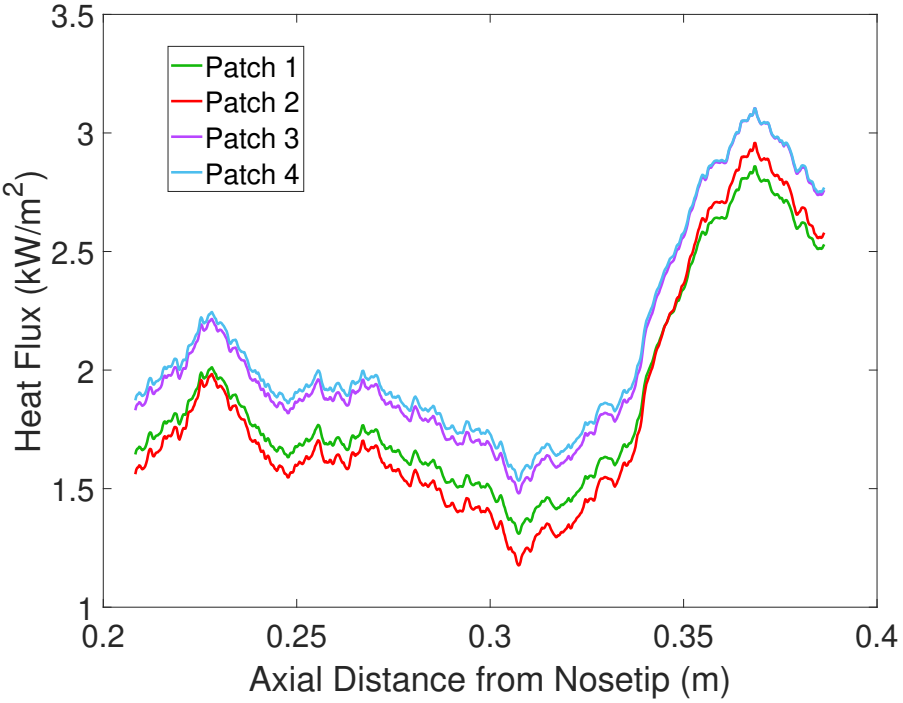

(b) Heat transfer along leeward streak for different calibration patches for image in Figure 5.10(a).

Figure 5.10. Heat transfer using 4 different patches for calibration. 203 μm insert (#7). $T_{w,i} = 302$ K, Re $= 8.5 \times 10^6$/m, $p_0 = 109.1$ psia, $T_0 = 420$ K. Run 215. Model at 6° angle of attack.

Two more runs were performed at the same stagnation conditions for both the runs in Figure 5.6(b) and Figure 5.10(a) to make a total of 6 runs. It is interesting to compare the variation in the SB data at the time the data was extracted. The SB data for the 3 runs done with the 152 μm insert are shown in Figure 5.11(a) while Figure 5.11(b) contains the SB data for the 3 runs done with the 203 μm insert. It is clear that the SB data from runs performed with the 203 μm has more variability between runs. The SB data extracted from runs completed with the 152 μm insert show little variation, making it hard to differentiate between the lines.

The SB heat transfer data was extracted by taking 40 data points before and after a time of 1 second. This is shown in Table 5.1. Note that a time of 1 second was chosen as this was the time of the run during which the previous streak heat transfer data was extracted. Any chosen time would have been able to show the same general trend.

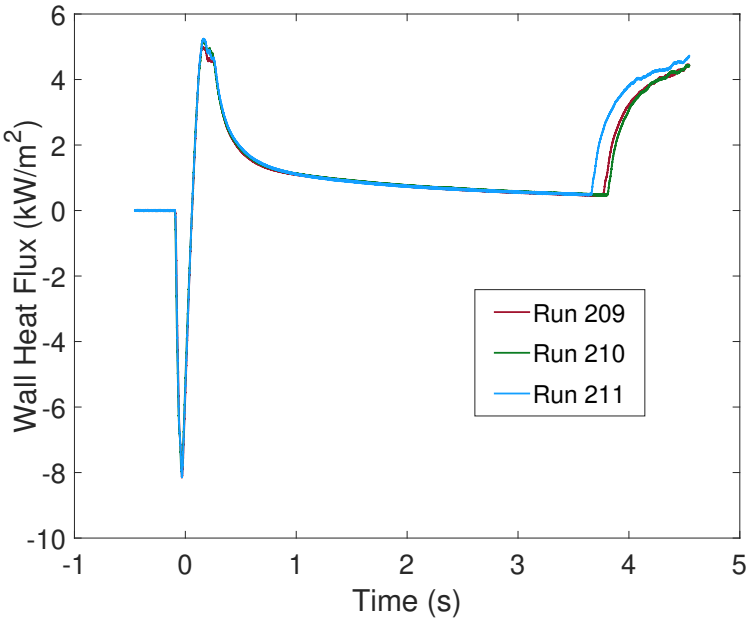

(a) 152 μm insert (# 6).

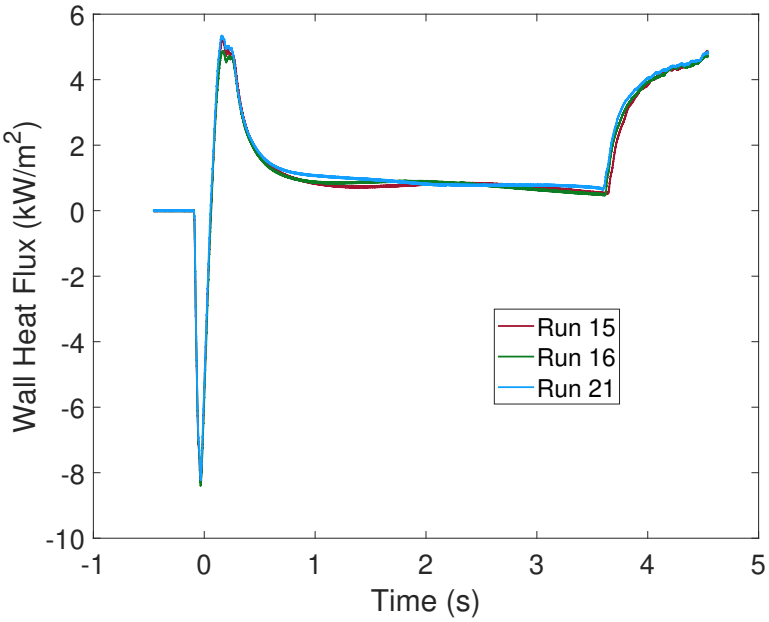

(b) 203 μm insert (# 7).

Figure 5.11. SB heat transfer for different runs done with the same initial conditions. Approximate run conditions are $T_{w,i}$ = 302 K, Re = 8.4×10^6/m, p_0 = 109.2 psia, T_0 = 420 K.

Table 5.1. SB data averaged for selected runs.

Roughness Insert #	**Run #**	**Heat Transfer from SB [kW/m^2]**
6 (152 μm)	209	1.105
6 (152 μm)	210	1.120
6 (152 μm)	211	1.114
7 (203 μm)	215	0.839
7 (203 μm)	216	0.876
7 (203 μm)	221	1.073

Table 5.1 helps to emphasize that the variability in the SB heat transfer for the 203 μm insert case is a lot higher than the 152 μm insert case. Because the TSP calibration seems to be more sensitive to the patch location, and the SB variation in between runs done with the same initial conditions is higher for the runs done with the 203 μm insert, this implies an adjacent streak in close proximity to the SB may be influencing the TSP calibration. Comparing Figure 5.6(b), displaying the ΔT map for a run performed with the 152 μm insert, with Figure 5.10(a), displaying the ΔT map for a run performed with the 203 μm insert, there seems to be a streak adjacent to the SB in both images. However, the streak for the 203 μm insert case looks visually stronger when comparing the magnitude of the temperature difference of the streak with the temperature difference of the area adjacent to the streak. The SB would likely be more sensitive to an adjacent streak that was stronger.

5.1.4 Calibration and Heat Transfer Along Streaks using Different SBs

Because the TSP calibration is highly dependent on the SB, it is necessary to examine the calibration of the same run using two different SBs. Figure 5.12 shows the TSP temperature change map for 2 different runs, each having 2 calibration patches and their respective SBs, which are labeled. SB #1 is at an axial location

of 0.2817 meters from the nosetip and 24.34° above the lee ray. SB #2 is at an axial location of 0.3132 m from the nosetip and 15.46° above the lee ray. Note that Figure 5.12(a) was done with a 203 μm insert (#7) and Figure 5.12(b) was done with a 254 μm insert (#8).

The heat transfer was extracted using both SBs for either run along the windward and leeward streaks, and this is shown in Figures 5.13(a) and 5.13(b) respectively. To better quantify the variance, an average percent change was calculated for the leeward and windward streaks. This was found by calculating the average heat transfer for a set of leeward (or windward) streaks at each axial location, averaging the percent difference for each SB, and then averaging over the range of axial locations. For the leeward streaks, the average % change when changing SBs was 6.3 % and 7.0 % for the 203 μm and 254 μm inserts respectively. For the windward streaks, the average percent change when changing SBs was 9.1 % and 12.7 % for the 203 μm and 254 μm inserts respectively. While both runs have approximately the same sensitivity to the SB change, the run done with the 254 μm insert is slightly more sensitive to the SB used for calibration. However, the higher sensitivity found with the 254 μm insert may also simply be because it creates streaks with a higher heat transfer which causes the sensitivity between the SBs to be amplified. Unfortunately, data from 2 SBs on a model are not enough to make clear conclusions. It would be interesting to repeat this experiment with a higher SB count to possibly quantify the effect of the location of a streak in relation to the SB on the TSP calibration.

Moving forward, it is apparent that streaks occur over much of the cone surface due to the 3-D geometry of crossflow. Thus, it should be taken into account that the heat transfer values extracted along the streak may be slightly SB sensitive. It seems that adjacent to the lee ray is the best place to install a sensor, so TSP calibration using an SB near this location was attempted whenever possible. The location of the SB used to calibrate the data will be given when displaying streak heat transfer so the reader can have a better idea of the uncertainty.

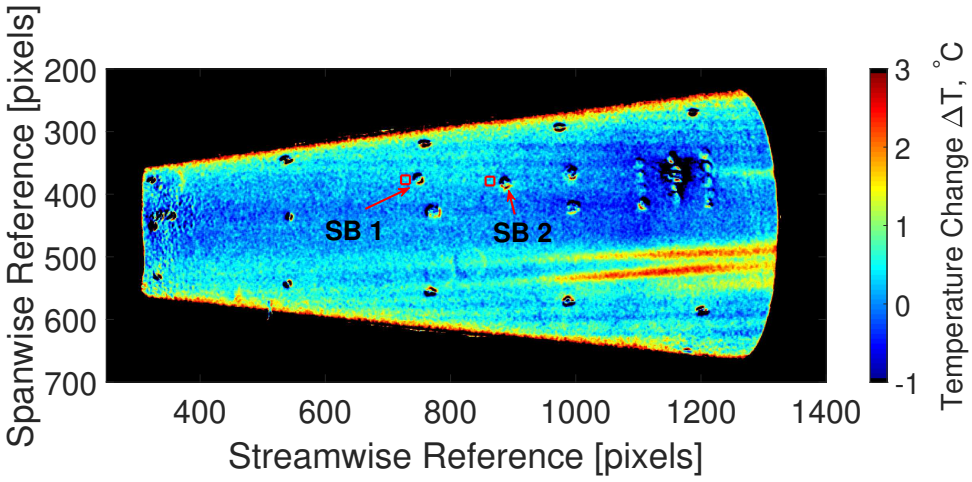

(a) 203 μm insert (#7).

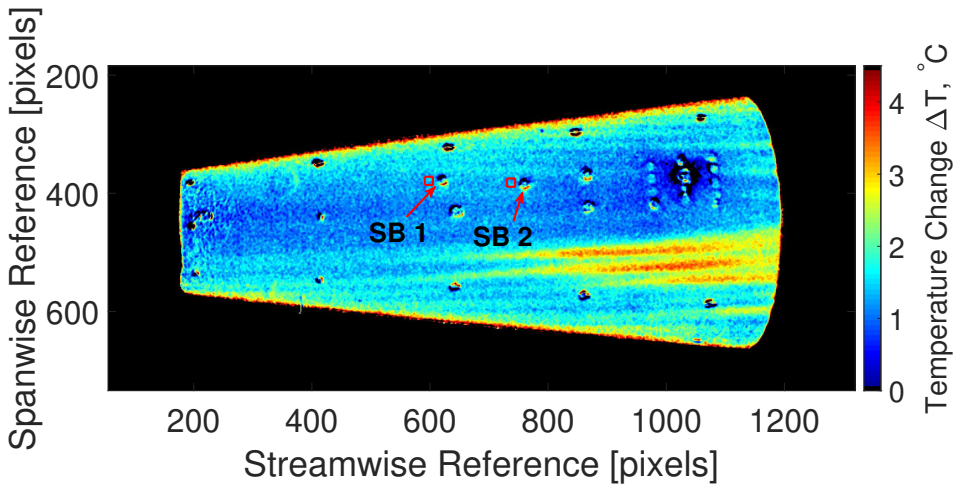

(b) 254 μm insert (#8).

Figure 5.12. Temperature change with 2 labeled SBs and their adjacent patches. Approximate run conditions are $T_{w,i} = 302$ K, Re $= 7.9 \times 10^6$/m, $p_0 = 102.4$ psia, $T_0 = 420$ K.

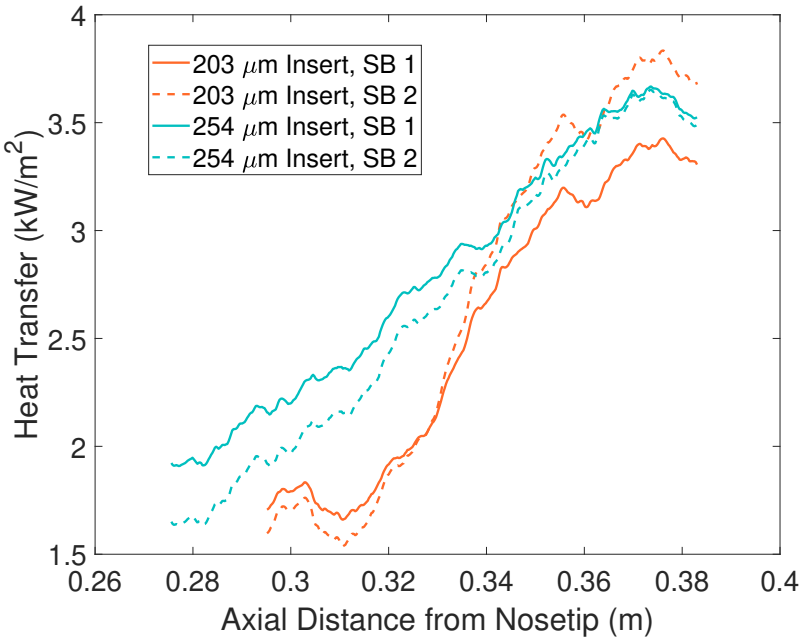

(a) Leeward streaks.

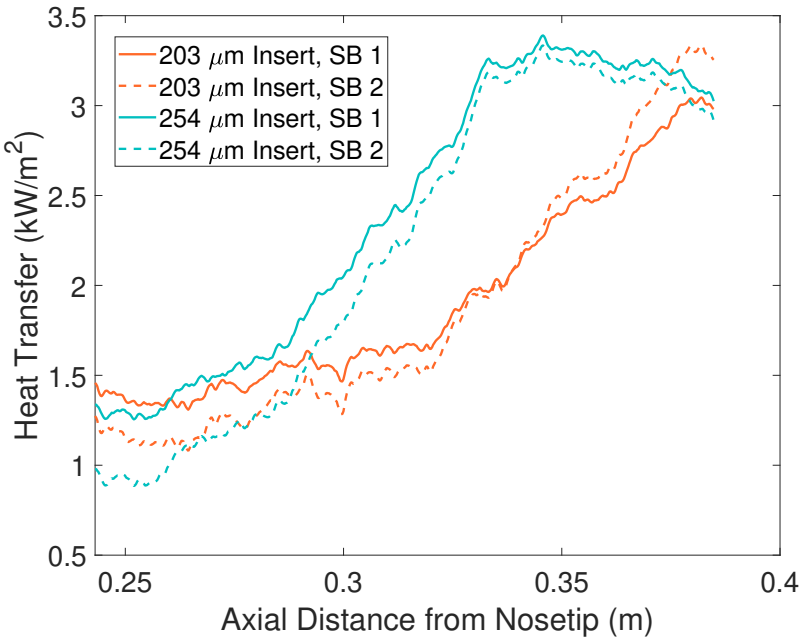

(b) Windward streaks.

Figure 5.13. Heat Transfer along leeward and windward streaks for the streaks in Figure 5.12 using both SBs.

5.2 Demonstrating Control over Streaks

Past experiments on high-speed flow suggest that stationary crossflow, excited by surface roughness on the model, dominates in quiet conditions. This would be similar to the patterns observed in low-speed flow. When the smooth insert (# 1) was placed on the cone frustum, however, stationary crossflow vortices were still observed. Ward found that these vortices were likely formed due to the paint step and distributed paint roughness [12]. Compared to the paint step in this experiment however, Ward's paint step was placed slightly farther upstream at an axial distance of 0.1524 m from the nosetip. The paint step for the present experiment was about 0.1854 m from the nosetip. The vortices may also be influenced by the step between the roughness insert and the frustum. In this experiment, the upstream step and downstream step of the roughness insert were about 0.0384 m and 0.0640 m downstream from the nosetip respectively, making them somewhat close to the neutral point of 0.051 m from the nosetip. Although it is unclear what effect these steps may have had on the flow, the steps were all measured to be less than 25.4 μm, making their heights less than the the roughness elements that were used.

Although it is interesting to observe the streaks that form on the cone when the smooth insert is used, the roughness that caused these vortices could not be reliably controlled. In order to vary the roughness in a more repeatable manner, RIM inserts with discrete roughness elements at fixed azimuthal locations were used. The discrete roughness elements on these RIM inserts have been shown by infrared thermography to form pairs of streaks caused by the characteristic horseshoe vortex [19]. These streaks merge downstream into one streak. This phenomenon can not be seen with TSP due to the lower signal-to-noise ratio, which makes confirming their origin more challenging. This section contains displays of streak locations in an attempt to attribute the streaks to the elements that were utilized. Note that this section will not contain heat transfer data, as it is important to ascertain that the

streaks being analyzed are being caused by the elements being used before studying the heat transfer along the streaks.

5.2.1 Repeatability of Streak Location for Same Roughness Insert

The first objective was to show that the streaks being analyzed on the cone were indeed being caused by the roughness elements. First, the repeatability of the streak locations for the same roughness element had to be shown. Figure 5.14(a) shows the location of the leeward streak for 3 different runs using roughness insert # 6, which contains elements 152 μm in height. The roughness insert was not removed in between these runs. Figure 5.14(b) shows the location of the leeward streak for 3 different runs using roughness insert # 7, which contains elements 203 μm in height. However, in contrast to Figure 5.14(a), the roughness insert was removed and reinstalled in the same orientation in between these runs. The figure caption gives the approximate run conditions. These are the run conditions averaged for all the runs in the image, as they were all done at approximately the same initial conditions. Table A.2 of Section A in the appendix lists the stagnation conditions of these 6 runs. The initial stagnation conditions for these runs along with the average and standard deviation are also shown here in Table 5.2 to emphasize the consistency between the stagnation conditions. Note that the roughness location has been removed because it was 52.4° for all 6 runs. It is apparent that the stagnation conditions are fairly consistent among the different runs.

It appears that the streak location is repeatable regardless of whether the roughness insert has remained in place or been removed and put back. At approximately an axial location of 0.32 m, there seems to be a jump in the streak location. The reason for this is unknown. This is visualized in Figure 5.15, which shows an unwrapped TSP image of Run 215.

It is also important to ascertain how accurate the azimuthal location of the roughness elements can be known with respect to the lee ray. This depends on 3 major

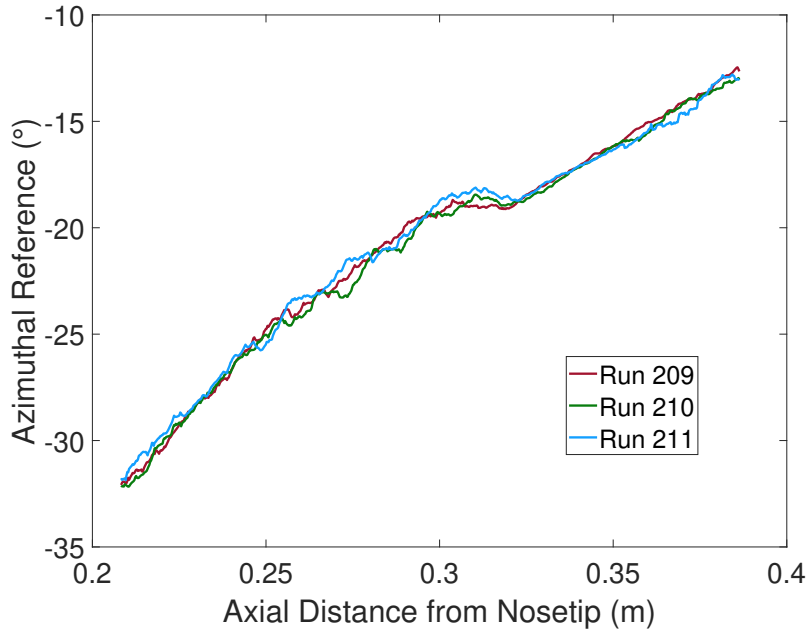

(a) Runs done with 152 μm (# 6).

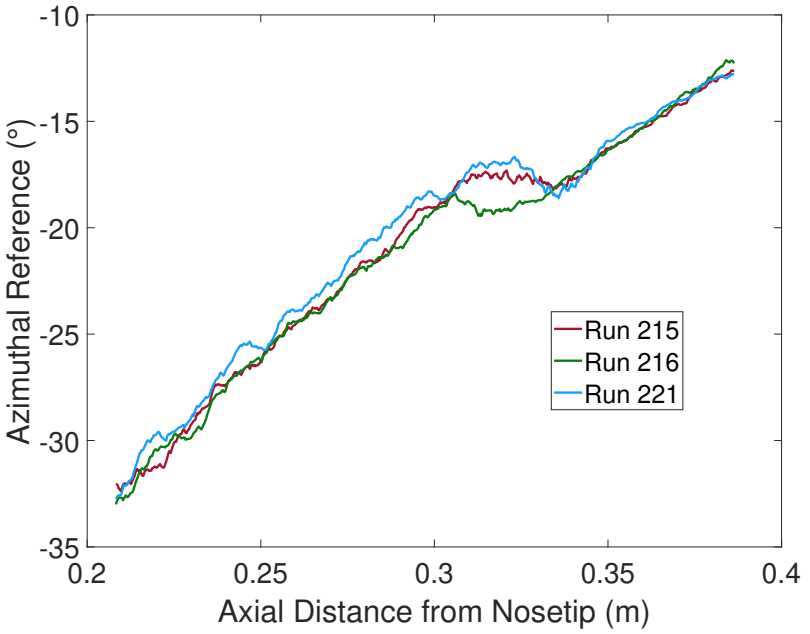

(b) Runs done with 203 μm insert (#7). Insert was removed in between runs.

Figure 5.14. Repeatability of location of leeward streak for runs done with the same roughness insert. Approximate run conditions are $T_{w,i}$ = 303 K, Re = 8.5×10^6/m , p_0 = 110 psia, T_0 = 420 K.

Table 5.2. Run conditions for the runs in Figure 5.14. This includes 3 runs done with the 152 μm insert and 3 runs done with the 203 μm insert all at approximately the same stagnation conditions.

Run #	**Roughness Insert #**	$p_{0,i}$ **(psia)**	$T_{0,i}$ **(K)**	$T_{w,i}$ **(K)**
209	6	117	428	302
210	6	116.8	427	302
211	6	116	427	302
215	7	116.4	427	302
216	7	116.2	427	303
221	7	116.6	432	302
Average	-	116.5	428.0	302.2
Standard Deviation	-	0.37	2.0	0.41

factors: the uncertainty of the azimuthal location of the lee ray, the uncertainty of the azimuthal location of the machined holes on top of the cone frustum that mate with the dowel pin on the roughness insert, and the repeatability of the actual placement of the roughness insert as the dowel pin is smaller than the machined holes on the frustum. Recall that the uncertainty of the azimuthal location of the lee ray is about 2.5° because the mark on the angle of attack adapter was 2.5° wide. Regarding the azimuthal location of the machine holes on the top face of the frustum, there was unfortunately no simple way to better quantify this measurement, so it is unknown how accurately the holes were machined. Finally, Figure 5.14 indicates that the repeatability of the placement of the roughness insert is high by showing similar variation in the streak location whether or not the roughness insert was removed and replaced in between runs. The next step was to show that the streaks being analyzed were being caused by the roughness elements. This was attempted in two different ways.

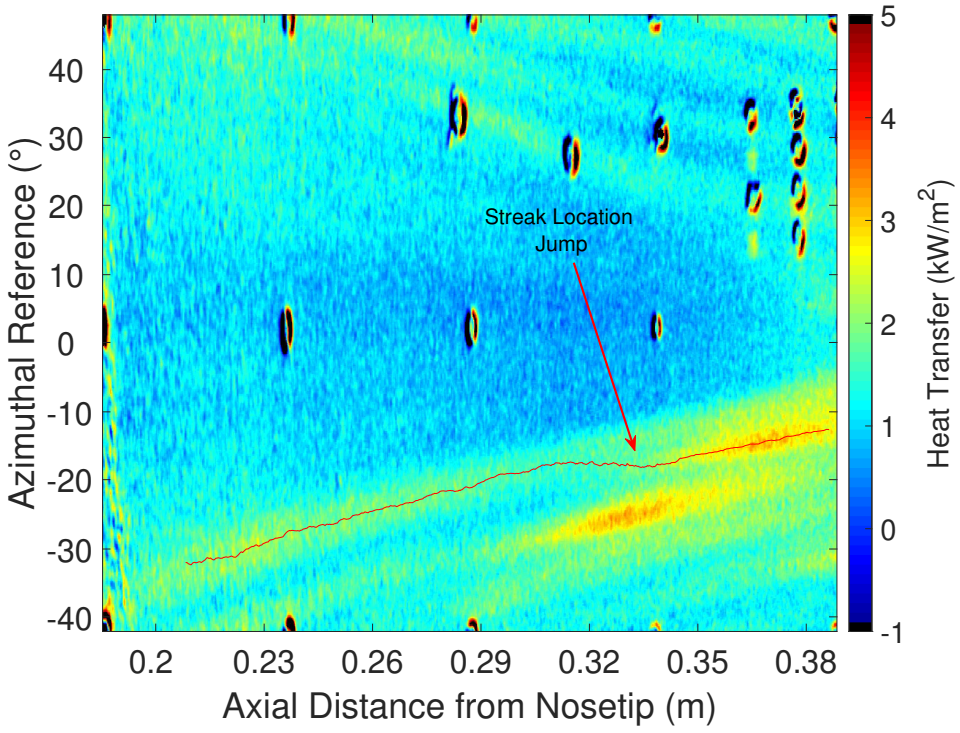

Figure 5.15. Unwrapped TSP heat transfer image of Run 215. 203 μm insert (#7). $T_{w,i}$ = 302 K, Re = 8.5×10^6/m, p_0 = 109.1 psia, T_0 = 420 K.

5.2.2 Rotating the Roughness Insert

Control over the streaks was first tested by varying the location of the roughness and observing if the streaks also rotated. Figure 5.16(a) shows an unwrapped TSP image of a run performed with roughness insert # 8 which contains elements 254 μm in height. Also note that all inserts used in this thesis contained elements with an azimuthal spacing of 7.2°. The most leeward roughness is 43.4° from the wind ray. The other two elements are 7.2° and 14.4° closer to the wind ray respectively. Three streaks are clearly seen below the lee ray. The roughness insert was then rotated 12° towards the lee ray. The corresponding unwrapped TSP image is shown in Figure 5.16(b).

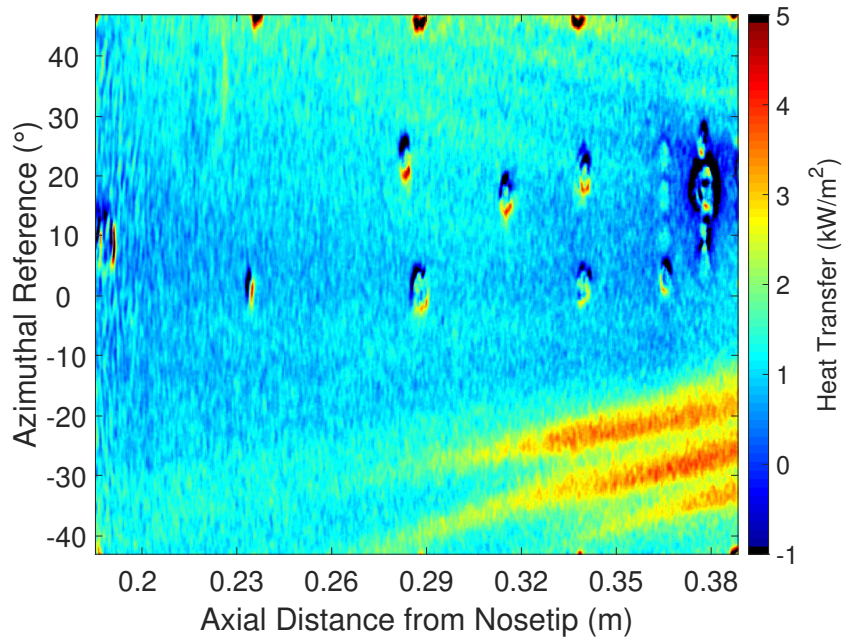

(a) Roughness insert in original position. $T_{w,i} = 302$ K, Re $= 8.0 \times 10^6$/m , $p_0 = 102.8$ psia, $T_0 = 420$ K. Run 411.

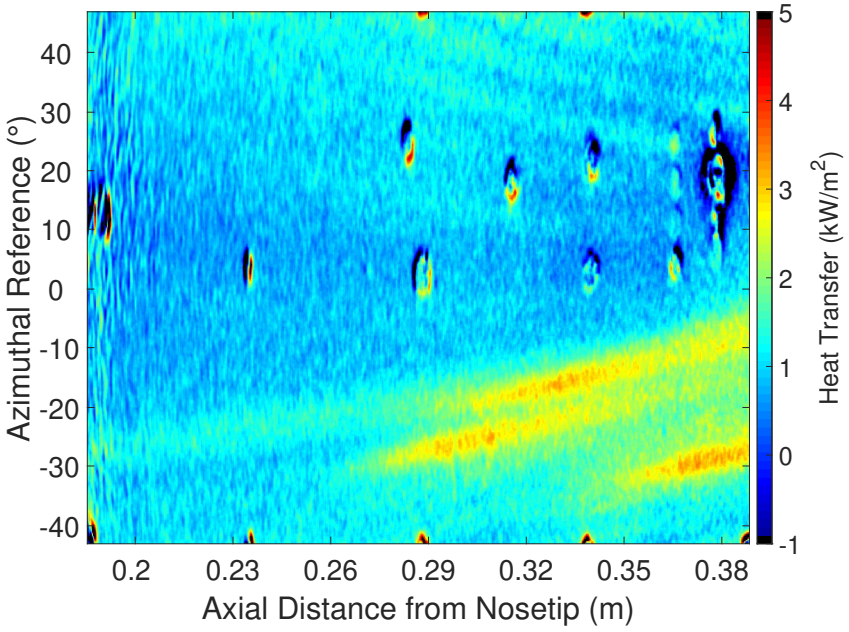

(b) Roughness insert rotated leeward by 12°. $T_{w,i} = 302$ K, Re $= 8.2 \times 10^6$/m , $p_0 = 102.9$ psia, $T_0 = 421$ K. Run 422.

Figure 5.16. Unwrapped TSP heat transfer images showing effect of roughness insert rotation towards lee ray by 12°. 254 μm insert (# 8).

It visually appears that these streaks have moved closer to the lee ray, which was to be expected. To better quantify the azimuthal difference of these peaks, a spanwise cut was taken at an axial location of 0.354 m. This axial location was picked as it was a location where all three streaks that were supposedly caused by the roughness element were visible with a strong signal-to-noise ratio on both figures. A moving average of 5 pixels was used in the spanwise direction. Both these cuts are shown in Figure 5.17. The peaks indicating the streaks are color coded.

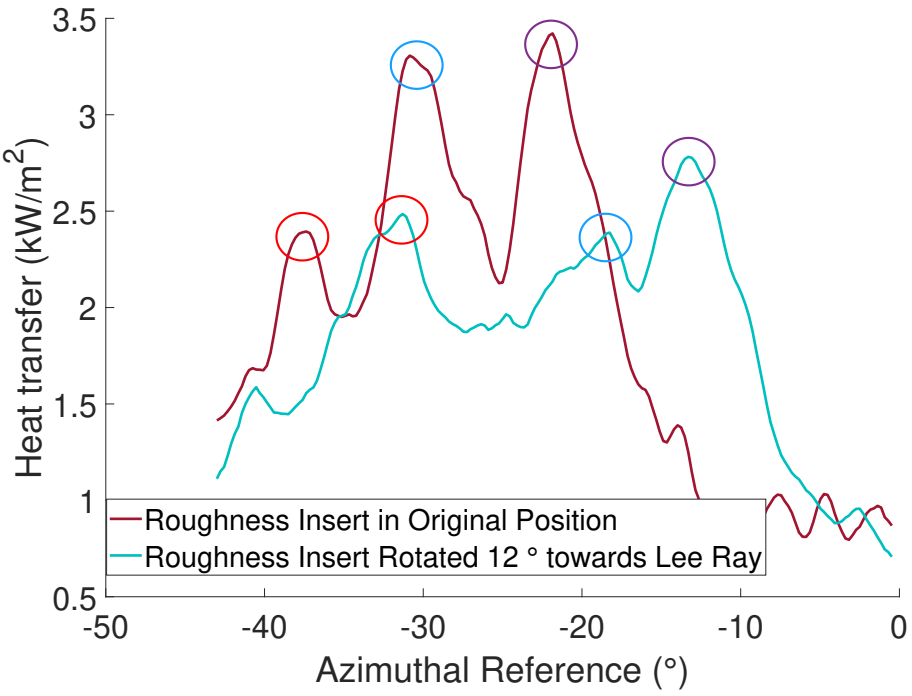

Figure 5.17. Spanwise cuts of Figure 5.16(a) and Figure 5.16(b) at an axial location of 0.354 m.

It is apparent that the effect of the rotation is ambiguous at best. Due to the large rotation, the vortex streamlines have now drastically changed. Thus, the strength of the vortices at the same axial location are not comparable. Although it appears that the streaks have moved towards the lee ray as indicated by the peaks in Figure 5.17, nothing conclusive can be drawn because the peak heat transfer values are

too different. It should also be noted that the elements were rotated by 12°, but the streamlines did not move by 12°. This may be due the three dimensional nature of the flow, which causes streamline spreading occurs. Closer to the wind ray, the vortex paths spread quickly, while farther from the wind ray, the paths remain almost parallel. This means, for example, that streaks originating from roughness elements 7.2° apart will not necessarily remain 7.2° apart as they grow downstream. This was analyzed more extensively by Edelman [19].

In order to decrease the rotation of the discrete roughness elements to 3°, a second hole was machined on the bottom surface of the roughness insert into which another dowel pin could be inserted. This was done because it was impossible to simply make a hole on the top face of the frustum that was 3° apart, because the present holes themselves were wider. By attaching the dowel pin to a different spot, this allowed the roughness insert to be nominally rotated 3°.

Shown in Figures 5.18(a) and 5.18(b) are the unwrapped TSP images of runs performed with roughness insert # 7 at the same initial conditions while the most leeward roughness element is 43.4° and 46.4 ° from the wind ray respectively. Although the change between the two images is subtle, Figure 5.18(b) shows that the leeward streak has moved slightly closer to the lee ray, and the windward streak has moved a larger distance towards the lee ray. Again, recall that of the 3 visible streaks below the lee ray, the upper streak has been defined as leeward streak and the one in the middle has been defined as the windward streak. To better quantify the trajectory for all 3 streaks, the location of each streak was extracted and compared with computations received from Moyes at Texas A & M. The path computations were extracted by using the inflection-point method on the undisturbed basic state [71]. This method essentially redefines the crossflow velocity component, w, to be 0 at the mass flux inflection point instead of at the edge of the boundary layer. This differs from the previous method of vortex path extraction which was simply set as the inviscid streamlines, where w was defined to be 0 at the edge of the boundary layer. To match the computations with experimental work, the azimuthal location from the

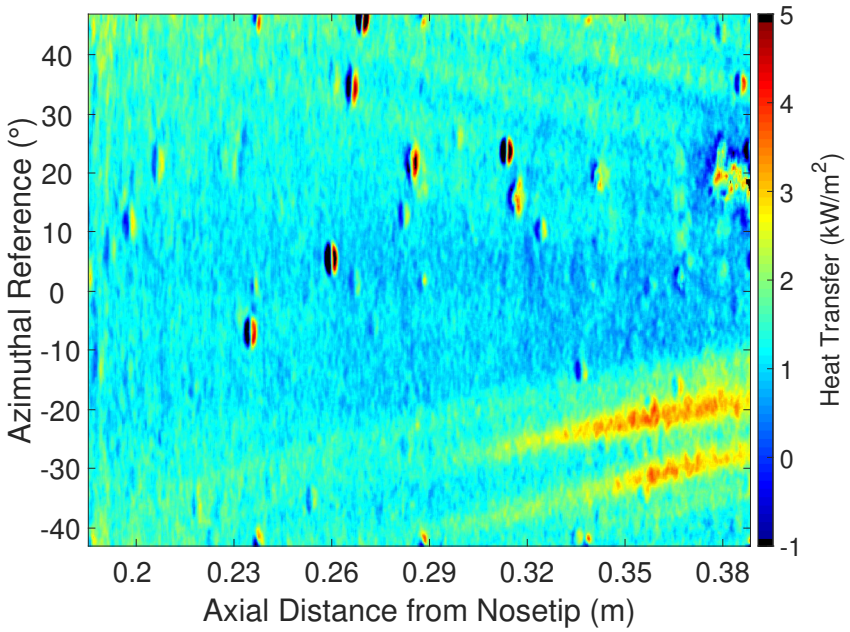

(a) Roughness insert in original position. $T_{w,i} = 296$ K, Re $= 8.1 \times 10^6$/m , $p_0 = 105.9$ psia, $T_0 = 422$ K. Run 503.

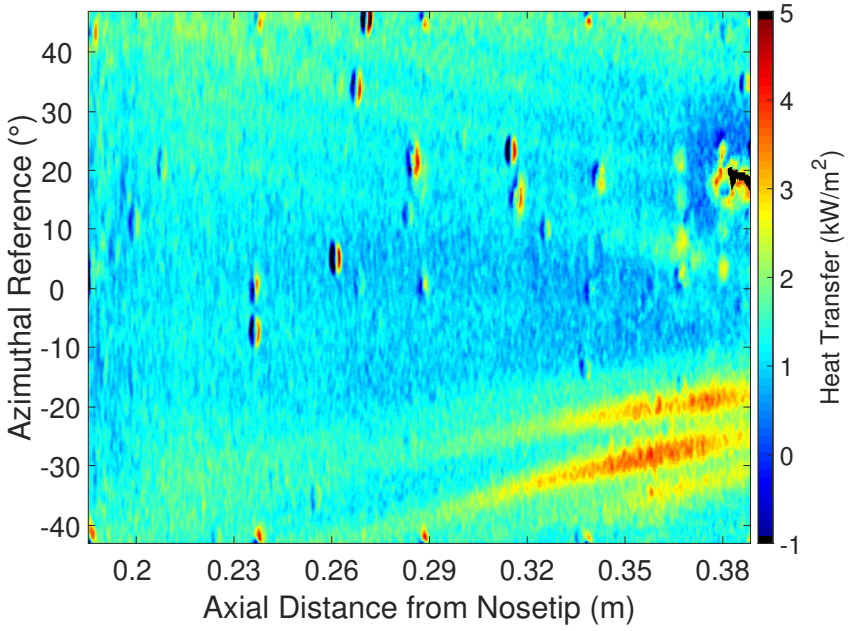

(b) Roughness insert rotated leeward by 3°. $T_{w,i} = 296$ K, Re $= 8.2 \times 10^6$/m , $p_0 = 106.1$ psia, $T_0 = 421$ K. Run 507.

Figure 5.18. Unwrapped images showing the effect of a 3° leeward rotation of a 203 μm insert (# 7).

computations was matched with the azimuthal location from the experiments at the axial location of the roughness. Because the computations consisted of discrete azimuthal intervals, a linear interpolation was used to extract the predicted location of the streak starting at the nominal experimental location of each roughness element.

Figure 5.19 shows the predicted locations for vortex paths originating at 36.2° and 43.4° from the wind ray which correspond to the azimuthal location of the roughness elements causing the windward and leeward streak respectively in Figure 5.18(a). It also shows the predicted paths if the initial location is rotated leeward by 3°, which correspond to the azimuthal location of the roughness elements causing the windward and leeward streak respectively in Figure 5.18(b).

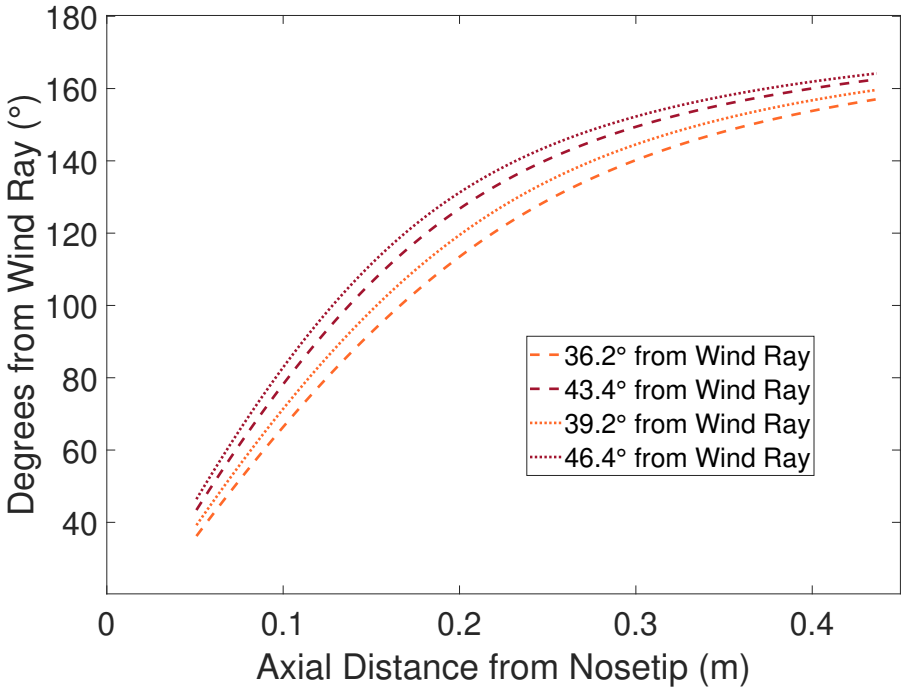

Figure 5.19. Computed vortex paths for the windward and leeward streaks in Figures 5.18(a) and 5.18(b).

Recall that because the flow is three-dimensional in nature, the azimuthal distance between streamlines may not remain the same as they move downstream. It is easy

to see that even though the 1st and 2nd path start off 7.2° apart, they deviate from this angle as they move downstream. For example, at an axial location of 0.2 m, they are almost 13° apart. Then, at an axial location of 0.4 m, they are only 6° apart. The 1st and 3rd path, which are originally 3° apart, seem to follow the same trend in azimuthal separation. To compare the computed paths with the extracted experimental streak locations, Figure 5.20 plots both the computed and experimental locations for the 3 paths originating from the 3 roughness elements on the roughness insert in Figure 5.18(a). Figure 5.20(a) shows the paths originating from the roughness elements in the original position, while Figure 5.20(b) shows the paths originating from the roughness elements after a 3° leeward rotation.

The windward streak can be seen to match up nicely with the computations both before and after rotation. As a reminder, the roughness insert that was used consisted of 3 roughness elements. The middle, windward streak, likely originates from a roughness element that is in the center of two other roughness elements. Because it is difficult to compare the effect the insert rotation had on the streaks from these figures, Figure 5.21 shows the spanwise heat transfer at an axial location of 0.351 m from the nosetip. The small change in the peak location is more evident in this image.

Figure 5.22 shows the same spanwise cuts as in Figure 5.21, but the 2nd line has been artificially translated windward. This was done in an attempt to negate the rotation caused by the leeward rotation of the roughness elements. While Figure 5.22(a) shows the line artificially rotated 3° windward, Figure 5.22(b) shows the line artificially rotated leeward by the predicted value it should have rotated due to the rotation of the roughness elements. This was done using a method devised by Edelman [19] and attempts to take in account the spreading of streamlines as the flow moves downstream.

Figure 5.22(a) shows the peaks lining up nicely, with the exception of the leeward peak. Figure 5.22(b) implies that this the misalignment seen in Figure 5.22(a) was because of not taking into account the spreading of streamlines. As previously stated,

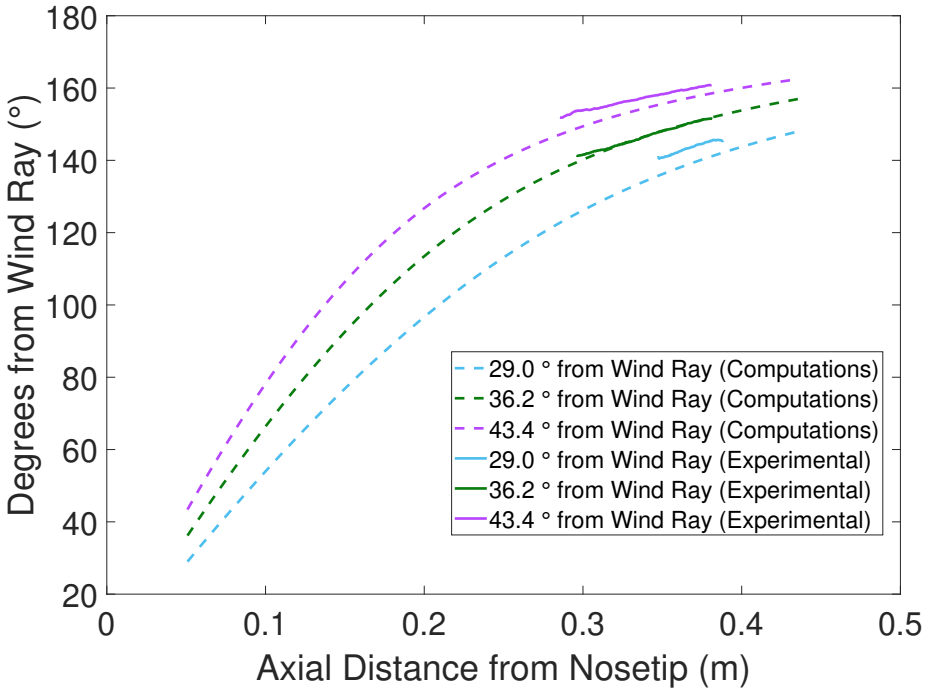

(a) Roughness insert in original position.

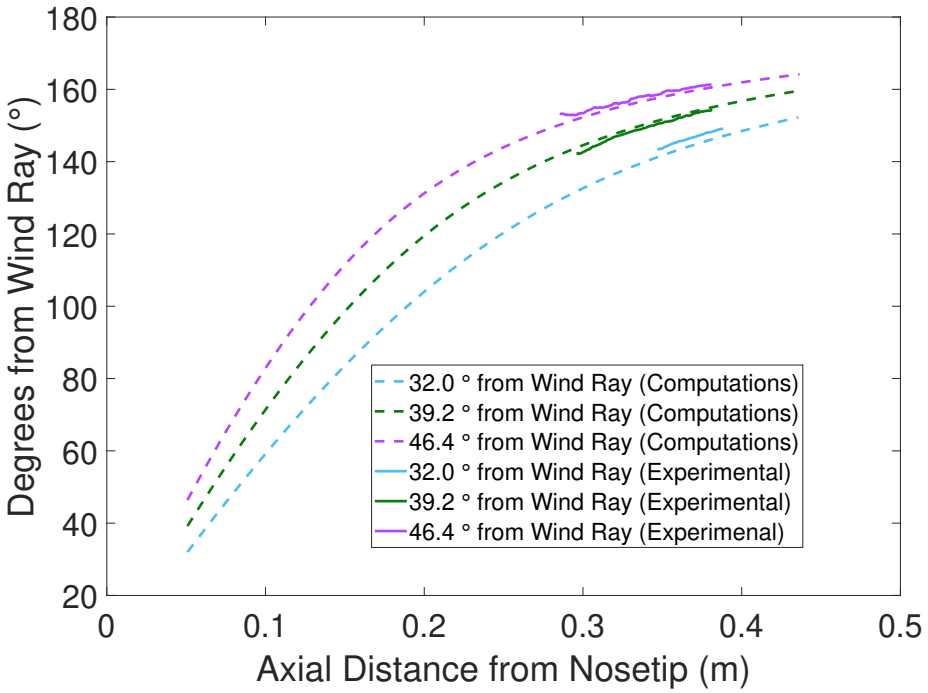

(b) Roughness insert rotated leeward by 3°.

Figure 5.20. Comparing the location of the streaks in Figures 5.18(a) and 5.18(b) with computations.

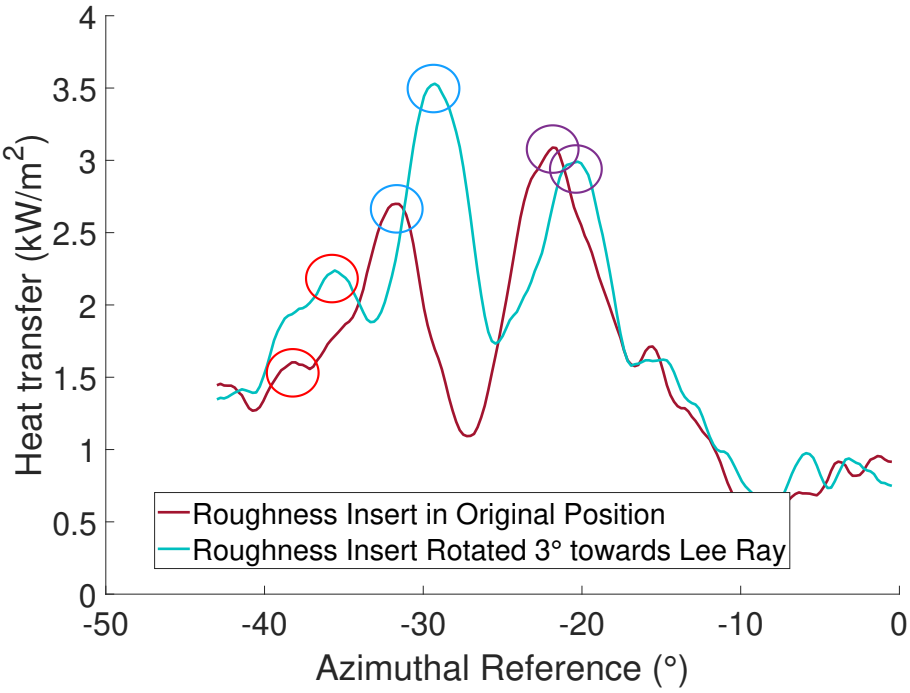

Figure 5.21. Spanwise cut of Figures 5.18(a) and 5.18(b) at an axial location of 0.351 m.

a rotation in a roughness element farther from the wind ray will have less of an effect on the streamlines downstream as a rotation in a roughness element closer to the wind ray. This is illustrated by Figure 5.22, which shows that the predicted rotation for the leeward streak at an axial location of 0.351 m is less than 3°.

It should be noted that the computations overpredict the rotation of the streak farthest from the lee ray by about 2° as seen in Figure 5.22(b). One of the reasons for this discrepancy may be due to the uncertainty in quantifying the actual rotation of the roughness elements. Although they were nominally rotated leeward by 3°, Figure 5.23 displays the same plot as Figure 5.22(b) in which the algorithm assumed a leeward rotation of 2.2°. There is clearly better agreement between the computation and experiment. Recall that the roughness insert was rotated by placing the dowel pin in a different hole that was also machined on top of the frustum. On this location

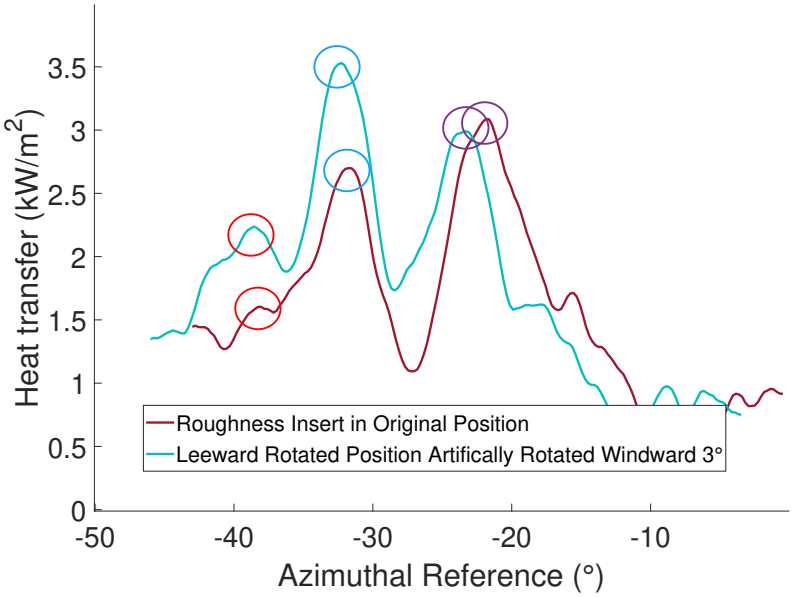

(a) 2nd line has been artificially rotated 3° windward.

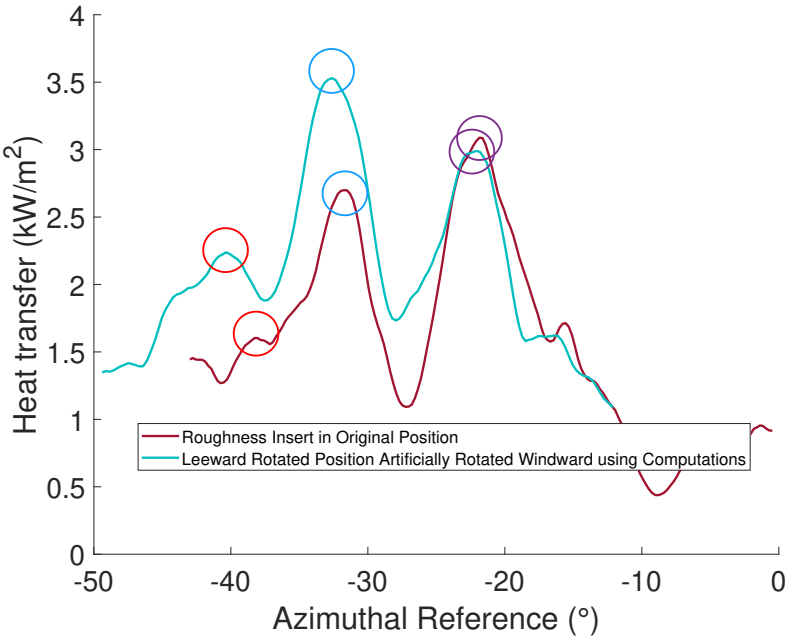

(b) 2nd line has been artificially rotated windward by the predicted shift given by computations by Moyes. This takes into account the spreading of streamlines.

Figure 5.22. Spanwise cut of Figure 5.18(a) and 5.18(b) at an axial location of 0.351 m. The roughness elements were nominally rotated leeward 3°.

of the cone, a 0.8° azimuthal difference corresponds to a distance of approximately 70 μm. Due to the uncertainty of the location of the machined hole, and the placement of the dowel pin in said hole, it is possible for this amount of uncertainty in the roughness rotation to exist. Note Edelman was able to more accurately measure the rotation by observing the streaks forming directly off the roughness elements with IR thermography [19]. Unfortunately, that was not an option with TSP. Regardless of the slight uncertainty, these figures show good indication of control over the streaks using the RIM inserts.

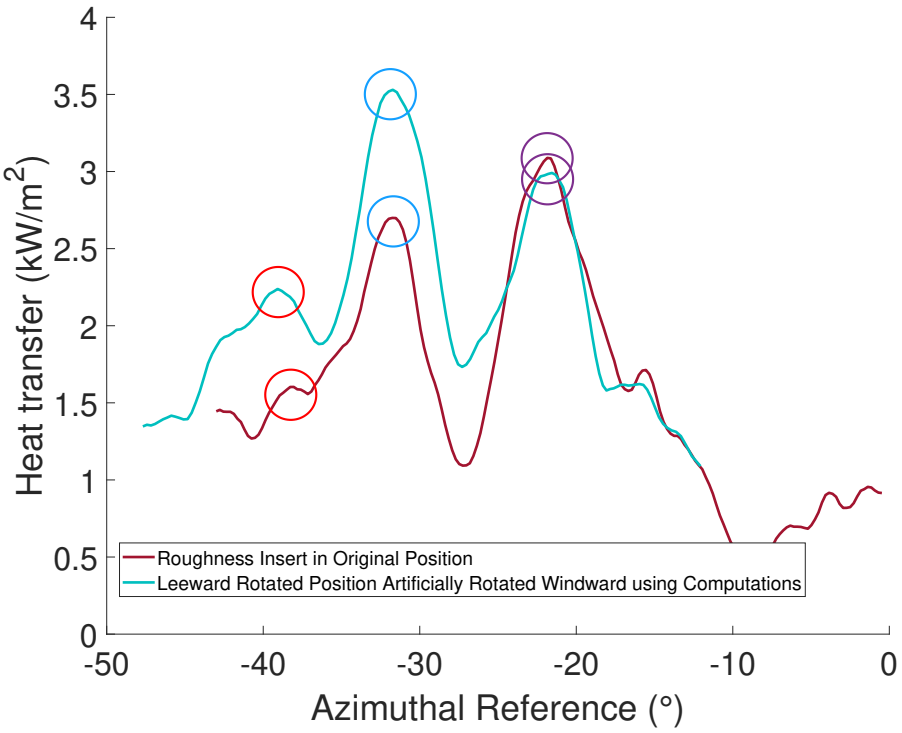

Figure 5.23. Spanwise cut of Figure 5.18(a) and 5.18(b) at an axial location of 0.351 m. 2nd line has been artificially rotated windward by the predicted shift given by computations by Moyes. This was done by assuming a nominal leeward rotation of 2.2° instead of 3°.

5.2.3 Eliminating other Possible Causes of Streaks

The second method that was used to confirm that the roughness was causing the streaks was by tracking and comparing the streaks formed using different roughness inserts in which the discrete roughness elements were placed in the same location. If the streaks were being caused by the roughness elements, they should approximately be in the same position. The only difference between the inserts was the height of the roughness elements, which should theoretically only affect the magnitude of the heat transfer along the streaks and not the location of the streaks. This is because the location of the streaks is solely dependent on the basic undisturbed state of the flow once the azimuthal placement of the roughness has been set as long as they are not large enough to cause mean-flow distortion farther upstream [71].

Although this does not preclude the streaks being caused by paint roughness (such as a paint step), this could help rule out the possibility that the streaks are being formed from the step between the insert and the frustum instead of the discrete elements. Figure 5.24(a) shows the location of the leeward streak when the roughness insert is placed such that most leeward roughness element is 52.4° from the wind ray. For each insert, the average streak location for 3 runs is shown. The inserts in Figure 5.24(a) correspond to inserts # 4, 6, and 7 respectively. There seems to be little variation in location of the leeward streak when different roughness elements are used in the same location for either plot. This is good indication that the streaks are not being caused by a step between the roughness insert and the frustum. If the streak was being caused by some type of roughness insert step or machine abnormality, we would expect the leeward streak locations for different roughness inserts to be unique. Note that the shape of the streak location with the 102 μm insert is different. It was suspected that this was due to a slight machining error (although it was unsure what exactly caused this), so a new one was made. This shape may have also been influenced by crossflow vortex merging.

However, this does not eliminate the possibility that the streaks may be being caused by the paint step, as the paint step remained the same while the roughness insert was swapped. Thus, Figure 5.24(b) compares the location of the leeward streak when the most leeward roughness element was 43.4° from the wind ray for two different paint jobs. In this figure, the average location over two runs is taken for the first paint job, and a single run's location is taken for the second paint job. The inserts in Figure 5.24(b) correspond to inserts # 6,7,and 8 respectively.

The variation in location still appears to be minimal. The maximum difference in location seems to be approximately 2°, making the differences in location on the same order as those in Figure 5.24(a). This seems to indicate that the streaks were not being caused by the paint step, as the streak location would be unique for each paint job if they were.

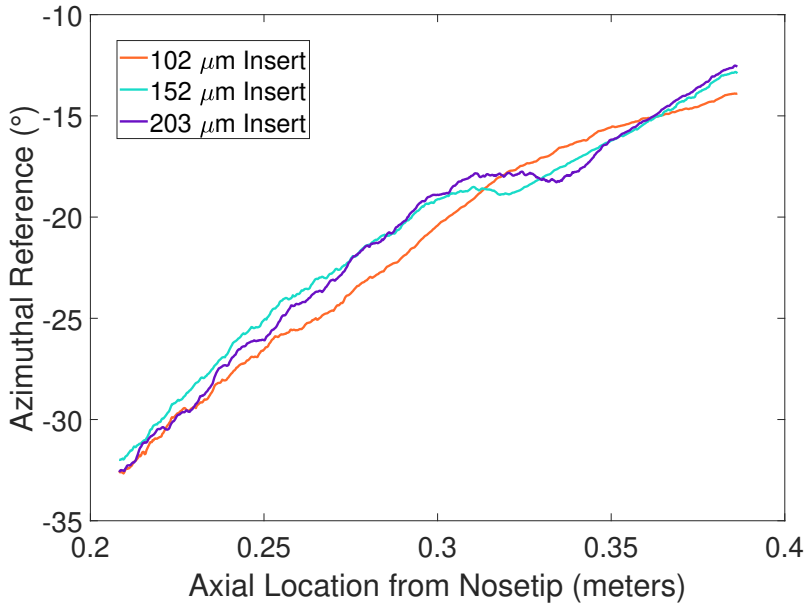

(a) Approximate run conditions are $T_{w,i}$ = 302 K, Re = 8.5×10^6/m , p_0 = 109.2 psia, T_0 = 420 K.

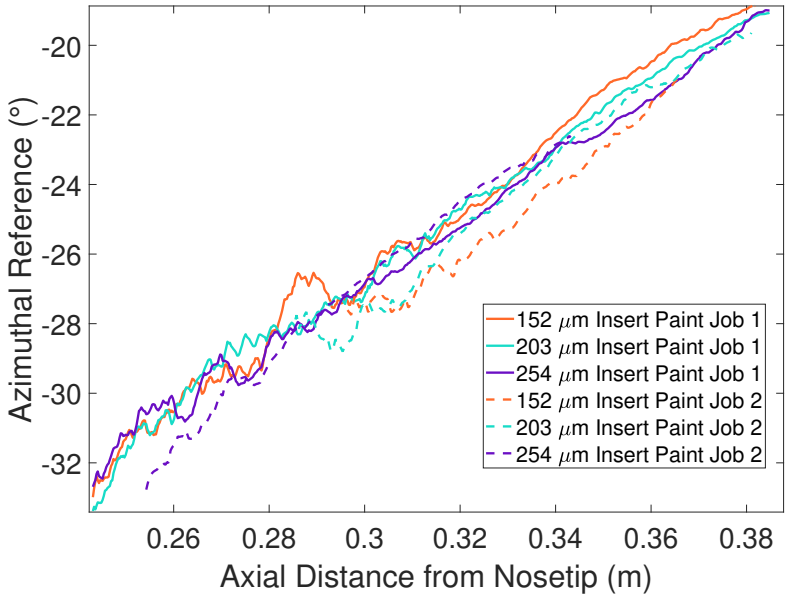

(b) Approximate run conditions are $T_{w,i}$ = 302 K, Re = 8.0×10^6/m , p_0 = 102.9 psia, T_0 = 420 K.

Figure 5.24. Locaion of leeward streak for different roughness inserts placed in the same location.

5.3 TSP Repeatability

5.3.1 Change in Heat Transfer due to Initial Model Temperature

Once control over the streaks was shown, the next step was to analyze the magnitude of the streaks. However, obtaining repeatable data from different runs done with the same initial freestream Reynolds number seemed to pose a challenge. To test the consistency of the results, 9 consecutive runs were performed with almost all the conditions remaining the same. This includes stagnation pressure, stagnation temperature, freestream Reynolds number, roughness element height, roughness element location, etc. However, the initial temperature of the model was not kept constant, as the model would heat up by approximately 1-2 K each run. It should be noted that for this entry, there was some bias uncertainty with respect to the initial wall temperature. The CJC that was utilized was not calibrated. However, while the absolute temperatures may not be accurate, the temperature differences should be reasonably accurate. Figure 5.25 shows the TSP heat transfer images for 3 of these runs. The 0 m reference point on the y axis corresponds to the lee ray. These data were calibrated using a sensor placed 0.2817 m from the nosetip and 21.34° above the lee ray. Note that this location has been labeled in the first image, Figure 5.25(a), for clarity.

To keep the plot uncluttered, Figure 5.26 shows the heat transfer along the leeward streak for only 5 of the 9 consecutive runs, although the other 4 runs approximately show the same pattern. Unfortunately, the azimuthal reference dots were not placed correctly for this entry, so there is some axial location uncertainty. This uncertainty is only about 0.001 m, as sensor ports were able to be used for axial reference.

There seems to be a noticeable trend; as the initial wall temperature increases, the heat transfer along the streak decreases. To further illustrate this trend, the average heat transfer along the streak from an axial location of 0.33 m to 0.34 m was plotted against the initial wall temperature in Figure 5.27.

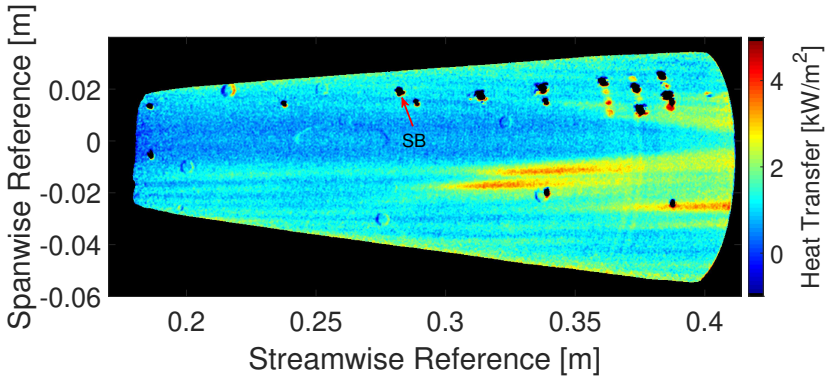

(a) $T_{w,i}$ = 296 K. Run 109.

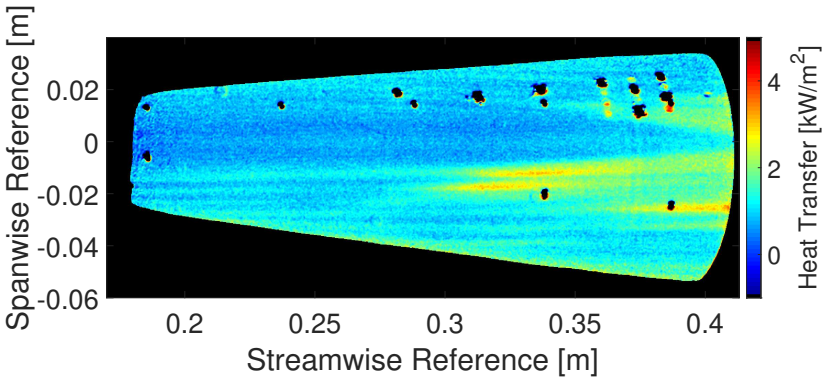

(b) $T_{w,i}$ = 303 K. Run 113.

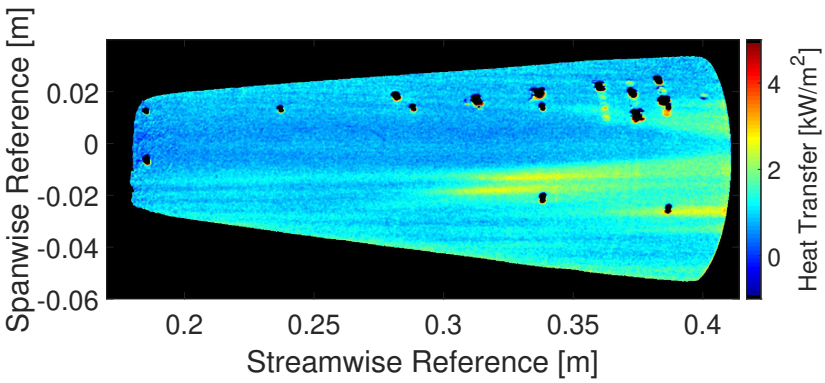

(c) $T_{w,i}$ = 305 K. Run 116.

Figure 5.25. Heat Transfer for runs done at the same conditions except for the initial model temperature. 203 μm insert (# 7) Approximate run conditions are Re = 8.8×10^6/m , p_0 = 112.8 psia, T_0 = 420 K for all runs.

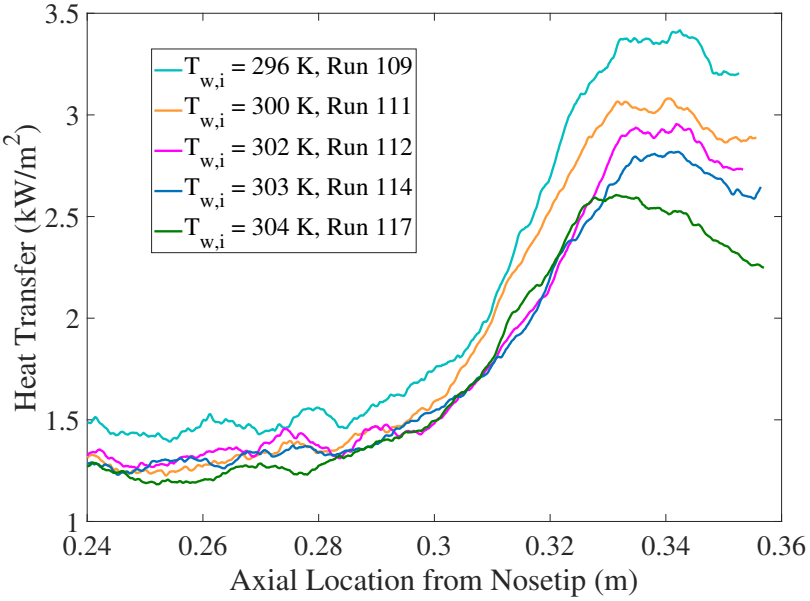

Figure 5.26. Heat Transfer along leeward streak for runs done with a different initial model temperature. 203 μm insert (# 7) Approximate run conditions are Re $= 8.7 \times 10^6$/m , $p_0 = 111.3$ psia, $T_0 = 420$ K.

Figure 5.27 shows that in general, the heat transfer along the streak decreases as the initial wall temperature increases. There is almost a 25% decrease in heat transfer with a 12 K increase in the wall temperature. There also appears to be a few outliers to this trend. This may be due to the uncertainty in the TSP or the in-situ SB calibration. Looking at Figure 5.25, the SB is adjacent to a streak. Although the strength of this streak is low, it may have a slight effect on the calibration as explained in Sections 5.1.3 and 5.1.4.

Figure 5.28 shows the same plots as those displayed in Figures 5.26 and 5.27 with the Stanton number substituted for heat transfer on the vertical axis. Recall that the Stanton number is the ratio of the heat transfer to the thermal capacity of the fluid, and it is defined using T_o instead of T_{aw}. Thus, the Stanton number should ideally take care of most of the change in heat transfer caused by a change in the initial wall temperature.

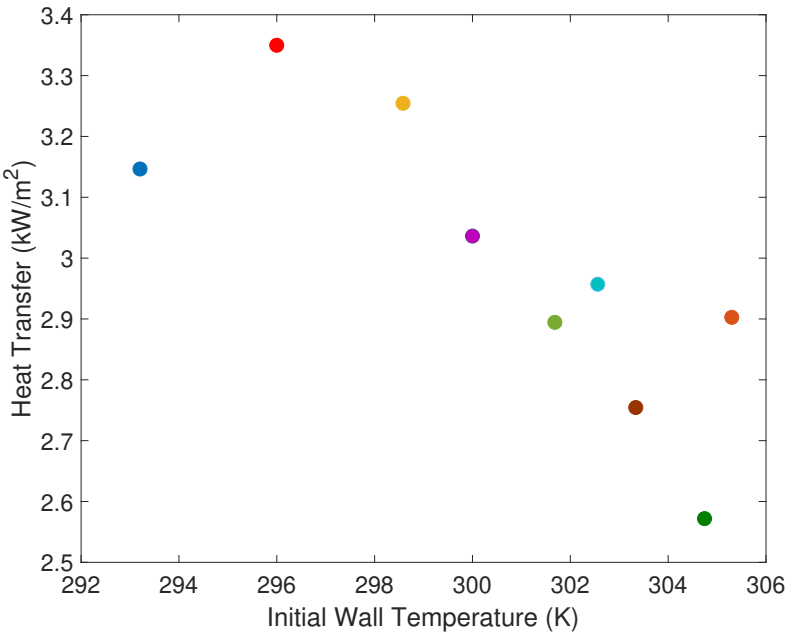

Figure 5.27. Heat transfer along the leeward streak averaged from 0.33 m to 0.34 m for the runs in Figure 5.26 and 4 additional runs.

Figure 5.28(a) shows 3 of the 5 streaks collapsing while the other 2 streaks do not collapse. Figure 5.28(b) shows that the Stanton number along the streak averaged from 0.33 m to 0.34 m is close in magnitude between different runs done with different initial wall temperatures. Note that although the magnitude of the scale on the vertical axis is different than in Figure 5.27, the percent difference in magnitude from bottom to top was left approximately the same to allow for easy comparison. Although ideally we would expect the percent difference to be marginal, the displayed variance can be attributed to uncertainty in the TSP, uncertainty in the SB and SB calibration,the use of T_0 instead of T_{aw}, and the use of $T_{w,i}$ instead of T_w. However, the overall trend implies that in order to obtain repeatable TSP results, the initial wall temperature is a parameter that must be well controlled.

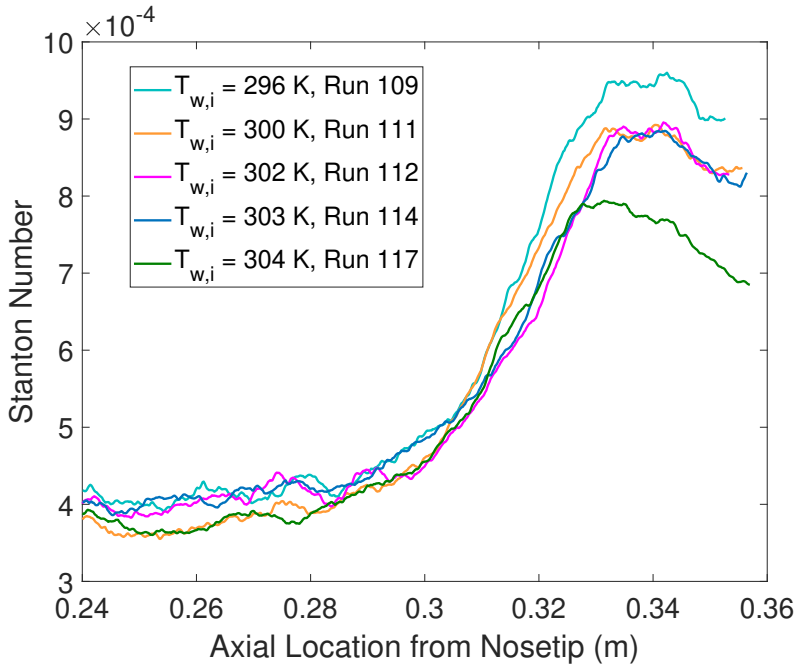

(a) Stanton number along leeward streak.

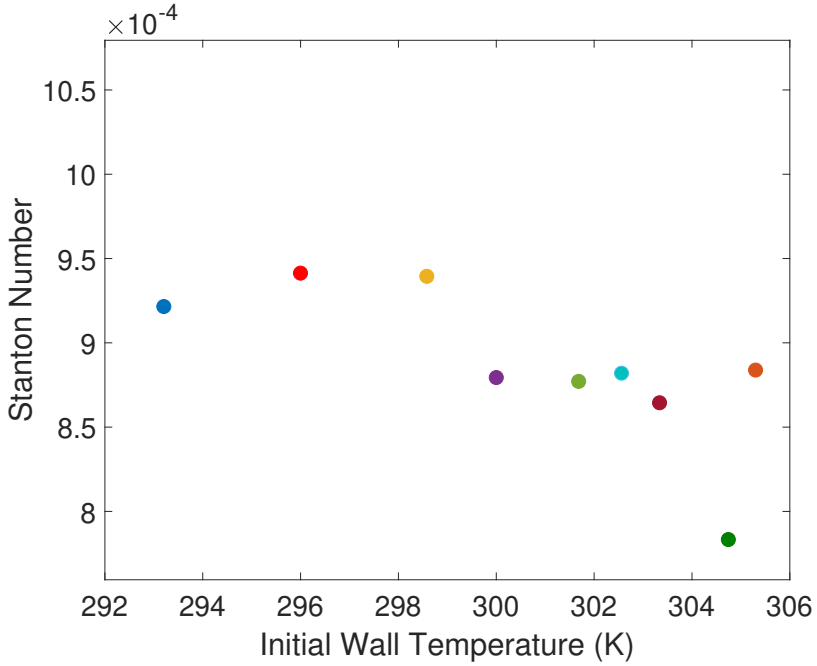

(b) Stanton number along the leeward streak averaged from 0.33 m to 0.34 m.

Figure 5.28. Stanton number along leeward streak for runs done with a different initial model temperature. 203 μm insert (# 7).

5.3.2 Cold Junction Compensator Calibration

Because the temperature of the model was found to be an important condition for repeatable heat transfer, a better understanding of the CJCs that were being utilized to measure the temperature was necessary. The CJCs were studied using a Hotpack Humidity Chamber Model 434304. The thermocouples were placed in this chamber along with a B61001-0400 Frio-Temp Incubator Verification Thermometer. Then, the temperature of the incubator was varied from 298.15 K to 308.15 K, the normal range of the temperatures of the model as it heats up in the BAM6QT. At each temperature in the incubator, the thermometer was read as the true value and the compensated thermocouple values were read using a Keysight 34970 data acquisition system. The incubator chamber had 2 shelves. The thermometer had to be placed on the top shelf because there was not enough height on the bottom shelf. The thermocouples were placed within 51 mm of each other on the top shelf as well. For the first calibration, 6 different T- type thermocouple-CJC arrangements were tested. Because each SB sensor is equipped with two output thermocouple wires, this meant 3 SBs had to be used. Figure 5.29 shows the calibration for these CJCs. These CJCs are arbitrarily numbered from 1 to 6. On the vertical axis is the thermocouple temperature converted from the output voltage using the universal 9 degree polynomial fit for T-Type thermocouples plotted versus the thermometer temperature on the horizontal axis.

It is clear from this figure that a calibration is necessary. If CJCs could be described by the universal 9-degree polynomial fit, we would expect all the data to line up on the black dashed line in Figure 5.29. Although four of the CJCs seem to be within 1 K of the polynomial fit, the other 2 are almost 4 K off. It should also be noted that the slopes of the calibration lines are approximately one even though each calibration line seems to have a different offset. Thus, if a quick calibration is needed, a measurement at room temperature can be used to give a good estimate of the calibration.

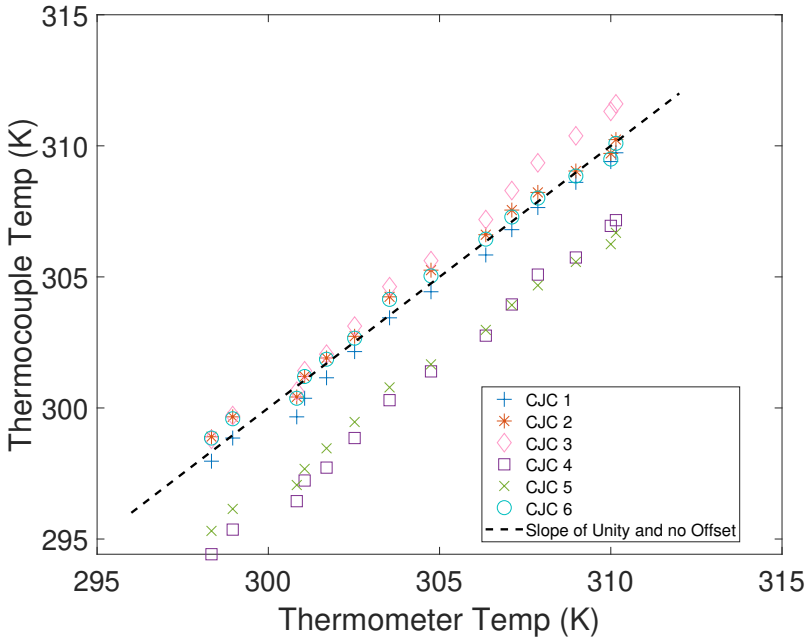

Figure 5.29. Calibration of 6 different CJCs using incubator thermometer and chamber.

It is interesting to test if the compensators retain their same calibration over time. For example, of the compensators in Figure 5.29, CJCs 2,3, and 6 were new while the others were old. Of the old compensators, only CJC 1 seemed to have a calibration curve close to black dashed line, while the other old compensators' calibrations were displaced from the line. This could just be a coincidence, but it is possible that the reason for this is due to the calibration of the compensators shifting over time.

Thus, a second calibration was performed 2 weeks after the first calibration. This was done to determine if the calibration remained constant. Unfortunately, 3 of the CJCs broke during calibration and the equipment needed to fix them was not available at the time. Calibration of the other 3 CJCs was still possible. The comparison between the two weeks for the 3 CJCs is shown in Figure 5.30. On the left is the thermocouple data plotted against the thermometer temperature. The right contains the thermocouple data plotted against the oven temperature. Note that although

the oven temperature was not an accurate reading of the temperature, its calibration likely stayed the same between the two weeks, and so it can be used to compare the calibration between the two separate weeks. Unfortunately, because of time constraints, repeat calibrations were not made on the same day to be used as a control.

As previously stated, the accuracy of the thermometer is ± 0.2 K. The quoted accuracy of the oven temperature, which uses a RTD for temperature sensing, is ± 0.1 K [72]. The oven temperature does not match up with the thermometer temperature. This is likely due to bias in the oven temperature reading, as the thermometer was new and recently calibrated. This would not be surprising as the incubator is about 20 years old. Also, each reading was done with a 15 minute waiting period in between, which was well above the time constant of the thermometer, eliminating the possibility of this temperature discrepancy being due to the thermometer not attaining equilibrium. It interesting to note that the calibrations for both weeks match up almost perfectly when using the oven temperature for CJC calibration as shown in Figures 5.30(b), 5.30(d), and 5.30(f). However, there is a slight variation between the 2 weeks when the CJC temperatures are calibrated using the thermometer temperature as shown in Figures 5.30(a), 5.30(c), and 5.30(e). This may be due to the slight difference in placement of the thermometer between the two weeks as the incubator may not have been completely spatially uniform in temperature. It should be noted, that this experiment was only done 2 weeks apart. It is possible that the CJC calibration would shift in a larger time span. In conclusion, there seems to be uncertainty in the calibration due to error in the incubator thermometer, spatially inconsistent temperatures inside the oven, and other factors. Thus, if a more accurate calibration is needed, more work must be done in devising a better way to calibrate these compensators.

Finally, note that nothing is mentioned about the specific thermocouple being used. This is because it was found that the reading depended primarily on the CJC being used and not the specific thermocouple. Data were collected to analyze this

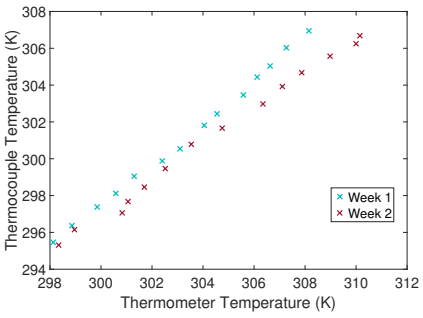

(a) Calibration of CJC 2 using incubator thermometer reading.

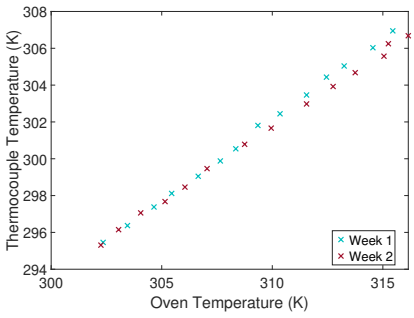

(b) Calibration of CJC 2 using oven temperature reading.

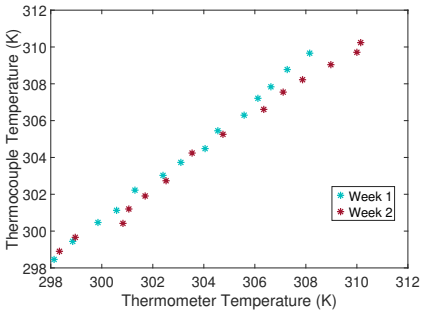

(c) Calibration of CJC 5 using incubator thermometer reading.

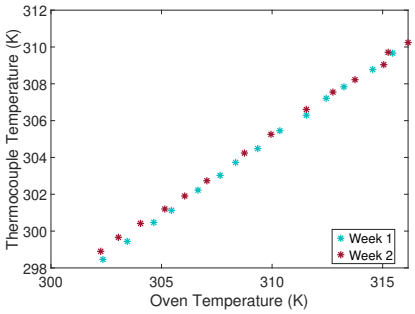

(d) Calibration of CJC 5 using oven temperature reading.

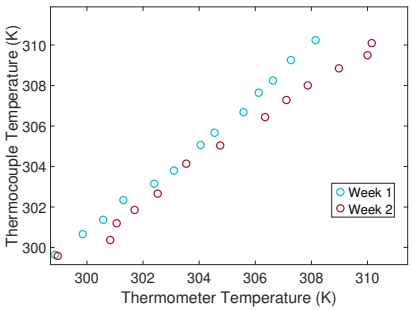

(e) Calibration of CJC 6 using incubator thermometer reading.

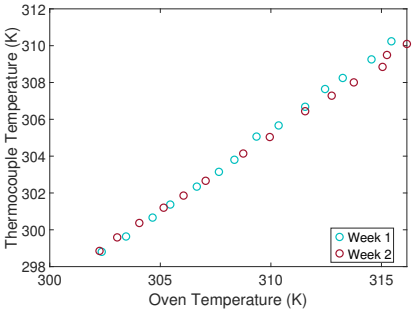

(f) Calibration of CJC 6 using oven temperature reading.

Figure 5.30. Calibration of 3 of the 6 CJCs in Figure 5.29 using both the incubator thermometer and oven temperature reading over two different weeks.

during the first week of calibration. While holding the incubator at room temperature, the output was recorded from 6 different thermocouples which were plugged into every compensator. Because this required 36 readings, this was done at room temperature to minimize the temperature change between readouts. The data are shown in Table 5.3. As previously stated, each SB gage has two thermocouple outputs. These outputs have been arbitrarily assigned #1 or #2. The temperatures have been obtained by using the universal 9-degree polynomial fit and are uncalibrated for their respective CJCs to emphasize the dependency on the CJC used as well as the insignificance of the used thermocouple.

Table 5.3. Dependancy of temperature output on thermocouple wiring.

CJC #	**Sensor 2016215 TC 1 [K]**	**Sensor 2016215 TC 2 [K]**	**Sensor 169255 TC 1 [K]**	**Sensor 169255 TC 2 [K]**	**Sensor 206214 TC 1 [K]**	**Sensor 206214 TC 2 [K]**	**Mean [mv]**	**Standard Deviation [K]**
1	293.19	293.24	293.17	293.17	293.19	293.22	293.20	0.03
2	293.91	293.99	293.86	293.86	293.79	293.76	293.86	0.08
3	293.81	293.84	293.81	293.86	293.74	293.79	293.81	0.04
4	289.18	289.18	289.18	289.20	288.98	288.98	289.12	0.11
5	289.75	289.73	289.75	289.78	289.68	289.68	289.73	0.04
6	293.86	293.94	293.94	293.91	293.86	293.89	293.90	0.04
Mean	292.28	293.32	292.29	292.30	292.21	292.22	-	-
Standard Deviation	2.21	2.24	2.21	2.20	2.25	2.26	-	-

As can be seen, the variation in different thermocouple readings for the same compensator is insignificant especially when compared to the variation in the same thermocouple from different compensators. The standard deviations are all 0.11 K or less, while the variations for the same thermocouple between CJC 3 and 4, for example, are significantly higher. Thus, the difference in calibration between the CJCs was attributed to the CJCs instead of the thermocouples. All the model temperature displayed in subsequent sections which are obtained from thermocouples have been calibrated using the described process.

5.3.3 0° Angle of Attack

In order to quantify the uncertainty of the inferred heat transfer from the TSP, the model was placed at a 0° angle of attack and heat transfer measurements were taken. These measurements were then compared to a theoretical solution using a code developed by Dr. John Sullivan of Purdue University and Dr. Tianshu Liu of Western Michigan University [66]. This theoretical solution is only applicable to laminar flow and was created using a similarity solution. The similarity equations for a compressible boundary layer along with the correctional factors to acount for the geometry of the cone can be found in Reference [1]. The viscosity was calculated using the model of Lemmon and Jacobson [73]. The edge flow conditions were calculated by solving the Taylor-Maccoll solution for conical flow [74]. Also, the wall temperature was assumed to be uniform and constant similar to the experimental assumption, and is the same as T_{wall} in the TSP data reduction process [66]. Note that the theoretical solution uses the initial wall temperature and not the instantaneous wall temperature as an input.

To place the model at a 0° angle of attack, 4 PCB sensors were spaced 90° apart at an axial location of 0.3888 m. One of the sensors was placed in hole #9 as measured in Table 3.1, and the other 3 were placed accordingly around the azimuth. The model was then aligned by adjusting the angle of attack until the frequency of the second-mode peaks were approximately equal. The frequency of the second mode was found to be between 200 kHz and 250 kHz, which matched the frequencies found in Turbeville's experiments [75]. Figure 5.31(a) displays the second-mode peaks before adjusting the angle of attack. The PCB in sensor hole # 9 is defined as 0°, and the subsequent PCBs are labeled in a clock-wise direction looking upstream. The frequency of the second-mode peak was found by drawing a horizontal line at 7×10^{-19} $\frac{psia'^2}{Hz}$, as this value seemed to be the highest amplitude that intersected all four peaks. This is shown as a purple dashed line in Figure 5.31(a). Then, the frequencies at which this line crossed the second-mode peaks on either side were found and averaged to

obtain the frequency at the center of the peaks. This was done for another threshold at $5\times10^{-19}\ \frac{psia'^2}{Hz}$, which is marked as a orange dashed line in Figure 5.31(a). Finally, the frequencies were averaged for their respective PCBs. The model was considered to be 0.0°, when the peaks were within 1% of each other. Note that a 1% change in frequency approximately corresponds to a 0.02° change in the angle of attack or yaw [75]. The peaks are clearly not aligned in Figure 5.31(a). After 4 runs and manipulating the screws to adjust the fine angle of attack adapter, the model was finally zeroed with the peaks aligned. This is shown in Figure 5.31(b), and the peaks are indicated by the small circles. The frequencies were obtained using the previously described method, and they are shown in Table 5.4. The difference between the frequencies is on the same level as Chynoweth and Turbeville [59] [75]. It is unsure why the peak amplitudes do not agree. This may be due to the uncertainty in PCB calibration, mild non-uniformity in the freestream flow, or small variation in the surface temperature of the model.

Table 5.4. Frequencies of the 4 azimuthal PCB sensors used for zeroing the model.

PCB Azimuthal Angle (°)	**Frequency [kHz]**
0	223
90	224
180	225
270	225

Once the model was zeroed, consecutive runs were done at the same pre-run conditions to observe the change in heat transfer as the initial model temperature increased. Nine consecutive runs were performed in which the model was barely given any time to cool down in between. The initial model temperature was recorded with 3 thermocouple/CJC combinations. These CJCs were calibrated using the process described previously, and the temperature was averaged to obtain the initial model

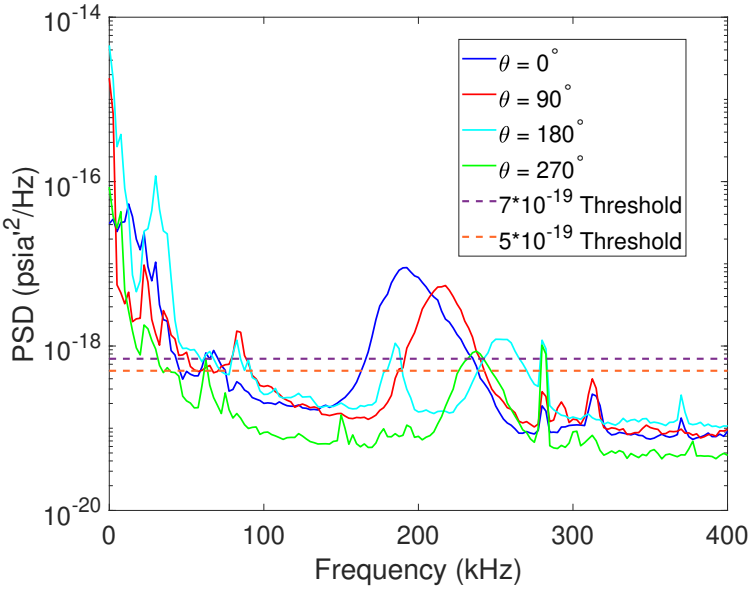

(a) First run of the tunnel entry with the 2nd mode peaks unaligned. Smooth insert (#1). $T_{w,i} = 302$ K Re $= 9.9 \times 10^6$/m , $p_0 = 126.6$ psia, $T_0 = 419$ K. Run 301.

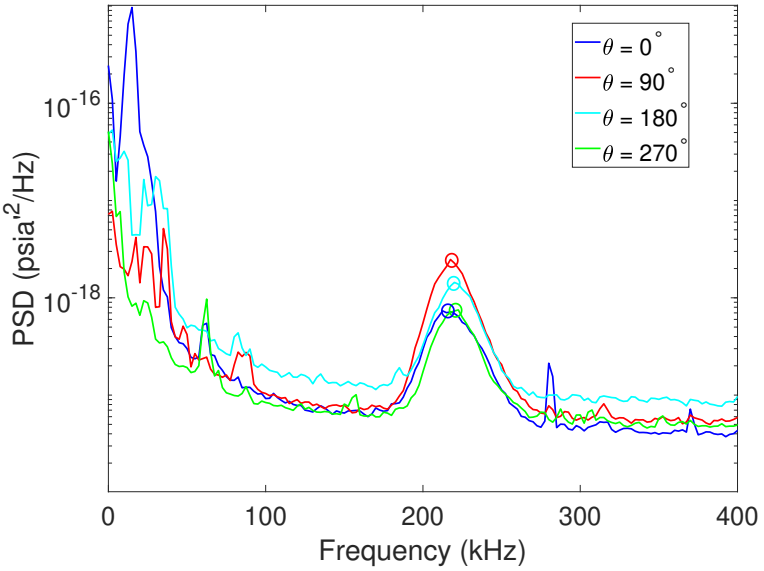

(b) PSD of PCBs after model was zerod, showing aligned peaks. Smooth insert (#1). $T_{w,i} = 305$ K Re $= 9.7 \times 10^6$/m , $p_0 = 124.5$ psia, $T_0 = 419$ K. Run 305.

Figure 5.31. Zeroing the model using the PSDs of 4 PCBs around the azimuth.

temperature. The initial model temperature was essential to both the TSP reduction code as well as the theoretical heat transfer solution. Figure 5.32 plots the theoretical heat transfer along the cone for 5 different initial wall temperatures in which the initial stagnation temperatures and pressures are approximately the same. The input conditions for each line, including the initial wall temperature, stagnation pressure, and stagnation temperature, are extracted from each of the 5 runs. For the exact initial conditions, the reader is referred to Table A.3. The heat transfer from 3 SBs are also shown in the same plot to compare.

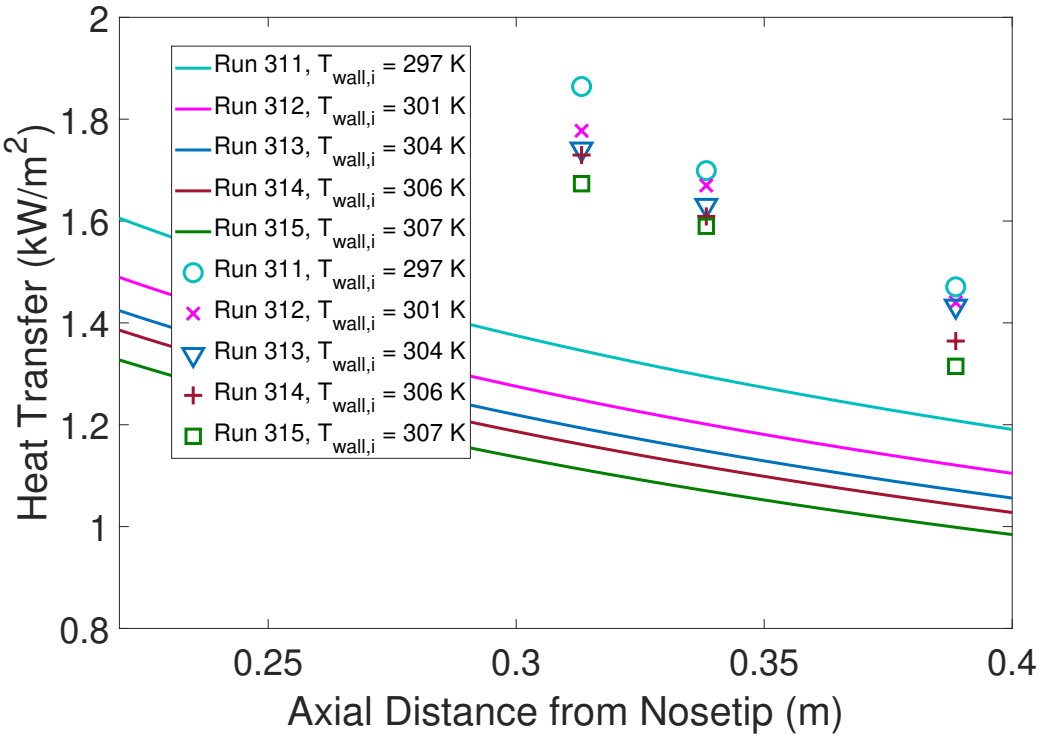

Figure 5.32. Comparing SB heat transfer (symbols) to similarity solution (solid line)for a 7° half-angle cone at a 0.0° angle of attack. Smooth insert (#1). Approximate run conditions are Re = 9.25×10^6/m , p_0 = 121.1 psia, T_0 = 422 K.

From Figure 5.32, it is clear that the theoretical solution predicts a decrease in heat transfer as the initial wall temperature increases. It is interesting to note that

a 10 K increase in initial wall temperature causes a 17% decrease in the predicted heat transfer. At these stagnation conditions, the solution predicts a wall adiabatic temperature, T_{aw}, of about 369 K. This makes $T_{aw} - T_{w,i}$ about 66 K. This makes the ratio of the change $T_{w,i}$ to $T_{aw} - T_{w,i}$ about 15 %. This may help explain why the predicted heat transfer dropped by about 17 %.

The experimental data shows a similar trend. It is unsure why the experimental data is higher than the predicted heat transfer. However, the discrepancy seems to be similar to that seen by Ward [66]. With a 10 K increase in the initial model temperature, the heat transfer drops by about 29%, 6%, and 11 % at axial locations of 0.313 m, 0.338 m, and 0.389 m respectively. These are significant heat transfer changes when considering that these runs are only 5 runs apart.

Figure 5.33 plots the same results as in Figure 5.32 with the Stanton number substituted for heat transfer on the vertical axis. Although T_{aw} is more readily known for this geometry, T_0 was used in the definition of Stanton number to maintain consistency.

Note the collapse of both the experimental data and the similarity solution. This helps imply that the shift that was seen previously when tracking the heat transfer along the leeward streak for a straight cone at a 6° angle of attack was a shift at least partially due to the increase in the initial temperature of the model.

5.3.4 Controlling Initial Model Temperature

Because it was found that controlling the initial temperature of the model was important to obtaining repeatable heat transfer data, a series of experiments were performed where the model was allowed to cool down in between runs. Although the initial temperature of the model before the run was not directly controlled, it could be held constant within 1 K by maintaining the same model temperature before starting the tunnel filling procedure. Waiting for the model to cool down was tedious, as natural convection took about four hours to cool the model back to the desired

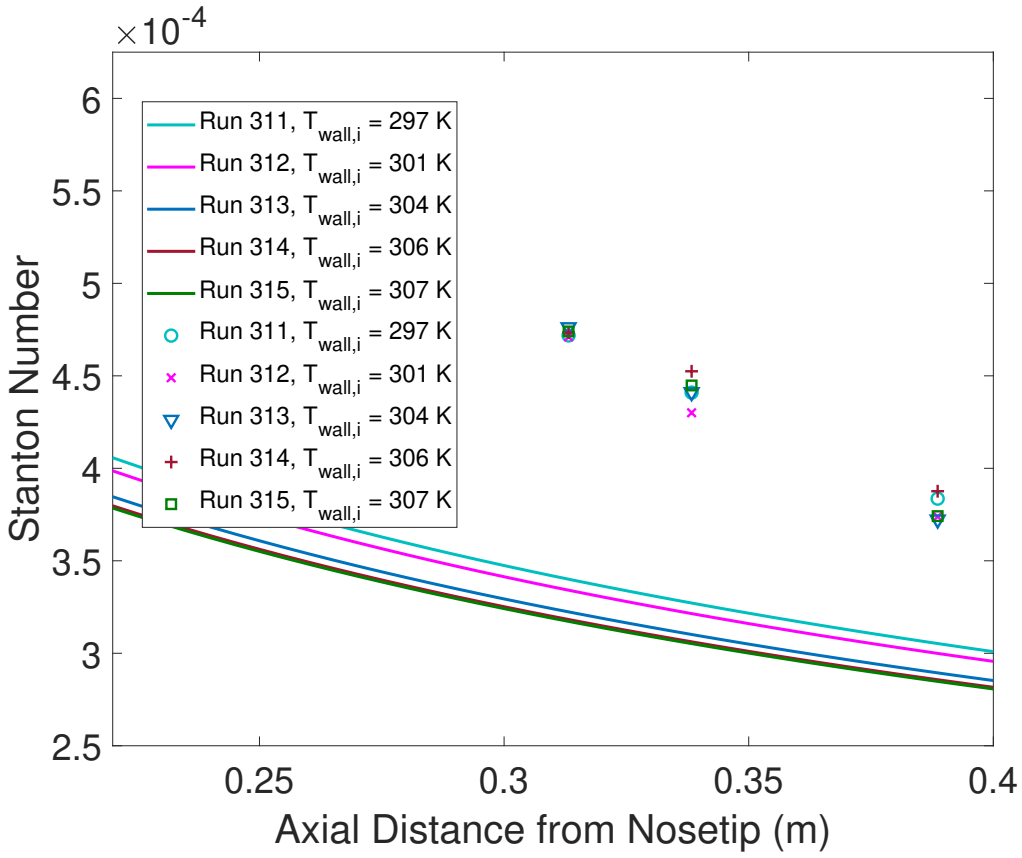

Figure 5.33. Comparing experimental Stanton number (symbols) to similarity solution (solid line) for a 7° half-angle cone at a 0.0° angle of attack. Smooth insert (#1). Approximate run conditions are Re $= 9.25 \times 10^6$/m , $p_0 = 121.1$ psia, $T_0 = 422$ K.

temperature. The reason this process took a large amount of time is that the test section was not opened while the model was cooling down. Only the diaphragm section was opened which allowed the tunnel downstream of the driver tube to cool down along with the model. If instead the model was allowed to cool by opening the test section, it only took about 30 minutes to cool down. This was done by opening the test section, and pulling the model back as far as possible. Pulling the model back meant that the bleed air, which was turned on to ensure no particulate travels upstream, would not heat up the model. However, it was noticed that the

initial model temperature was harder to control by this method, because it did not allow the tunnel to cool down along with the model. Thus, after the model was allowed to cool down to the desired temperature, the temperature would slowly rise due to the heat transfer between the tunnel wall and the model. If consecutive runs were done, and the model was allowed to cool down by opening the test section, the initial model temperature would be slightly higher with each consecutive run even if the model temperature before starting the filling process was the same. This is what made the initial model temperature before the run harder to control. Thus, the tunnel was cooled down in conjunction with the model, which took a significant amount of time in between runs. To monitor the model temperature, six thermocouples/CJC pairs were used. Each was calibrated and the average of the six readings was recorded as the initial model temperature.

The model was yawed at a nominal 6° angle of attack, and roughness # 7 was installed. Three runs were performed at the same initial conditions. The closest roughness element was 45.5° from the wind ray. These runs were performed under quiet flow. The TSP heat transfer images for these runs are shown in Figure 5.34. Recall that these images were all extracted from data one second into the run. They were calibrated using an SB at an axial distance of 0.338 m from the nosetip and 20.27° above the lee ray.

The images in Figure 5.34 look nearly identical. These images suggest that data taken from the BAM6QT can be repeatable if all the pre-run conditions are controlled properly. Comparing these images to those in Figure 5.25, there is clearly more repeatability in heat transfer between the images in Figure 5.34. To quantify the repeatability, Figure 5.35 shows the heat transfer in a spanwise cut at an axial location of 0.3 m from the nosetip for the runs in Figure 5.34. The good agreement is clear from the spanwise cut. However, it is also interesting to look at the temperature change maps that were used to form these heat transfer maps. These are shown in Figure 5.36.

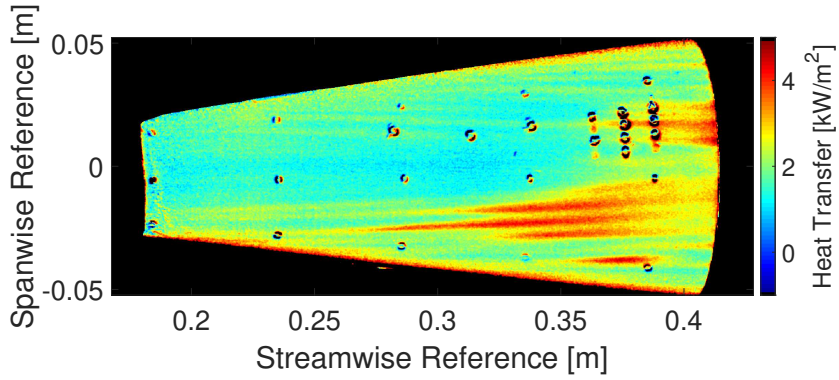

(a) Run 204.

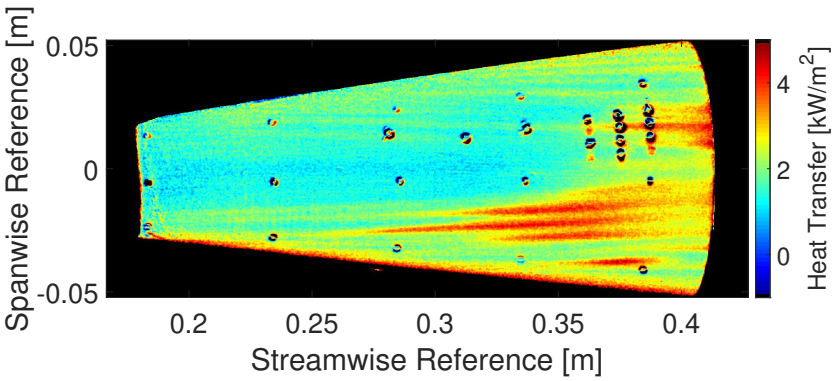

(b) Run 205.

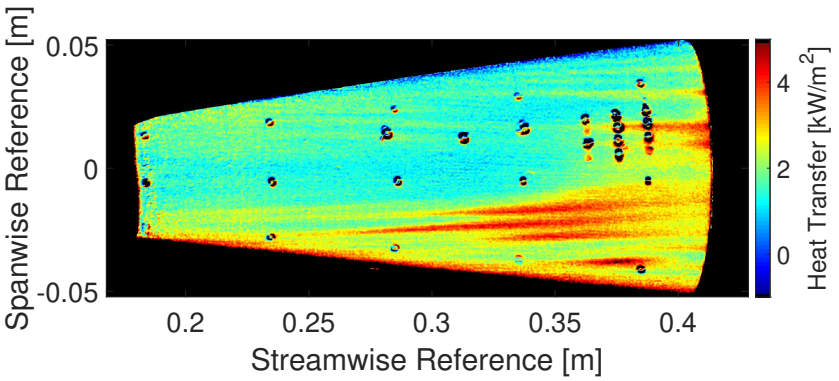

(c) Run 206.

Figure 5.34. Heat transfer of 3 runs done with same initial conditions including the initial model temperature. 203 μm insert (# 7). Approximate run conditions are $T_{w,i} = 298$ K, Re $= 9.1 \times 10^6$/m , $p_0 = 118$ psia, $T_0 = 420$ K.

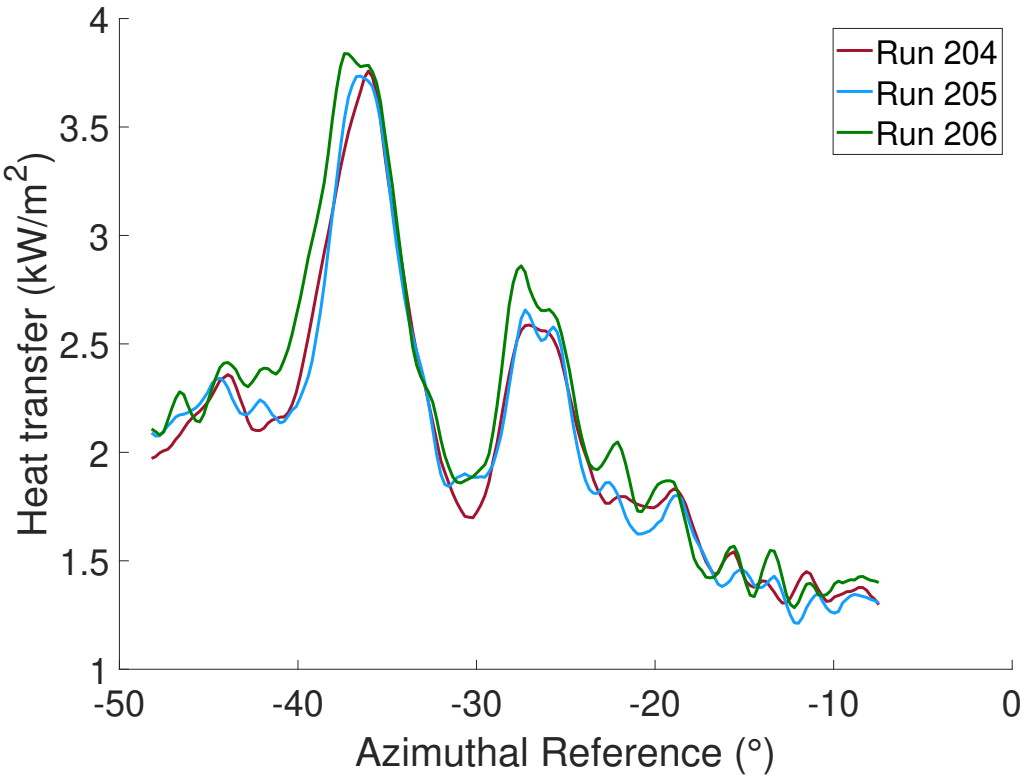

Figure 5.35. Spanwise cuts at an axial location of 0.3 m for the runs in Figure 5.34.

It is clear that the temperature maps between each run have much higher variation than the heat transfer maps in Figure 5.34. This makes it surprising that the heat transfer maps seem to be in such great agreement despite the disagreement between the temperature maps. This again confirms that the temperature change maps should only be used qualitatively and that the in-situ SB calibration properly takes care of the variation in the extracted temperature change in between runs.

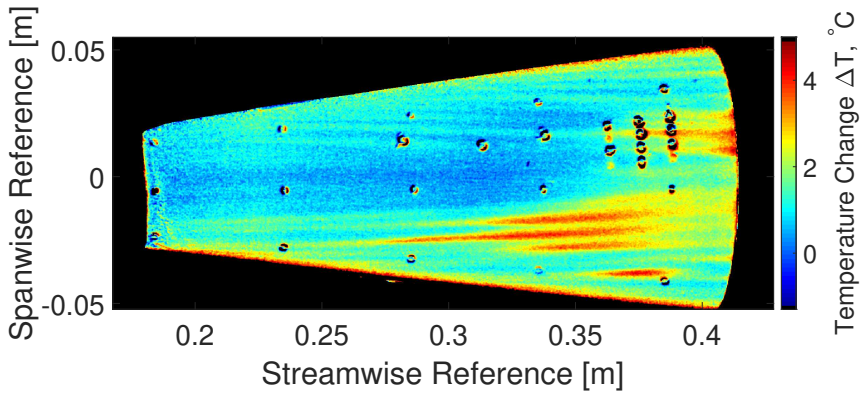

(a) Run 204.

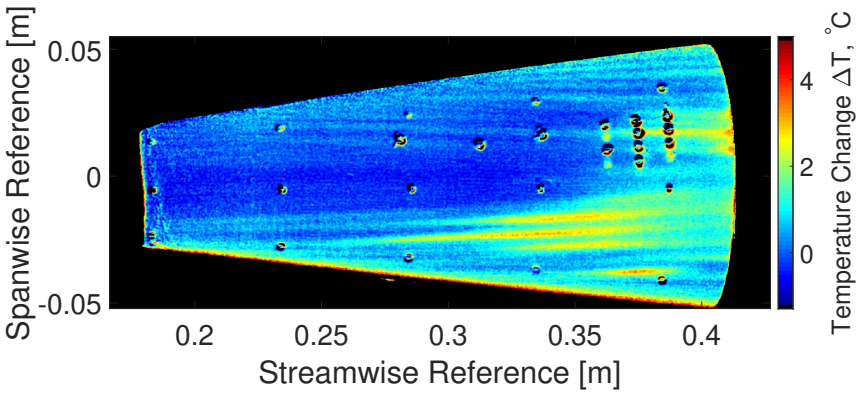

(b) Run 205.

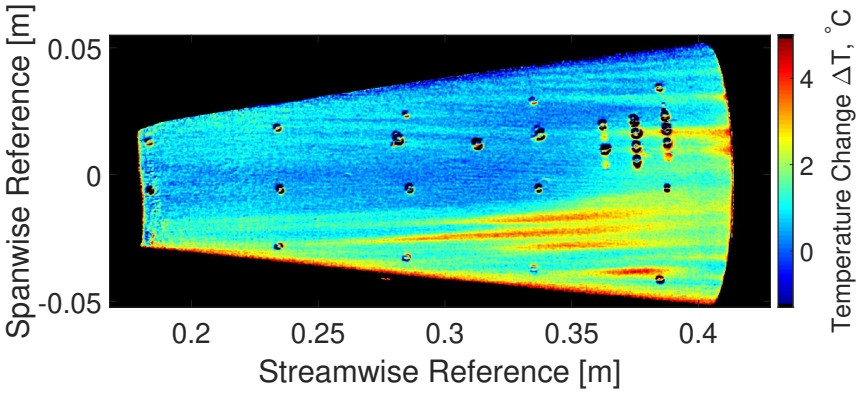

(c) Run 206.

Figure 5.36. Temperature change of runs in Figure 5.34.

5.4 Effect of Roughness on Heat Transfer of Stationary-Crossflow Streak

5.4.1 Effect of Roughness Height on Streaks

Once repeatability had been demonstrated, runs were performed at the same flow conditions while varying the roughness height from 51 μm to 254 μm in increments of 51 μm, in order to determine the relationship between the streak magnitude and the initial roughness height. The closest roughness element to the lee ray was placed 52.4° from the wind ray and each insert was tested 3 times to assess the repeatability. Some runs were done in order while others were done out of order to confirm the repeatability of the placement of the roughness insert. Figure 5.37 shows both the wrapped and unwrapped heat transfer images from one of the three runs that was performed with roughness insert # 2 which contained roughness elements with a height of 50.8 μm. These were calibrated using an SB that was placed at an axial location of 0.3383 m from the nosetip and 27.27° above the lee ray. Note that the lee ray is at the spanwise reference of 0 m. The bottom half of the image below the lee ray is the flow affected by the roughness insert. The flow in the top half of the image should theoretically not be affected by the roughness elements on the roughness insert. This is simply due to the nature of crossflow and its symmetry about the lee ray. However, it still may be affected by the step between the roughness insert and the frustum.

Below the lee ray, there is one apparent streak that is likely being caused by the roughness insert. Although the streak possibly starts to grow at the location of the roughness insert [19], the signal-to-noise ratio in the TSP is too low to detect the streak until 0.35 m. This is a disadvantage of TSP when compared to IR which can sometimes pick up streak growth right at its origin. Also note that there is a large streak above the lee ray near the sensors. The cause of this streak on the "smooth" side is unknown. Two other runs were done with this same configuration. Figure 5.38 shows the location of the streak below the lee ray for each of the 3 runs to illustrate the repeatability of the streak location between runs done at these conditions.

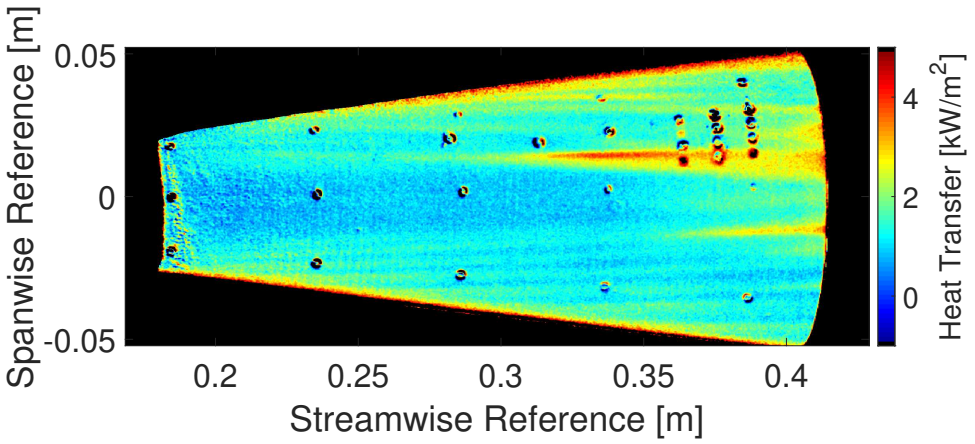

(a) Wrapped image.

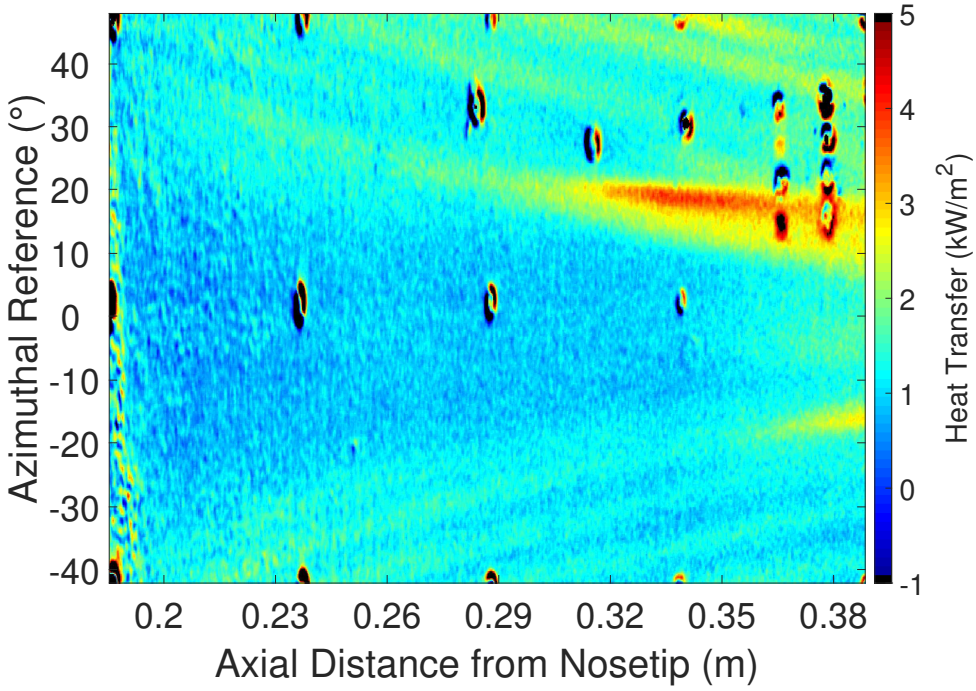

(b) Unwrapped image.

Figure 5.37. Heat transfer image wrapped and unwrapped using 50.8 μm insert (# 2). $T_{w,i}$ = 303 K, Re = 8.5×10^6/m , p_0 = 109.1 psia, T_0 = 419 K. Run 217.

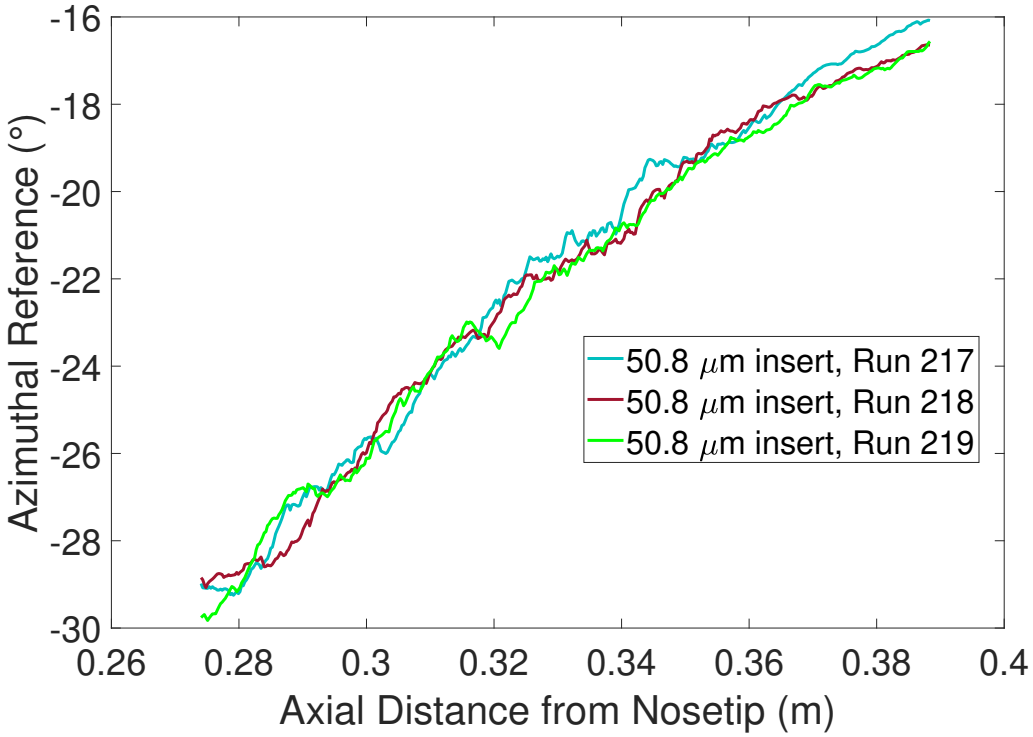

Figure 5.38. Location of streak for the run done in Figure 5.37(a) and two more runs done with the 50.8 μm insert. Approximate run conditions are $T_{w,i}$ = 302 K, Re = 8.4×10^6/m , p_0 = 108.4 psia, T_0 = 420 K.

Figure 5.38 shows that the location of the streak is repeatable. Repeatability of the streak location implies that the TSP is able to detect the streaks with reasonable signal-to-noise ratio. However, note that it is not specified whether this is the leeward streak or the windward streak. That is because there is only one visible streak. This is likely because the roughness element was too small produce any other visible streaks. Because there is only one streak, it is not obvious which roughness element the streak originates from. However, based on its location, it is likely forming off the same element generating the windward streak in other roughness inserts. Figure 5.39 shows the location of the streak averaged over the runs done with this roughness insert compared with the location of the windward and leeward streak averaged from

3 runs using roughness insert # 6 which contained elements with a height of 152 μm. Note that there is no particular reason for picking the 152 μm roughness except the fact that the windward and leeward streak originating from this roughness were clearly visible.

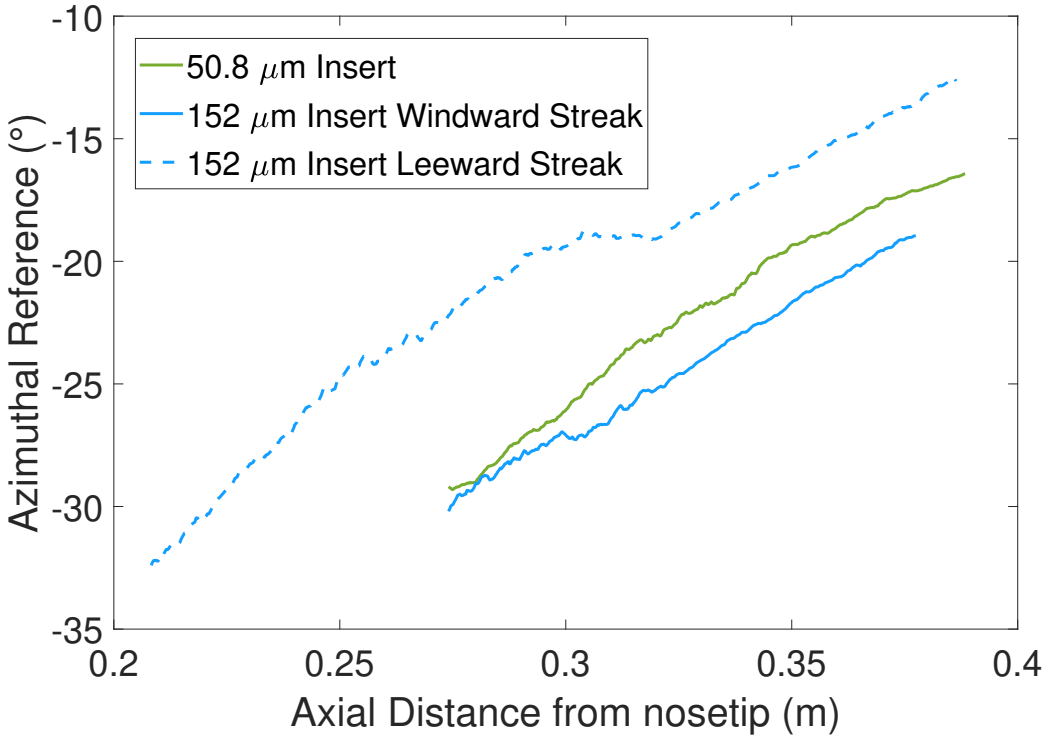

Figure 5.39. Comparing the location of the streak in Figure 5.38 to the location of the windward and leeward streak of the 152 μm insert. Approximate run conditions are $T_{w,i}$ = 302 K, Re = 8.4×10^6/m , p_0 = 108.8 psia, T_0 = 420 K.

The figure clearly shows the 50.8 μm streak being closer to the windward streak caused from the 152 μm insert. In addition, Figure B.2 in the appendix shows the roughness elements on the 50.8 μm insert to be slightly more leeward than the elements on the 152 μm insert which can be see in Figure B.5. This is good indication that the streak in Figure 5.38 is similar to the windward streak from the other roughness element and is shifted leeward due to slight machining errors. In fact, this is

why another 50.8 μm insert was made. Thus, this streak will be compared to the windward streak from other roughness inserts. The heat transfer along the streak for each of the 3 runs performed with the 50.8 μm insert is shown in Figure 5.40.

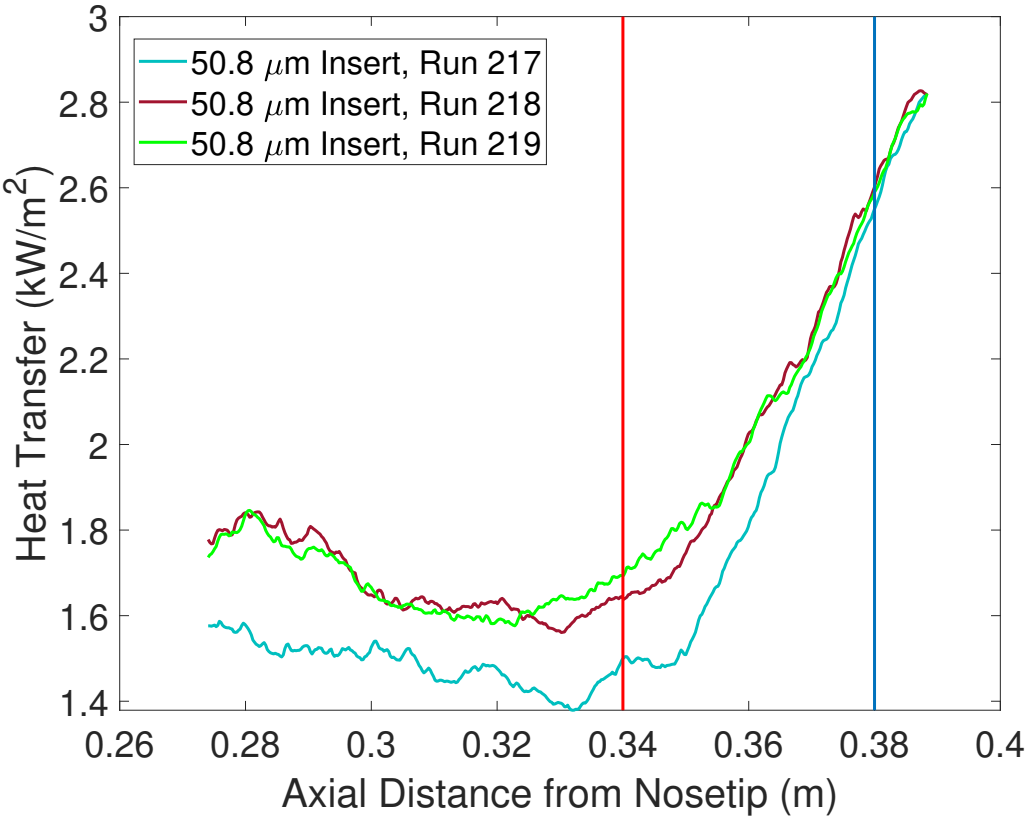

Figure 5.40. Heat transfer along the streaks in Figure 5.37(a). Approximate run conditions are $T_{w,i} = 302$ K, Re $= 8.4 \times 10^6$/m , $p_0 = 108.4$ psia, $T_0 = 420$ K.

These runs were performed with approximately the same initial wall temperature +/- 0.3 K. While the heat transfer for runs 218 and 219 are repeatable, run 217 does not agree. The reason for this is unknown. To get a better of why this occured, Figure 5.41 shows the linear calibration for all 3 runs. First, it is interesting to note that while the calibrations for run 218 and 219 seem to differ by a lot, the streak heat transfers match up nicely. This illustrates how vital the TSP calibration process

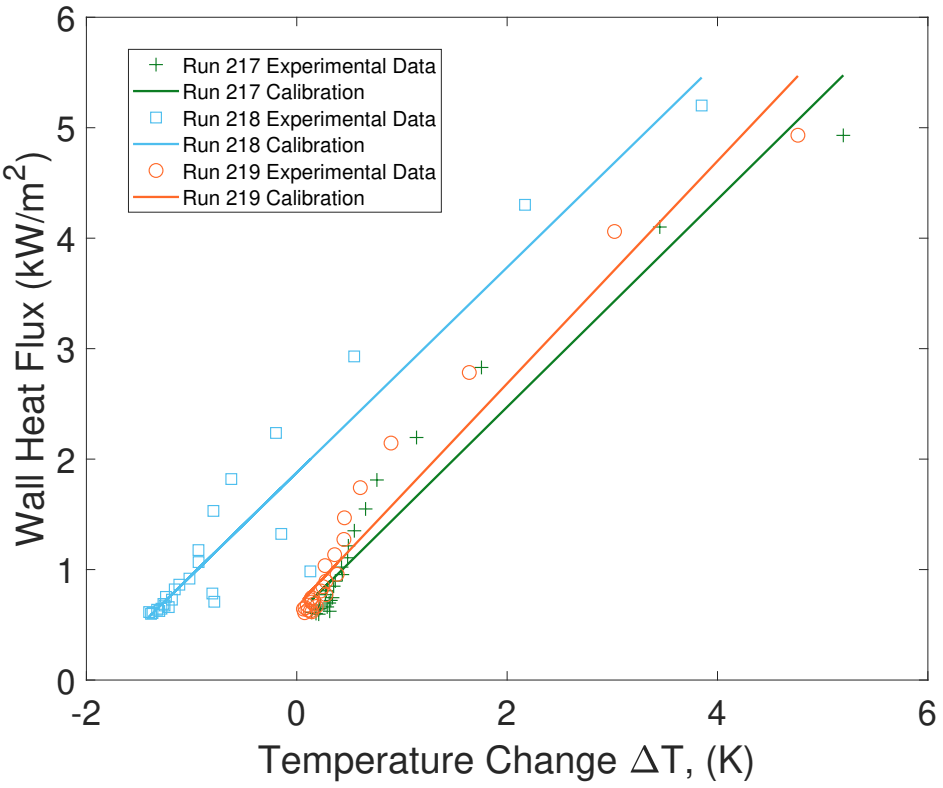

Figure 5.41. Calibration for the 3 runs in Figure 5.40 which were done with the 50.8 μm insert.

is in minimizing uncertainty. Second, a quick comparison between the calibrations for runs 217 and 219 does not reveal any glaring differences or areas for possible concern. Thus, it is unclear why the streak heat transfer values are quite different. It should be noted, however, that this repeatability issue is primarily manifested on the portion of the streak before it starts to grow, which indicates that at least part of this repeatability issue is due to low signal-to-noise. The heat transfer for all 3 runs is repeatable downstream of 0.36 m, likely due to the higher signal-to-noise ratio.

Although the vortex probably started growing farther upstream, its growth is only able to be seen with the TSP at an axial distance of 0.34 m. The heat transfer along spanwise cuts at axial locations of 0.34 m and 0.38 m for all 3 runs are shown

in Figure 5.42. These axial locations are marked with red and blue vertical lines respectively in Figure 5.40.

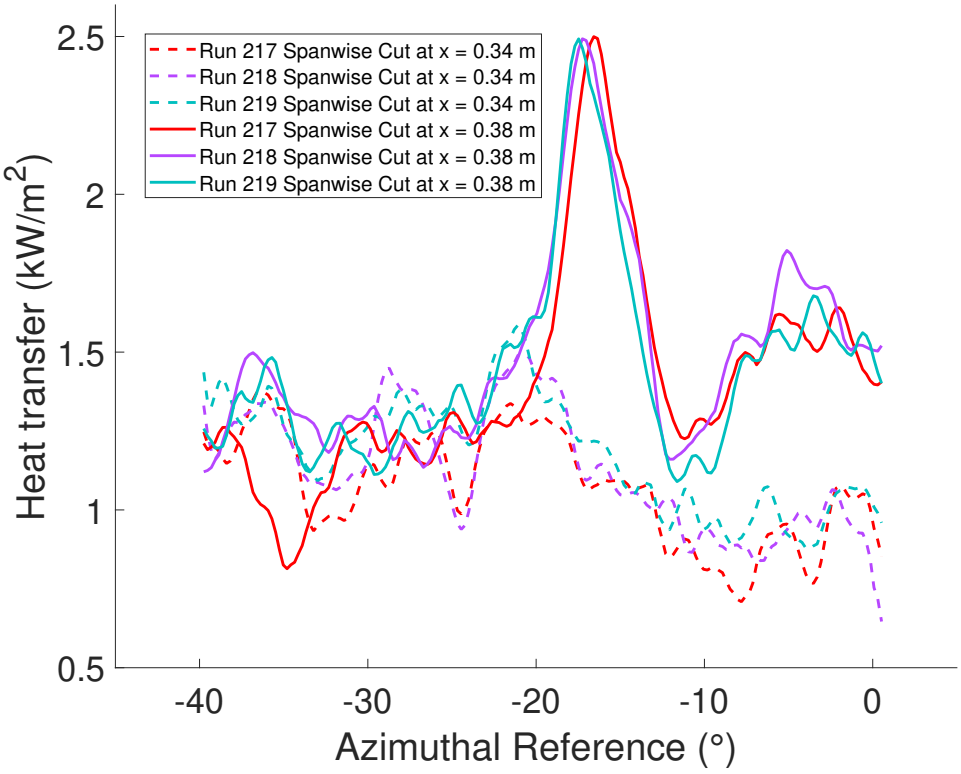

Figure 5.42. Spanwise cut of the heat transfer at the axial locations marked by the red and blue vertical lines in Figure 5.40.

First, note the decent repeatability between the 3 runs for the spanwise cut at x = 0.38 m. A peak in the heat transfer can be seen for the spanwise cut at x = 0.38 m for all 3 runs at approximately -17.5°. This peak corresponds to the streak seen below the lee ray in Figure 5.37(a). However, no major peak can be seen for the spanwise cut of any of the 3 runs at x=0.34 m. There appear to be several local maxima, but it is not possible to attribute these peaks to actual streaks, as the heat transfer magnitudes remain too close to the noise floor.

Figure 5.43 shows a run with the same flow conditions, except the roughness insert was changed to roughness # 4 which had roughness elements with a height of 102 μm. Here it seems that the leeward streak starts growing farther upstream, the streak below it is more noticeable, and that there also seems to be a third streak below it. It is likely that these three streaks are being caused by the three roughness elements on the roughness insert. Also note that the streak that was on the upper half of the cone in Figure 5.37 has disappeared. This implies that this streak was possibly caused by a step between the roughness insert and cone frustum. However, the nothing of concern was seen when the step was measured using the Zygo.

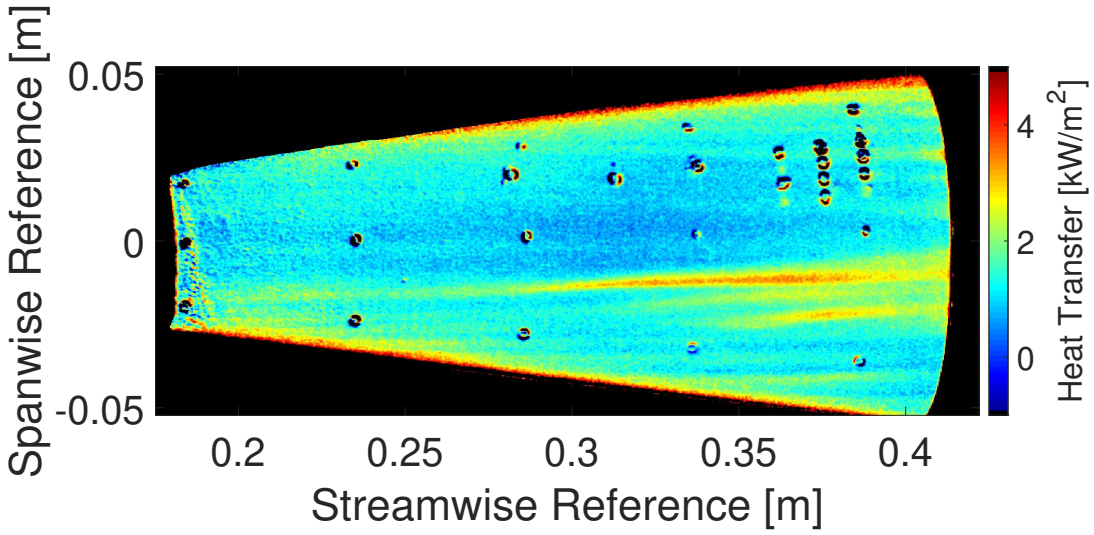

Figure 5.43. Heat transfer image using 102 μm insert. (# 4). $T_{w,i}$ = 303 K, Re = 8.5×10^6/m , p_0 = 109.7 psia, T_0 = 420 K. Run 212.

The signal-to-noise ratio still seems low between 0.2 m and 0.25 m, as the streaks are barely visible at this axial location. Figure 5.44 shows the location of the leeward streak for 3 runs performed at the same conditions with the 102 μm. Again, the repeatability of the location of the streak seems fairly high. As the streaks grow downstream, the variation in the location between the 3 runs is less than 1°. Shown

in Figures 5.45(a) and 5.45(b) are the heat transfer for all 3 runs for the leeward and windward streak respectively.

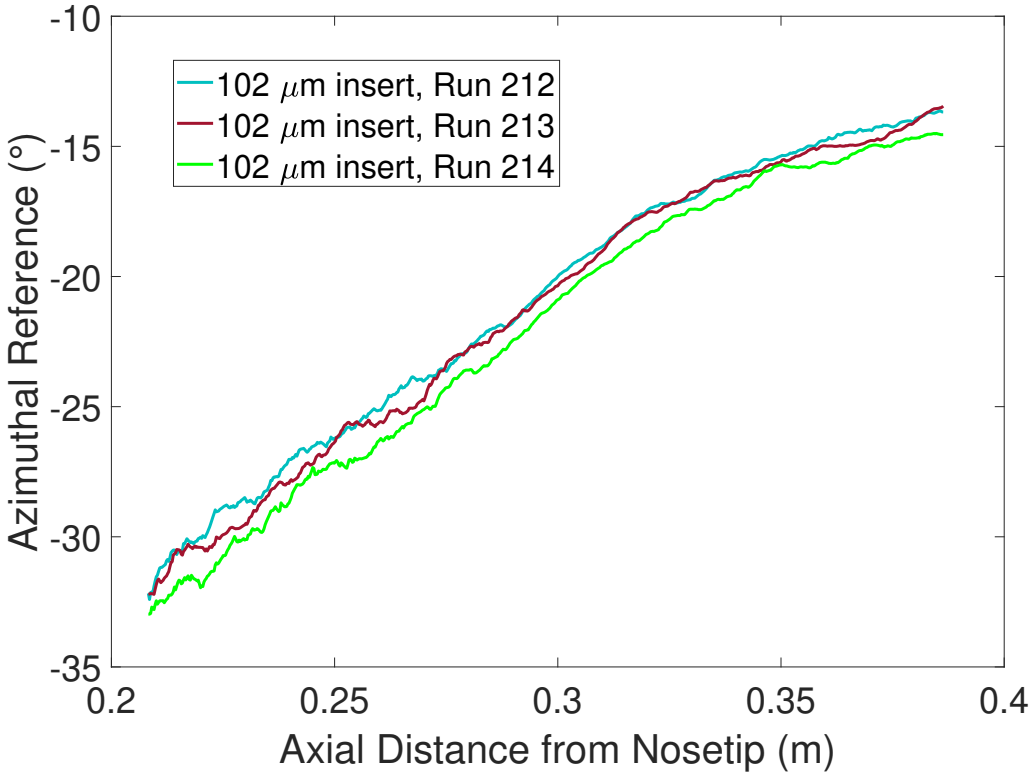

Figure 5.44. Location of leeward streak for the run in Figure 5.43 as well as 2 more runs with the same insert. Approximate run conditions are $T_{w,i} = 303$ K, Re $= 8.5 \times 10^6$/m , $p_0 = 109.3$ psia, $T_0 = 420$ K.

Again, the repeatability of the heat transfer for the 3 runs between 0.3 m and 0.4 m is fairly high for both the leeward streak and the windward streak. Before 0.3 m, the results seem to suffer from poor signal-to-noise ratio as indicated by the high scatter in the heat transfer of either streak for different runs. The leeward streak seems to peak at around 0.35 m, while the windward streak grows all the way up to 0.38 m. Although this peak may be saturation, the flow may already be transitioned at this location. The reader is referred to Section 5.4.3, where Reynolds number scaling is used to determine if the flow is laminar or turbulent at this peak.

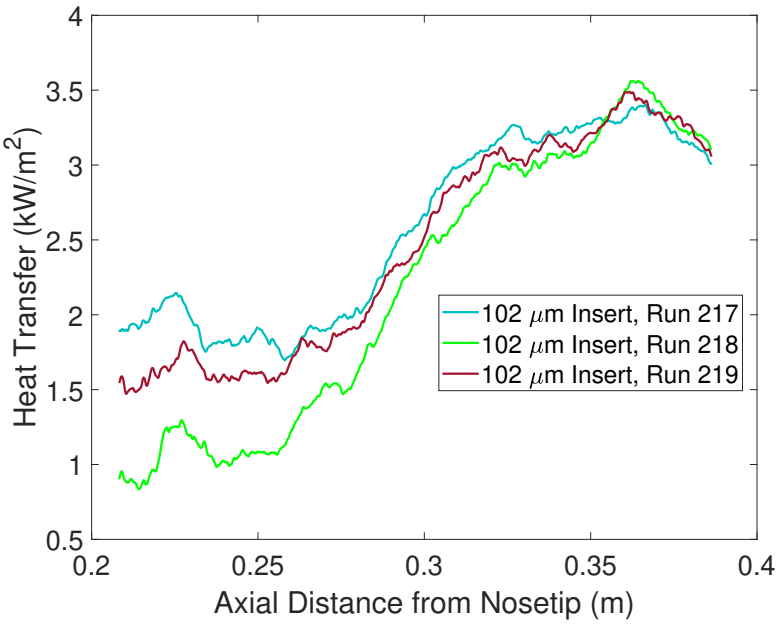

(a) Heat transfer along leeward streaks.

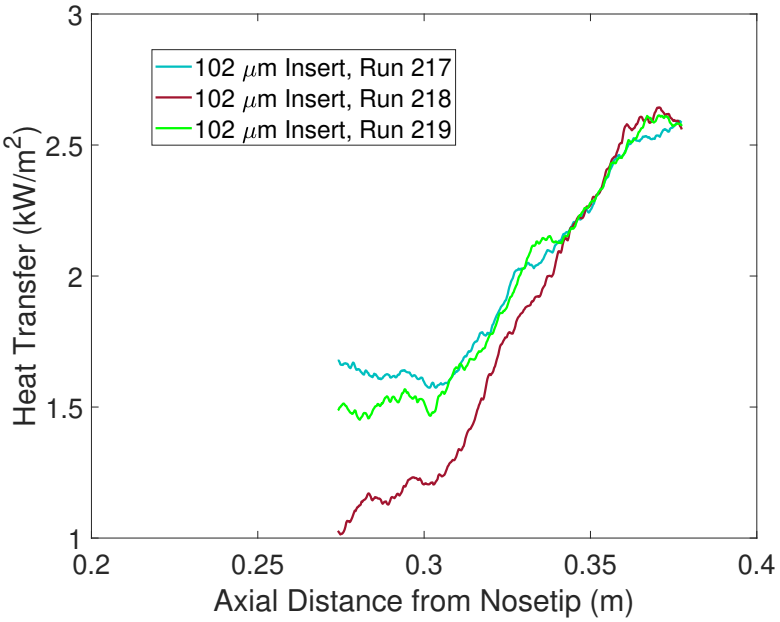

(b) Heat transfer along windward streaks.

Figure 5.45. Heat transfer along the leeward and windward streak in the run in Figure 5.43 as well as 2 more runs with the same insert. Approximate run conditions are $T_{w,i}$ = 303 K, Re = 8.5×10^6/m , p_0 = 109.3 psia, T_0 = 420 K.

Figure 5.46 shows a run with the same conditions but using roughness insert # 6 which contained roughness elements with a height of 152 μm. The leeward streak

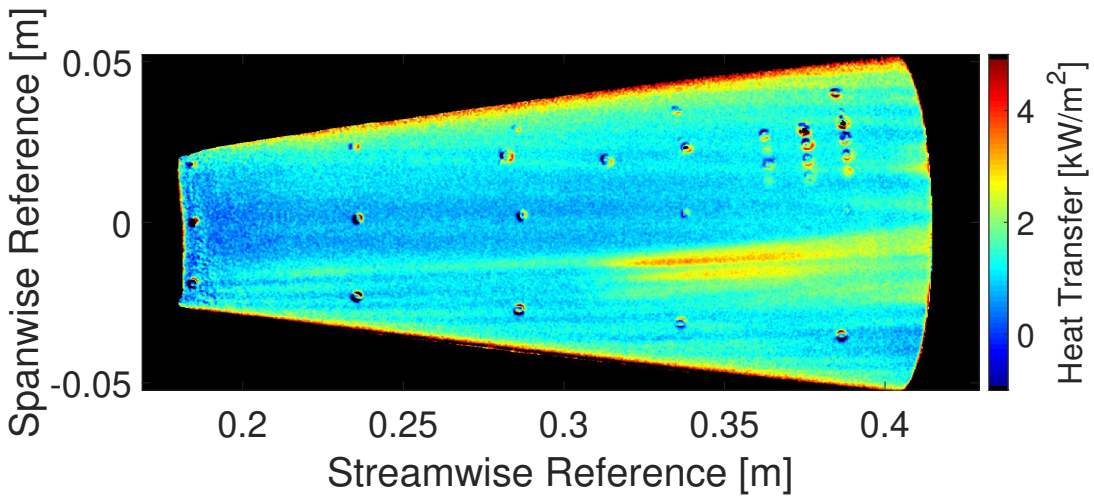

Figure 5.46. Heat transfer image using 152 μm insert. (# 6). $T_{w,i}$ = 302 K, Re = 8.5×10^6/m , p_0 = 109.5 psia, T_0 = 420 K. Run 209.

is not seen until farther downstream than in the 102 μm case. This is unexpected and the reason for this is unknown as Figure B.5 in the appendix shows the most leeward element of the 152 μm insert to have a larger height than the most leeward element in the 102 μm insert which is shown in Figure B.3. However, the streak seems to be wider and peaks at a more upstream location than the leeward streak in Figure 5.45(a) which was caused by a 102 μm element. The windward streak appears earlier upstream than the windward streak for the 102 μm insert case. The third streak, directly below the windward streak also seems to appear earlier upstream than the streak caused by by the 102 μm insert. Two more runs were done with the 152 μm roughness and the heat transfer along the leeward and windward streaks are shown in Figures 5.47(a) and 5.47(b) respectively.

Downstream of 0.3 m, the heat transfer along the streak is again repeatable, especially for the leeward streak. This is another indication that repeatable results

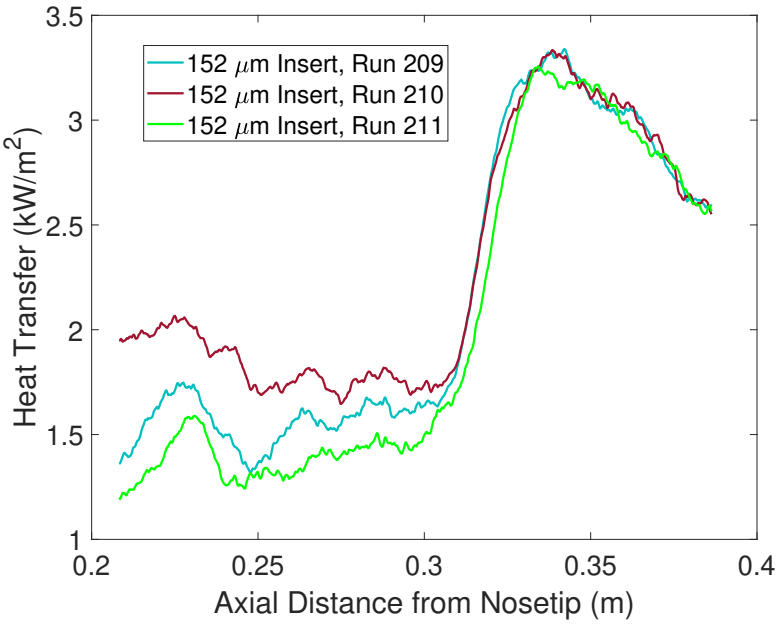

(a) Heat transfer along leeward streaks.

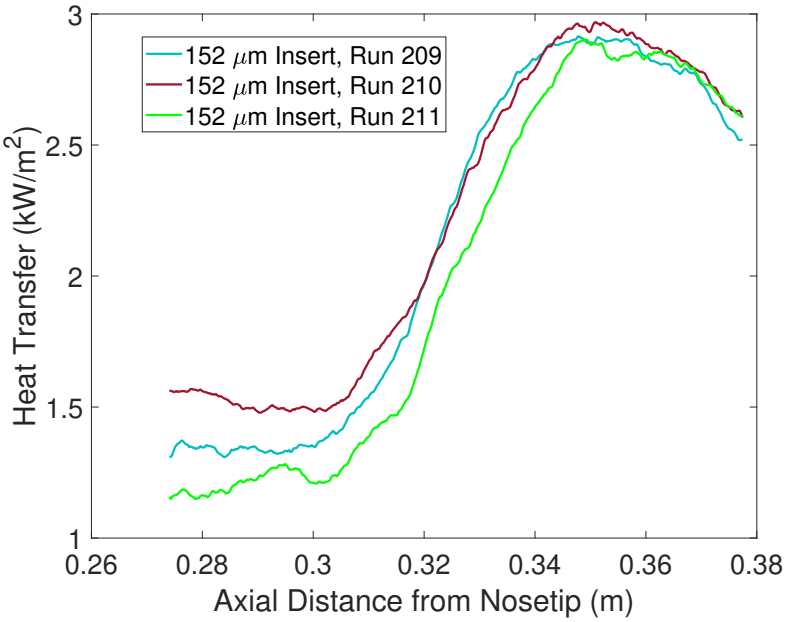

(b) Heat transfer along windward streaks.

Figure 5.47. Heat transfer along the leeward and windward streak in the run in Figure 5.46 as well as 2 more runs with the same insert. Approximate run conditions are $T_{w,i}$ = 302 K, Re = 8.5×10^6/m , p_0 = 109.2 psia, T_0 = 420 K.

can be acheived with TSP if care is taken to control the initial conditions properly. To quantify the variation in heat transfer between the different runs, the average heat transfer was calculated for the 3 runs. Then, at each axial location, a normalized rms variation was calculated by subtracting each heat transfer magnitude from the average. Finally, the normalized rms variation was averaged over the axial length of the data to receive an average normalized rms. This turned out to be 7.11 % and 5.27 % for the leeward and windward streaks respectively. However, if the normalized rms variation is only considered downstream of 0.31 m, the values become 0.82 % and 2.18 % for the leeward and windward streaks respectively. This variation shows how repeatable the data is, especially in the region of streak growth.

The leeward streak seems to grow from 0.30 m to around 0.34 m at which point it peaks. The windward streak grows from 0.30 m to 0.35 m. Although the noise upstream of 0.30 m is lower than the noise using the 50.8 μm and 102 μm roughness, it still shows that the TSP is unable to reliably detect the streaks unless the contrast between the heat transfer at the location of the streak and the heat transfer adjacent to the streak is high enough. In other words, it needs a higher signal-to-noise ratio to be effective.

Finally, Figure 5.48 shows a run with the same conditions and with the roughness insert replaced with the roughness insert # 7 which contains roughness elements with a height of 203 μm. The leeward streak appears farther downstream than in Figure 5.46 with the 152 μm insert. The reason for this is unknown. It should be noted that Figure B.6 in the appendix shows the most leeward element of the 203 μm insert to be slightly greater in height than the most leeward element in the 152 μm insert, which can be seen in Figure B.5. This makes it even more surprising that the leeward streak is weaker for the 152 μm case. The windward streak starts to grow farther upstream than windward streak from the 152 μm insert case, which is expected due to the forcing of larger magnitude disturbances. The third streak directly below this also seems to start growing farther upstream than in the streak from the 152 μm insert. Following the previous pattern, 2 more runs were performed

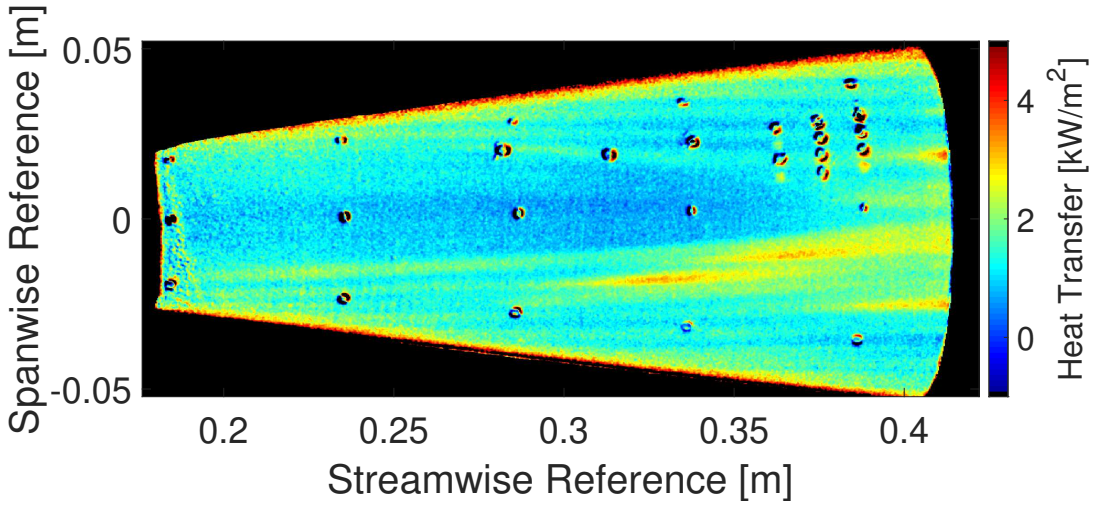

Figure 5.48. Heat transfer image using 203 μm insert. (# 7). $T_{w,i}$ = 302 K, Re = 8.5×10^6/m , p_0 = 109.1 psia, T_0 = 419 K. Run 215.

and the heat transfer along the leeward and windward streaks were extracted. These are shown in Figures 5.49(a) and 5.49(b) respectively.

While the leeward streak is seen to grow from 0.3 m to about 0.36 m, the windward streak appears to start growing farther upstream at 0.28 m. The variability between runs of the heat transfer on the windward streak is higher than the variability of runs done with the other roughness inserts. Although the streak heat transfer does not vary significantly between runs while it is increasing, there seems to be some variability between runs for the heat transfer at the peak. Around the peak at 0.33 m, the difference in heat transfer between run 216 and run 221 is about 13%. Although this is not a huge difference, it is surprising, since all the initial conditions including the initial wall temperature were kept constant. To get a better idea why, Figure 5.50 compares the linear calibration for all 3 runs done with the 203 μm insert with the linear calibration for 3 runs done with the 152 μm insert, which had much higher repeatability.

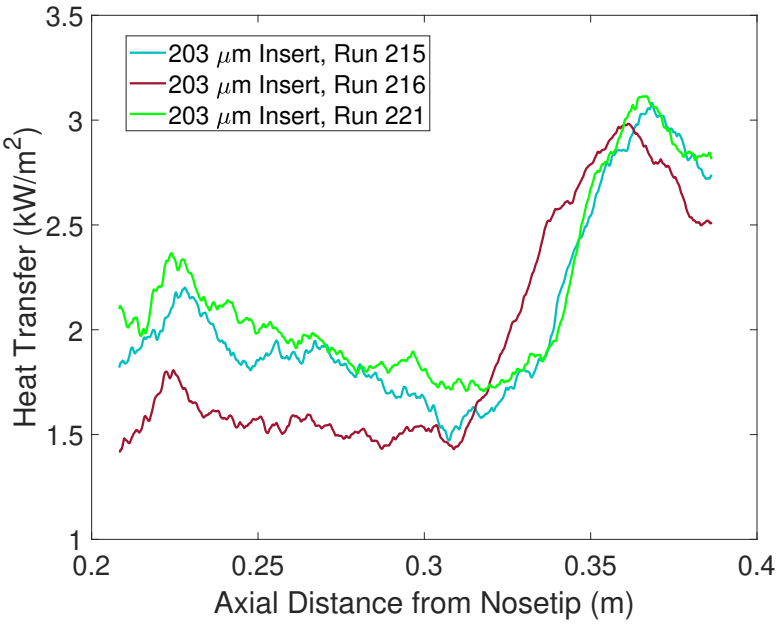

(a) Heat transfer along leeward streaks.

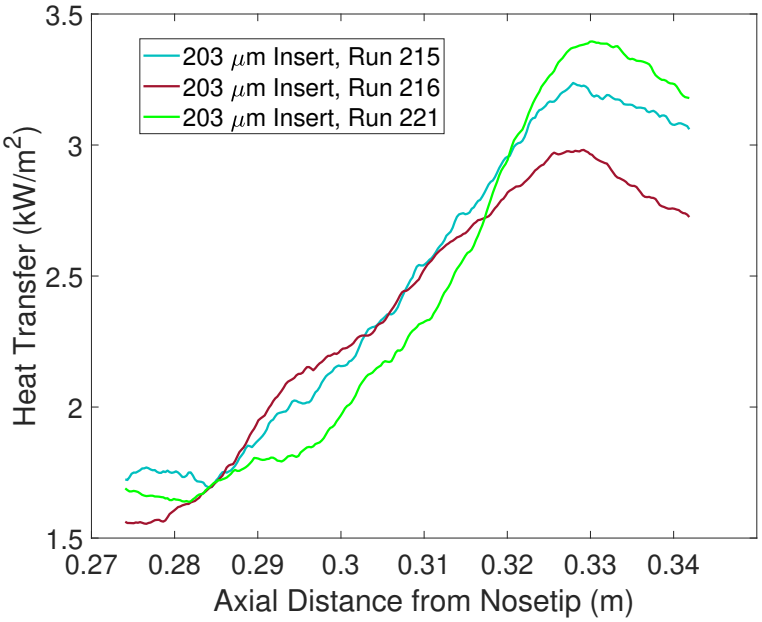

(b) Heat transfer along windward streaks.

Figure 5.49. Heat transfer along the leeward and windward streak in the run in Figure 5.48 as well as 2 more runs with the same insert. Approximate run conditions are $T_{w,i} = 302$ K, Re $= 8.4 \times 10^6$/m, $p_0 = 109.2$ psia, $T_0 = 421$ K.

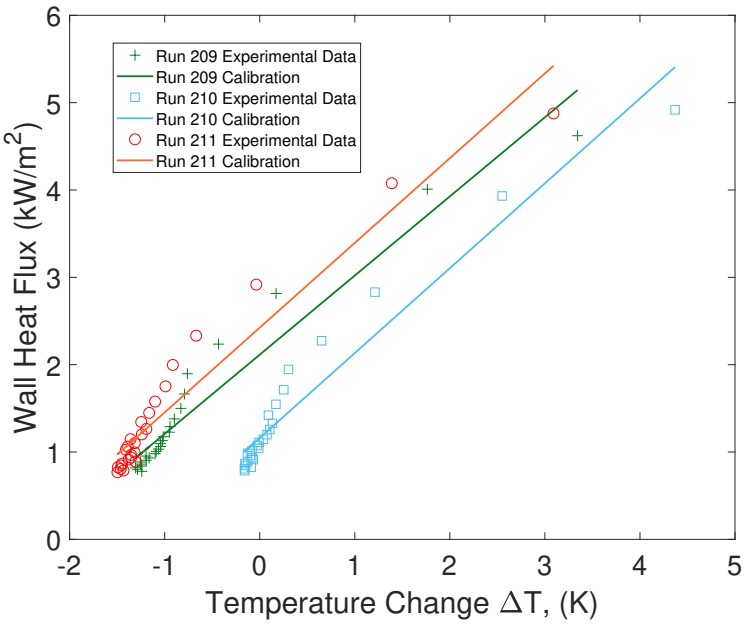

(a) Linear calibration for runs done with 152 μm insert.

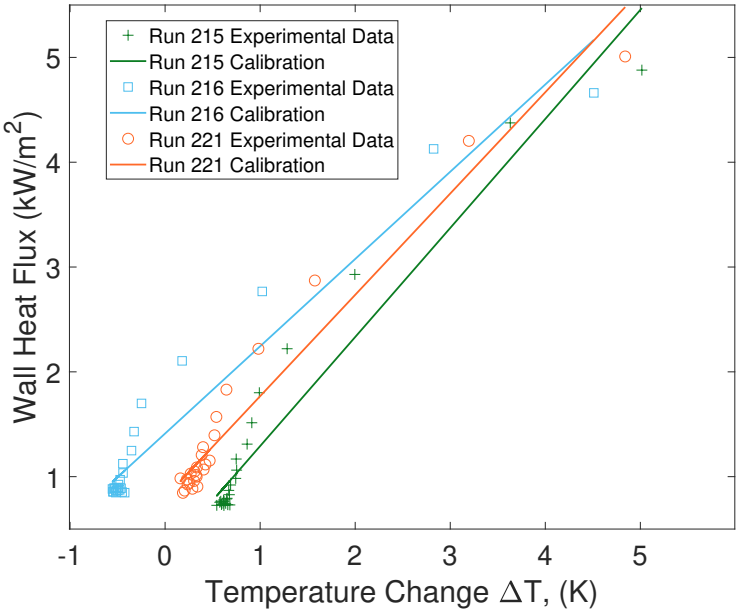

(b) Linear calibration for runs done with 203 μm insert.

Figure 5.50. Linear calibration comparison of 2 different sets of runs. Approximate run conditions are $T_{w,i}$ = 302 K, Re = 8.5×10^6/m , p_0 = 109.2 psia, T_0 = 420 K.

It is clear there is more variability in the linear calibrations for the 203 μm insert which can be seen by the differing slopes. Interestingly, it seems that the last 2 data points (with the highest heat transfer) for the calibration for Run 216 pull the curve to the right. It is likely this pull that causes the heat transfer for Run 216 in Figure 5.49 to be lower then the other runs, especially at the peak. These calibration points were taken during the startup process of the tunnel. Unfortunately, while the heat transfer during this time period is mostly unclear, it is necessary in order to properly calibrate the TSP for higher heat transfer. Thus, the TSP calibration fits are at the mercy of this unpredictable startup process until a better method can be discovered.

Finally, the upper half of each TSP heat transfer image, which is the flow above the lee ray, has been different for each image, even though the only supposed difference between each run was the roughness element height on the roughness insert. Note this region can be seen in every TSP image above the 0 m mark. However, the roughness elements should not have impacted the upper portion of the image as previously stated because of the symmetric geometry. Thus, the variation in the streak spacing and strength is likely due to the step between the roughness insert and frustum. It is unclear how much this step may have affected the data below the lee ray, but is likely less significant for the flow below the lee ray, as the utilized element heights were much larger in magnitude than the insert steps.

Due to the generally decent repeatability, the heat transfer along each streak for all 3 runs of each roughness insert case was averaged to get the representative heat transfer for each roughness insert. This was plotted in Figures 5.51(a) and 5.51(b) for the leeward and windward streaks, respectively.

In Figure 5.51(a), it is not clear why there is no consistent trend for the leeward streak. The streak from the 152 μm insert can be seen before the streak from the 203 μm insert, and the streak from the 102 μm insert is seen to grow before either of them. It was suspected that this may be because of the proximity to the lee ray. Using the CFD mean-flow solution provided by Dr. Bitter, a good estimate of the

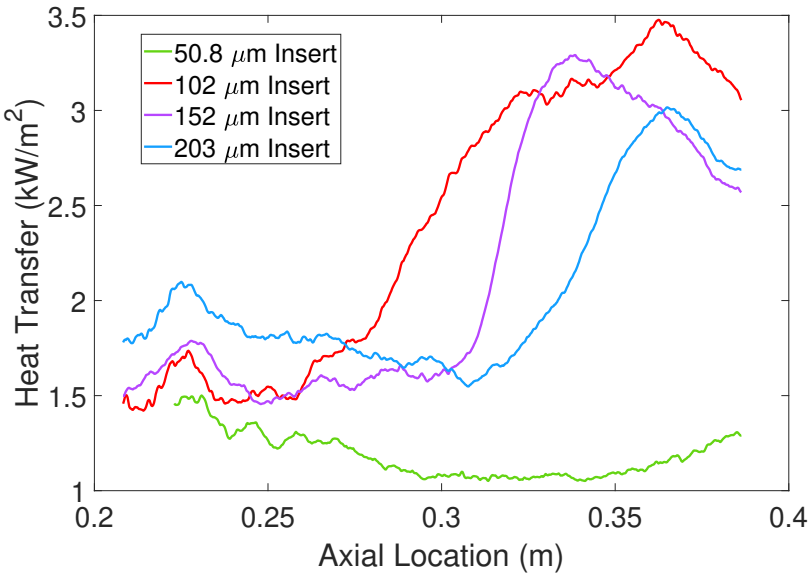

(a) Heat Transfer along the leeward streak.

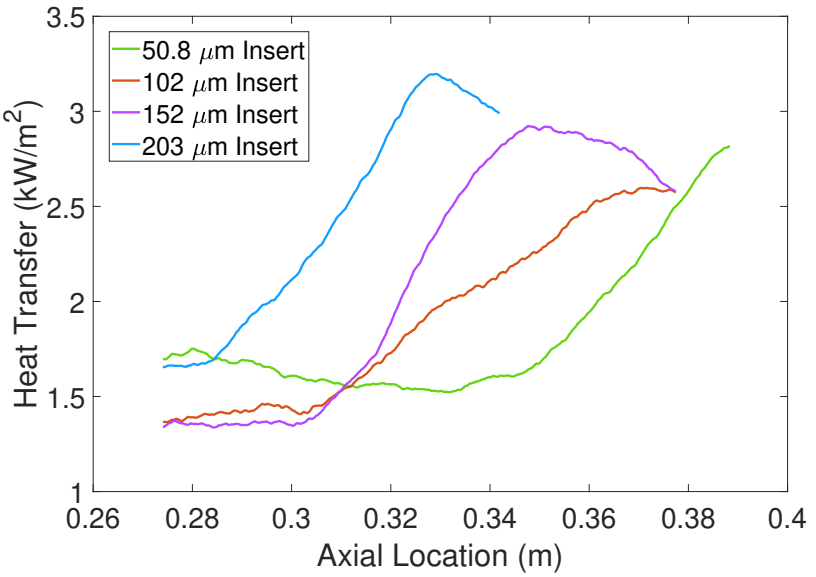

(b) Heat transfer along the windward streak.

Figure 5.51. Heat transfer along the leeward and windward streak for runs performed at the same conditions with different roughness inserts. Each line is averaged from 3 runs. Approximate run conditions are $T_{w,i} = 303$ K, Re $= 8.5 \times 10^6$/m , $p_o = 109.0$ psia, $T_o = 428$ K.

mushroom location can be obtained. Looking at Figure 4.9, this location was defined as the azimuthal location at which the mushroom structure intersects the normal boundary layer. Because it was found that the azimuthal scope of the mushroom vortex did not vary significantly when the stagnation pressure was changed from 155 psia to 75 psia, the location of the mushroom vortex for the experimental conditions was taken as an average of the location obtained from the 2 computations. Ten axial locations were extracted, and the location between them was interpolated. Note that this method of location selection may have a couple degrees of uncertainty. However, this is likely insignificant when looking at Figure 5.52, which displays the mushroom vortex location along with the average streak location of the leeward streak for each insert. There is a decent amount of separation between the mushroom vortex and

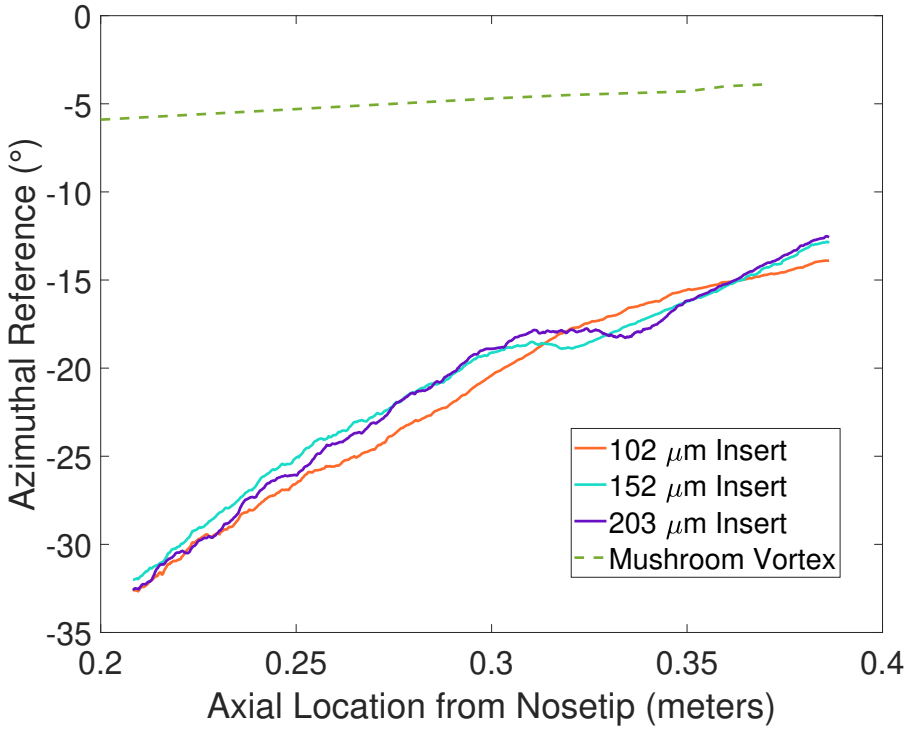

Figure 5.52. Location of leeward streak for different inserts and mushroom vortex. Approximate run conditions are $T_{w,i} = 302$ K, Re $= 8.0 \times 10^6$/m , $p_0 = 102.9$ psia, $T_0 = 420$ K.

the leeward streaks. There is almost a 10° separation even at the most downstream location. Given this amount of separation between the two, it seems unlikely that the mushroom vortex would have a big effect on the leeward streak.

It should also be noted that the streak from the 102 μm insert seems to have a different shape than the other streaks. This is what prompted another 102 μm insert to be made. Unfortunately, due to time constraints there is no data to compare runs done at the same initial conditions with the different 102 μm inserts.

Also, Figure 5.51(a) contains a line for the 50.8 μm insert, even though there was no streak. This data was extracted the same way as the other streaks, although the peak that was seen in the spanwise cut for each axial location was likely just noise. The initial guess for the streak location was the same as the initial guess for the other streak locations.

Figure 5.51(b), displaying the heat transfer along the windward streaks, shows a clearer trend. As the roughness element height increases, the growth of the streak moves farther upstream. A similar result was found in computations done by Moyes on an elliptical cone who found that the growth of the vortex moved upstream as the amplitude of the initial disturbance increased [56].

As previously mentioned, these runs were performed with a 3-4 hour waiting period in between runs to allow the model and tunnel to cool down. Although this was able to produce repeatable TSP heat transfer data, a 3 hour waiting period in between runs was too inefficient for general operations. Thus, during the subsequent tunnel entry, the model was allowed to cool down by opening the test section and exposing the model to room temperature. Because this did not allow the tunnel wall to cool down as well, the initial temperature of the model before a run was less controllable as the model would increase slightly in temperature, absorbing heat from the hotter tunnel. As more runs were done, the tunnel wall increased in temperature, which increased the model's initial temperature before a run even if the model temperature before filling was the same. However, the initial temperature of the model was only found to vary by +/- 0.6 K. This led to relatively repeatable TSP heat transfer results.

Shown in Figure 5.53 are the unwrapped images of two consecutive runs performed at the same initial conditions with insert # 7 which contained 203 μm elements. The closest element to the lee ray was now placed 43.4° away from the wind ray instead of 52.4°. These images were calibrated using an SB at an axial location of 0.282 m from the nosetip and 26.34° above the lee ray.

Although there are minor differences in the heat transfer, the repeatability is great. Again, it is important to keep in mind that the flow above the lee ray, which is marked as the 0° reference point in the figure, was not affected by the roughness elements on the roughness insert due to the symmetry of the crossflow. To characterize the repeatability of the heat transfer along the streaks, Figures 5.54(a) and 5.54(b) show the heat transfer along the leeward and windward streaks respectively for the set of runs in Figure 5.53 which used the 203 μm insert as well as 2 other sets done with the 152 and 254 μm insert.

The average percent changes for the leeward streaks were found to be 10.47 % , 2.69 % , and 8.61 % for runs performed with the 152 μm, 203 μm, and 254 μm inserts respectively. Note that the majority of the percent change for the leeward streaks from the 152 μm insert comes from before the streak starts to grow. The average percent changes for the windward streaks were found to be 10.28 % , 2.09 % , and 7.02 % for runs performed with the 152 μm, 203 μm, and 254 μm inserts respectively. Although the average percent change for the runs with the 152 μm insert is slightly higher, the heat transfer along either streak for both sets of runs is reasonably repeatable, showing again that it is possible to achieve repeatable results with TSP if the initial conditions are controlled properly. It also shows that cooling the model for 30 minutes is long enough, as long as the test section is opened and the model is exposed to room temperature. Runs were also performed with a 50.8 μm and 102 μm insert. Note that the 50.8 μm and 102 μm roughness used in these cases are different than those that were used previously, due to the aforementioned possible machining errors. However, the nominal dimensions of these inserts are the same. Figure 5.55 displays the unwrapped TSP image for runs done with the 50.8 μm, 152

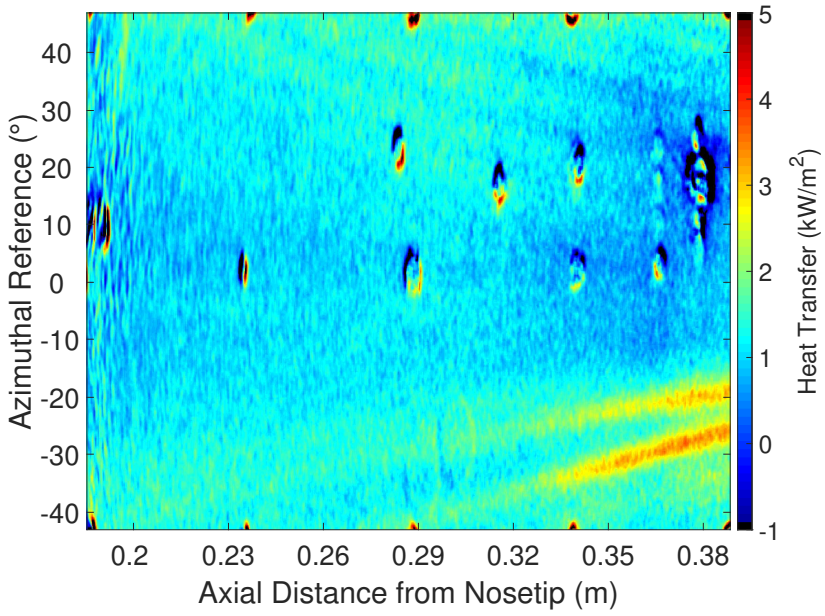

(a) Run 416.

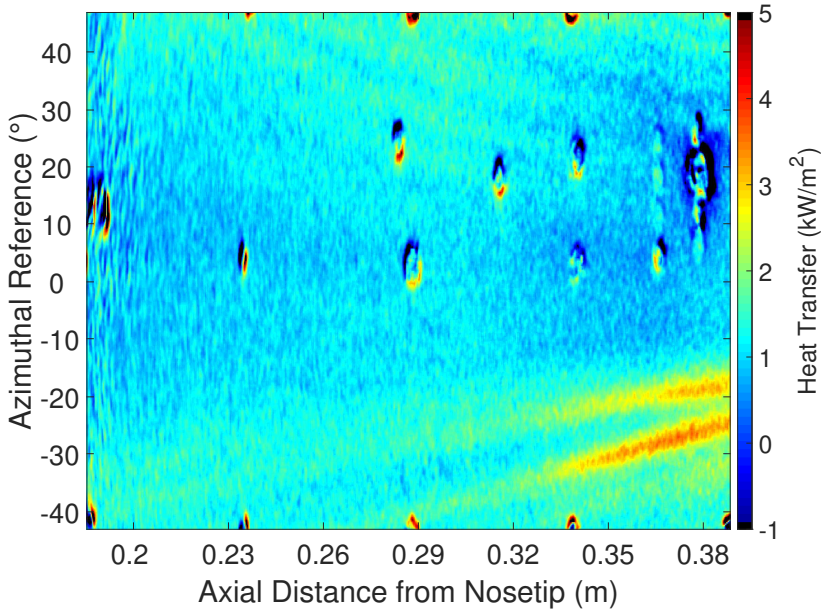

(b) Run 417.

Figure 5.53. Unwrapped images of two runs done at the same conditions. 203 μm insert (#7). Approximate run conditions are $T_{w,i} =$ 303 K, Re $= 7.9 \times 10^6$/m , $p_0 = 101.9$ psia, $T_0 = 420$ K.

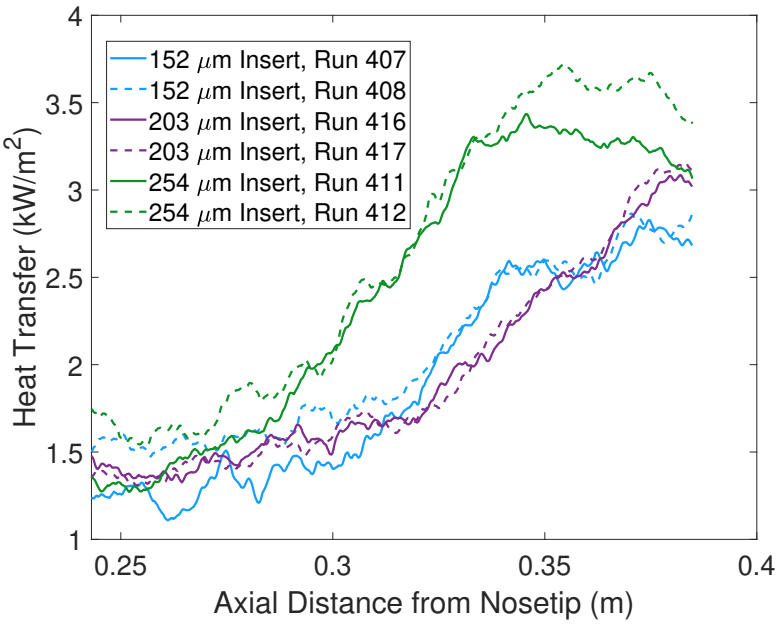

(a) Heat transfer along leeward streaks.

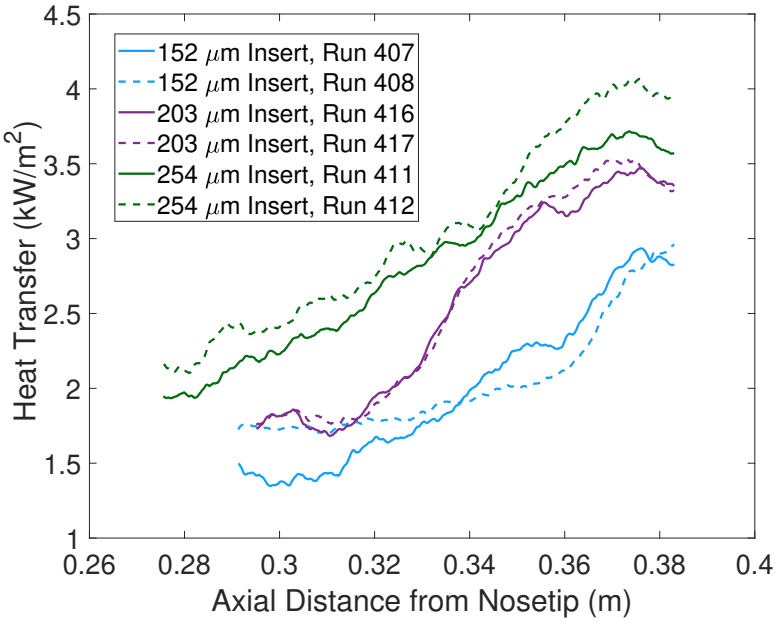

(b) Heat transfer along windward streaks.

Figure 5.54. Heat transfer along the leeward and windward streaks for runs in Figure 5.53 as well as 2 more sets of runs done with 2 other roughness inserts. Approximate run conditions are $T_{w,i}$ = 302 K, Re = 8.0×10^6/m , p_0 = 102.9 psia, T_0 = 420 K.

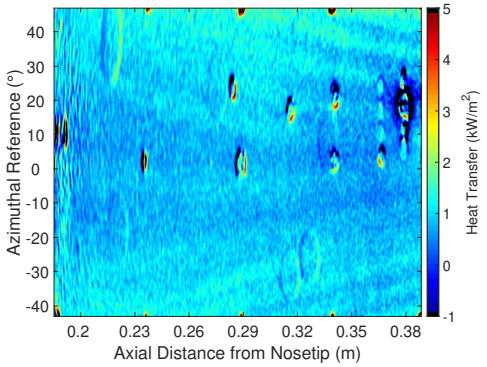

(a) Run 410. 50.8 μm insert (# 3).

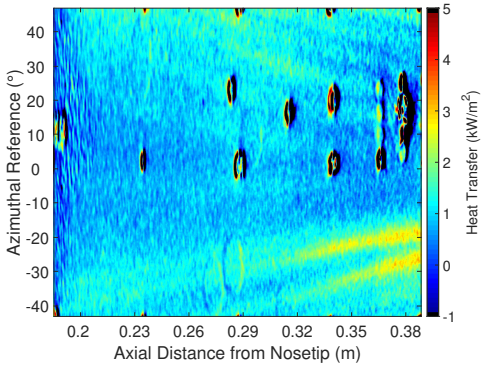

(b) Run 407. 152 μm insert (# 6).

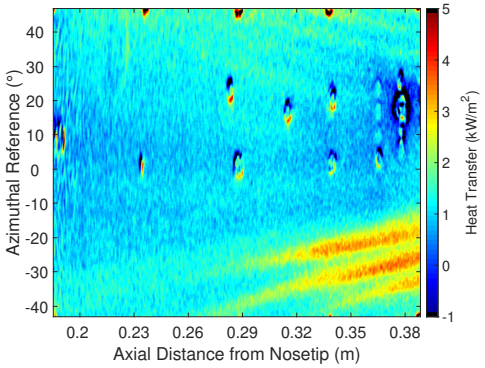

(c) Run 411. 254 μm insert (# 8).

Figure 5.55. Unwrapped TSP image of runs done with different roughness inserts. Approximate run conditions are $T_{w,i}$ = 301 K, Re = 8.5×10^6/m , p_0 = 110.3 psia, T_0 = 421 K.

μm, and 254 μm insert. It is easy to see that as the height of the utilized roughness elements increases, the streaks grow stronger and their growth moves upstream.

It should also be noted that there was only one detectable streak from the 102 μm insert case. Thus, it is challenging to know with certainty which roughness element it originated from. Figure 5.56 compares the location of the lone streak originating from the 102 μm insert with both the windward and leeward streaks originating from the 152 μm and 203 μm roughness inserts.

Figure 5.56 shows the streak from the 102 μm insert closer to the leeward streak than the windward streak from the other inserts. It is about 2° from the leeward

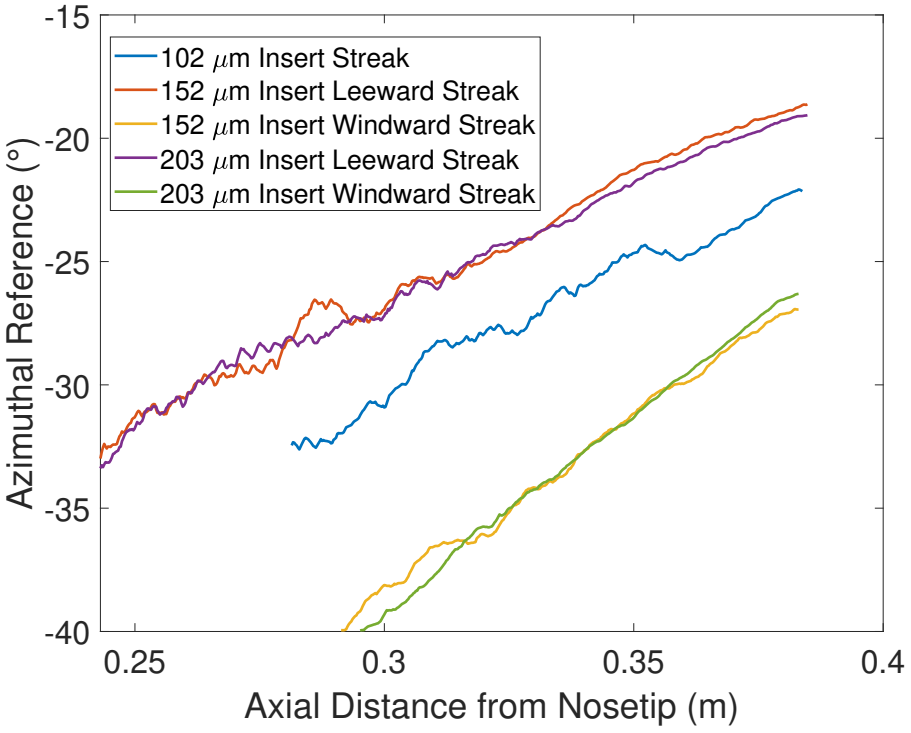

Figure 5.56. Comparing the location of the streak caused by the 102 μm insert (# 5) to the location of the windward and leeward streak casued by other inserts. Approximate run conditions are $T_{w,i} = 302$ K, Re $= 8.0 \times 10^6$/m , $p_{o0} = 103.2$ psia, $T_0 = 420$ K.

streaks but about 6° from the windward streaks. Also, Figure B.4 in the appendix shows the most leeward element of the 102 μm insert to be slightly shifted towards the wind ray when compared to the location of the most leeward elements of the 152 μm and 203 μm inserts which are shown in Figures B.5 and B.6 respectively. This may account for the slight shift of the steak in Figure 5.56. Thus, this streak will be compared with the leeward streaks from the other roughness inserts, but it should be noted that it can not be shown with certainty that it is in fact originating from the same roughness element as the other streaks.

The heat transfer along the leeward and windward streak for each roughness insert was then analyzed and compared. This is shown in Figures 5.57(a) and 5.57(b)

respectively. Note that the line for each insert is an average of 2 runs except the 104 μm insert which is only 1 run. For the leeward streaks, the streak caused by the 254 μm roughness element starts to grow the furthest upstream. The streak originating from the 203 μm roughness and 152 μm roughness elements start to grow at the same axial location. It is unclear which streak of the 2 starts to grow farther upstream. It is unsure why the leeward streak caused by the 203 μm roughness does not start to grow farther upstream than that from the 152 μm roughness, but this behavior seems to mimic the trend seen in Figure 5.51 which was a similar plot in which runs were done with a 3 hour cooling period in between. This seems to imply that this can be explained by slight machining errors. The streak from the 102 μm insert starts to grow downstream of the streaks from the 3 inserts with taller elements. Finally, there is no measurable streak from the 50.2 μm roughness insert, suggesting that the roughness height was too small to cause a noticeable disturbance.

Figure 5.57(b) displays a clearer trend for the windward streak. As the roughness element height increases, the appearance and growth of the streak moves farther upstream. However, there do not seem to be discernible streaks from the 102 μm or 50.2 μm inserts. As previously stated,"streak" heat transfer data obtained in these cases were mainly just noise to illustrate the absence of a detectable streak.

It is also interesting to compare the streak heat transfer when a different SB was used for calibration. For simplicity, the SB that was previously used will be labeled SB # 1 and the other SB will be labeled SB # 2. SB # 2 was placed at an axial location of 0.3131 m from the nosetip and 15.46° above the lee ray. Figure 5.58 compares unwrapped TSP images captured using the 254 μm insert and calibrated utilizing different SBs.

At first glance, although the heat transfer along the streaks do not show much change, the heat transfer near the lee ray seems to have changed. This is likely due to the lower values of heat transfer in these areas, where the magnitude is close to the noise floor. To better illustrate the difference in streak heat transfer, Figure 5.59 shows the streaks in Figure 5.57, with the TSP calibrated using SB # 2. Although

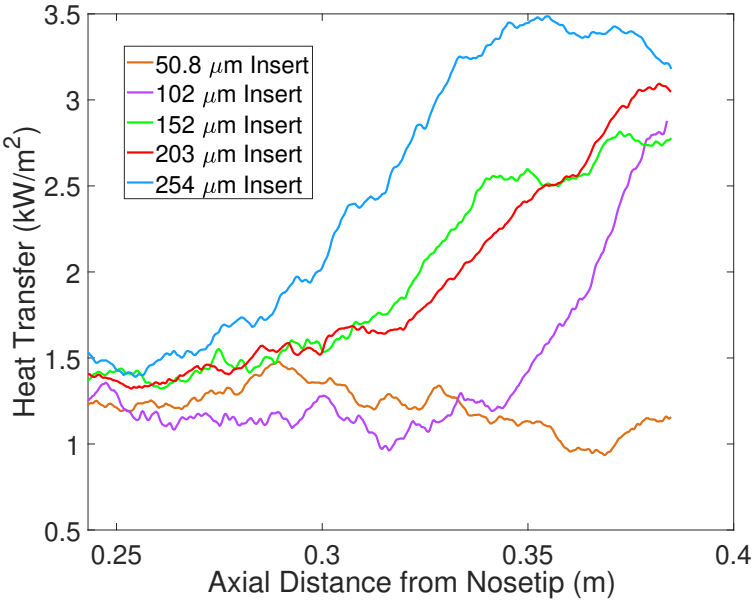

(a) Heat transfer along leeward streaks.

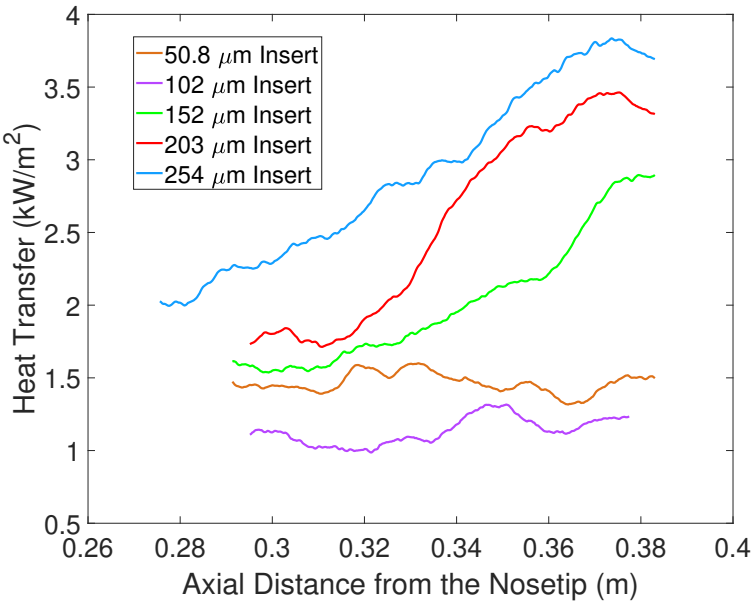

(b) Heat transfer along windward streaks.

Figure 5.57. Heat transfer along the leeward and windward streak for runs performed at the same condition with different roughness inserts. Each line is averaged from 2 runs, except the 102 μm insert case which is obtained from 1 run. Approximate run conditions are $T_{w,i} = 302$ K, Re $= 8.0 \times 10^6$/m, $p_0 = 102.8$ psia, $T_0 = 420$ K.

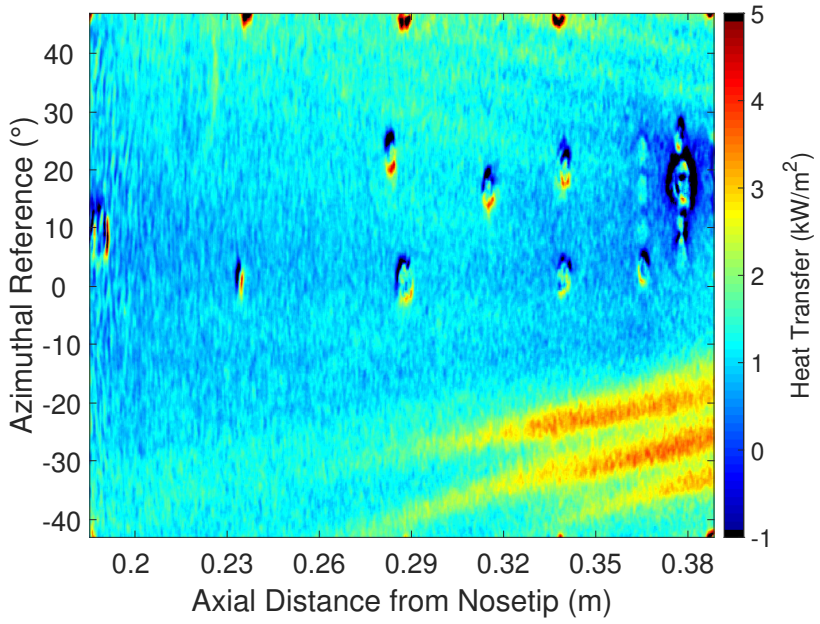

(a) SB # 1.

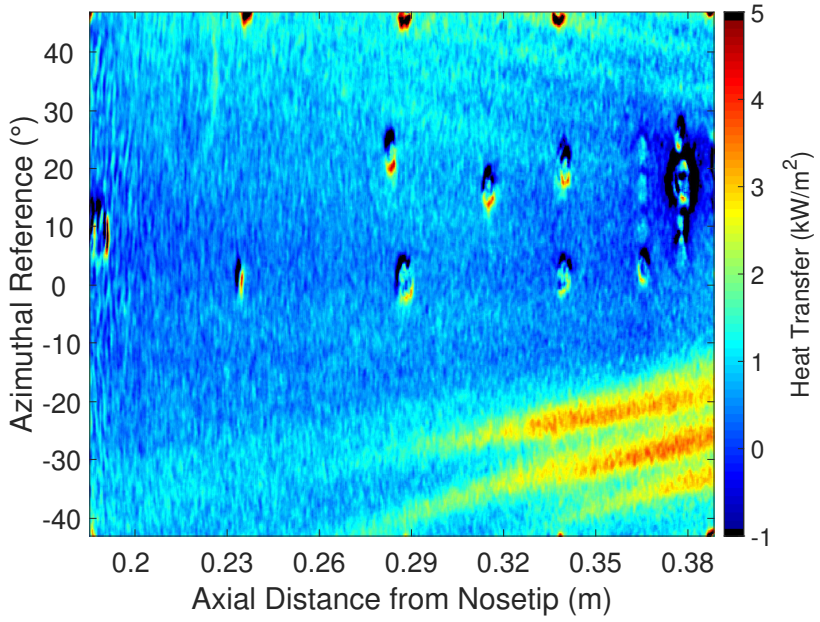

(b) SB # 2.

Figure 5.58. Unwrapped TSP images calibrated using 2 different SBs. 254 μm insert. (# 8). $T_{w,i}$ = 302 K, Re = 8.0×10^6/m , p_0 = 102.8 psia, T_0 = 420 K. Run 411.

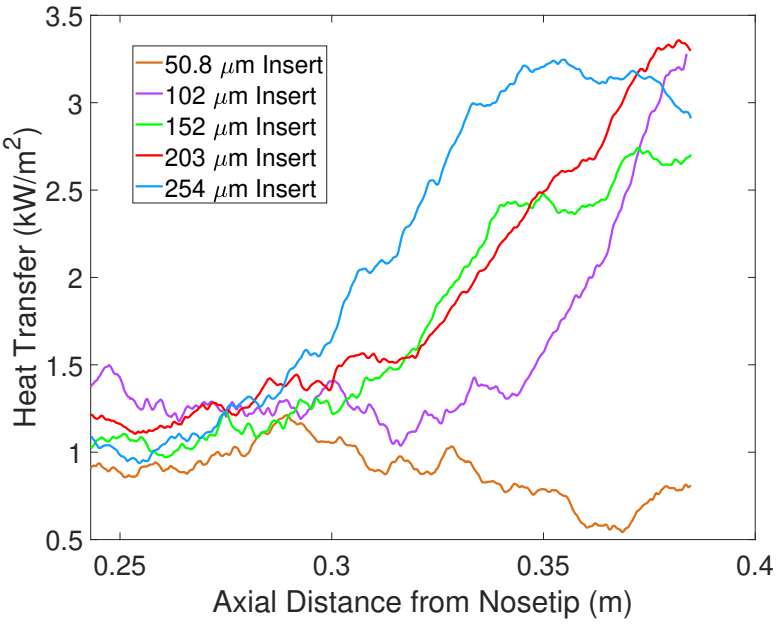

(a) Heat transfer along leeward streaks.

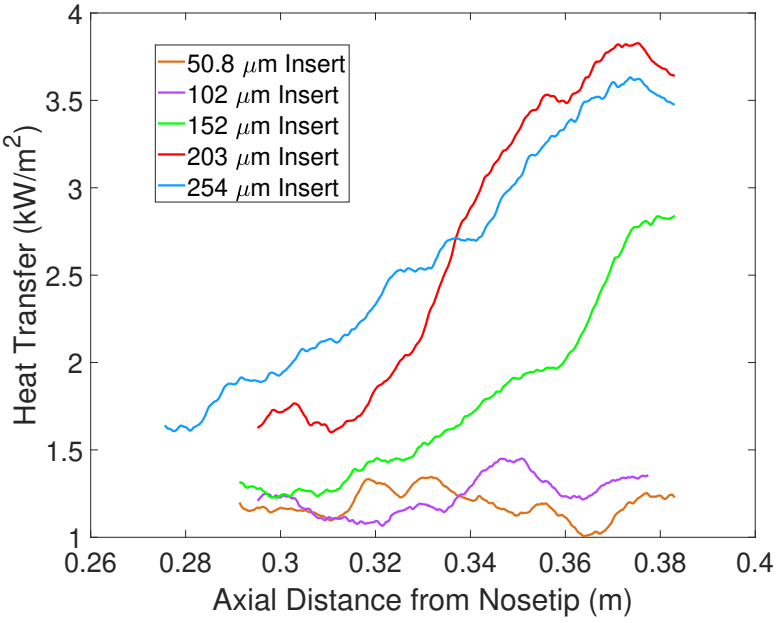

(b) Heat transfer along windward streaks.

Figure 5.59. Heat transfer along the same leeward and windward streaks as in Figure 5.57(a) with the TSP calibrated using a different SB.

there are some slight differences between Figures 5.59 and 5.57, the same trend is generally observed. The main differences, which occur in the windward streak, are the slight increase in the heat transfer for the 203 μm insert case and the slight decrease in the heat transfer for the 152 μm insert case.

5.4.2 Effect of Freestream Reynolds Number on Streaks

It is also interesting to compare the change in the observed streaks due to a small change in the freestream Reynolds number. Initially, this was attempted by analyzing the flow a second later into the run, where the stagnation pressure would have dropped. However, Figure 5.60 shows 2 different runs performed with the same initial conditions except for the initial stagnation pressure. Thus, to make sure Figure 5.60(b) had the same freestream Reynolds number, these data were processed 2.2 seconds into the run instead of 1 second like in Figure 5.60(a).

The difference between the images is large. It seems that analyzing the data at a time further into the run to account for the different initial conditions may not provide an accurate analysis of a freestream Reynolds number change. Shown in Figure 5.61 is the heat transfer along the leeward and windward streak for both images. There is a clear difference in the heat transfer between the different runs even though the stagnation conditions are supposedly the same. To emphasize the difference in heat transfer, Table 5.5 shows the heat transfer from the SB and stagnation conditions for these 2 runs and 4 others. The SB was averaged 40 samples before and after desired process times.

The difference in heat transfer for the same stagnation pressure and freestream Reynolds number but different times during a run is possibly due to the surface of the paint layer being a different temperature. It may also be due to the drop in stagnation temperature. Note that the stagnation temperature difference was 10 K.

Because it was unknown what was causing this difference in heat transfer, sets of runs were done with only a slight difference in initial conditions and the runs were

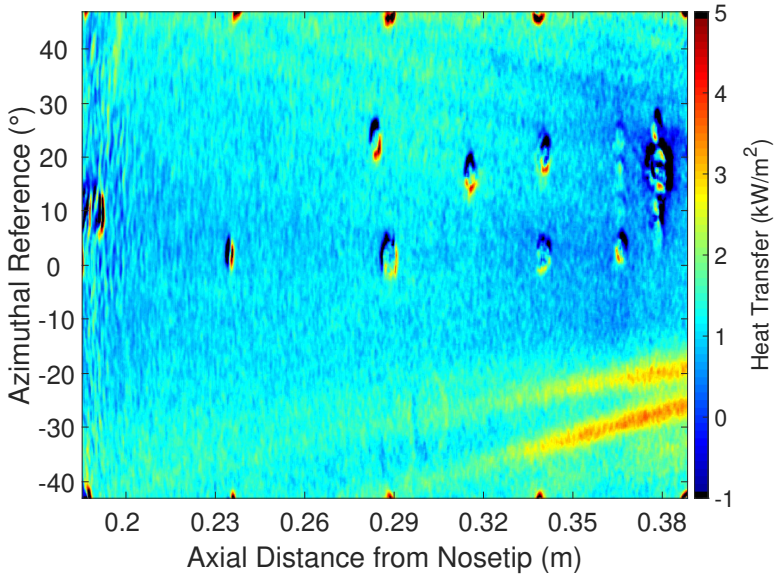

(a) $p_{o,i} = 109.7$ psia, $T_{w,i} = 302$ K Re $= 7.9 \times 10^6$/m , $p_0 = 102.0$ psia, $T_0 = 420$ K. Time $= 1.0$ seconds. Run 416.

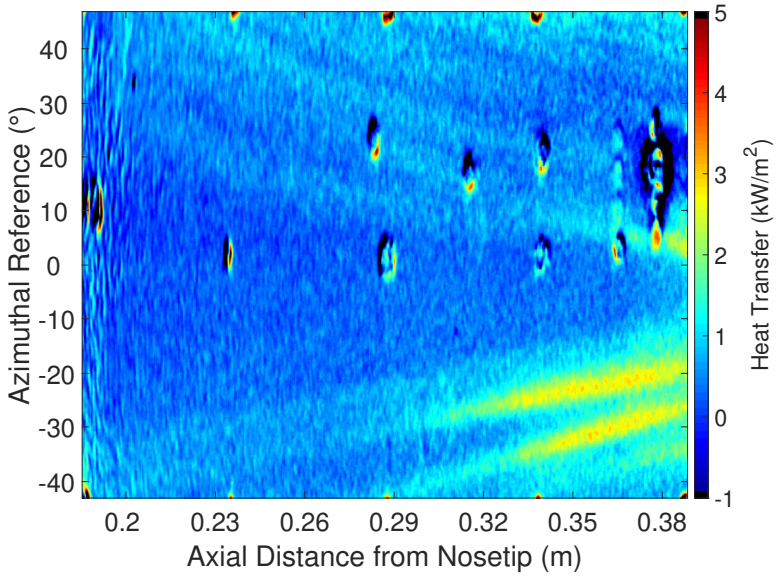

(b) $p_{o,i} = 118.7$ psia, $T_{w,i} = 301$ K Re $= 8.1 \times 10^6$/m , $p_0 = 101.8$ psia, $T_0 = 410$ K. Time $= 2.2$ seconds. Run 427.

Figure 5.60. Unwrapped TSP image showing the heat transfer for 2 runs at the same freestream Reynolds number but done with a different initial stagnation pressure. 203 μm insert (#7).

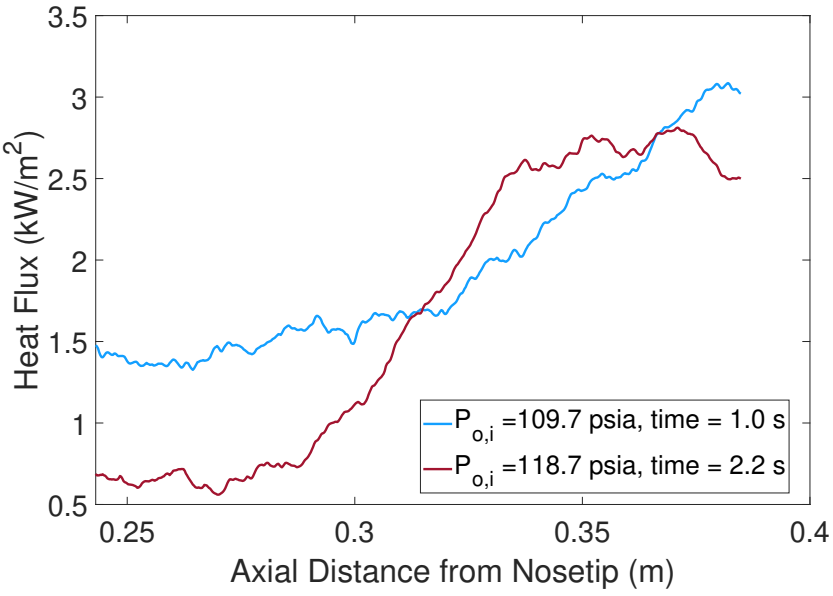

(a) Heat transfer along leeward streaks.

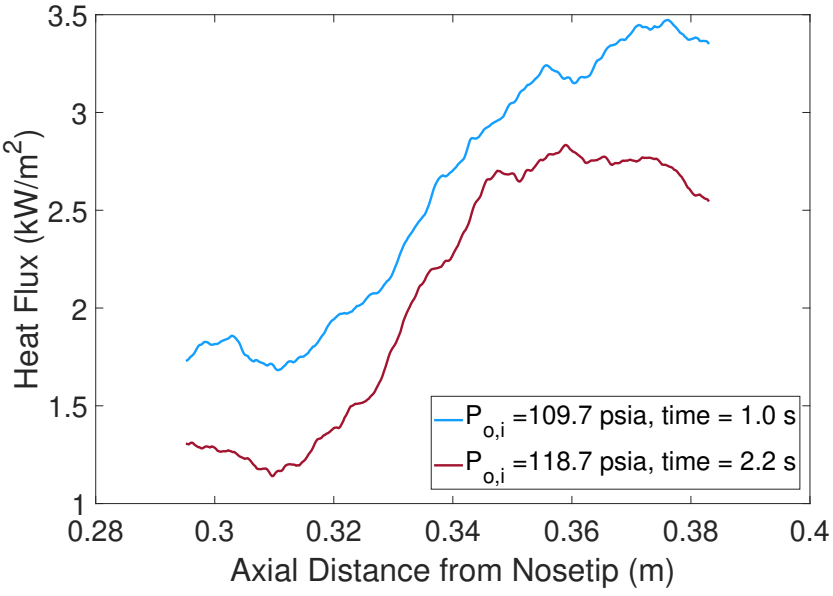

(b) Heat transfer along windward streaks.

Figure 5.61. Heat transfer along leeward and windward streaks in Figure 5.60.

Table 5.5. SB data averaged 40 samples before and 40 samples after the desired process time.

Roughness Insert #	**time (s)**	P_o **(psia)**	$\mathbf{Re}_\infty(\frac{1}{m})$	**Heat Transfer from SB (kW/m^2)**
6	2.2	103.15	8.3×10^6	0.75
6	1.0	104.37	8.1×10^6	1.31
7	1.0	101.76	8.2×10^6	0.55
7	1.0	102.04	7.9×10^6	1.52
8	2.2	101.93	8.2×10^6	0.80
8	1.0	102.78	8.0×10^6	1.33

processed at the same time. The time was chosen to be 1.8 second as this was far enough into the run to preclude any tunnel startup contamination, and early enough to avoid the tunnel unstart process due to the end of the run. It should be noted that this time was somewhat arbitrary and does not have any specific significance. Shown in Figure 5.62(a) and 5.62(b) are the unwrapped heat transfer images of a run using the 254 μm insert (#8) with a stagnation pressure of 100.0 psia, and one with a stagnation pressure of 106.8 psia respectively. The following images were calibrated using an SB 0.3635 m from the nosetip and 2.76° from the lee ray as this was deemed the safest place on the cone devoid from streaks. Note the slight qualitative difference between the images in Figure 5.62. The streaks are stronger in the second image.

To further illustrate the effect of the freestream Reynolds number, Figure 5.63 displays the unwrapped TSP images of runs using the 203 μm insert (#8) with a stagnation pressure of 100.0 psia and 107.0 psia. Again, the same qualitative trend is seen regarding the heat transfer along the streaks. Also, note that the streaks are weaker than those in Figure 5.62 because the roughness elements utilized were weaker. Spanwise cuts of the TSP images in Figure 5.62 and 5.63 are shown in Figure 5.64(a) and 5.64(b) respectively. Note that the axial location of the spanwise cut for the runs performed with the 253 μm is 0.32 m, while it is 0.34 m for the runs performed with the 203 μm insert. This is because the 253 μm insert runs had already started to

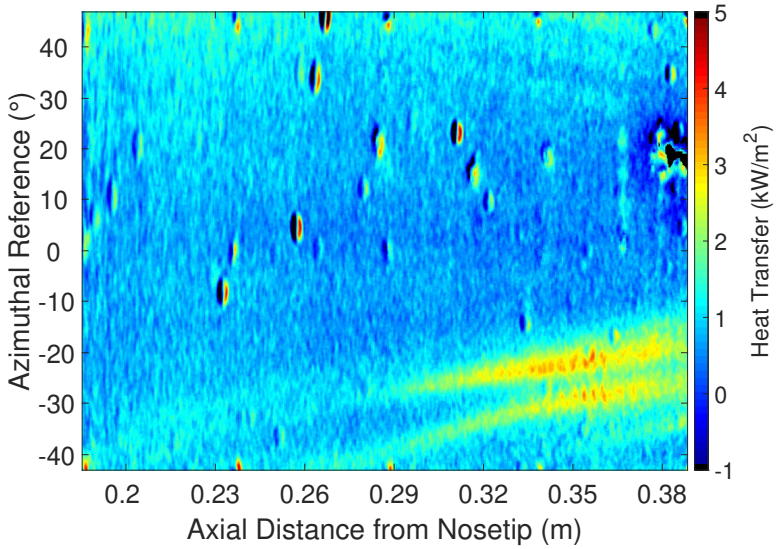

(a) $T_{w,i}$ = 299 K Re = 7.9×10^6/m , p_0 = 100.0 psia, T_0 = 416 K. Time = 1.8 seconds. Run 512.

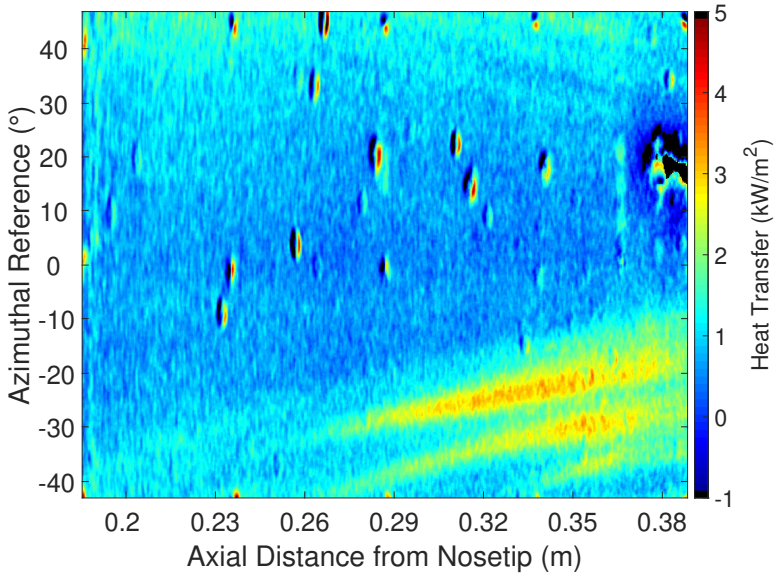

(b) $T_{w,i}$ = 299 K Re = 8.4×10^6/m , p_0 = 106.8 psia, T_0 = 415 K. Time = 1.8 seconds. Run 511.

Figure 5.62. Effect of small freestream Reynolds number changes on heat transfer. 254 μm insert (#8).

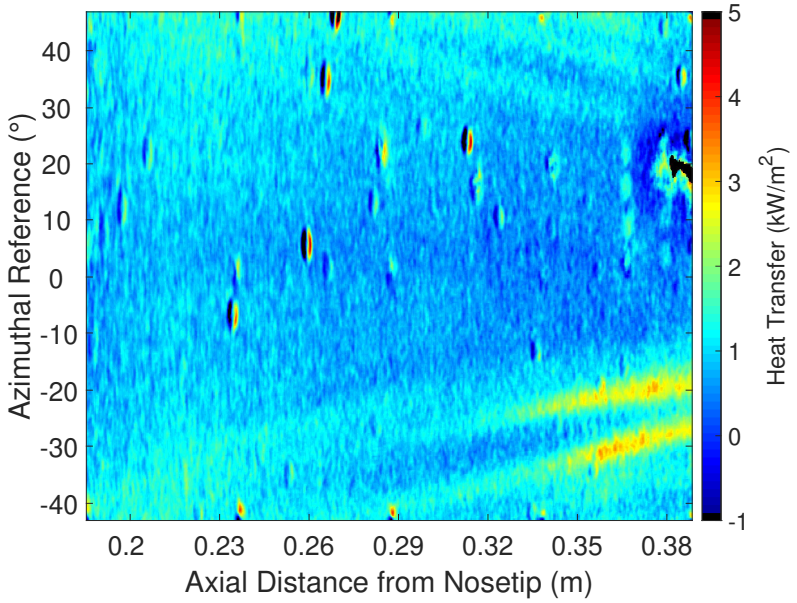

(a) $T_{w,i} = 297$ K Re $= 7.9 \times 10^6$/m , $p_0 = 100.0$ psia, $T_0 = 415$ K. Time = 1.8 seconds. Run 509.

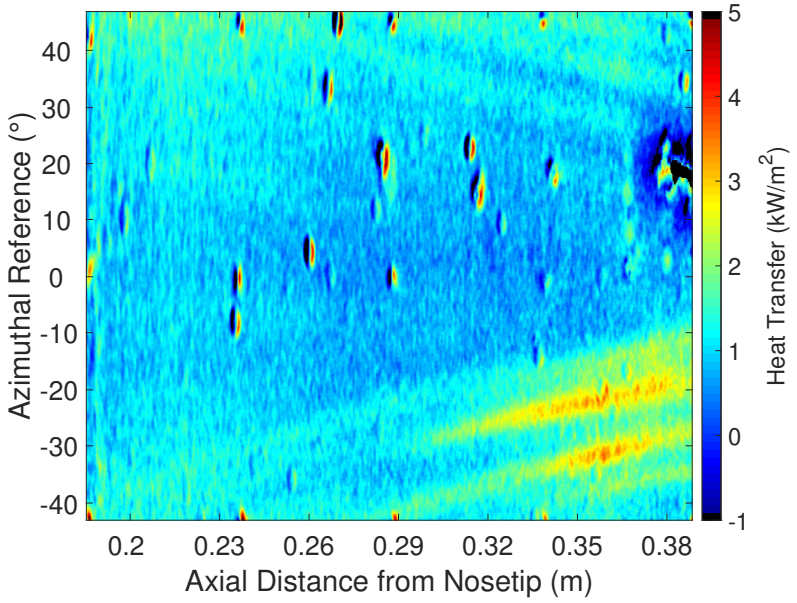

(b) $T_{w,i} = 299$ K Re $= 8.5 \times 10^6$/m , $p_0 = 107.0$ psia, $T_0 = 415$ K. Time = 1.8 seconds. Run 510.

Figure 5.63. Effect of small freestream Reynolds number changes on heat transfer. 203 μm insert (#7).

peak by 0.34 m, so an axial location farther upstream was chosen to better illustrate the effect of the freestream Reynolds number change.

One more set of runs was completed with the 152 μm insert. The heat transfer along the leeward and windward streaks for runs performed with all 3 roughness inserts are shown in Figure 5.65(a) and Figure 5.65(b) respectively.

For all three roughness inserts, as the freestream Reynolds number increases, the growth of both streaks moves farther upstream. This is consistent with expected behavior [12] and implies good control over the streaks. Additionally, although it is not the focus of this plot, the growth of either streak moves farther upstream as the roughness height is increased while the stagnation pressure is kept constant.

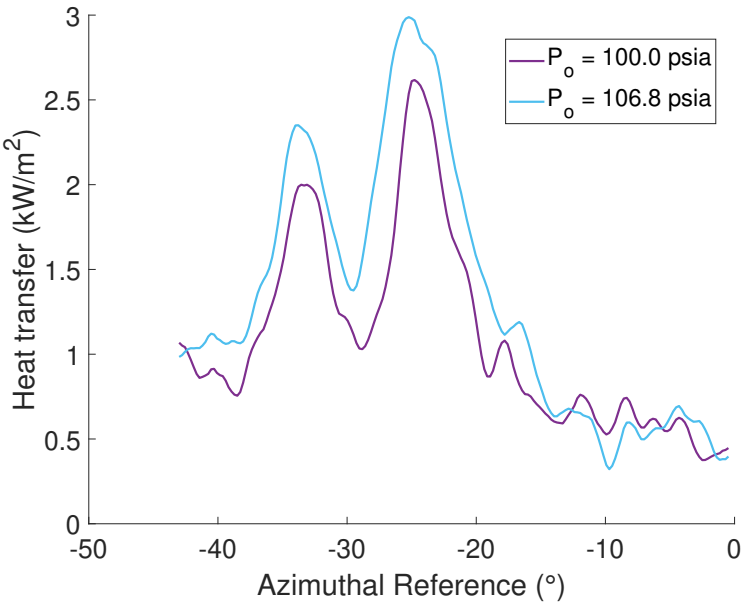

(a) Spanwise cut at an axial location of 0.32 m. 253 μm insert (# 8).

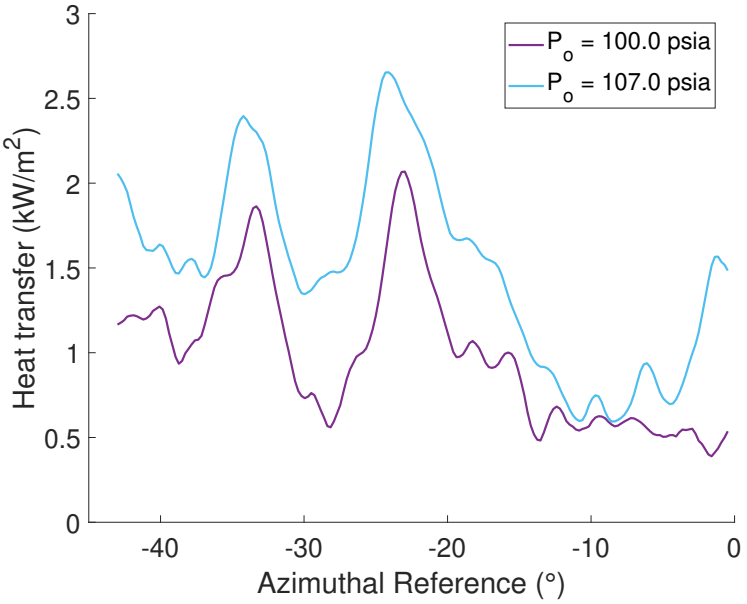

(b) Spanwise cut at an axial location of 0.34 m. 203 μm insert (# 7).

Figure 5.64. Spanwise cut of heat transfer of images in Figure 5.62 and 5.63, displaying effect of small freestream Reynolds number changes on heat transfer.

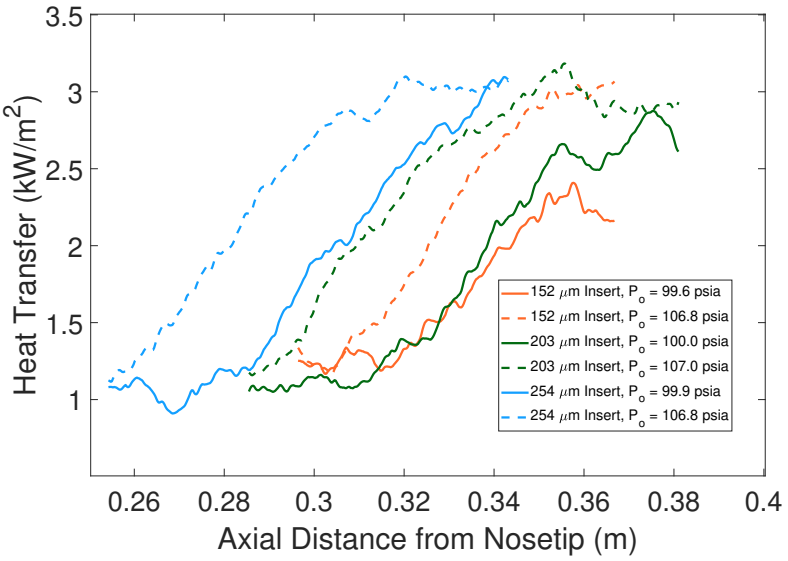

(a) Leeward streaks.

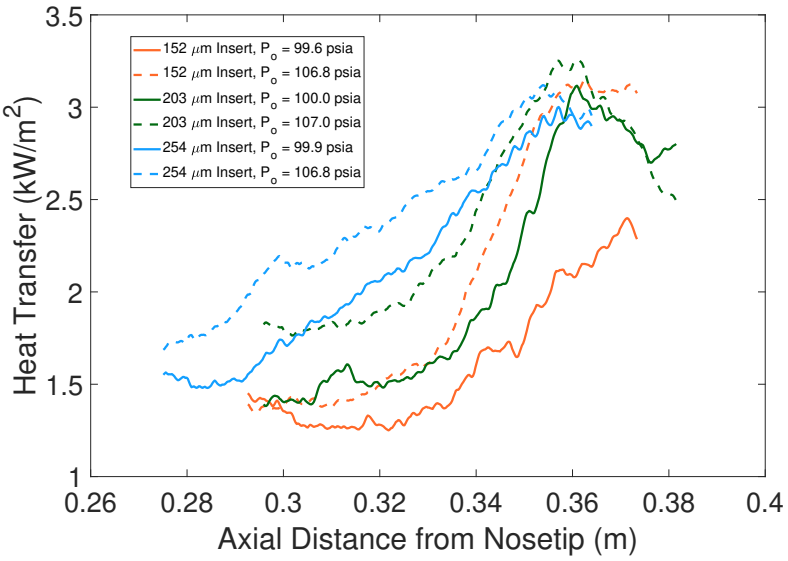

(b) Windward streaks.

Figure 5.65. Heat transfer along leeward and windward streaks for runs in Figures 5.62 and 5.63 and 1 more set of runs. Runs 509-514.

The change in heat transfer along the streak caused by the change in Reynolds number can be used to analyze the peaks seen in the streak. As previously stated, it is unsure whether these ubiquitous peaks are due to the saturation of the stationary crossflow or if the flow has already transitioned. And, because no pressure sensors were used along the streaks, there is no PSD spectra to use as a gauge for transition. However, recall that the Stanton number is proportional to the inverse of square-root of the freestream Reynolds number in laminar flow. Turbulent data, on the other hand, scales according to Equation 5.1 [12].

$$St \sim Re_{\infty}^{-1/5} \tag{5.1}$$

Thus, the heat transfer data along the windward streak for the 6 runs in Figure 5.65 were scaled using both the laminar and turbulent scaling in an effort to better characterize the heat transfer. This is shown in Figure 5.66. If the heat transfer was laminar or turbulent, we would expect data using the same roughness insert to collapse using the laminar or turbulent scaling respectively. Unfortunately, none of the data truly collapses using either scaling, so it is not possible to draw any conclusions from these images. Thus, it should be kept in mind that it is unclear if the peaks in the stationary crossflow streaks are due to saturation or not.

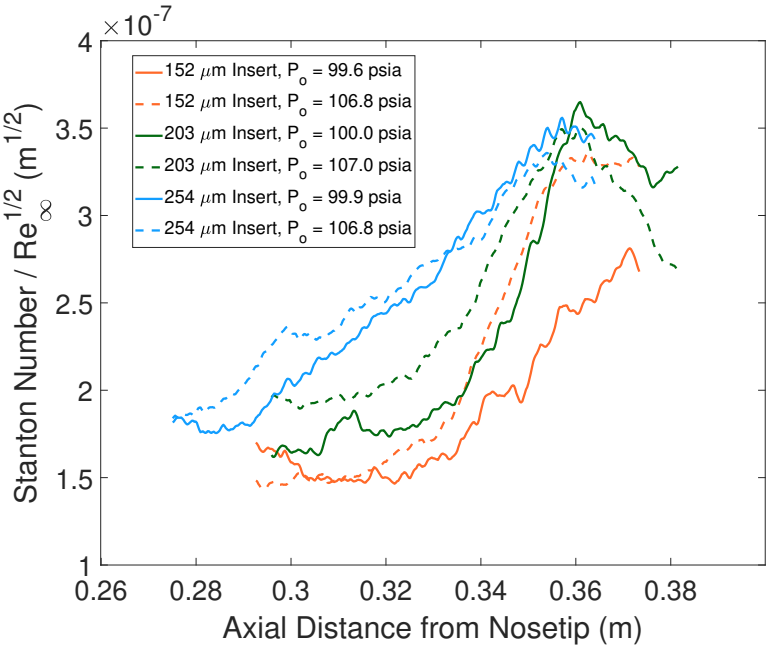

(a) Laminar scaling.

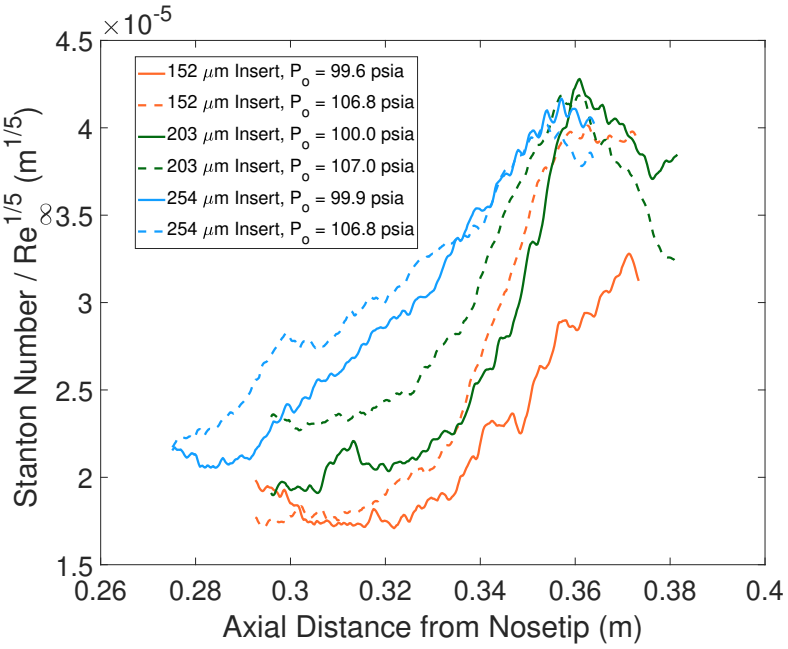

(b) Turbulent Scaling.

Figure 5.66. Scaled Stanton number along windward streaks in Figure 5.73(b). Runs 509-514.

5.5 Amplitude of Stationary Crossflow

5.5.1 Amplitude Definition

Once the heat transfer along the streak was obtained, a stationary crossflow amplitude was sought. Initially, Equation 5.2, proposed by Edelman [6], was used in an effort to non-dimensionalize the heat transfer. This amplitude definition will be given a subscript of "a".

$$Amplitude_a = \frac{q_{max} - q_{min}}{0.5(q_{max} + q_{min})} \tag{5.2}$$

Note that q_{max} is the heat transfer along the streak while q_{min} is the heat transfer along an adjacent trough. This is visualized in Figure 5.67(a) which displays an unwrapped TSP image along with a red and purple line marking the streak and the adjacent trough respectively. The windward trough was chosen to avoid the lee ray. Note that the purple line is found using the same algorithm as the red line with the targeted value being a minimum in heat transfer instead of a maximum. Figure 5.67(b) shows a spanwise cut at different axial locations. The peaks have been circled in red, and the troughs have been circled in blue.

Figure 5.68(a) shows the heat transfer along streak and trough in Figure 5.67 as well as 2 other runs with approximately the same stagnation conditions, while Figure 5.68(b) displays the calculated amplitude using Equation 5.1. The heat transfer along the minimum is also fairly repeatable downstream of the location it starts to grow. However, note that the amplitudes do not show the typical amplitude growth pattern seen in other literature. Besides the clear repeatability problem upstream of 0.3 m, there is barely any axial growth, and the amplitude peaks upstream of the peak in the streak heat transfer. A quick look at Figure 5.67(a) illustrates that this is because of the similar growth rate between q_{max} and q_{min}. The amplitude for every roughness insert shows approximately the same trend using this definition. This may be due to lateral conduction on the surface of the model or poor TSP spacial resolu-

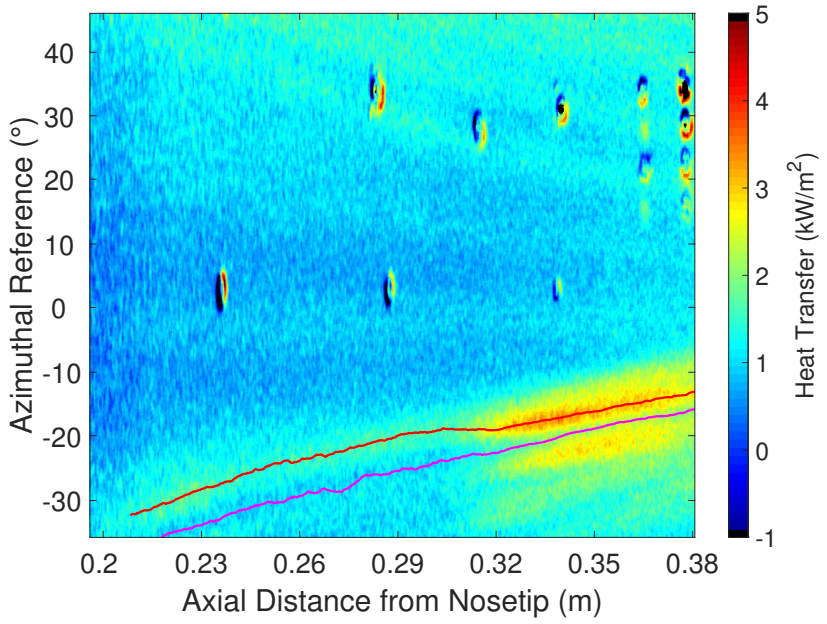

(a) Unwrapped TSP image illustrating the extracted heat transfer along the trough.

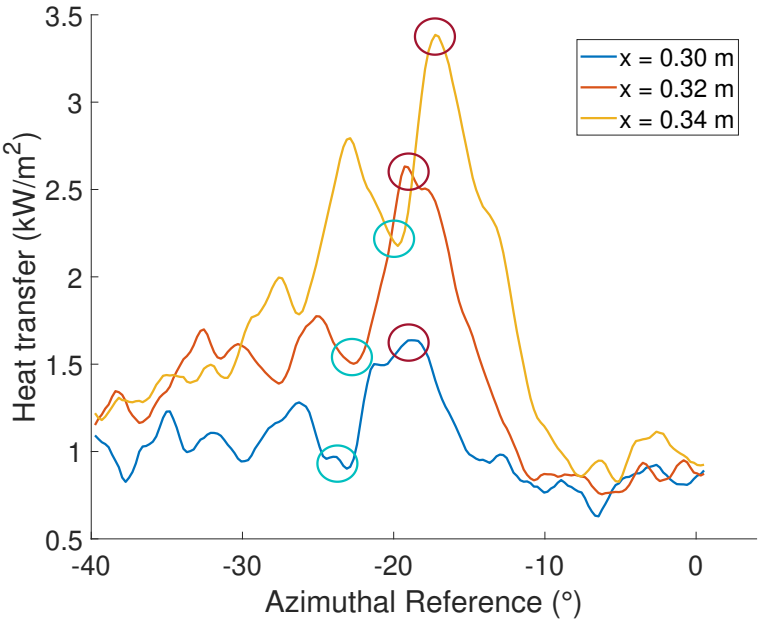

(b) Spanwise cut at several axial locations displaying the peak and trough of the leeward streak.

Figure 5.67. Extracting the trough adjacent to the streaks. 152 μm insert (# 6). $T_{w,i}$ = 303 K, Re = 8.5×10^6/m , p_0 = 110 psia, T_0 = 419 K. Run 209.

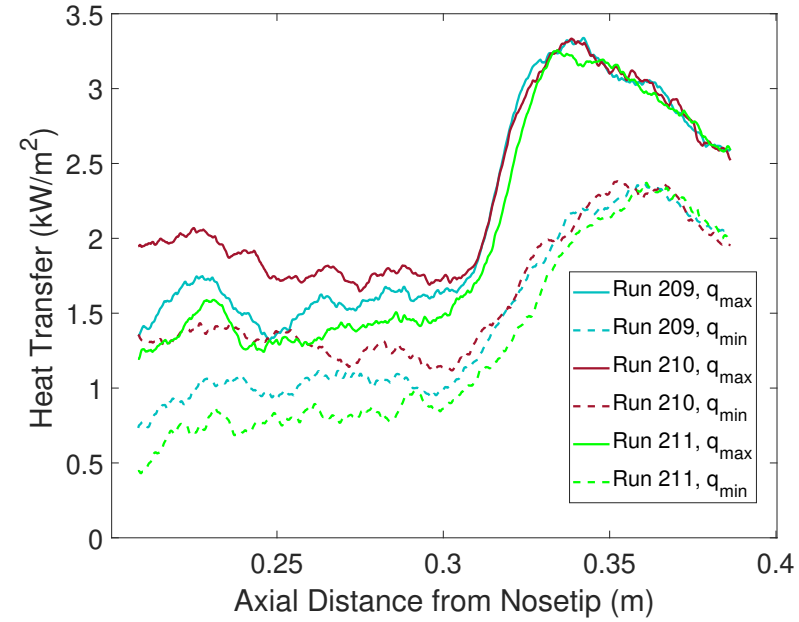

(a) Heat transfer along leeward streaks and adjacent troughs.

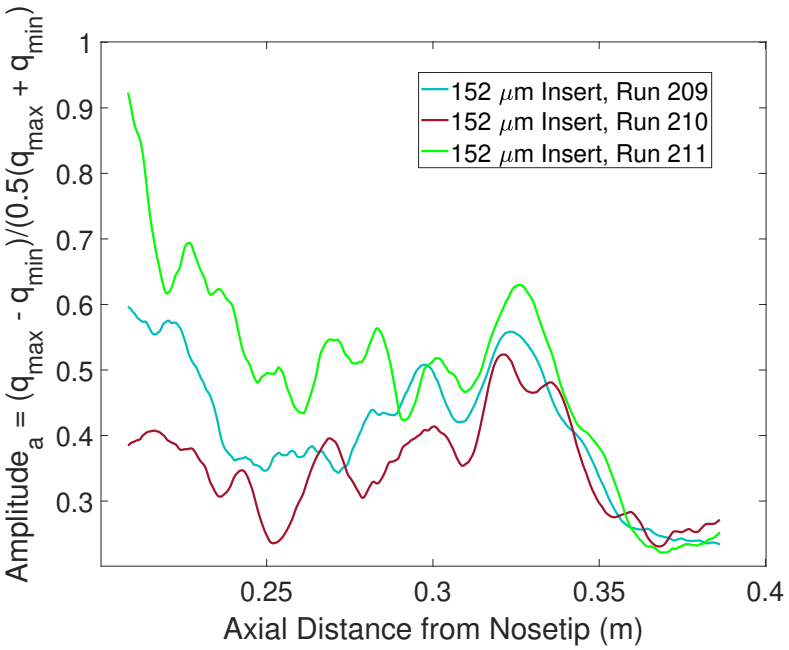

(b) Amplitude along leeward streaks.

Figure 5.68. Amplitude of the leeward streak for the run in Figure 5.67 and 2 other runs performed at the same stagnation conditions. 152 μm insert (# 6). Approximate run conditions are $T_{w,i}$ = 302 K, Re = 8.5×10^6/m, p_0 = 109.2 psia, T_0 = 420 K.

tion. It may also be representative of the actual growth of the minimum between the streaks. In any case, it shows that a different definition is needed.

The amplitude was then calculated in a different way using a method similar to Ward [12]. The equation is repeated here for clarity. This amplitude definition will be given a subscript of "b".

$$Amplitude_b = \frac{q_{max} - q_{th}}{q_{th}} \tag{5.3}$$

However, instead of defining q_{th} as the theoretical heat transfer on a 7° half-angle cone at a 0° angle of attack as Ward did, q_{th} is defined as the mean-flow heat transfer solution for the same cone at a 6° angle of attack. Note that the theoretical value is calculate at the nominal azimuthal location of the respective streak for each axial location. The theoretical heat transfer was calculated using the Stanton number which was found using the procedure described in Section 4.7. Figure 5.69(a) displays the heat transfer along the streak in addition to the theoretical heat transfer at the nominal streak locations. Figure 5.69(b) shows the amplitude, calculated using Equation 5.2. These data are extracted from the same leeward streaks as the ones in Figure 5.68. Recall that a 152 μm insert was used.

The amplitude shows the same trend in growth rate as the heat transfer along the streak, and its repeatability is primarily unaffected which is as expected. Because this amplitude definition shows a clearer and more intuitive trend with respect to the streaks, the stationary crossflow amplitude will subsequently be defined by Equation 5.3.

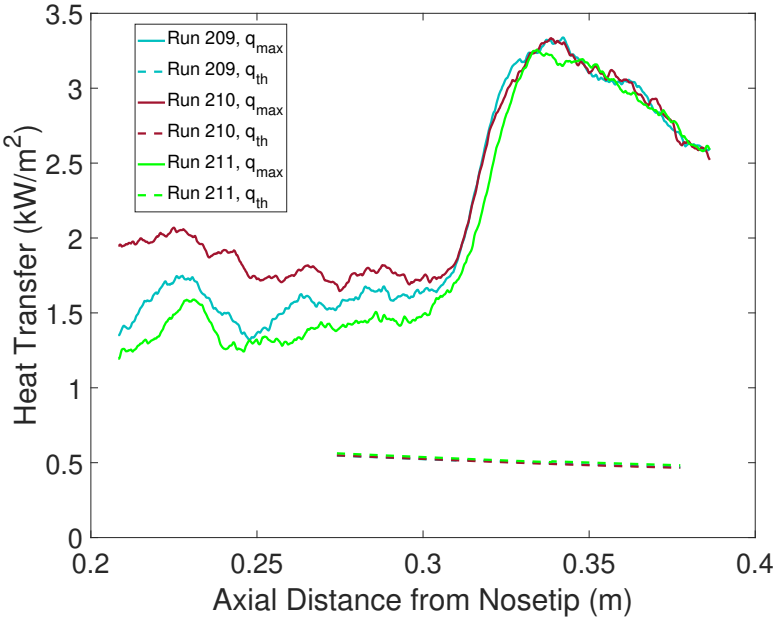

(a) Heat transfer along leeward streaks and mean-flow theoretical heat transfer at nominal streak locations.

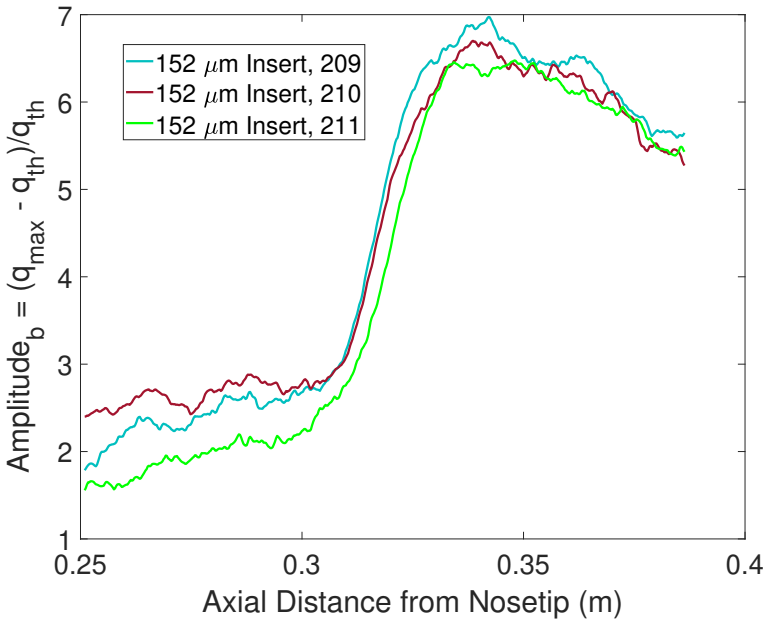

(b) Amplitude along leeward streaks.

Figure 5.69. Amplitude of the leeward streak for the run in Figure 5.67 and 2 other runs performed at the same stagnation conditions. 152 μm insert (# 6). Approximate run conditions are $T_{w,i}$ = 302 K, Re = 8.5×10^6/m, p_0 = 109.2 psia, T_0 = 420 K.

5.5.2 Effect of Roughness Height on Amplitude of Streaks

Figure 5.70 shows the amplitude along the leeward and windward streaks for runs done with different roughness inserts. These data correspond to the streaks in Figure 5.51. Recall that the closest roughness element to the lee ray was placed 52.4° from the wind ray and that each line is taken as an average from 3 runs all done at the same stagnation conditions. Note that the same trend is seen with the amplitude as with the heat transfer for different roughness element heights.

Figure 5.71 shows the amplitude along the windward and leeward streaks corresponding to Figure 5.57. Recall that the closest roughness element to the lee ray was placed 43.3° from the wind ray and that each line is taken as an average from 2 runs all done at the same stagnation conditions with the exception of the 102 μm case for which only one run was performed. Again, note that the trend is similar to the trend found with the streak heat transfer.

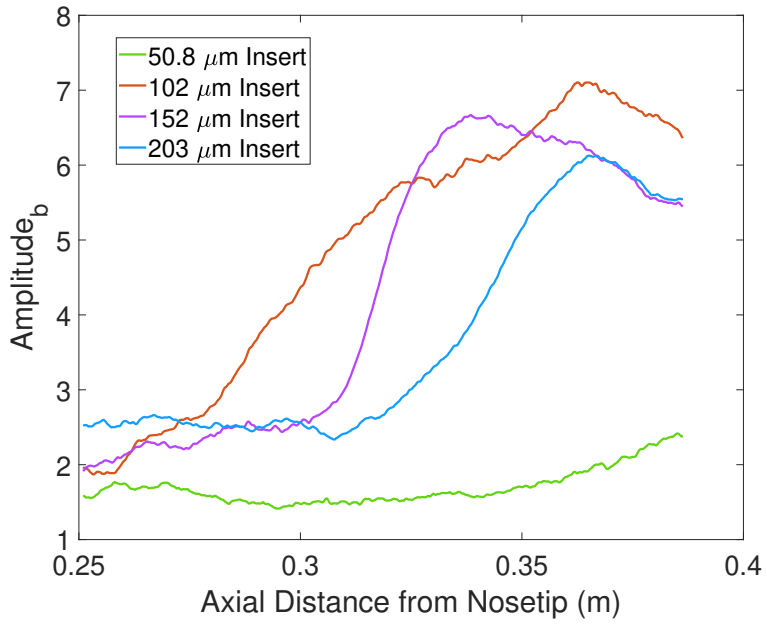

(a) Amplitude along leeward streak.

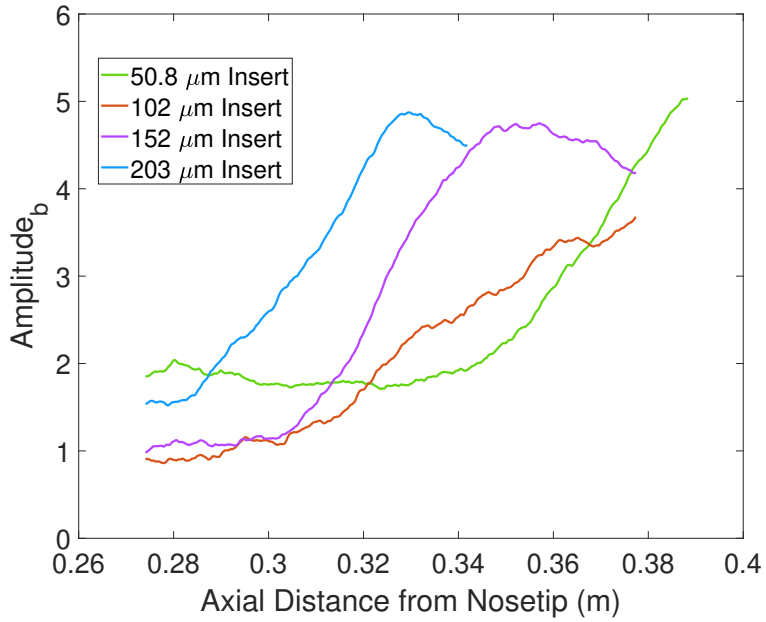

(b) Amplitude along windward streak.

Figure 5.70. Amplitude along the windward and leeward streak for different roughness inserts. Each line is averaged from 3 runs. Approximate run conditions are $T_{w,i} = 303$ K, Re $= 8.5 \times 10^6$/m , $p_0 =$ 109.0 psia, $T_0 = 420$ K.

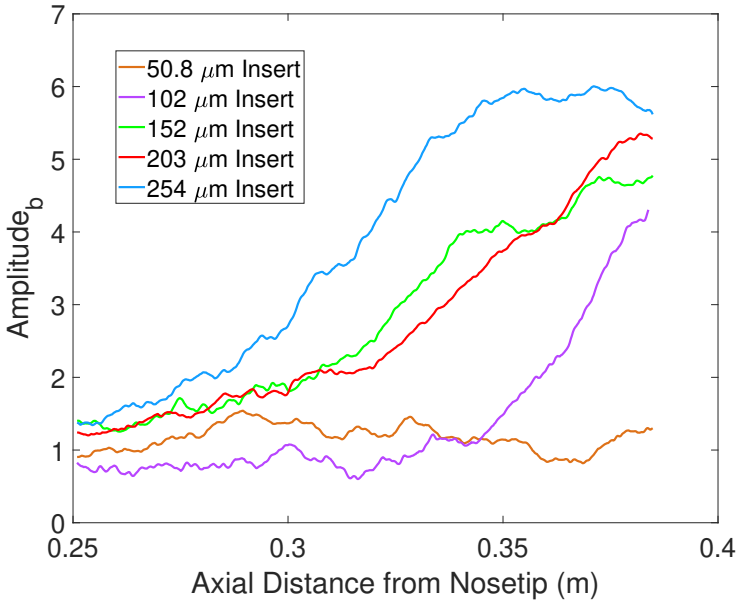

(a) Amplitude along leeward streaks.

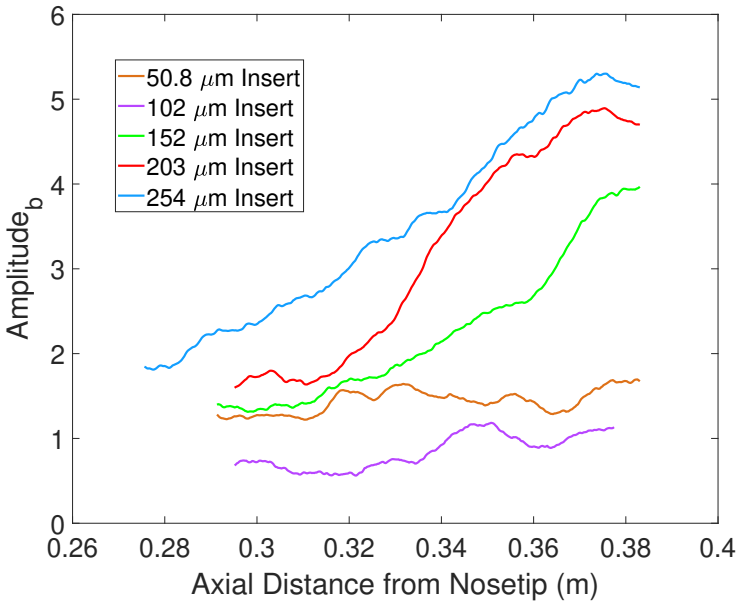

(b) Amplitude along windward streaks.

Figure 5.71. Amplitude along the leeward and windward streak for runs performed at the same condition with different roughness inserts. Each line is averaged from 2 runs, except the 102 μm insert case which is obtained from 1 run. Approximate run conditions are $T_{w,i} = 302$ K, Re $= 8.0 \times 10^6$/m, $p_0 = 102.8$ psia, $T_0 = 420$ K.

In an effort to better quantify the effect of the roughness heights on the amplitude, the amplitudes in Figure 5.71 were averaged from an axial location of 0.335 m to 0.355 m and plotted against the non-dimensional roughness height, $\frac{k}{\delta}$, for both the leeward and windward streaks. These axial locations were chosen because all the streaks were in the growth phase in this region. Figure 5.72(a) contains the amplitude data for all roughness inserts. While Figure 5.72(a) displays the amplitude data with some roughness inserts that did not cause visible streaks, Figure 5.72(b) displays the amplitude data with these inserts removed. These data are tabulated in Table 5.6, while the linear fits are given in Table 5.7. Note that Figure 5.72(b) simply has the lowest data point (with respect to the non-dimensional roughness height) for the leeward streak and the 2 lowest data points for the windward streak removed.

Table 5.6. Amplitude averages for different non-dimensional roughness heights. Data taken from Figure 5.72.

Streak	**k/δ**	**Average Amplitude from 0.335 m to 0.355 m**
Leeward Streak	0.175	1.141
Leeward Streak	0.349	1.312
Leeward Streak	0.524	3.964
Leeward Streak	0.698	3.479
Leeward Streak	0.873	5.669
Windward Streak	0.181	1.471
Windward Streak	0.362	1.030
Windward Streak	0.543	2.311
Windward Streak	0.724	3.702
Windward Streak	0.905	3.984

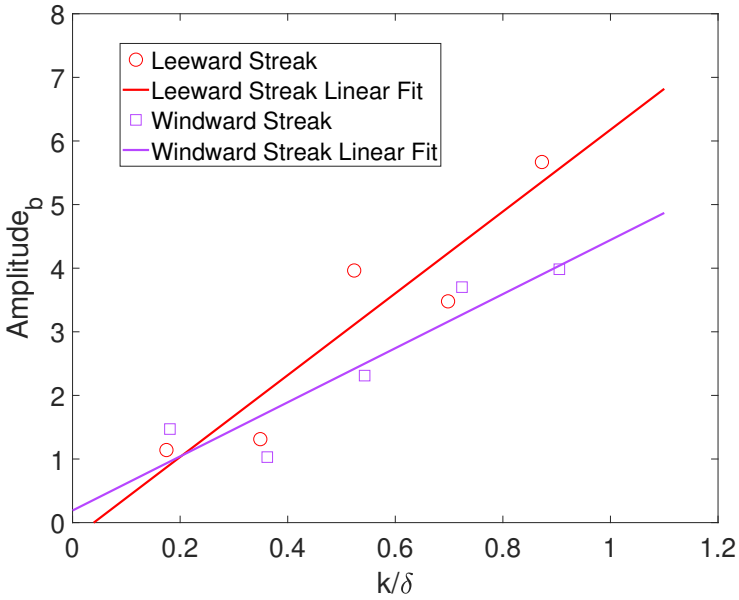

(a) Amplitude data for all roughness inserts.

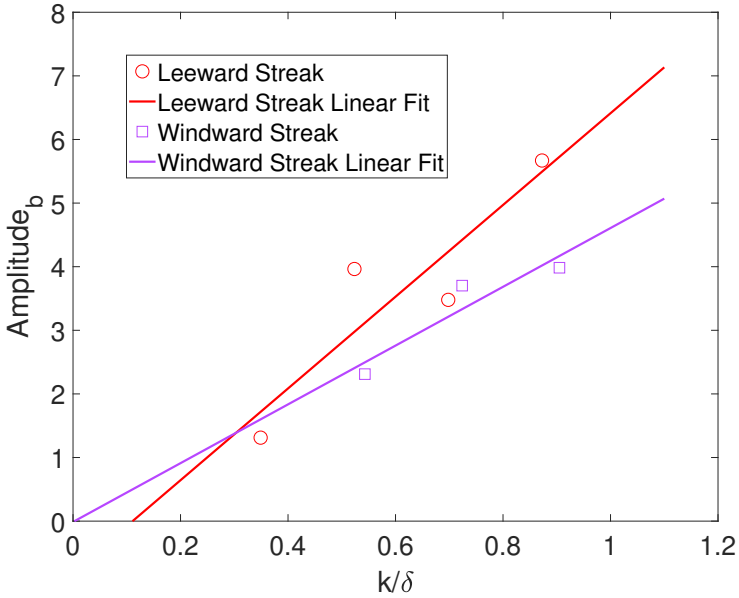

(b) Amplitude data with non-visible streaks removed.

Figure 5.72. Average amplitude from an axial location of 0.335 m to 0.355 m for different roughness inserts. Approximate run conditions are $T_{w,i} = 302$ K, Re $= 8.0 \times 10^6$/m, $p_0 = 102.8$ psia, $T_0 = 420$ K.

Table 5.7. Coefficient of linear fits for data in Figure 5.72.

Figure #	**Streak**	**Slope of Linear Fit**	**Vertical Axis Intercept of Linear Fit**
5.72(a)	Leeward Streak	6.434	-0.257
5.72(a)	Windward Streak	4.253	0.190
5.72(b)	Leeward Streak	7.212	-0.800
5.72(b)	Windward Streak	4.622	-0.014

The way amplitude is defined, it should theoretically be 0 for a $\frac{k}{\delta}$ of 0. It can be seen for both images that the vertical intercept is close to 0 when the data is approximated by a linear fit, which is a good sign that the data is linear. It should be noted that the rms deviation of the linear fits in Figure 5.72(a) is 0.62 and 0.44 for the leeward streak and windward streak respectively. In Figure 5.72(b) where the data points which did not contain a visible streak are removed, however, the rms deviations become 0.42 and 0.21 for the leeward and windward streak respectively. The growth of the windward streak better fits a linear profile. It is interesting that the the amplitude maintains a linear profile even near a $\frac{k}{\delta}$ value of 1. The average amplitude of the leeward streak increases by approximately 450 % as the roughness height is increased from 102 μm to 254 μm. Meanwhile, the average amplitude of the windward streak increases by about 200 % when the roughness height is increased from 152 μm to 254 μm.

5.5.3 Effect of Freestream Reynolds Number on Amplitude of Streaks

The amplitude along the leeward and windward streaks corresponding to Figure 5.65 are shown in Figure 5.73(a) and Figure 5.73(b) respectively. Recall that the closest roughness element to the lee ray was placed 43.3° from the wind ray. Again, note the similarities between the heat transfer and amplitude trends.

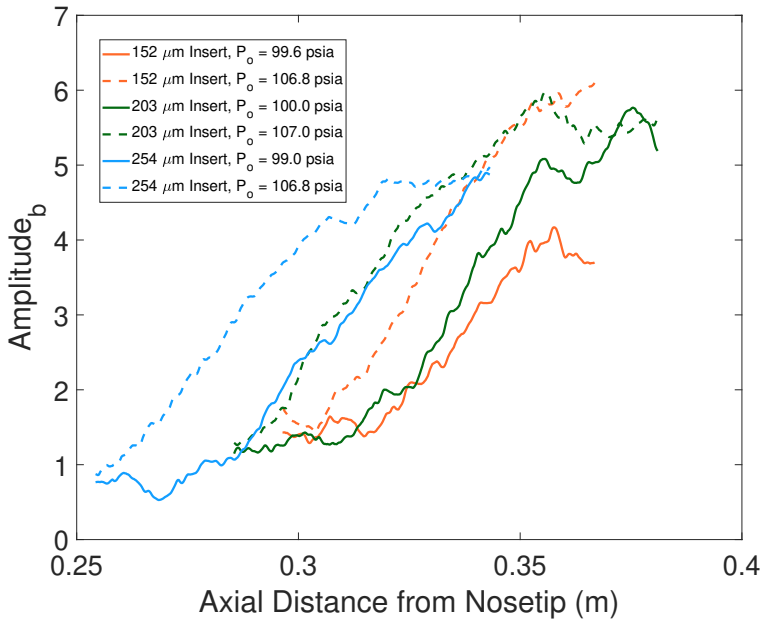

(a) Leeward streaks.

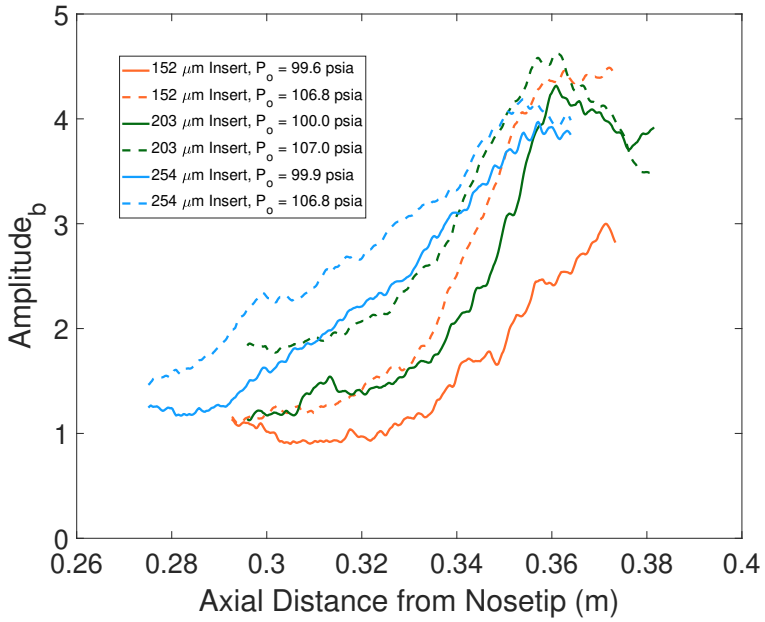

(b) Windward streaks.

Figure 5.73. Amplitude along leeward and windward streaks for runs performed with different freestream Reynolds numbers. Runs 509-514.

To quantify the effect of the freestream Reynolds number, Figure 5.74 displays the amplitude averaged from an axial location of 0.330 m to 0.335 m for different non-dimensional roughness heights. A small region was chosen as this was the only location in which all the streaks were growing. There appears to be linear growth for all the cases excluding the high Reynolds number leeward streak case. It also seems that the Reynolds number had more of an effect on the windward streak than the leeward streak. These data are tabulated in Table 5.8, while the linear fits are given in Table 5.9. Note that the vertical intercept is close to 0 for most cases which is a good sign that the growth is linear. The intercept for the leeward streak for the high Reynolds number, however, is especially high. This is due to the data point from the highest roughness height, where the streak already seems to be peaking in this axial region.

Table 5.8. Amplitude averages for different non-dimensional roughness heights and freestream Reynolds numbers. Data taken from Figure 5.74.

$\boldsymbol{Re_\infty}$	**Streak**	$\mathbf{k}/\delta$	**Average Amplitude from 0.330 m to 0.335 m**
7.75×10^6 (low)	Leeward Streak	0.520	2.390
7.90×10^6 (low)	Leeward Streak	0.694	2.789
7.85×10^6 (low)	Leeward Streak	0.867	4.227
7.75×10^6 (low)	Windward Streak	0.540	1.172
7.90×10^6 (low)	Windward Streak	0.719	1.667
7.85×10^6 (low)	Windward Streak	0.899	2.686
8.40×10^6 (high)	Leeward Streak	0.540	4.151
8.46×10^6 (high)	Leeward Streak	0.720	4.721
8.45×10^6 (high)	Leeward Streak	0.899	4.763
8.40×10^6 (high)	Windward Streak	0.560	1.802
8.46×10^6 (high)	Windward Streak	0.746	2.546
8.45×10^6 (high)	Windward Streak	0.933	3.146

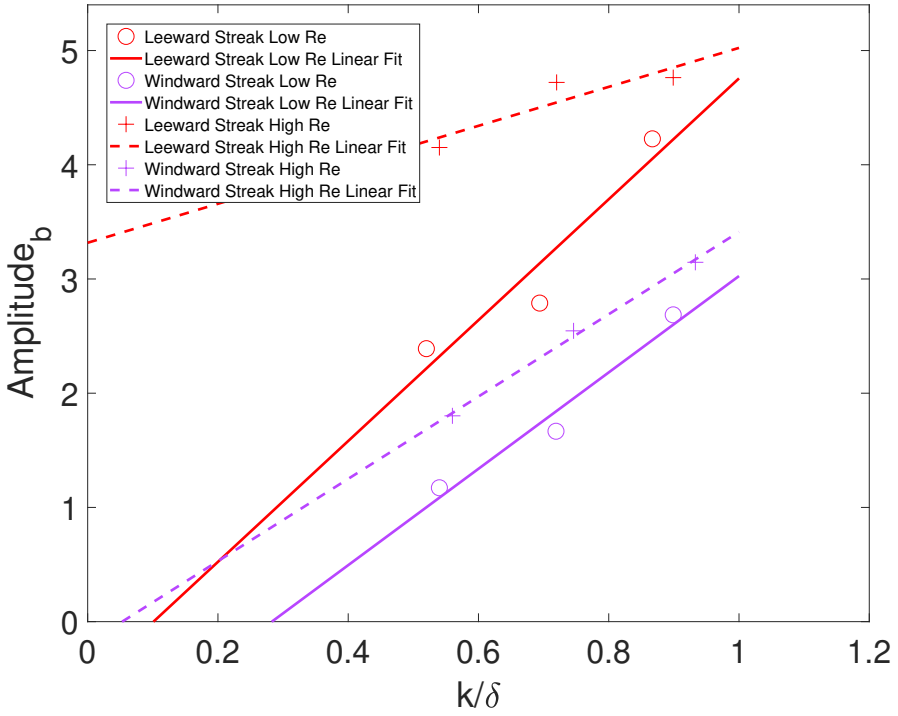

Figure 5.74. Average amplitude from an axial location of 0.330 m to 0.335 for different roughness inserts and freestream Reynolds numbers. Runs 509-514.

Table 5.9. Coefficient of linear fits for data in Figure 5.74.

Average Re_∞	**Streak**	**Slope of Linear Fit**	**Vertical Axis Intercept of Linear Fit**
7.83×10^6 (low)	Leeward Streak	5.291	-0.535
7.83×10^6 (low)	Windward Streak	4.219	-1.193
8.44×10^6 (high)	Leeward Streak	1.706	3.317
8.44×10^6 (high)	Windward Streak	3.603	-0.191

6. SUMMARY OF WORK AND FUTURE RECOMMENDATIONS

The effect of roughness elements on the amplitude of the stationary crossflow instability was investigated on a 7° half-angle cone at a 6° angle of attack. . To excite the primary instability, the RIM roughness was utilized. The stationary vortices manifested as patterned streaks in the TSP images. By rotating the roughness element by 3°, observing the subtle change in the location of the streaks, and comparing the location to computed locations, it was shown that the roughness inserts were creating the streaks being analyzed. Roughness elements with heights between 50.8 μm and 254 μm were used. The heat transfer was extracted along the streaks, and a general trend was observed of linear growth until a certain axial location at which point the streak peak and then subsequently decayed. This may have been due to the saturation of the stationary vortex.

To assess TSP repeatability, tests were performed at a 0° angle of attack. Consecutive runs showed that the heat transfer measured by the SB decreased as the model's initial temperature increased, which agreed with the results computed from a similarity solution. Thus, to obtain consistent results, the model was allowed to cool down in between runs to keep the initial temperature constant. At a 6° angle of attack, for higher roughness elements, the growth of the streaks generally moved farther upstream. The amplitude was averaged from an axial location of 0.335 m to 0.355 m while the most leeward roughness element was placed 43.4° from the wind ray. This axial region was chosen because all visible streaks were observed to grow. Farther upstream, some streaks were not visible, while farther downstream, some streaks had already started to peak. The average amplitude of the leeward streak was found to increase by approximately 450 % as the roughness height was increased

from 102 μm to 254 μm. At the same time, the average amplitude of the windward streak increased by about 200 % when the roughness height was increased from 152 μm to 254 μm. Similar trends were seen when the freestream Reynolds number was increased. The average crossflow wave amplitude plotted against the non-dimensional element height, $\frac{k}{\delta}$, seemed to be described well by a linear fit in most cases.

6.1 Recommendations for Future Work

More work needs to done to study the roughness elements that are used to excite the flow. First, the azimuthal angle between the elements with respect to the diameter of the elements should likely be larger. This current experiment placed them 7.2° apart to force a wavenumber of 50, but a wavenumber of 40 was likely more than enough. Alternatively, the diameter may also be decreased as long as it is big enough to affect the flow. Additionally, it may be wise to obtain a more accurate way of making these roughness inserts. When dealing with elements that differ in size by 50.8 μm, it is very important that their dimensions are as exact as possible.

One of the main issues with the 3-D geometry of this flow is that the streaks are ubiquitous, also being present near the lee ray. This makes it challenging to get a reliable calibration from the SB. In the future, the best possible location for the SB is likely upstream and adjacent to the lee ray, but not directly on it. This, however, poses other issues regarding the signal-to noise-ratio, due to the feathering technique used to paint the model.

It may also be wise to continue this approach with different measuring techniques. Infrared thermography poses a higher signal-to-noise ratio than TSP and does not rely on a SB for calibration, although one can be used for confirmation. The infrared data can also be compared to the TSP data for runs done under the same conditions for validation. Finally, a micro-pitot-pressure transducer may also be able to measure the amplitude of the crossflow waves, using off-surface measurements such as velocity disturbances and amplitudes of the vortices.

REFERENCES

REFERENCES

[1] F. M. White. *Viscous Fluid Flows*. McGraw Hill, December 2006.

[2] A. Fedorov. Transition and Stability of High-speed Boundary Layers. *Annual Review of Fluid Mechanics*, Vol. 43:79–95, 2011.

[3] S. P. Schneider. The Development of Hypersonic Quiet Tunnels. *Journals of Spacecraft and Rockets*, Vol. 45 No. 4:641–664, August 2008.

[4] S. P. Schneider. Effects of High-Speed Tunnel Noise on Laminar-Turbulent Transition. *Journal of Spacecraft and Rockets*, Vol. 38, No. 3:323–333, June 2001.

[5] D. C. Reda. Boundary-layer Transition Experiments on Sharp, Slender Cones in Supersonic Free Flight. *AIAA Journal*, Vol. 17, No. 8:803–810, August 1979.

[6] J. Edelman. Secondary Instabilities of Hypersonic Stationary Crossflow Waves. Master's thesis, Purdue University, December 2019.

[7] S. A. Craig and W. S. Saric. Experimental Study of Crossflow Instability on a Mach 6 Yawed Cone. *AIAA Paper 2015-2774*, June 2015.

[8] R. H. Radeztsky, M. S. Reibert, and W. S. Saric. Effect of Isolated Micron-sized Roughness on Transition in Swept-Wing Flows. *AIAA Journal*, Vol. 37, No. 11:1371–1377, November 1999.

[9] H. L. Reed, W. S. Saric, and D. Arnal. Linear Stability Theory Applied to Boundary Layers. *Annual Review of Fluid Mechanics*, Vol. 28:389–428, 1996.

[10] W. S. Saric, H. L. Reed, and E. B. White. Stability and Transition of Three-dimensional Boundary Layers. *Annual Review of Fluid Mechanics*, Vol. 35:413–440, January 2003.

[11] H. Deyhle and H. Bippes. Disturbance Growth in an Unstable Three-dimensional Boundary Layer and Its Dependence on Environmental Conditions. *Journal of Fluid Mechanics*, Vol. 316:73–113, 1996.

[12] C. A. C. Ward. *Crossflow Instability and Transition on a Circular Cone at Angle of Attack in a Mach-6 Quiet Tunnel*. PhD thesis, Purdue University, December 2014.

[13] M. P. Borg, R. L. Kimmel, and S. Stanfield. Traveling Crossflow Instability for the HIFiRE-5 Elliptic Cone. *Journal of Spacecraft and Rockets*, Vol. 52, No. 3:664–673, June 2015.

[14] M. P. Borg and R. L. Kimmel. Measurements of Crossflow Instability Modes for HIFiRE-5 at Angle of Attack. *AIAA Paper 2017-1681*, January 2017.

[15] M. R. Malik, F. Li, M. M. Choudhari, and C. Chang. Secondary Instability of Crossflow Vortices and Swept-wing Boundary-layer Transition. *Journal of Fluid Mechanics*, Vol. 399:85–115, 1999.

[16] E. B. White and W. S. Saric. Secondary Instability of Crossflow Vortices. *Journal of Fluid Mechanics*, Vol. 525:275–308, 2005.

[17] M. R. Malik and C.-L. Chang. Nonlinear Crossflow Disturbances and Secondary Instabilities in Swept-wing Boundary Layers. In P. W. Duck and P. (Eds.) Hall, editors, *IUTAM Symposium on Nonlinear Instability and Transition in Three-Dimensional Boundary Layers*, pages 257–266, 1996.

[18] J. Edelman and S. P. Schneider. Secondary Instabilities of Hypersonic Stationary Crossflow Waves. *AIAA Journal*, Vol. 56, No. 1:182–192, 2018.

[19] J. B. Edelman. *Nonlinear Growth and Breakdown of the Hypersonic Crossflow Instability*. PhD thesis, Purdue University, August 2019.

[20] W. E. Gray. The effect of wing sweep on laminar flow. Royal Aircraft Establishment Technical Memo No. 255, 1952.

[21] P. R. Owen and D. G. Randall. Boundary Layer Transition on a Swept-Back Wing. R.A.E. TM Aero 277, May 1952.

[22] D. I. A. Poll. Some Observations of the Transition Process on the Windward Face of a Long Yawed Cylinder. *Journal of Fluid Mechanics*, Vol. 150:329–356, 1985.

[23] P. Nitschke-Kowsky and H. Bippes. Instability and Transition of a Three-dimensional Boundary Layer on a Swept Flat Plate. *The Physics of Fluids*, Vol. 31, No. 4:786–795, April 1988.

[24] H. Bippes and P. Nitschke-Kowsky. Experimental Study of Instability Modes in a Three-dimensional Boundary Layer. *AIAA Paper 1987-1336*, June 1987.

[25] E. B. White, W. S. Saric, R. D. Gladden, and P. M. Gabet. Stages of Swept-wing Transition. *AIAA Paper 2001-0271*, January 2001.

[26] R. H. Radeztsky, M. S. Reibert, and W. S. Saric. Development of Stationary Crossflow Vortices on a Swept Wing. *AIAA Paper 1994-2373*, June 1994.

[27] B. Müller and H. Bippes. Experimental Study of Instability Modes in a Three-Dimensional Boundary Layer. In *In AGARD, Fluid Dynamics of Three-Dimensional Turbulent Shear Flows and Transition 15 p*, April 1989.

[28] H. Deyhle and H. Bippes. Disturbance Growth in an Unstable Three-dimensional Boundary Layer and Its Dependence on Environmental Conditions. *Journal of Fluid Mechanics*, Vol. 316:73–113, 1996.

[29] J. D. Swearingen and R. F. Blackwelder. Spacing of Streamwise Vortices on Concave Walls. *AIAA Journal*, Vol. 24:1706–1709, October 1986.

[30] M. S. Reibert and W. S. Saric. Review of Swept-wing Transition. *AIAA Paper 1997-1816*, 1997.

[31] M. Choudhari. Roughness-induced Generation of Crossflow Vortices in Three-dimesnional Boundary Layers. *Theoretical and Computational Fluid Dynamics*, Vol. 6:1–30, 1994.

[32] M. S. Reibert, W. S. Saric, R. B. Carillo, and K. L. Chapman. Experiments in Nonlinear Saturation of Stationary Crossflow Vortices in a Swept-wing Boundary Layer. *AIAA Paper 1996-0184*, January 1996.

[33] T. S. Haynes and H. L. Reed. Simulation of Swept-wing Vortices Using Nonlinear Parabolised Stability Equations. *Journal of Fluid Mechanics*, 405:325–349, 2000.

[34] W. S. Saric, R. B. Carrillo, and M. S. Reibert. Nonlinear Stability and Transition in 3-D Boundary Layers. *Meccanica*, Vol. 33:469–487, 1998.

[35] L. E. Hunt and W. S. Saric. Boundary-layer Receptivity of Three-dimensional Roughness Arrays on a Swept-wing. *AIAA Paper 2011-3881*, June 2011.

[36] W. S. Saric and H. L. Reed. Supersonic Laminar Flow Control on Swept Wings Using Distributed Roughness. *AIAA Paper 2002-0147*, January 2002.

[37] R. A. King. Three-Dimensional Boundary-Layer Transition on a Cone at Mach 3.5. *Experiments in Fluids*, Vol. 13:305–314, 1999.

[38] N. V. Semionov, A. D. Kosinov, and V. Ya. Levchenko. Experimental Study of Turbulence Beginning and Transition Control in a Supersonic Boundary Layer on Swept Wing. In *6th IUTAM Symposium on Laminar-Turbulent Transition*, pages 355—-361, December 2006.

[39] A. Kroonenberg, R. Radespiel, G. Candler, and M. Estorf. Infrared Measurements of Boundary-layer Transition on an Inclined Cone at Mach 6. *AIAA Paper 2010-1063*, January 2010.

[40] F. Li, M. Choudhari, C. Chang, and J. White. Analysis of Instabilities in Non-axisymmetric Hypersonic Boundary Layers over Cones. *AIAA Paper 2010-4643*, June 2010.

[41] P. Balakumar and L. R. Owens. Stability of Hypersonic Boundary Layers on a Cone at Angle of Attack. *AIAA Paper 2010-4718*, June 2010.

[42] J. E. Gronvall, H. B. Johnson, and G. V. Candler. Hypersonic Three-dimensional Boundary Layer Transition on a Cone at Angle of Attack. *AIAA Paper 2012-2822*, June 2012.

[43] C. A. C. Ward. Hypersonic Crossflow Instability and Transtion on a Circular Cone at Angle of Attack. Master's thesis, Purdue University, December 2010.

[44] E. O. Swanson and S. P. Schneider. Boundary-layer Transition on Cones at Angle of Attack in a Mach-6 Quiet Tunnel. *AIAA Paper 2010-1062*, January 2012.

[45] C. Y. Schuele, T. C. Corke, and E. Matlis. Control of Stationary Crossflow Modes in a Mach 3.5 Boundary Layer Using Patterned Passive and Active Roughness. *Journal of Fluid Mechanics*, Vol. 718:5–38, 2013.

[46] S. A. Craig and W. S. Saric. Crossflow Instability on a Yawed Cone at Mach 6. *Procedia IUTAM*, Vol. 14(C):15–25, 2015.

[47] S. A. Craig and W. S. Saric. Experimental Study of Crossflow Instability on a Mach 6 Yawed Cone. *AIAA Paper 2015-2774*, June 2015.

[48] S. A. Craig and W. S. Saric. Crossflow Instability in a Hypersonic Boundary Layer. *Journal of Fluid Mechanics*, Vol. 808:224–244, October 2016.

[49] E. Matlis, A. Arndt, T. Corke, M. Semper, and T. McLaughlin. Effect of Discrete Roughness on Crossflow Transition. In *AIAA Aerospace Sciences Meeting, 2018*, pages 1080–1087. American Institute of Aeronautics and Astronautics Inc, AIAA, January 2018.

[50] M. Huntley and A. Smits. Transition Studies on an Elliptic Cone in Mach 8 Flow Using Filtered Rayleigh Scattering. *European Journal of Mechanics / B Fluids*, Vol. 19, No. 5:695–706, September 2000.

[51] R. Kimmel, J. Poggie, and S. Schwoerke. Laminar-Turbulent transition in a Mach 8 elliptic cone flow. *American Institute of Aeronautics and Astronautics. AIAA Journal*, Vol. 37, No. 9:1080–1087, September 1999.

[52] M. P. Borg, R. L. Kimmel, and S. Stanfield. Traveling Crossflow Instability for HIFiRE-5 in a Quiet Hypersonic Wind Tunnel. *AIAA Paper 2013-2737*, June 2013.

[53] T. J. Juliano, M. Borg, and S. P. Schneider. Quiet Tunnel Measurements of HIFiRE-5 Boundary-layer Transition. *AIAA Journal*, Vol. 53, No. 4:832–846, January 2015.

[54] I. Neel, A. Leidy, and R. Bowersox. Preliminary Study of the Effect of Environmental Disturbances on Hypersonic Crossflow Instability on the HIFiRE-5 Elliptic Cone. *AIAA Paper 2017-0767*, January 2017.

[55] D. Dinzl and G. Candler. Direct Simulation of Hypersonic Crossflow Instability on an Elliptic Cone. *AIAA Journal*, Vol. 55, No. 6:1769–1782, June 2017.

[56] A. Moyes, T. S. Kocian, D. Mullen, and H. L. Reed. Effects of Initial Disturbance Amplitude on Hypersonic Crossflow Instability. *AIAA Paper 2018-1820*, January 2018.

[57] L. S. Steen. Characterization and Development of Nozzles for a Hypersonic Quiet Wind Tunnel. Master's thesis, Purdue University, December 2010.

[58] D. Turbeville. Nozzle Wall Hot Film and Static Pressure Kulite Overview. Technical report, Purdue University, February 2018.

[59] B. C. Chynoweth. A New Roughness Array for Controlling the Nonlinear Breakdown of Second-mode Waves at Mach 6. Master's thesis, Purdue University, August 2015.

[60] D. Watring. Personal E-mail Communication. Medtherm Corporation, June 2019.

[61] Cole-Parmer. *H-B Instrument B61001-0400 FRIO-Temp Incubator Verification Thermometer; 25 to 45C.*

[62] PCB Piezotronics. *Model 132A31 Micro ICP Pressure Sensor, 140 mV/psi, pigtail conn. (for high frequency Installation and Operating Manual).*

[63] D. C. Berridge. *Generating Low-pressure Shock Waves for Calibrating High-frequency Pressure Sensors*. PhD thesis, Purdue University, December 2015.

[64] M. P. Wason. Measurements of Low-pressure Shock Waves Towards a Calibration Method for High-frequency Pressure Sensors. Master's thesis, Purdue University, May 2019.

[65] T. Liu and J. P. Sullivan. *Pressure and Temperature Sensitive Paints*. Springer Berlin Heidelberg New York, 2005.

[66] J. P. Sullivan, S. P. Schneider, J. Liu, T. Rubal, C. A. C. Ward, J. Dussling, C. Rice, R. Foley, Z. Cai, B. Wang, and S. Woodiga. Quantitative Global Heat Transfer in a Mach-6 Quiet Tunnel. Final Technical Report for Cooperative Agreement NNX08AC97A, National Aeronautics and Space Administration, November 2011.

[67] T. Liu, B. T. Campbell, S. P. Burns, and J. P. Sullivan. Temperature and Pressure-sensitive Luminescent Paints in Aerodynamics. *Applied Mechanics Review*, Vol. 50, No. 4:227–246, 1994.

[68] J. P. Sullivan. Personal Communication, November 2018.

[69] R. P. K. Luersen. Techniques for Application of Roughness for Manipulation of Second-Mode Waves on a Flared Cone at Mach 6. Master's thesis, Purdue University, December 2012.

[70] G. V. Candler, H. B. Johnson, I. Nompelis, P. K. Subbareddy, T. W. Drayna, and V. Gidzak. Development of the US3D Code for Advanced Compressible and Reacting Flow Simulations. In *AIAA Aerospace Sciences Meeting, 2015*. American Institute of Aeronautics and Astronautics Inc, AIAA, January 2015.

[71] N. Oliviero, T. Kocian, A. Moyes, and H. Reed. EPIC: NPSE Analysis of Hypersonic Crossflow Instability on Yawed Straight Circular Cone. *AIAA Paper 2015-2772*, June 2015.

[72] HotPack. *Operating and Maintenance Manual;Relative Humidity Chambers*, April 2002.

[73] E. W. Lemmon and R. T. Jacobsen. Viscosity and Thermal Conductivity Equations for Nitrogen, Oxygen, Argon, and Air. *International Journal of Thermophysics*, Vol. 25, No. 1:21–69, January 2004.

[74] J. D. Anderson. *Computational Fluid Mechanics and Heat Transfer*. McGraw-Hill Book Company, 1984.

[75] F. D. Turbeville. Parametric study of a 7° Half-angle Cone with Highly Swept Fins at Mach 6. Master's thesis, Purdue University, May 2018.

APPENDICES

A. Selected Run Conditions

This section of the appendix contains a log of the runs that were selected for use in this report. The first digit is the entry number and the next 2 digits are the run number. Note that all runs were quiet.

Table A.1. Entry 1.

Run #	**Roughness Insert #**	$p_{o,i}$ **(psia)**	$T_{o,i}$ **(K)**	$T_{w,i}$ **(K)**	**Roughness Location** (°) [1]	$\frac{k}{\delta}$ [2]
108	7	116.5	425	293	40.4	0.77
109	7	121.8	428	296	40.4	0.78
110	7	121.3	428	299	40.4	0.78
111	7	121.6	428	0.300	40.4	0.78
112	7	118.4	428	302	40.4	0.77
113	7	121.8	427	303	40.4	0.78
114	7	116.4	427	303	40.4	0.77
116	7	120.9	428	305	40.4	0.78
117	7	121.1	428	305	40.4	0.78

[1]Given angle is angle of the element closest to the lee ray. The angle is with respect to the wind ray.
[2]Value is given for the middle of the 3 elements.

Table A.2. Entry 2.

Run #	**Roughness Insert #**	$p_{o,i}$ **(psia)**	$T_{o,i}$ **(K)**	$T_{w,i}$ **(K)**	**Roughness Location (°)**	$\frac{k}{\delta}$
204	7	117	428	302	45.4	0.75
205	7	116.8	427	302	45.4	0.75
206	7	116	427	302	45.4	0.75
209	6	117	428	302	52.4	0.54
210	6	116.8	427	302	52.4	0.54
211	6	116	427	302	52.4	0.54
212	4	117	428	303	52.4	0.36
213	4	117.3	426	303	52.4	0.37
214	4	115.9	427	302	52.4	0.36
215	7	116.4	427	302	52.4	0.72
216	7	116.2	427	303	52.4	0.72
217	2	116.5	426	303	52.4	0.18
218	2	116.0	428	303	52.4	0.18
219	2	114.7	428	303	52.4	0.18
221	7	116.6	432	302	52.4	0.72

Table A.3. Entry 3.

Run #	**Roughness Insert #**	$p_{o,i}$ **(psia)**	$T_{o,i}$ **(K)**	$T_{w,i}$ **(K)**	**Roughness Location (°)**	$\frac{k}{\delta}$
301	1	140.2	431	277	N/A	N/A
305	1	133.7	429	303	N/A	N/A
311	1	131.4	433	297	N/A	N/A
312	1	129.0	433	301	N/A	N/A
313	1	131.1	432	304	N/A	N/A
314	1	131.3	432	306	N/A	N/A
315	1	128.6	432	307	N/A	N/A

Table A.4. Entry 4.

Run #	**Roughness Insert #**	$p_{o,i}$ **(psia)**	$T_{o,i}$ **(K)**	$T_{w,i}$ **(K)**	**Roughness Location (°)**	$\frac{k}{\delta}$
407	6	112.1	429	302	43.4	0.55
408	6	112.7	428	303	43.4	0.56
410	3	111.9	429	302	43.4	0.19
411	8	110.4	428	302	43.4	0.92
412	8	109.2	429	302	43.4	0.91
413	3	108.9	428	303	43.4	0.19
414	5	109.9	428	302	43.4	0.37
416	7	109.7	429	302	43.4	0.73
417	7	109.3	428	302	43.4	0.73
422	8	118.4	430	302	55.4	0.89
427	7	118.7	429	301	43.4	0.76

Table A.5. Entry 5.

Run #	**Roughness Insert #**	$p_{o,i}$ **(psia)**	$T_{o,i}$ **(K)**	$T_{w,i}$ **(K)**	**Roughness Location (°)**	$\frac{k}{\delta}$
502	7	111.9	431	296	43.4	0.74
503	7	113.9	431	296	43.4	0.74
507	7	114.1	431	296	46.4	0.73
508	7	114.4	430	297	46.4	0.73
509	7	113.5	431	297	43.4	0.74
510	7	121.4	430	299	43.4	0.77
511	8	121.3	430	299	43.4	0.96
512	8	113.4	432	299	43.4	0.93
513	6	113.0	434	299	43.4	0.55
514	6	121.2	432	298	43.4	0.57

B. Zygo Measurements of RIM Roughness Inserts

This section contains the Zygo measurements of all the inserts that contained roughness elements that were used in the present thesis. The nominal heights were measured by Jim Younts, one of the AAE machinists. Although the azimuthal and axial scales are accurate, they are referenced with respect to an arbitrary point. However, this arbitrary point is the same for all drawings, allowing for easy comparison of the axial and azimuthal locations. Because precise azimuthal adjustments made by the motor were unavailable at the time, the structure had to remain in place for all measurements. This meant that some images were slightly cut off in the azimuthal direction due to the variation in the azimuthal location of the roughness elements. Also, note that the sides of the roughness elements in the Zygo 2-D images do not appear perfectly straight. This is likely due to the noise caused by the small separation between the elements. However, these lines are similar to those measured by Edelman [19]. (His lines may appear straighter due to the scaling of the horizontal axis.) Finally, note that 2-D images are not presented for the 50.8 μm insert because the elements were too small to extract a proper image.

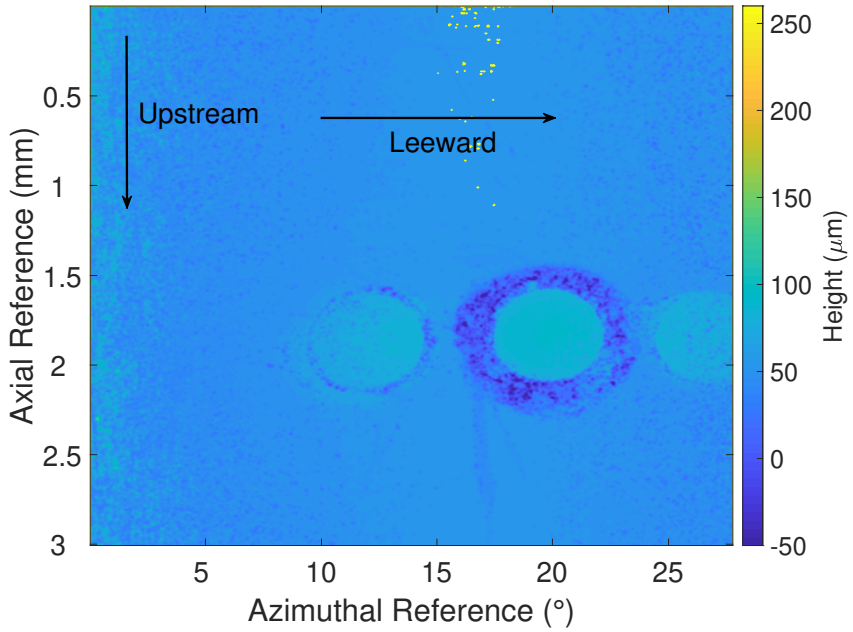

Figure B.1. Zygo measurements of roughness insert # 2 which contains elements with a nominal height of 50.8 μm. The 2-D slice is not shown as the elements were too small to obtain a proper image.

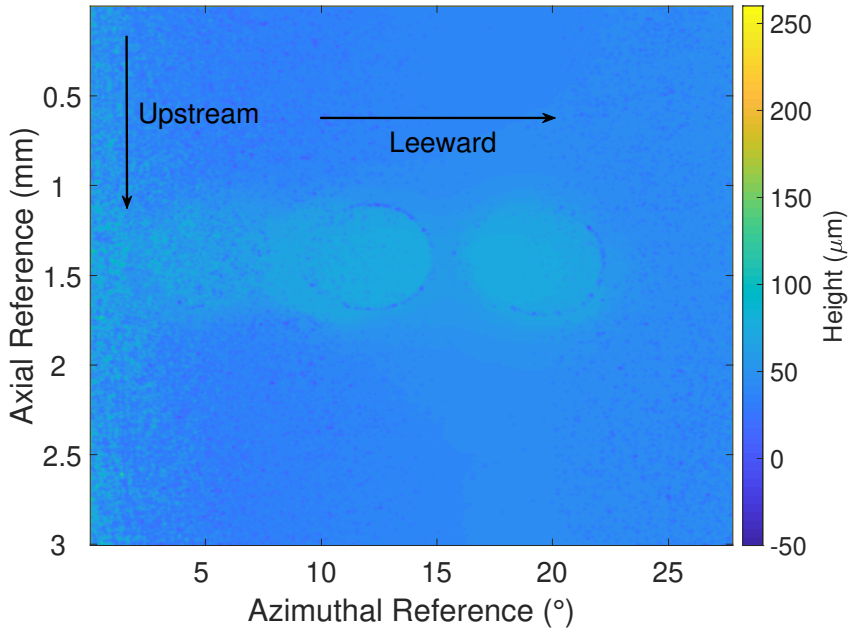

Figure B.2. Zygo measurements of roughness insert # 3 which contains elements with a nominal height of 50.8 μm. The 2-D slice is not shown as the elements were too small to obtain a proper image.

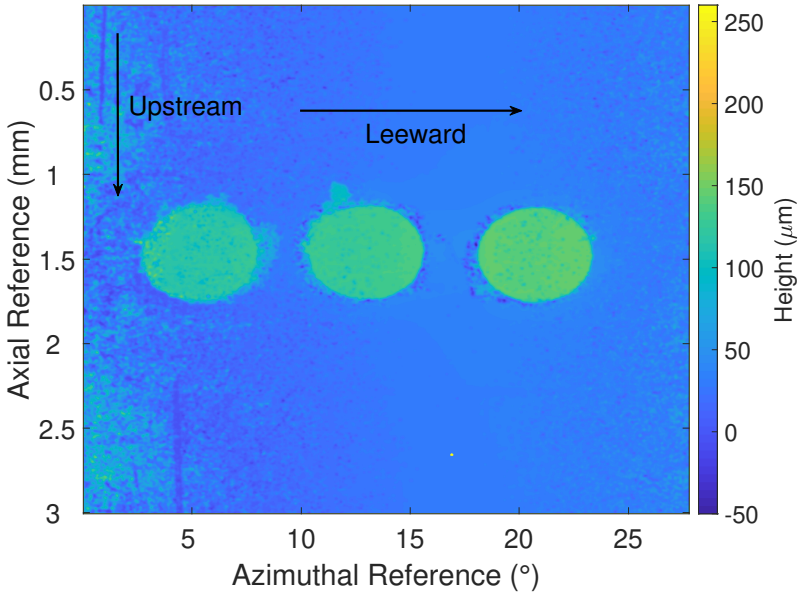

(a) Contour map of roughness insert # 4.

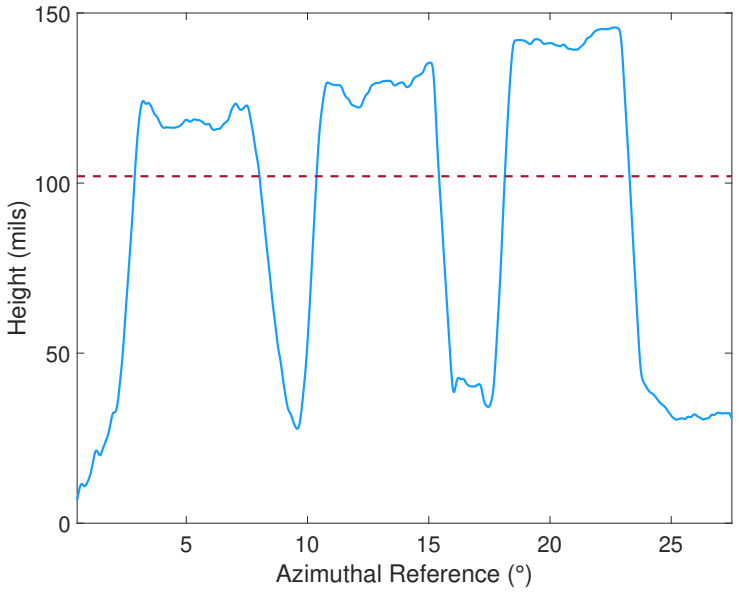

(b) 2-d slice of roughness insert # 4. The red dotted line marks the nominal height.

Figure B.3. Zygo measurements of Roughness insert # 4 which contains elements with a nominal height of 102 μm.

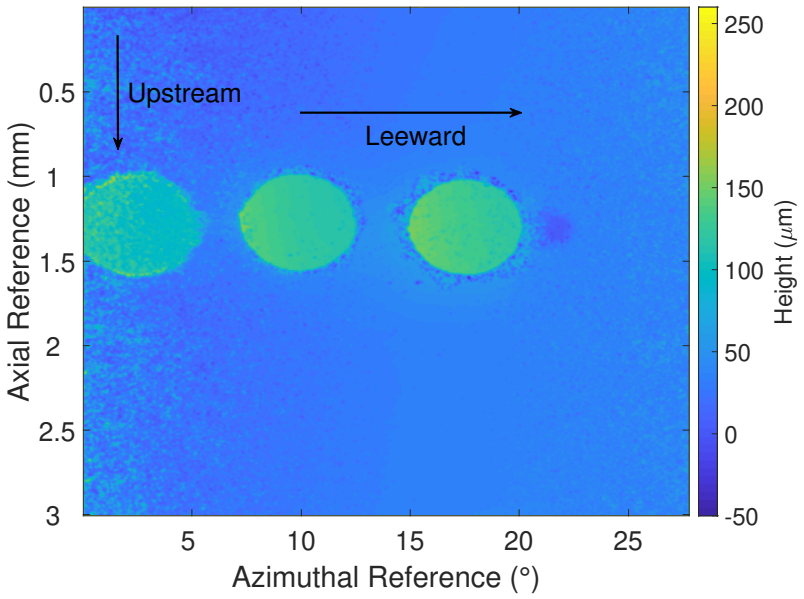

(a) Contour map of roughness insert # 5.

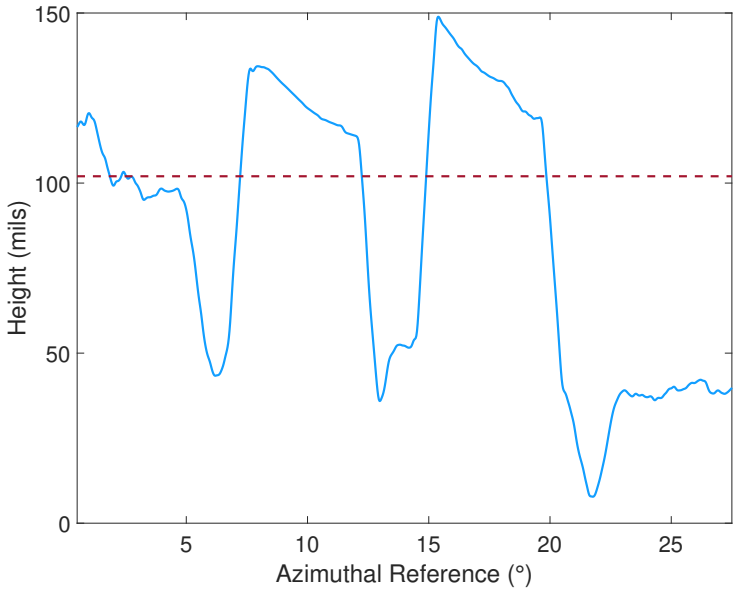

(b) 2-d slice of roughness insert # 5. The red dotted line marks the nominal height.

Figure B.4. Zygo measurements of Roughness insert # 5 which contains elements with a nominal height of 102 μm.

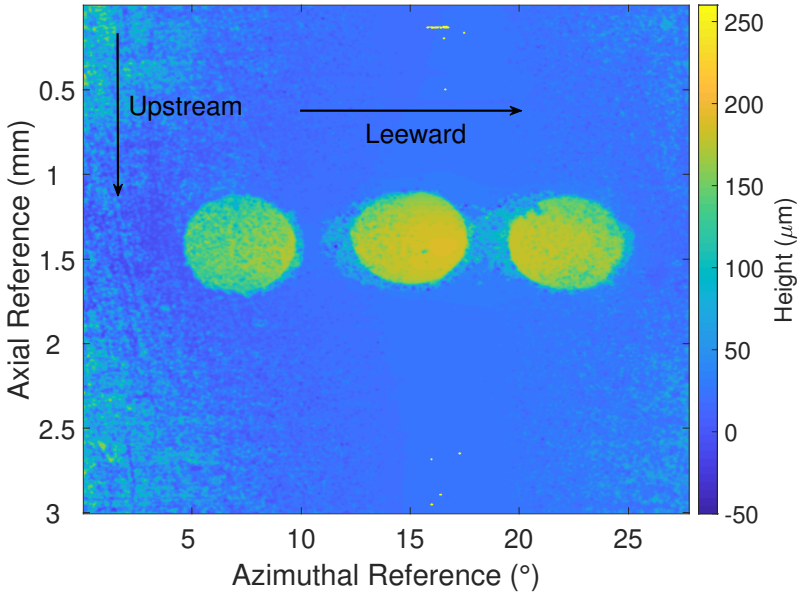

(a) Contour map of roughness insert # 6.

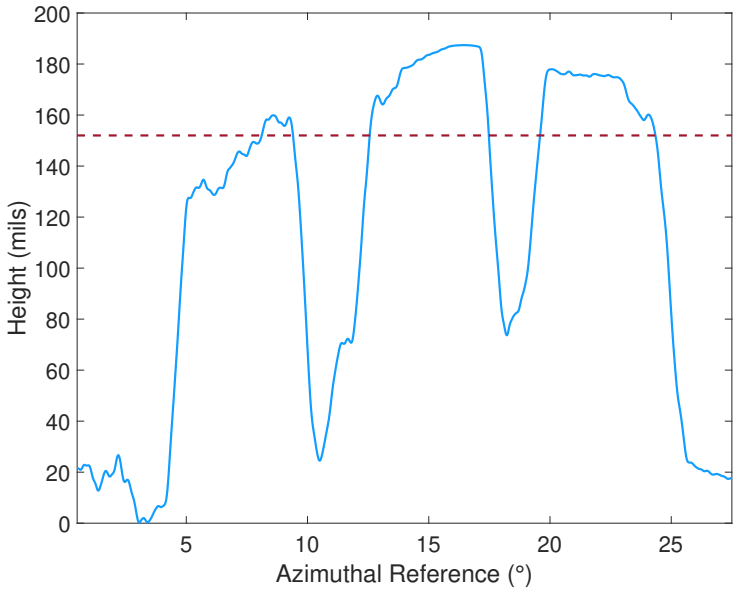

(b) 2-d slice of roughness insert # 6. The red dotted line marks the nominal height.

Figure B.5. Zygo measurements of Roughness insert # 6 which contains elements with a nominal height of 152 μm.

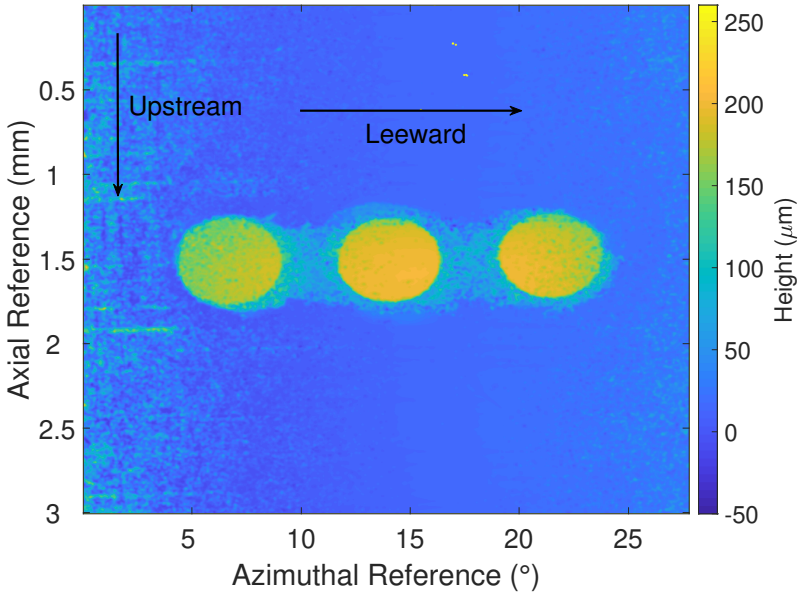

(a) Contour map of roughness insert # 7.

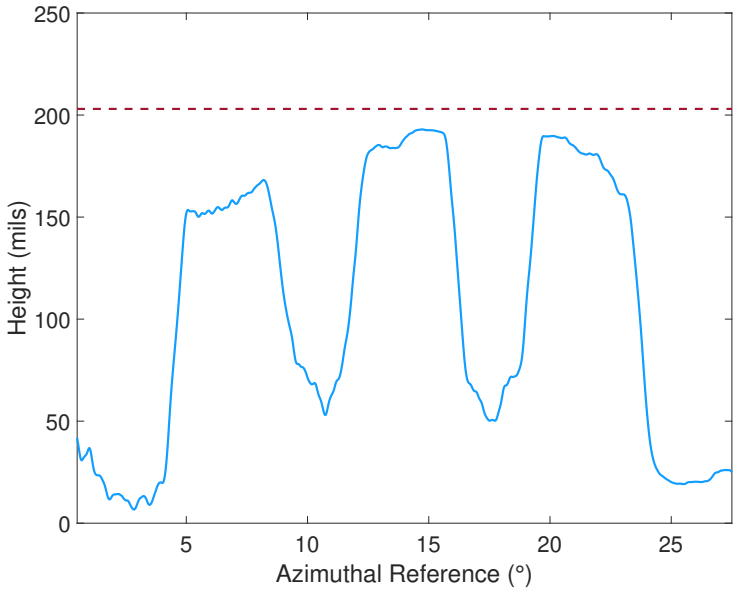

(b) 2-d slice of roughness insert # 7. The red dotted line marks the nominal height.

Figure B.6. Zygo measurements of Roughness insert # 7 which contains elements with a nominal height of 203 μm.

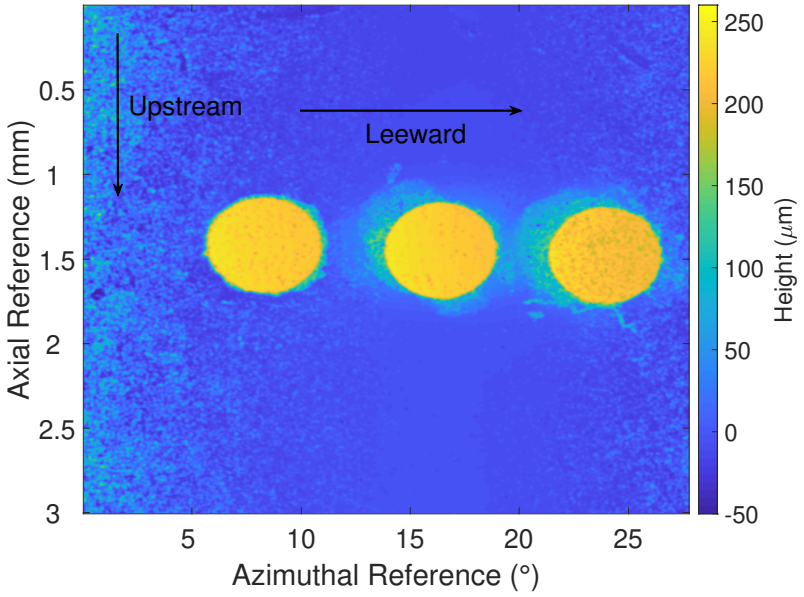

(a) Contour map of roughness insert # 8.

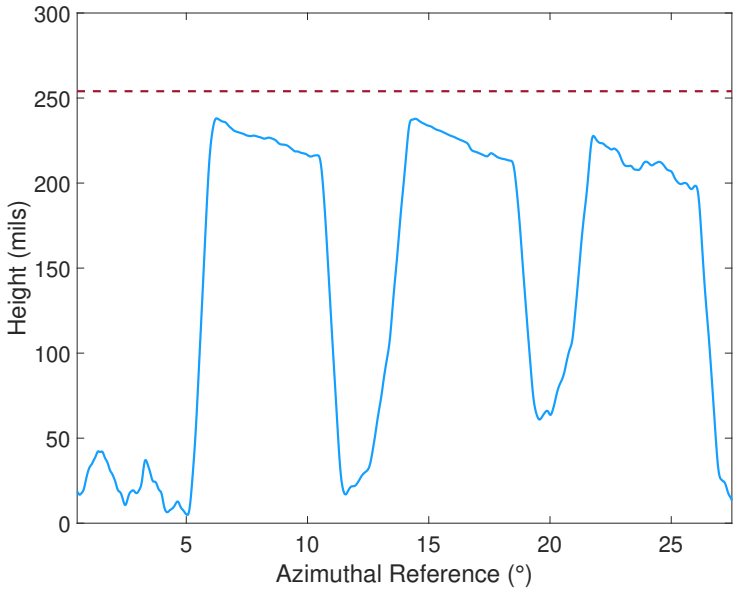

(b) 2-d slice of roughness insert # 8. The red dotted line marks the nominal height.

Figure B.7. Zygo measurements of Roughness insert # 8 which contains elements with a nominal height of 254 μm.

C. Replacing the Power Supplies that Heat the Driver Tube of the BAM6QT

Initially, there were 5 Electronic Measurements Inc. TCR 10T750 power supplies, while only 4 were being used simultaneously to heat the BAM6QT. Note that the 10 in 10T750 is for the maximum output voltage in Volts and the 750 is the maximum current output in Amps. However, the power supplies were more than 20 years old and were beginning to fail. Furthermore, many parts were no longer available. A new set of driver heating power supplies was needed. A power supply identified as a suitable replacement was the TSD10-900/480 +LXI from Magna-Power Electronics, which is a 10kW DC power supply. The first number in the product name is the maximum voltage, the second number is the maximum current, and the third number is the required input voltage. However, this power supply uses switching frequencies which emit electromagnetic field (emf) noise at 600 Hz and 28.8 kHz. Thus, before making a purchase, it was important to test these power supplies to make sure that the noise did not interfere with sensitive electronics used for boundary-layer instability research. Unfortunately, Magna Power did not have any power supplies matching this exact model that they were able to loan out. Thus the loaner that was utilized for the test was a TSD25-600/480+LXI.

To test this loaner, a 500 A current was run at 10 V through a testing load. This was approximately 5 kW of power, somewhat comparable to the maximum possible power drawn from the old power supplies. This meant that the resistance of the load had to be about 0.02 ohms. However, designing a load with a resistance this small that could handle that much power was not simple. For a metal, resistance is proportional to length and inversely proportional to the cross sectional area. However, the thermal mass of the load also had to be considered to make sure it could take

5 kW. The length also had to be reasonable in size. The loads used were two 1095 spring steel strips in a parallel configuration. They had a length of 10.0 feet, a width of 0.5 inches, and a thickness of about 0.042 inches. Two were used so that the power generated could be split between both the loads. The resistance of these 2 strips in parallel was measured using a 4 wire measurement, and was about 0.024 ohms.

The power supply was then hooked up to a disconnect box using a 480-V 3 phase input. To connect the power supply to the load, mechanical lugs and 0000 gage welding cable were utilized. Two of the lugs were used to attach the outgoing and returning welding cables to the power supply. The other 4 lugs were used to connect the welding cable to the load. Two fans were then placed near the setup for convectional cooling. To test the electronic noise levels, a XCE-062-15A Kulite pressure transducer was positioned about 1 foot away from the power supply and load. This sensor was selected because it is one of the most sensitive sensors used in the BAM6QT. The Kulite was hooked up to an Tektonix DPO7054 Oscilloscope using a Kulite box manafactured in-house by the AAE electronic specialist John Phillips. This box amplifies the input signal and comes with 2 outputs: a DC output with a 100 gain, and an AC output with a 10,000 gain. The AC output was used for this experiment. The current was increased from 0 A to 400 A at intervals of 100 A. Unfortunately, 500 A was not able to be tested because as the power supply was kept on, the steel load was heated, and its resistance increased. Thus, the voltage had to be increased to account for the change in resistance. To avoid running an excess of power through the steel loads, the current for the power supply tests was capped at 400 A. Figure C.1 shows the time signal from the Kulite when 400 A was output from the power supply. Figure C.1(a) shows the time signal with the power supply off as a control, Figure C.1(b) shows the time signal when the power is off and then turns on, and Figure C.1(c) shows the time signal when the power is on and then turns off. Note that the power was turned off by pressing the stop button on the power supply. The results may be different when a different method is used such as merely turning

down the set point temperature. The time at which the power supply is turned on or off are marked with a red circle.

As expected, it was found that the level of noise was proportional to the current being drawn into the load. Although it is clear that the noise levels are relatively high at 400 A, the noise levels seem to drop off almost immediately after the power supply is turned off. It is also interesting to look at the PSD of the created noise. This is shown in Figure C.2. The frequency resolution is 2.5 kHz, and the total time over which the signal is analyzed is 0.1 seconds. The first line is the PSD of a time signal of the Kulite output when the power supply has been off for a significant amount of time. The second line is the PSD of a time signal when the power supply is outputting 400 A. The third line is the PSD of a time signal 2 seconds after the power supply at 400A has been turned off.

It is clear that the power supply outputting 400 A adds significant noise to the Kulite. Two seconds after the power supply has been turned off, it appears that most of the noise has subsided except for a few peaks. It should be noted that this is a worst case scenario, as runs in the BAM6QT are usually conducted minutes after the power supplies are turned off. Thus, it was concluded that if normal procedures are followed in the BAM6QT, and the power supplies are turned off before every run, there should not be any problems with noise. Thus, 4 TSD10-900/480 +LXI power supplies were purchased, and a new design was created to improve the old system.

Initially, the welding cables and copper bus bars connecting the positive and negative terminals to the I-beams that would carry the current to and from the tunnel were of different length for each power supply. This made connecting them in a master-slave configuration inefficient. Thus, the new system involves mounting 2 tin-coated copper blocks onto either side of both I-beams, and threading in mechanical lugs that would hold the welding cable. This allows the welding cable to be the same length for all power supplies. The housing for the power supplies was also improved. The past support merely consisted of plywood laid directly on structural I-beams. Because this not only posed a fire hazard but also did nothing to filter the air enter-

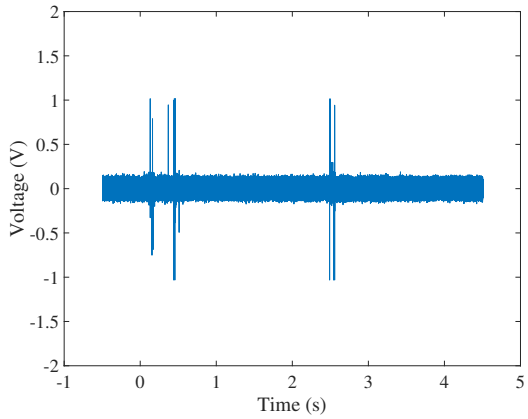

(a) Power supply off.

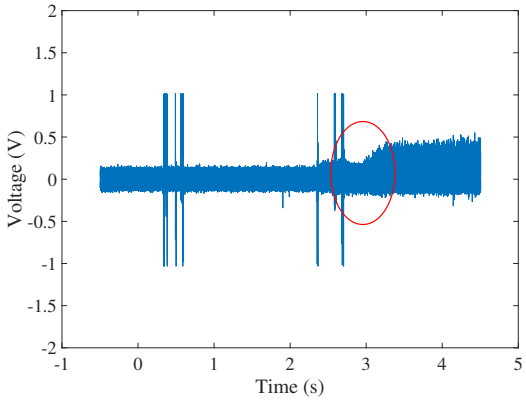

(b) Power supply turned on.

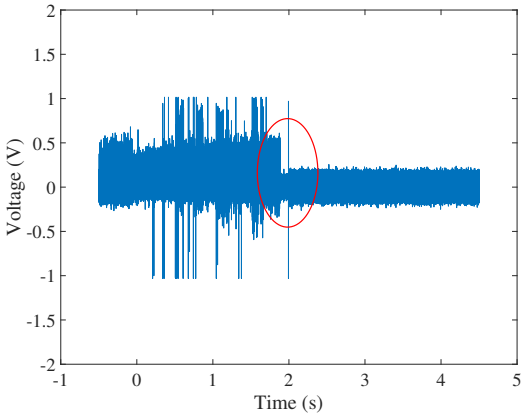

(c) Power supply turned off.

Figure C.1. Time signal from a XCE-062-15A Kulite pressure transducer adjacent to a power supply outputting 400 A.

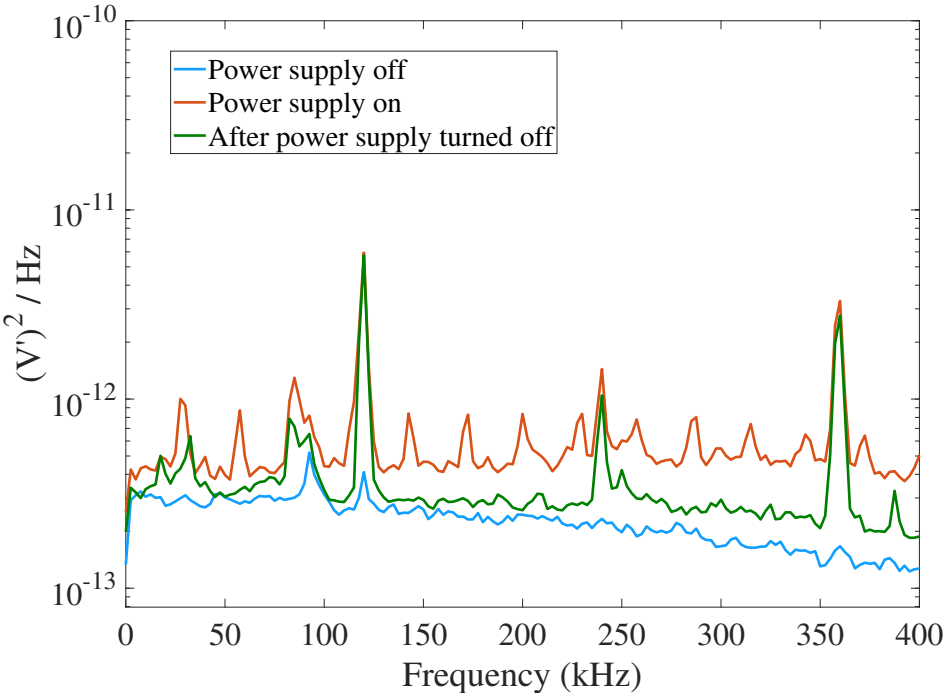

Figure C.2. PSD of a time signal from a XCE-062-15A Kulite pressure transducer adjacent to a power supply outputting 400 A.

ing the power supplies, a new design was created. The new power supply support, which is made entirely of welded steel, consists of two shelves with one power supply on the bottom and one on the top. An identical one was made to hold four power supplies in total. Holes will be drilled and tapped on the two side-by-side structural I-beams that support these shelves, allowing the shelves to be threaded in. The power supplies can be mounted to these shelves to ensure they can not move once in place. The sides of the supports contain space for 14 inch by 24 inch air filters. These filters remove 90%-99% of particles with a size of 3 μm or higher. The tops of the supports contain a steel plate to ensure air cannot enter in through the top. To ensure air does not enter in through the front in between the power supplies, aluminum spacers were mounted onto the front of the supports. The remaining gaps in the front and the back of the support were filled with rubber sealing foam. These power supplies are

also controlled with a 0-10 V signal. Although their maximum output is 900A, they have been capped at 750 A to decrease risk.

One disadvantage of the new power supplies is that when the power to the disconnect boxes is shut off and turned back on, these power supplies do not turn back on automatically. Instead, they wait on standby mode, posing a huge problem if a power outage occurs in the middle of the night. Thus, the standby button is currently shorted to the start button. However, this means that the stop button on the power supplies will not be able to fulfill its function, since the power supplies will just turn back on once the stop button is pressed. For that reason, this is only a temporary fix. The AAE electronics specialist, John Phillips, is currently working on a better circuit that will be able automatically turn the power supplies back on if the power is turned on and off, while also allowing the stop button to be used properly. The stop button may be helpful to lower the noise levels of the power supplies before initiating a run in the BAM6QT. It should also be noted that the power supplies have an alarm mode in case a problem occurs such as phase loss or overheating. If this occurs, the clear button on the power supply which experienced the problem must be pressed before it will start running again. Figure C.3 shows the current master-slave setup of the power supplies. The power supply on the top left is the master, and the others are slaves.

Figure C.3. Image showing current power supply setup.

Finally, the shutdown and startup process for these power supplies is much simpler than the older power supply system. To shut the new power supplies down, the temperature control panel should be turned down and then the disconnect box for the master power supply must be shut off. To turn them back on, the temperature control panel should be set at the appropriate temperature and the disconnect box for the master power supply should be turned on.

D. Streak Tracking Algorithm

```
clear all
clc
close all;
runcount=[9 10]; %run numbers to loop over
timecount=[1 1]; %time during the run to examine
sbcount=[1 1];  %sb that was used to calibrate the TSP data
for ppp=1:length(runcount) %loop over each run

    run=runcount(ppp);
    sb=sbcount(ppp);
    timefile=timecount(ppp)*10;
    filename=['Run ',num2str(run),'warp_SB',num2str(sb),num2str...
        (timefile),'second'];  %filename of saved unwrapped image
    load(filename,'Img_deform');
```

plot unwrapped image

```
    a2 =   [-1 5];
    figure(ppp)
    imagesc(Img_deform,a2);
    xlabel('Axial Distance from Nosetip (m)','FontSize',33);
    string=['Azimuthal Reference (',char(176),')'];
    ylabel(string,'FontSize',33);
    colorbar;
    t = colorbar('peer',gca);
```

```
set(get(t,'YLabel'),'String','Heat Transfer, [kW/m^2]','FontSize',27)
load TSPcolormap
colormap(TSPcolormap);
colorbar;
set(gca,'YTick',[36 80 124 169 213 258 302 347 391] );
set(gca,'YTickLabel',[40 30 20 10 0 -10 -20 -30 -40 ] );
%This is what it's going to appear in those places.
set(gca,'XTick',[33.9370 152.0472 270.1575  388.2677 506.3780 ...
    624.4882 742.5984 ] );
set(gca,'XTickLabel',[0.38 0.35 0.32 0.29 0.26 0.23 0.20])
```

extracting streak location

```
for qqq=1:2 %loop over windward and leeward streak

    clear xlocationv xlocationv1 xlocationv2  xlocationv3 ...
        ylocationv ylocationv1 1 ylocationv2 ylocationv3 qvortex
    %clear variables that will be used to store location and
    %heat transfer
    vortex=qqq;
    if vortex==1
        %input of initial guess, can be changed depending on
        %streak location
        xstart1=710;
        xfinish1=539;
        ystart1=360;
        yfinish1=324;
        xstart2=xfinish1-1;
        xfinish2=400;
        ystart2=yfinish1;
```

```
    yfinish2=307;
    xstart3=xfinish2-1;
    xfinish3=9;
    ystart3=yfinish2;
    yfinish3=275;
elseif vortex==2
    xstart1=451;
    xfinish1=359;
    ystart1=347;
    yfinish1=332;
    xstart2=xfinish1-1;
    xfinish2=221;
    ystart2=yfinish1;
    yfinish2=319;
    xstart3=xfinish2-1;
    xfinish3=44;
    ystart3=yfinish2;
    yfinish3=300;
end
xstart=xstart1;
xfinish=xfinish1;
ystart=ystart1;
yfinish=yfinish1;
vortexslope=(yfinish-ystart)./(xfinish-xstart);
%slope for starting basis
check=-1*round(1/vortexslope); %inverse of slope
yloc1=ystart; %starting y pixel location for initial guess
of streak
countt=((xstart-xfinish))+1; %pixel length of streak tracking
```

```
for t=1:countt
    if mod(t,check) == 0 %checking if y value should be changed
        yloc1=yloc1-1;
    else
        yloc1=yloc1;
    end
    xloc1=xstart-(t-1); %defining x pixel loocation of streak
    xlocationv1(t)=xloc1;
    addd=20; %amount of pixels to add above and below initial guess
    ybot1=yloc1+addd; %bot margin for vortex
    ytop1=yloc1-addd; %top margin for vortex
    M1=Img_deform(ytop1:ybot1,xloc1);
    %obtaining heat transfer for spanwise cut
    [~,vindex]=max(M1); %max=vortex location
    ylocationv1(t)=ytop1+vindex-1; %y pixel location of streak
end
%repeat for lines 2 and 3
xstart=xstart2;
xfinish=xfinish2;
ystart=ystart2;
yfinish=yfinish2;
vortexslope=(yfinish-ystart)./(xfinish-xstart);
check=-1*round(1/vortexslope);
yloc1=ystart;
countt=round(((xstart-xfinish))+1);
for t=1:countt
    if mod(t,check) == 0
        yloc1=yloc1-1;
    else
```

```
        yloc1=yloc1;
    end
    xloc1=xstart-(t-1);
    xlocationv2(t)=xloc1;
    M1=Img_deform(ytop1:ybot1,xloc1);
    [~,vindex]=max(M1);
    ylocationv2(t)=ytop1+vindex-1;
end
xstart=xstart3;
xfinish=xfinish3;
ystart=ystart3;
yfinish=yfinish3;
vortexslope=(yfinish-ystart)./(xfinish-xstart);
check=-1*round(1/vortexslope);
yloc1=ystart;
countt=round(((xstart-xfinish))+1);
for t=1:countt
    if mod(t,check) == 0
        yloc1=yloc1-1;
    else
        yloc1=yloc1;
    end
    xloc1=xstart-(t-1);
    xlocationv3(t)=xloc1;
    addd=20;
    ybot1=yloc1+addd;
    ytop1=yloc1-addd;
    M1=Img_deform(ytop1:ybot1,xloc1);
    [~,vindex]=max(M1);
```

```
    ylocationv3(t)=ytop1+vindex-1;
end
xlocationv=[xlocationv1,xlocationv2,xlocationv3];
%adding together all 3 parts of streak
ylocationv=[ylocationv1,ylocationv2,ylocationv3];
ylocationv=movmean(ylocationv,30);
xlocationreal=((15.3-7.3)/-800).*xlocationv+15.3;
%converting pixel coordinates to real coordinates
xlocationreal=xlocationreal.*.0254;
ylocationreal=(-90/400).*ylocationv+48;
```

plotting streak locations and heat transfer along streak

```
if vortex==1
    figure(length(runcount)+1)
    string=['Run ',num2str(runcount(ppp))];
    plot(xlocationreal,ylocationreal,'DisplayName',string,...
        'linewidth',2.5)
    h_lgnd =legend('-DynamicLegend','fontsize',27);
    %update legend dynamically
    xlabel('Axial Distance from Nosetip (m)','fontsize',33);
    string=['Azimuthal Reference (',char(176),')'];
    ylabel(string,'fontSize',33);
    hold on;
    figure(length(runcount)+2)

    for vv=1:length(xlocationv);
        qvortex(vv)=Img_deform(round(ylocationv(vv)),...
            xlocationv(vv));
```

```
    end
    qvortex=movmean(qvortex,30);
    figure(length(runcount)+2)
    plot(xlocationreal,qvortex,'DisplayName',string,...
        'linewidth',2.5);
    string=['Run ',num2str(runcount(ppp))];
    h_lgnd =legend('-DynamicLegend','fontsize',27);
    %update legend dynamically
    hold on
    xlabel('Axial Distance from Nosetip (m)','fontsize',33);
    ylabel('Heat Flux (kW/m^{2})','fontsize',33);
elseif vortex==2
    figure(length(runcount)+3)
    string=['Run ',num2str(runcount(ppp))];
    plot(xlocationreal,ylocationreal,'DisplayName',string,...
        'linewidth',2.5)
    h_lgnd =legend('-DynamicLegend','fontsize',27);
    %update legend dynamically
    xlabel('Axial Distance from Nosetip (m)','fontsize',33);
    string=['Azimuthal Reference (',char(176),')'];
    ylabel('string','fontSize',33);
    hold on;
    figure(length(runcount)+4)
    for vv=1:length(xlocationv);
        qvortex(vv)=Img_deform(round(ylocationv(vv)),...
            xlocationv(vv));
    end
    qvortex=movmean(qvortex,30);
    string=['Run ',num2str(runcount(ppp))];
```

```
            plot(xlocationreal,qvortex,'DisplayName',string,...
                'linewidth',2.5);
            h_lgnd =legend('-DynamicLegend','fontsize',27);
            %update legend dynamically
            hold on
            xlabel('Axial Distance from Nosetip (m)','fontsize',33);
            ylabel('Heat Flux (kW/m^{2}','fontsize',33);
        end

    end

end
```

E. RIM insert Drawing

This section contains the drawing for the RIM inserts that were used in this experiment. Note that the exposed height of the brass rod is not included because this was varied from 2 to 10 mil. For detailed drawings of the Mark II cone, the reader is referred to reference [6]. For a drawing of the nosetip, the reader is referred to reference [12].

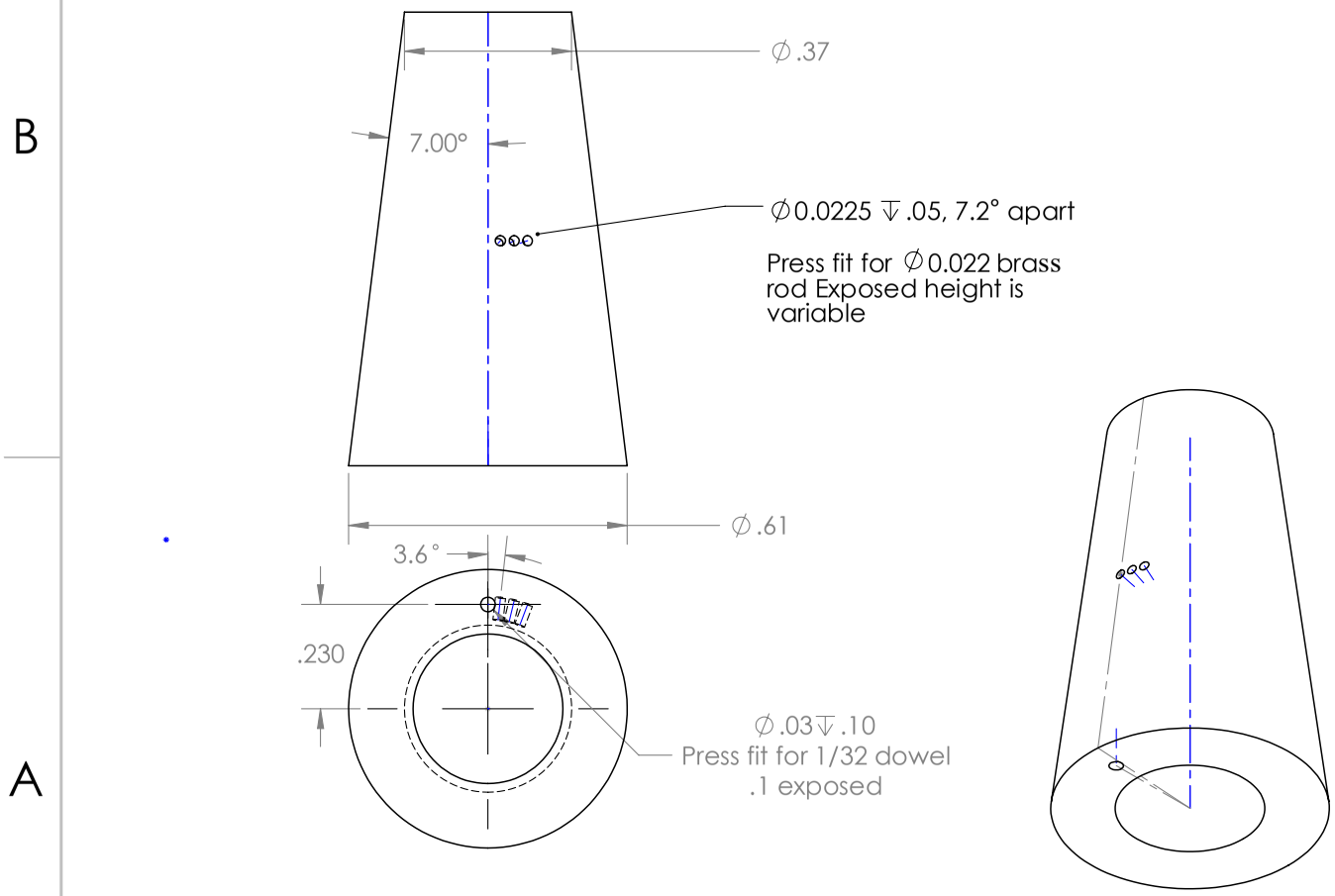

RIM Insert	Material: Aluminum	All dimensions in inches